UC Berkeley
UC Berkeley Electronic Theses and Dissertations

Title
Galaxies through Cosmic Time: The Role of Molecular and Atomic Gas

Permalink
https://escholarship.org/uc/item/9nm5390d

Author
Bauermeister, Amber

Publication Date
2012

Peer reviewed|Thesis/dissertation

eScholarship.org Powered by the California Digital Library
University of California

Galaxies through Cosmic Time: The Role of Molecular and Atomic Gas

By

Amber Nicole Bauermeister

A dissertation submitted in partial satisfaction of the

requirements for the degree of

Doctor of Philosophy

in

Astrophysics

in the

Graduate Division

of the

University of California, Berkeley

Committee in charge:

Professor Leo Blitz, Chair
Professor Chung-Pei Ma
Professor Carl Heiles
Professor Bernard Sadoulet

Fall 2012

Galaxies through Cosmic Time: The Role of Molecular and Atomic Gas

Copyright 2012
by
Amber Nicole Bauermeister

Abstract

Galaxies through Cosmic Time: The Role of Molecular and Atomic Gas

by

Amber Nicole Bauermeister

Doctor of Philosophy in Astrophysics

University of California, Berkeley

Professor Leo Blitz, Chair

In the past decade, molecular gas observations have begun probing the high redshift universe in a systematic way using increasingly powerful millimeter instruments. This work has significantly advanced our understanding of the history of gas consumption by star formation in galaxies, revealing the high redshift universe to be similar in many ways to what we know locally. Specifically, molecular gas studies suggest that at both high and low redshift, the molecular gas reservoir in galaxies is insufficient to support on-going star formation. This is the molecular gas depletion problem, and motivates the research presented in this dissertation.

I first investigate the molecular gas depletion problem on cosmic scales. Using the observed cosmic densities of the star formation rate, atomic gas and molecular gas, combined with measurements of the molecular gas depletion time in local galaxies, I derive the history of gas consumption by star formation from $z = 0$ to $z \sim 4$. I show that models in which the molecular gas is not replenished, or is only replenished by atomic gas, are not consistent with observational constraints. I find that star formation on cosmic timescales must be fueled by intergalactic ionized gas at an average rate that roughly traces the star formation rate density of the universe. Further, I predict the volume averaged density of molecular gas to increase by a factor of 1.5 – 10 to $z \sim 1.5$ over the currently measured value, which implies that galaxies at high redshift must, on average, be more molecular gas-rich than they are at the present epoch, consistent with observations.

Next I focus on the observational constraints on the molecular gas content of galaxies from $z \sim 1 - 2$ to today. Recent observations suggest $z \sim 1 - 2$ galaxies harbor molecular gas reservoirs an order of magnitude larger than their local counterparts, implying significant evolution of the molecular gas content of galaxies over the past 8 billion years. However, this period of time has been relatively un-observed in molecular gas. To fill in this observational gap, I carry out the Evolution of molecular Gas in Normal Galaxies (EGNoG) survey, a study of molecular gas in 31 star-forming galaxies from $z = 0.05$ to $z = 0.5$.

With observations of the CO($J = 1 \rightarrow 0$) and CO($J = 3 \rightarrow 2$) rotational lines using the Combined Array for Research in Millimeter-wave Astronomy (CARMA), the EGNoG survey accomplishes two goals: tracing the evolution of the molecular gas content of galaxies at intermediate redshifts and constraining the excitation of the molecular gas in these galaxies. With 24 detections out of 31 observed galaxies, I calculate an average molecular gas fraction of 7-20% at $z \sim 0.05 - 0.5$, which is in line with observations at high and low redshift and agrees well with the evolution predicted by a simple empirical prescription for gas consumption by star formation in galaxies from $z \sim 1 - 2$ to today. The EGNoG observations of four galaxies at $z \approx 0.3$ (the gas excitation subsample) yield robust detections of both lines in three galaxies (and an upper limit on the fourth). I find an average line ratio, $r_{31} = L'_{\mathrm{CO}(3-2)}/L'_{\mathrm{CO}(1-0)}$, of 0.46 ± 0.07 (with systematic errors $\lesssim 40\%$), which implies sub-thermal excitation of the CO($J = 3 \rightarrow 2$) line. As the EGNoG galaxies are representative of the main sequence of star-forming galaxies, I extend this result to include main sequence galaxies at high redshift.

To support the observations carried out at CARMA as part of the EGNoG survey, I give two appendices. The first details the data reduction and flux measurement for the EGNoG survey, including a description of the use of polarized calibrators to calibrate data from single, linearly polarized feeds. In the second appendix, I describe the absolute flux calibration of CARMA data and the automated monitoring system I helped put in place in order to maintain a historical record of the flux of common calibrators.

Finally, I return to the gas depletion problem in the local universe. I carry out a pilot study of atomic (H I) gas in groups of galaxies in order to investigate the role of tidal interactions in transporting atomic gas from the outskirts of galaxy disks to the central regions so that it may replenish the molecular gas and fuel ongoing star formation. I image three groups of galaxies in the 21 cm line of H I with the Allen Telescope Array (ATA), detecting many galaxies not previously observed in H I as well as four previously undetected clouds of H I between galaxies that account for up to 3% of the H I reservoir of the groups. To investigate the potential role of this gas in the ongoing star formation in the group, I compare the mass of the detected H I gas in and between galaxies in the group to the estimated star formation rates of the group members.

"We travelled for Science, ...that mass of material, less spectacular,
but gathered just as carefully, hour by hour in wind, darkness and cold,
were striven for in order that the world may have a little more knowledge,
that it may build on what it knows instead of what it thinks."
– Apsley Cherry-Garrard, *The Worst Journey in the World*

Contents

List of Figures

List of Tables

Acknowledgments

This dissertation is the culmination of many years of work, and would not have been possible without the help and support of a vast array of people.

First, I'd like to thank my research advisor, Leo Blitz, who introduced me to the often under-appreciated field of gas in galaxies, which forms the core of this work. His passion for astronomy and life in general has been an inspiration to me, and his guidance, from radio observations to what to eat and drink in locales around the world, has been invaluable. I would also like to thank all my co-authors for their contributions, scientific and otherwise, to this dissertation. Specifically, I'd like to thank Chung-Pei Ma for her guidance as my academic advisor as well as her help with the cosmological implications of this work, and the entire EGNoG team for the technical knowledge and scientific insight that has been critical to the project: Alberto Bolatto, Mel Wright, Peter Teuben, Martin Bureau, Tony Wong, Adam Leroy, Eve Ostriker, and Kevin Bundy. I further thank my thesis committee members, Chung-Pei Ma, Carl Heiles, and Bernard Sadoulet for helping shape this project in its early stages and for reviewing the results.

The bulk of my work at UC Berkeley has involved observing at radio wavelengths, and I cannot sufficiently express my gratitude for the unparalleled community of radio astronomers at Berkeley and associated observatories. First I have to thank Dick Plambeck and Mel Wright for my introduction to radio astronomy at the CARMA Summer School, and their continued assistance over the past several years. Further thanks to the MMM group and the PIRATES, Peter Williams, Statia Luzscz-Cook, Chat Hull, Garrett Keating, Steve Croft, Casey Law, and James McBride: sitting in a room with all of you has been so helpful – I hope my presence was useful in return. Finally, I want to acknowledge specifically the Radio 101 cohort, Statia, Chat, Peter and Jonnie: we dreamed a dream and I think we succeeded... most importantly, we stretched regularly.

I must also thank the observers and staff at the observatories I have been a part of: CARMA and the ATA. Without all of you, the work of this dissertation would not have been possible. At the ATA, I thank all the staff that kept it running for the time it did, and especially thank Samantha Blair and Rick Forster. At CARMA, I'd like to thank Cecil for feeding me so well, and Nikolaus Volgenau for, at times, single-handedly keeping CARMA running, and supporting the observers, who have a difficult and sometimes thankless job. Further, thanks to the graduate students that taught me how to be an observer at CARMA, Lisa Wei and Holly Maness, and also to my frequent co-observers, Statia and Chat, who

helped keep things fun through those long weeks at the high site. I'd like to acknowledge the members of the CARMA fluxcal team as well, who taught me more than I ever thought I'd know about flux calibration, and gave me the opportunity to learn how to run telecons – I hope I served you all well.

I want to thank all the BADgrads for maintaining the strong community of graduate students that I have been privileged to be a part of these past six years. Also, many thanks to Dexter Stewart for all her help with everything – she's not a BADgrad, but the BADgrads would be lost without her. Special further thanks go to my graduate student mentor family and my office- and cubicle-mates, Anna, Statia, Yookyung, Sarah, Chat, and, of course, Charlie the dog. I am deeply grateful for all the amazing friendships I've developed in my time here, and would like to particularly acknowledge the members of my class, MONSTER, and the MONSTER spouses – it has been an amazing journey and I will miss you all so much. Of these, I'd like to especially thank Statia, who has been an incredible officemate, co-observer, scientific sounding board, figure line color selection analyst, and general partner in crime for many years – you've taught me a lot about being a good scientist and friend. After all, galaxies and Neptune are basically the same thing.

Finally, I'd like to thank my entire family: my grandparents, my many aunts, uncles and cousins and my parents-in-law have taught me so much over the years and their support has been invaluable. I offer special thanks to my sister, who has helped me to be a better person, and to my parents, who I cannot thank enough for their unwavering support and the amazing example they've set in their own lives – I would not be the person I am without them. Lastly, I thank my husband, Skyler, who has been by my side these past six years and more. Thank you for your confidence and encouragement, and for being my constant companion in all our adventures – I cannot wait for all our future adventures together.

Chapter 1

Introduction

1.1 Astronomy: the Study of Light

Astronomy is unique among the physical sciences in that we cannot influence the objects and phenomena we study. While a physicist may set up an experiment in a controlled environment to test a hypothesis, an astronomer has no such control. For instance, we have no power over our position relative to the object we study, which has been a significant obstacle in our attempts to understand the astronomical environment we live in. Careful observation and analysis were required to determine that the Earth and other planets rotate around the Sun from our observation point here on Earth. Similar feats of observation and insight were required in the interpretation of the Milky Way painted across the night sky. From our humble position on Earth, astronomers determined that the Milky Way is a galaxy, similar to others in the universe, and that our Solar System is located not at the center, but in the disk, roughly two thirds of the way out from the center.

As astronomers, we are at the mercy of the universe: we must determine what we can from the information available to us. As this information consists almost exclusively of electromagnetic radiation, we begin with a brief discussion of light. Light boasts a dual nature: it behaves as an electromagnetic wave as well as a particle. A photon (a particle of light) travels at a constant, finite speed and can be described by the properties of its wave nature: the wavelength (the distance between crests of the wave) and the frequency (number of crests to arrive in some time frame). The product of the wavelength and the frequency is the speed of light.

The range of wavelengths that light can have is described by the electromagnetic spectrum. As shown in Figure 1.1, the electromagnetic spectrum goes from radio waves, with wavelengths the size of your hand and larger, to X-rays and γ-rays, with wavelengths the size of atoms and subatomic particles. Long wavelength light, like radio waves, has a low energy compared to short wavelength light, like X-rays, which has a high energy and can be harmful to humans as a result. Our eyes perceive only a small fraction of the spectrum, which we call visible or optical light. However, the photons emitted due to the various as-

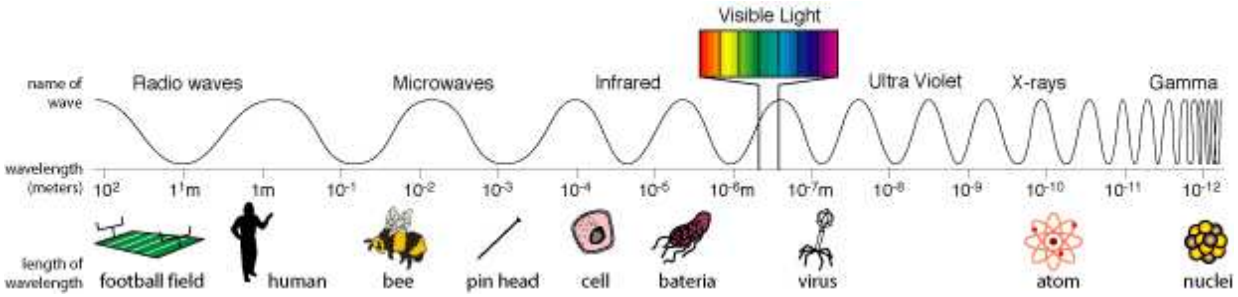

Figure 1.1: The electromagnetic spectrum. *Image credit: NASA*

trophysical phenomena currently studied cover the breadth the electromagnetic spectrum. Limiting astronomical observations to visible light would significantly hinder our understanding of the universe. As a result, a wide variety of detectors exist which are sensitive to the various wavelengths of light of interest.

In this Chapter, I introduce the concepts relevant to the work in this dissertation in order to both confer a basic understanding of the physics and astrophysics involved as well as place this work in the context of the field as a whole. As the research presented in subsequent chapters focuses on the relationship between gas and star formation in galaxies, I begin with an overview of the anatomy of a galaxy in Section 1.2. Having reviewed the overall structure of galaxies, I then focus on the cold gas component of galaxies in Section 1.3, discussing both the physical mechanisms that allow us to observe this gas and how we detect the light emitted by these mechanisms. For each type of cold gas, I briefly review where the gas is found in typical galaxies and the significance of this distribution. In Section 1.4, I explain how the evolution of galaxies over the history of the universe is observed and discuss the role of cold gas in this evolution. I describe the gas depletion problem, which motivates the research in this dissertation. I give an outline of the rest of this dissertation in Section 1.5.

1.2 Anatomy of a Galaxy

1.2.1 Visible

We will first discuss the details of galaxies that are revealed to us in the visible portion of the electromagnetic spectrum. The appearance of galaxies in visible light ranges widely, from smooth, spherical objects to those with loosely wound spiral arm structure. This wide array of observed galaxies was classified systematically in 1926 by Edwin Hubble (Hubble 1926) into three morphological categories: elliptical, spiral and irregular. The irregular classification serves as a repository for any galaxies which do not conform to a spiral or elliptical morphology (e.g. merging galaxies). The types of spiral and elliptical galaxies are typically represented in the 'Hubble tuning fork' diagram, shown in Figure 1.2.

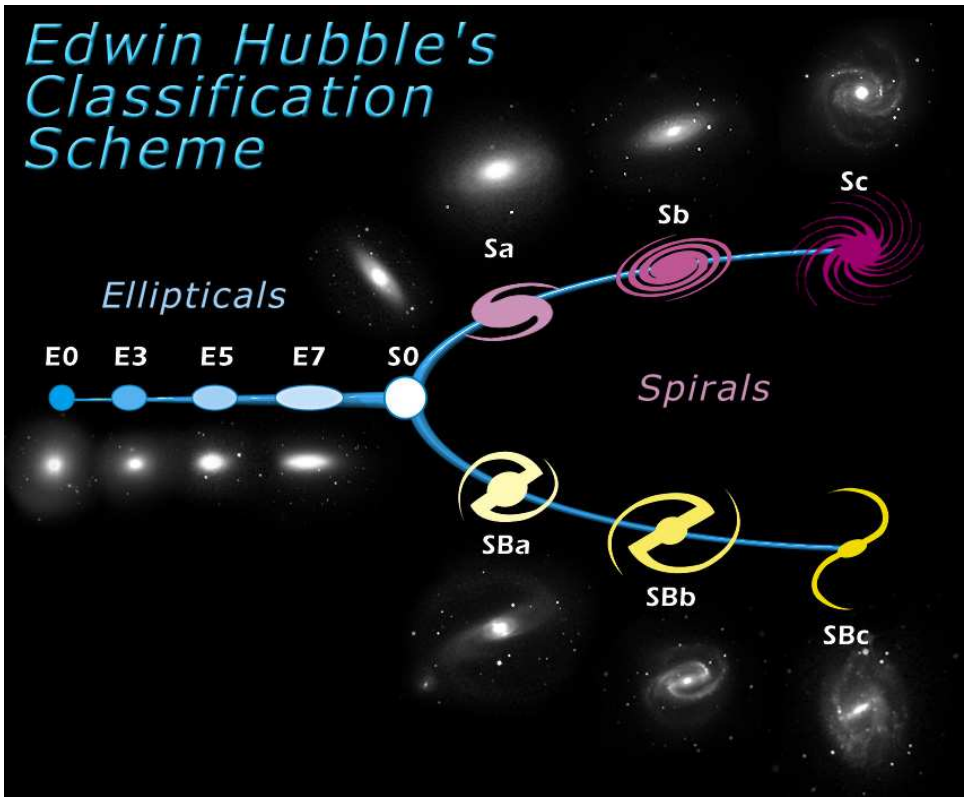

Figure 1.2: An example of the 'Hubble tuning fork' diagram. Elliptical galaxies are on the left, going from nearly spherical (E0) to flattened (E7). The S0 class marks the transition between elliptical and spiral galaxies. Spiral galaxies (on the right) are split into two classes: normal spirals (top) or barred spirals (bottom). In each sequence, the galaxies further to the right (Sc and SBc) show a smaller bulge and more extended (loosely wound) spiral arms. *Image credit: SDSS*

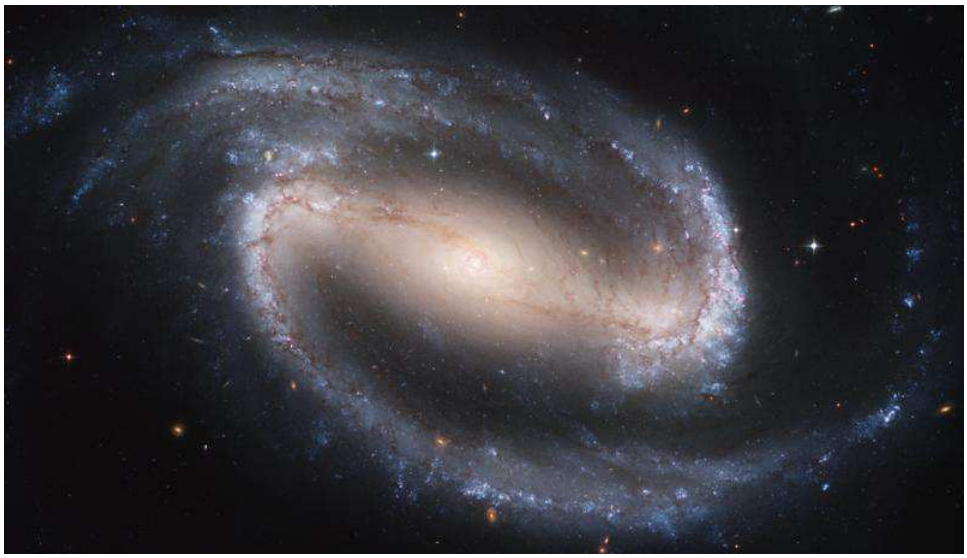

Figure 1.3: NGC 1300, a barred spiral galaxy, in visible light. The bright yellow center shows the bulge, composed of old stars, in contrast to the blue spiral arms in which stars are forming. The dark filaments along the bar and spiral arms show dust obscuring the star light. *Image credit: NASA, ESA, and The Hubble Heritage Team (STScI/AURA)*

On the left is the sequence of elliptical galaxies, going from nearly spherical (E0) to flattened (E7). Elliptical galaxies show a smooth brightness distribution and are composed of old stars, with little to no formation of new stars. The lack of young stars means that elliptical galaxies appear red since old (cool) stars emit most of their light in the red portion of the spectrum. Between elliptical and spiral galaxies lies the S0 class (also known as lenticular galaxies). These galaxies show a bright central bulge like elliptical galaxies as well as a more extended disk, as seen in spiral galaxies, but without spiral structure.

Spiral galaxies, which comprise the right half of Figure 1.2, are split into two sequences: normal spirals and barred spirals. In both cases, the stars in the galaxy are organized in two components: a spheroidal bulge (similar to elliptical galaxies) and a flat, extended disk. In barred spirals, a bar-like structure is observed between the bulge and the spiral arms. Moving from the Sa to Sc classification, the bulge becomes less prominent and the spiral arms become less tightly wound. In contrast to elliptical galaxies, spiral galaxies tend to be actively forming new stars. This gives spiral galaxies a blue appearance since young, massive, hot stars emit most of their light in the blue portion of the spectrum.

As an illustration of the information carried by the visible spectrum, Figure 1.3 shows the barred spiral galaxy NGC 1300 in visible light. First, the color of the different parts of the galaxy reveals the type of stars present: the spiral arms appear blue, indicating the ongoing formation of young, hot stars while the central bulge appears redder (somewhat yellow-orange) since it is composed of old, cool stars. Further, we see evidence of dust in this galaxy: while this image does not show light emitted by the dust directly, the presence

of dust is indicated by the obscuration of starlight in thin filaments along the bar and spiral arms. Finally, by restricting our view to specific wavelengths of red light, we can observe Hα emission, which is a particular wavelength (6563 nanometers) of light that is emitted by hot gas around young stars. In Figure 1.3, the small pink dots show Hα emission, identifying individual regions containing newly formed stars. However, while visible light gives us information about the stars, dust and star formation in a galaxy, it does not paint a complete picture of galaxy structure.

1.2.2 Invisible

Two components of a galaxy are actually not directly observable in any wavelength of light: black holes (by definition, light cannot escape their extreme gravity) and dark matter, which only interacts with its surroundings through gravity. In both cases, astronomers have inferred the presence of these dark components through their gravitational pull on nearby visible matter, like stars. In the Milky Way, the orbits of stars at the center of the galaxy suggest that a supermassive black hole with a mass 4 million times that of the Sun resides there, within a region smaller than Mercury's orbit around the Sun (Ghez et al. 2008). The presence of dark matter is inferred from the orbital velocity of stars and gas in the outer regions of galaxies. At large radii from the center of a galaxy, stars and gas are observed to move faster than predicted from the distribution of visible matter. Thus, there must be some invisible (dark) matter component of the galaxy that influences the orbits of the stars and gas through gravity. In other words, each galaxy sits within a large halo of dark matter.

1.2.3 Invisible to our Eyes, but not to our Instruments

By expanding our view to wavelengths of light outside of the visible portion of the electromagnetic spectrum, a new side of galaxies is revealed: the gaseous component, referred to as the inter-stellar medium in galaxies or the inter-galactic medium between galaxies. Most (roughly 75%) of the gas is made up of Hydrogen (composed of one proton and one electron), which comes in three forms: ionized, atomic and molecular, illustrated in Figure 1.4.

Ionized gas, in which the protons and electrons are unbound, is hot and diffuse. In the disk of a spiral galaxy, it is found around young, hot stars, which emit high-energy photons that ionize the surrounding gas. As the ionized gas naturally recombines to form Hydrogen atoms, recombination lines, such as Hα, are emitted at particular wavelengths corresponding to energy differences between the allowed energy levels of the Hydrogen atom. Hot ionized gas is also found outside of galaxies, in the form of a spherical halo of ionized gas around individual galaxies as well as a reservoir of hot gas in the centers of galaxy clusters. One method of observing this hot, ionized gas is in X-rays, which are emitted via Bremsstrahlung (German for "braking radiation"). As the protons and electrons move around in the ionized gas, the electromagnetic attraction between the positive and negative

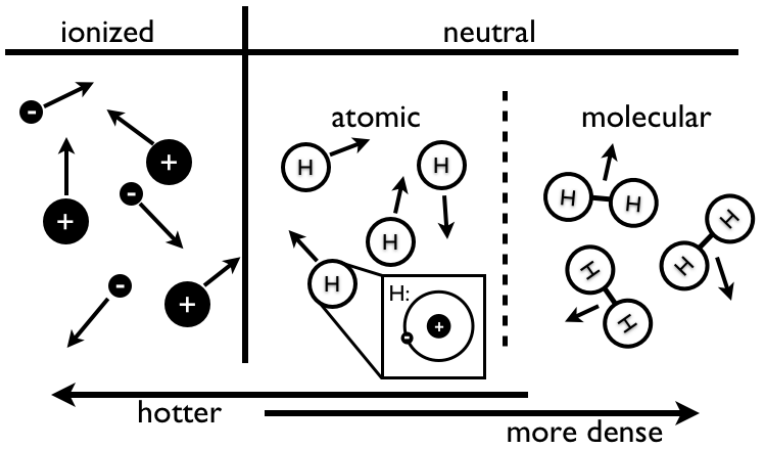

Figure 1.4: Ionized, atomic and molecular Hydrogen gas. In ionized gas, the proton (+) and electron (-) are not bound to one another. In neutral gas, the protons and electrons are bound in Hydrogen (H) atoms. Neutral gas may come in the form of atomic gas (composed of Hydrogen atoms) or molecular gas (in which Hydrogen atoms are bound in Hydrogen molecules, H_2). In galaxies, ionized gas is hot and diffuse while atomic and molecular gas is cooler and increasingly dense.

charges will accelerate the particles as they pass close to one another, which produces ultraviolet and X-ray photons.

In contrast to the ionized gas, neutral gas is cooler and denser. In neutral gas, the protons and electrons are bound in Hydrogen atoms (atomic gas). If the gas becomes cool and dense enough, the Hydrogen atoms will combine to form H_2 molecules, in which two Hydrogen atoms are joined by a covalent bond. As neutral gas is the focus of this disseration, we discuss it in detail in Section 1.3. We conclude our tour of the structure of galaxies in this section by noting that neutral gas is found mainly in the disks of spiral galaxies. While elliptical galaxies can harbor some neutral gas, it is very little, so we will focus on the neutral gas in spiral galaxies.

1.2.4 Summary

Through observations at various wavelengths of light and inferences from the motion of visible matter, the following simple picture of a galaxy has emerged. Each galaxy resides in a spherical dark matter halo. The stars are distributed in an elliptical distribution or a combination of a spheroidal distribution (the bulge) and a disk. In both cases, a massive black hole likely resides at the center. Finally, the gaseous component consists of three states: ionized, atomic and molecular. While ionized gas is found near young, hot stars and surrounding the disk, the atomic and molecular gas is mainly confined to the disk.

We have described the main components of galaxies, but one important consideration

remains: environment. Galaxies are not isolated systems. Most galaxies are part of a group of a few to tens of galaxies or a cluster of hundreds or thousands of galaxies. Gravitational interactions between galaxies in a group or cluster can have a significant effect on the structure of the involved galaxies, ranging from the minor disruption of the atomic gas disk to the merger of two galaxies, in which the structure of both systems is completely re-arranged to form a new galaxy.

1.3 Cold Gas

1.3.1 Observing Cold Gas

With a general picture of galaxy structure in mind, we now revisit and discuss in detail the cold (neutral) gas component of galaxies. First, we describe the physical mechanisms typically exploited to observe atomic and molecular gas. We then give a brief description of how these long wavelength phenomenon are observed. Finally, we revisit the distribution of the atomic and molecular gas in spiral galaxies and discuss the significance of each component to our understanding of the life of a galaxy.

Physical Mechanism

Neutral gas is cold: the temperature of the atomic gas in galaxies is typically only 100 degrees Kelvin (-173 °C). Colder still is the molecular gas, which can get as cold as tens of degrees Kelvin above absolute zero. The cool temperature of the gas means that it emits photons which have very low energies. Thus, we observe atomic and molecular gas at long wavelengths, in the radio portion of the electromagnetic spectrum.

We can observe the atomic Hydrogen gas directly via the 21 cm (or, in frequency, 1.42 GHz where GHz = 10^9 cycles per second) emission line of the Hydrogen atom, the spin-flip transition. In a Hydrogen atom, the proton and electron each have an associated quantum mechanical spin. The state in which the spins are parallel has a slightly higher energy than the state in which they are anti-parallel. As a result, if the spin of the electron or proton spontaneously flips, causing the spins to go from being parallel to anti-parallel, the atom has gone from a higher to a lower energy state, and gives off this excess energy in the form of a 21 cm photon. While this spontaneous spin flip is extremely unlikely to occur for any given Hydrogen atom (about once every 10 million years), there are so many Hydrogen atoms in a galaxy that it occurs frequently: for example, the Milky Way contains roughly 5×10^9 solar masses of atomic gas (Dame 1993), which corresponds to 10^{67} Hydrogen atoms. So in the Milky Way, approximately 10^{52} spin flip transitions occur every second!

In the study of molecular gas, astronomers take advantage of the rotational transitions of molecules. A rotating molecule has some amount of angular momentum, which is quantized. This means that a molecule can either not rotate, or rotate at the lowest allowable rate, or at the second lowest allowable rate, etc. Faster rotation rates correspond to higher energy so

that (similar to the 21 cm transition of Hydrogen atoms) if a molecule spontaneously drops from a higher rotational energy state to a lower one, a photon will be emitted carrying the energy difference. Unfortunately, since a Hydrogen molecule (composed of two Hydrogen atoms) is perfectly balanced, its rotational transitions (quadrupole transitions) are very weak. However, in the carbon monoxide molecule (CO, the second most abundant molecule in the inter-stellar medium) is polar. This means that the center of electric charge is offset from the center of mass (about which the molecule rotates), which results in a strong (dipole) rotational transition. Therefore, we use observations of the rotational transitions of the CO molecule (at mm wavelengths, or, equivalently, frequencies in the hundreds of GHz) to trace the distribution of molecular gas.

Observation

In order to observe the long wavelength (low frequency) photons discussed above, we employ a technique more similar to an AM/FM radio than to a digital camera. The atomic Hydrogen line at 1.42 GHz lies between the FM radio band (around 0.1 GHz) and the frequency used to excite water molecules in a microwave oven (2.5 GHz). In this modern age of wireless communication, these frequencies are becoming increasing populated: cellular phone communication, for example, uses various frequencies between 0.5 and 3 GHz. These terrestrial signals are booming compared to weak astronomical signals, so that the detection of astronomical emission at these frequencies is becoming increasingly dependent on how well we can remove the unwanted signal (termed radio frequency interference, or RFI). For now, the higher frequencies at which we observe the rotational transitions of the CO molecule (the lowest frequency transition is at 115 GHz or 3 mm) remain relatively free of RFI.

The simple dipole antenna, as used by your car radio, would be sufficient to observe the radio frequencies of interest for studying cold gas. However, in the midst of the terrestrial noise described above it is important that an antenna for astronomical purposes be able to point at the object of interest and isolate the signal from that object, blocking out unwanted emission. These requirements give rise to the dish-shaped radio antenna, which is sensitive (almost exclusively) to the small area of the sky at which it is pointed. The size of the patch of sky to which an antenna is sensitive is inversely related to the size of the antenna: a larger dish is sensitive to a small region, a small dish is sensitive to a large region. Therefore, with a single radio antenna, you may essentially take a picture of your object of interest, but the resulting image only has one pixel, the size of which is determined by the size of your antenna. While much science can and has been done in this way, we would naturally like to make multi-pixel images of astronomical objects in order to resolve the spatial structure of the emission. This can be done in two ways: first, by pointing a single antenna at multiple positions, we can build up a multi-pixel image by imaging the object one pixel at a time. The second method, which we use extensively in this work, is to observe the object of interest with an array of many of antennas and calculate the multi-pixel image by correlating the signals from all the antennas. This process is radio

interferometry. Both single dish and interferometer observations in the last 60 years have revealed the complex structure of the cold gas in the Milky Way and other galaxies.

1.3.2 Distribution

Atomic Gas

In spiral galaxies, the atomic gas disk can be very large, extending outward well past the stellar disk, as shown in Figure 1.5: the left panels show the stars and the right panels show atomic gas in two nearby spiral galaxies, NGC 3184 and NGC 3198. This gas, at large distances from the center of the galaxy, is particularly susceptible to gravitational disruption by close encounters with other galaxies. In fact, in many cases, while the stars remain unperturbed, the atomic gas shows evidence of interaction. The M81 group of galaxies is an example of this, as illustrated by the optical and atomic gas images shown in Figure 1.6. Thus observations of atomic gas in galaxies and groups of galaxies can reveal a history interactions between galaxies that may not be evident in the optical images.

Aside from the debris left from interactions between galaxies, a significant amount of atomic gas is also detected around the Milky Way and other nearby galaxies in the form of small clouds which appear to be raining down on the disks of these galaxies. These clouds of atomic gas are observed at higher velocities than the disk gas (which indicates they are disconnected from the disk), and are thus termed 'high velocity clouds'. These clouds are thought to be due to a combination of infall of cooling gas from the hot, ionized gas halo and the galactic fountain mechanism, in which gas is blown out of the disk by vigorous star formation and supernovae and slowly returns to the disk as it cools. Thus observations of these clouds of atomic gas provide important constraints on the rate of infall of gas onto the disk.

Molecular Gas

Unlike atomic gas, the molecular gas is confined to the stellar disk, as shown in the middle panels of Figure 1.5. The molecular gas is not smoothly distributed, but instead is assembled into gravitationally bound clouds, the most massive of which are termed giant molecular clouds. The more massive the cloud, the denser the center can become under the weight of the outer layers. If the center of a molecular cloud becomes sufficiently cold and dense so that the gravitational pull can overcome the pressure from turbulence and magnetic fields, the core can collapse under the weight of the cloud to form a star. Thus, giant molecular clouds are the birthplace of stars. Molecular gas is the building block from which stars, and by extension, galaxies are formed.

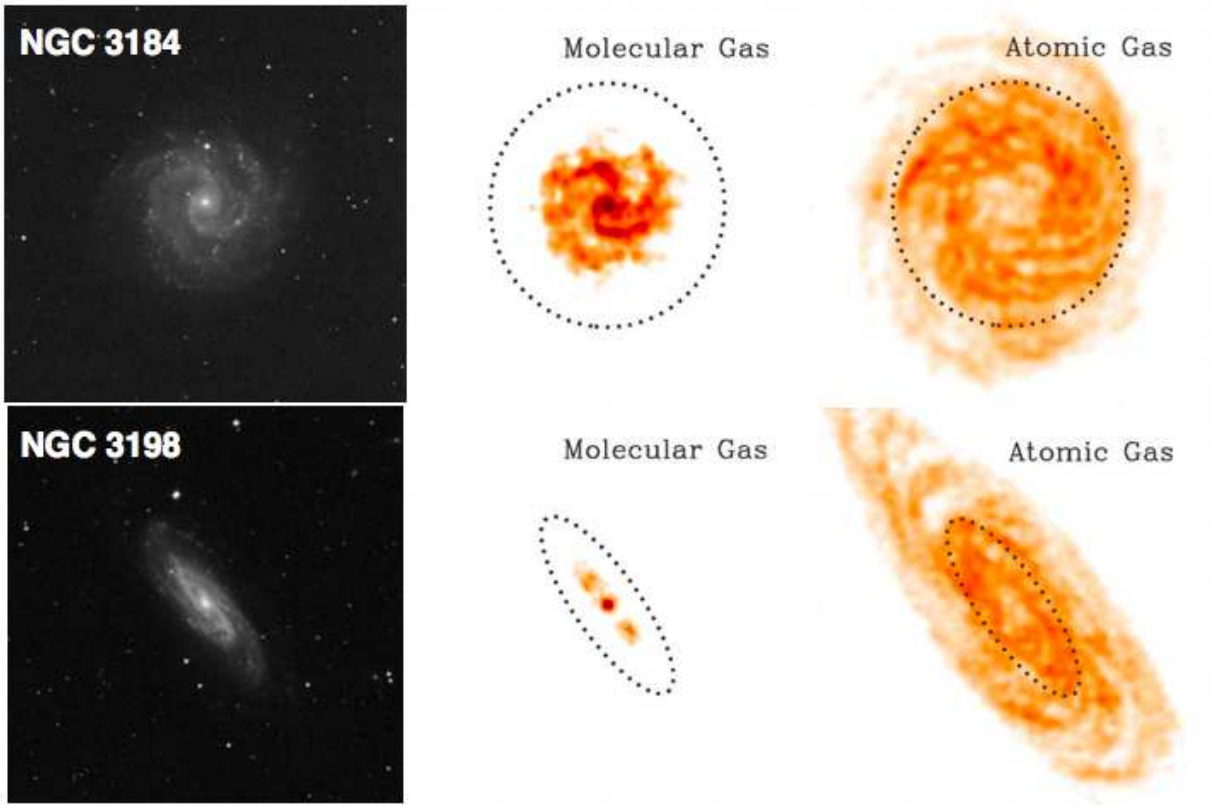

Figure 1.5: Neutral gas in spiral galaxies. For spiral galaxies NGC 3184 and NGC 3198, we show the optical image in the left panels, the molecular gas in the middle panels and the atomic gas in the right panels. *Image credit: STScI Digitized Sky Survey (left), Leroy et al. 2008 (middle and right)*

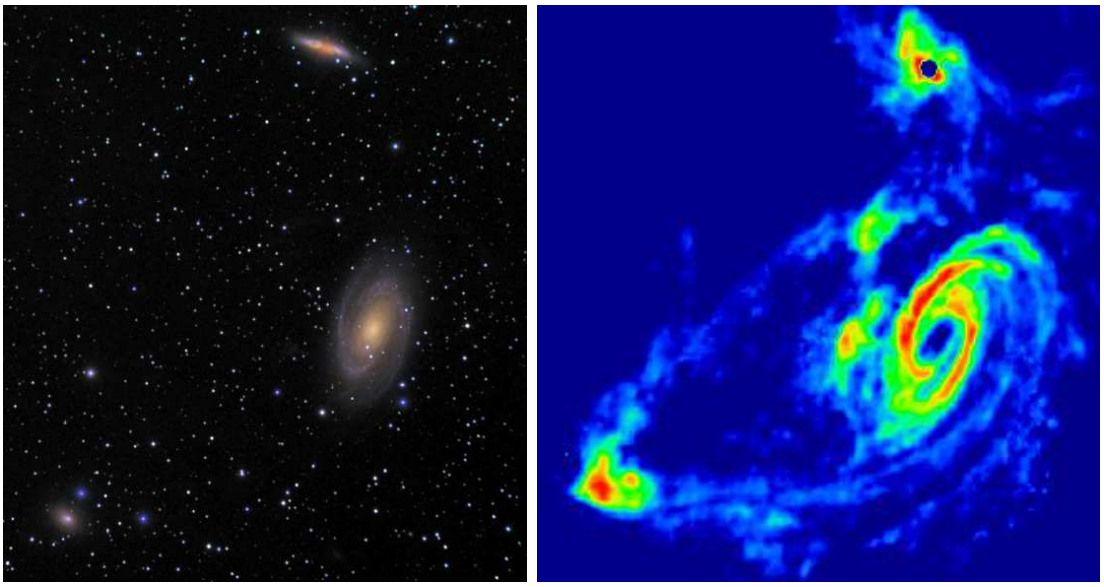

Figure 1.6: M81 group of galaxies. The optical image in the left panel shows the three members of the group seemingly undisturbed. The image of the atomic gas in the right panel presents a much different picture of strong gravitational interaction between the galaxies. *Image credit: Dick Miller Images / Min Yun (Yun et al. 1994)*

1.4 Evolution of Galaxies

Galaxies evolve over timescales of billions of years. Therefore, we cannot learn about the evolution of galaxies by watching a single galaxy: even a long human timescale of 100 years is insignificant in the context of the life of a galaxy. However, due to the finite speed of light, astronomers are privileged with the unique ability to look back in time. The further away an object is, the longer it takes for its light to reach us, so that we see the object as it was when the light was emitted. For example, observations of a galaxy 2 billion light-years away show what that galaxy looked like 2 billion years ago. Thus, astronomers deduce the evolutionary journey of galaxies over the lifetime of the universe from snapshots of different galaxies at different points in time.

When observing distant galaxies, how long ago the light was emitted depends on how far away the galaxy is. While this is a simple calculation in a normal scenario (distance = velocity $\times$ time), in the astrophysical context presented here, it becomes complicated by the fact that the universe is expanding. Thus, the distant galaxy is moving away from us when it emits the photon and subsequently, while the photon is traveling to us, the universe through which the photon travels is expanding. As a result, the photon is Doppler shifted to longer (redder) wavelengths. This shift is referred to as the redshift. This phenomenon has two important implications. First, the redshift of the observed photons (in combination with an understanding of the expansion of the universe) tells us the distance to the galaxy,

and thus how long ago the galaxy looked the way we observe it today. High-redshift refers to early times in the history of the universe and low-redshift refers to relatively recent times. Second, comparing the emission of a particular wavelength of light in high and low redshift galaxies becomes complicated by the fact that the *observed* wavelengths will be different. While emission at particular wavelength of light may be simple to observe in nearby galaxies, observation of the same emission from high-redshift galaxies may require a different instrument or may be impossible altogether due to insufficient observing technology at the required wavelength or the Earth's atmosphere blocking all incoming electromagnetic radiation at the required wavelength. Further complicating observations of high-redshift galaxies is the difficultly of resolving very distant objects, which will appear smaller corresponding to their distance. Despite these challenges, much progress has been made in the past decade in unveiling the nature of galaxies at early times in the history of the universe.

While the evolution of each component of galaxies is an active area of research deserving a detailed discussion, we continue to focus on the cold gas in galaxies as we discuss the evolution of galaxies. Specifically, we investigate the relationship between the gas and star formation rate in galaxies at high redshift and low redshift.

1.4.1 The Gas Depletion Problem

Looking back in time, the star formation rate of the universe is observed to increase dramatically, peaking around 10 billion years ago, when the universe was only 3.7 billion years old. This peak in the star formation rate marks the height of galaxy building, when most of the stars in present-day galaxies were formed. In the local universe, studies of spiral galaxies have found the star formation rate to be proportional to the mass of molecular gas: galaxies with more molecular gas form more stars per year. If this relation holds true at high-redshift as well, we would expect high-redshift galaxies to harbor massive reservoirs of molecular gas, in proportion to their higher star formation rates.

Recent studies of molecular gas are now showing this prediction to be true: highly star-forming galaxies at high-redshift are observed to contain proportionally more molecular gas than the moderately star-forming galaxies observed in the local universe. In fact, the ratio of the molecular gas mass to the star formation rate appears roughly constant over the past 10 billion years. This ratio is the molecular gas depletion time, roughly equal to the amount of time a galaxy can form stars at the current rate given the available molecular gas reservoir. For normal star-forming galaxies at low and high redshift, the molecular gas depletion time is observed to be roughly 2 billion years. This brings us to the molecular gas depletion problem: how has star formation continued over the past 10 billion years when a given galaxy has only enough molecular gas to sustain star formation for 2 billion years? As stated above, the average star formation rate in the universe has decreased significantly in the past 10 billion years, but it has not declined in the dramatic way that a 2 billion year molecular gas depletion time would predict.

The solution to the gas depletion problem appears simple: the molecular gas reservoir in galaxies must be replenished in some way. In detail, this is a complex, multi-faceted issue. Obvious initial questions include the following: How much gas is required to replenish the molecular gas and maintain star formation? How does this change from high-redshift to low-redshift? What is the source of this gas and how is it transported to the star-forming regions of galaxies? The research presented in this dissertation aims to constrain the answers to these questions, investigating the gas depletion problem from a theoretical standpoint by building a simple model of cosmic gas consumption as well as from an observational standpoint, constraining the properties of the atomic and molecular gas in galaxies at high and low redshift.

1.5 Dissertation Outline

In Chapter 2, I examine the gas depletion problem on cosmic scales. Building a simple model of mass flow from ionized gas to atomic gas to molecular gas to stars, I use the observed average star formation rate and atomic gas density of the universe as a function of redshift to predict the molecular gas content of high-redshift galaxies as well as the required average inflow rate of ionized gas. In a restricted model that does not allow the molecular gas reservoir to be replenished, I find that the average star formation rate of the universe should be declining twice as fast as observed. This discrepancy is resolved by including the replenishment of the molecular gas reservoir by the ionized gas at a rate equal to the star formation rate. This model predicts enhanced molecular gas fractions in high-redshift galaxies, which is corroborated by observations of molecular gas in redshift $1-2$ galaxies.

As discussed above and in Chapter 2, the molecular gas content of galaxies at all redshifts is an important constraint on the evolution of galaxies. The molecular gas in galaxies in the nearby universe has been relatively well-studied, and recent work by two groups (Daddi et al. 2010; Tacconi et al. 2010) has begun to fill in our knowledge at high redshift. However, the intermediate redshifts, from 8 billion years ago to today, remain relatively un-studied. In order to fill in this observational gap, I have undertaken the Evolution of molecular Gas in Normal Galaxies (EGNoG) Survey with the Combined Array for Research in Millimeter-wave Astronomy (CARMA). This survey traces the molecular gas in intermediate redshift galaxies ($z = 0.05 - 0.5$) using rotational transitions of carbon monoxide (CO). In Chapter 3, I describe the sample selection, observations and resulting detections of the EGNoG Survey. In Chapter 4, I use the results of the EGNoG Survey to fill in the picture of the evolution of the molecular gas content of galaxies over the past 10 billion years. I construct a simple model of star formation in galaxies in order to place the observations in the context of our current understanding. In Chapter 5, I discuss the gas excitation sample of the EGNoG survey. Using observations of two rotational transitions of the CO molecule in four galaxies, I constrain the excitation of the gas in star-forming galaxies at redshift 0.3, which is necessary to the interpretation of work at higher redshift.

Next, I return to the local universe and investigate the role of environment in the gas depletion problem. Galaxies typically have large reservoirs of atomic gas in the outskirts of the disk, but it must be moved into the center in order to be used to form stars. One way to move gas inwards is by removing angular momentum through gravitational interactions between galaxies in groups. In Chapter 6, I use the Allen Telescope Array to image the atomic gas in groups of galaxies to look for evidence of interactions between group members. While I find evidence for atomic gas between galaxies, likely as a result of interaction, the mass of inter-galaxy gas is not sufficient to significantly extend the gas depletion time in these systems.

The work presented in Chapters 3 through 6 could not have been carried out without a deep understanding of the details of observation using a radio interferometer. In Appendix A, I explain the reduction and analysis of the EGNoG data from CARMA. One challenge of the reduction involved using significantly polarized sources to calibrate a system that is not designed to observe polarization. This is discussed specifically in Section A.3. Finally, as good calibration is necessary for trustworthy observations, I give an overview of the monitoring of calibrator fluxes at CARMA in Appendix B. As part of the flux calibration on science tracks team, I helped build an automated system for the ongoing monitoring of calibrators at CARMA, critical to maintaining a historical record of fluxes. This system is described in Appendix B.

Chapter 2

The Gas Consumption History to Redshift 4

Using the observations of the star formation rate and H I densities to $z \sim 4$, with measurements of the Molecular Gas Depletion Rate (MGDR) and local density of H_2 at $z = 0$, we derive the history of the gas consumption by star formation to $z \sim 4$. We find that closed-box models in which H_2 is not replenished by H I require improbably large increases in $\rho(H_2)$ and a decrease in the MGDR with lookback time that is inconsistent with observations. Allowing the H_2 used in star formation to be replenished by H I does not alleviate the problem because observations show that there is very little evolution of $\rho_{HI}(z)$ from $z = 0$ to $z = 4$. We show that to be consistent with observational constraints, star formation on cosmic timescales must be fueled by intergalactic ionized gas, which may come from either accretion of gas through cold (but ionized) flows, or from ionized gas associated with accretion of dark matter halos. We constrain the rate at which the extragalactic ionized gas must be converted into H I and ultimately into H_2. The ionized gas inflow rate roughly traces the SFRD: about 1 – 2 $\times 10^8$ $M_\odot$ Gyr^{-1} Mpc^{-3} from $z \simeq 1 - 4$, decreasing by about an order of magnitude from $z = 1$ to $z = 0$ with details depending largely on MGDR(t). All models considered require the volume averaged density of ρ_{H_2} to increase by a factor of 1.5 – 10 to $z \sim 1.5$ over the currently measured value. Because the molecular gas must reside in galaxies, it implies that galaxies at high z must, on average, be more molecule rich than they are at the present epoch, which is consistent with observations. These quantitative results, derived solely from observations, agree well with cosmological simulations.[1]

[1]This chapter has been previously published as Bauermeister, Blitz & Ma 2010, ApJ, 717, 323, and is reproduced with the permission of all coauthors and the copyright holder. Copyright 2010 American Astronomical Society.

2.1 Introduction

The time variation of the mean star formation rate in galaxies is by now well established (Madau et al. 1996; Steidel et al. 1999; Hippelein et al. 2003; Hopkins & Beacom 2006). The star formation rate is either flat or slowly rising with time, reaching a maximum near $z \sim 1 - 2$, and then declines precipitously down to the current epoch. This change in the star formation rate must be closely coupled to both the inventory of gas available for star formation, and the way in which this gas is channeled into galaxies.

Stars condense only from molecular gas at the current epoch and at all epochs in the past. This statement derives from both observational and theoretical considerations. Observationally, the youngest stars are always found to be associated with their nascent molecular material both in the local Universe and at high z (e.g. Blaauw 1964; Herbig & Kameswara Rao 1972; Schwartz et al. 1973; Omont et al. 1996; Carilli et al. 2002). The interstellar gas in star forming regions is almost completely molecular, representing a stable phase of the ISM with little atomic content (Burton et al. 1978). Theoretically, there is general consensus that the initiation of star formation requires the nascent gas to become Jeans unstable, probably mediated by magnetic fields (Shu et al. 1987). In star forming regions, T is typically 10 - 20 K, but in any event cannot be less than 2.7 K. In order to get a solar mass star at 10 K, the Jeans instabiliy criterion would require a density of $\rho_J > (kT/\mu m_H G)^3(\pi^5/36M_J^2) \sim 10^6 \mathrm{cm}^{-3}$ if a molecular core forms a star at 100% efficiency. The density must be higher if the efficiency is lower as many observations now suggest (e.g. Motte et al. 1998; Alves et al. 2007; Myers 2008). In order to reach these temperatures and densities, the gas must be fully molecular in order to achieve the necessary cooling. We would therefore expect that, in a broad sense, the gas consumption rate is closely tied to the star formation rate.

Unfortunately, there are few constraints on the gas from observations because little is known about the distribution of neutral gas at high z. There are very few detections of atomic gas in emission at $z \gtrsim 0.1$, and what little we know about the atomic gas comes from Lyman-alpha lines seen in absorption toward quasars and radio-loud AGN (e.g. Prochaska & Wolfe 2009; Wolfe et al. 2005; Zwaan & Prochaska 2006). Molecular line observations at high-z have been largely limited to the brightest objects, though some recent observations at $z \sim 2$ have begun to probe lower luminosity systems (Förster Schreiber et al. 2009; Daddi et al. 2010; Tacconi et al. 2010).

Gas consumption by star formation in galaxies has been investigated previously via observations of the gas depletion time, $\tau_{dep} = M_{gas}/SFR$. This represents the amount of time it will take the galaxy to completely exhaust its gas supply at the current star formation rate. Studies of individual local disk galaxies find depletion times on the order of a few Gyr, much shorter than the Hubble time (e.g. Larson et al. 1980; Kennicutt et al. 1994). This is the gas depletion problem: without some form of gas replenishment, star formation in disk galaxies should be coming to an abrupt end. One proposed solution is stellar recycling, which Kennicutt et al. (1994) find can extend the gas depletion times in

many local disk galaxies by a factor of 1.5 to 4. Gas accretion has long been suggested as a solution to the gas depletion problem as well, and observational support for inflow is accumulating. Sancisi et al. (2008) review the observational evidence for gas accretion such as galaxy interactions and minor mergers, high velocity clouds (HVCs), extra-planar gas and warped or lop-sided HI disks. These observations yield an estimate for the 'visible' gas accretion rate onto a typical disk galaxy of ~ 0.2 $M_\odot$ yr^{-1}, which falls short of the typical star formation rate of ~ 1 $M_\odot$ yr^{-1}. These studies focus on recycling and inflow in local disk galaxies, but one may ask how does gas consumption evolve with redshift?

The time evolution of gas in disk galaxies has been studied on large scales using observations of damped Lyα systems (DLAs) to infer the cosmic mass density of HI as a function of redshift. The cosmic mass density is the mass density averaged over a large volume so as to be representative of a typical Mpc^{-3} of the universe. Lanzetta et al. (1995) and Pei & Fall (1995) build simple models of gas consumption focusing on the chemical evolution of the gas using the cosmic mass density of HI and observed metallicities as inputs. Their models predict the star formation rate density (SFRD) of the universe as a function of redshift for their chosen inflow and outflow parameters. However, the SFRD is now becoming increasingly well constrained by observations and we can use SFRD(z) as an input to our models in order to place constraints on the gas inflow rates.

Finally, this problem has been approached using numerical simulations to explain observations of the SFRD and galaxy properties. The shape of the SFRD has been investigated using cosmological, hydrodynamical simulations that include prescriptions for star formation and feedback (e.g. Hernquist & Springel 2003; Schaye et al. 2010). These studies suggest that the shape of the SFRD at high redshifts is determined by the buildup of dark matter halos and the gas brought in with them, and the decline of the SFRD at low redshifts is due to lower cooling rates in the halo gas, gas exhaustion and stellar and black hole feedback. The results of simulations have also been used to build simple models in order to better understand gas accretion to fuel star formation in galaxies. Bouché et al. (2010) build a simple model of gas consumption starting with simulated halo growth histories with different prescriptions for gas accretion and star formation. The predictions from the different prescriptions are compared to the observed SFR-Mass and Tully-Fisher relations for galaxies from $z \sim 2$ to $z = 0$. The authors find that the prescription for gas accretion modeled on cold flows with halo mass cutoffs agrees best with observations.

In this chapter, we look at the issue in reverse. We build simple models of gas consumption based solely on observations in order to understand the roles of the different phases of gas in star formation in galaxies. Using observations at $z = 0$, we examine which quantitative conclusions can be extrapolated to high z, and using observations of the star formation history, we make several inferences about how the gas consumption into stars must have proceeded. We find that the relationship of the inventory of gas to that of the stars is not straightforward: the observations imply that that all phases of the interstellar and intergalactic medium must be taken into account in order to understand how the gas forms stars. Building a model that includes all the gas phases, we make predictions about

gas densities and their variation at intermediate- and high-z, and how this gas must have been accreted into galaxies.

This chapter is organized as follows. Section 2.2 describes the observations of the SFRD, MGDR, ρ_{H_2} and ρ_{HI} that we use as inputs to our models. In Section 2.3, we build three models to fit the observations: the restricted closed box model, the general closed box model and the open box model. In Section 2.4, we discuss potential changes to our star formation prescription at high redshift and examine the predictions of the open box model. Throughout this chapter, we adopt a standard ΛCDM cosmology with (h, Ω_M, Ω_Λ) = (0.7, 0.3, 0.7). All of the densities are in comoving units.

2.2 Observations

2.2.1 SFRD

The (comoving) star formation rate density, SFRD, was first observed by Madau et al. (1996) and Lilly et al. (1996) over a large range of z and has since been re-examined by several other investigators (Steidel et al. 1999; Hippelein et al. 2003; Hopkins & Beacom 2006). We will focus on the results of Hopkins & Beacom (2006), a compilation of SFRD measurements at different wavelengths. The measurements are converted to a common cosmology, SFRD calibration, and dust obscuration correction; the data are then fit to a piecewise linear form in $\log(1+z)$ vs. $\log(SFRD)$ space as well as the parameterization from Cole et al. (2001). Hopkins & Beacom (2006) find that changing the assumed IMF corresponds to a simple change in the overall amplitude of the SFRD, so each fit is done using two extreme IMF forms in order to provide bounds on the actual form. These two extreme forms for the IMF are a modified Salpeter A IMF and the form of Baldry & Glazebrook (2003). Figure 2.1 plots the fits for the two IMFs in red and blue. We have smoothed the original piecewise linear fits from Hopkins & Beacom (2006) for our models (solid lines). The original piecewise function is defined by intercept and slope a and b for $z < z_1$ and c and d for $z > z_1$ (we only consider $z < 4$). The smoothed section is just a quadratic form in the $\log(1+z)$ vs $\log(SFRD)$ plane over a distance 2Δ in $\log(1+z)$. We give the piecewise function for the SFRD below, with $x = \log(1+z)$ and $x_1 = \log(1+z_1)$.

$$\log(SFRD) = \begin{cases} a + bx & 0 \leq x \leq x_1 - \Delta \\ a + b(x_1-\Delta) + \frac{(d-b)}{4\Delta}\left(x^2 - (x_1-\Delta)^2\right) & \\ \quad + \frac{1}{2}\left[b+d+(b-d)\frac{x_1}{\Delta}\right](x - x_1 + \Delta) & x_1 - \Delta \leq x \leq x_1 + \Delta \\ c + dx & x_1 + \Delta \leq x \leq x_{max} \end{cases} \quad (2.1)$$

In the Table 2.1, we give a,b,c,d and z1 for each of the two piecewise linear fits from Hopkins & Beacom (2006) (for the Modified Salpeter A IMF and the Baldry & Glazebrook (2003) IMF). To produce reasonable smoothing, we used $2\Delta = \log(1.5)$.

	Mod SalA IMF	BG 2003 IMF
a	-1.82	-2.02
b	3.28	3.44
c	-0.724	-0.930
d	-0.26	-0.26
z_1	1.04	0.97

Table 2.1: Fit parameter values for the two piecewise linear fits from Hopkins & Beacom (2006): the Modified Salpeter A IMF and the Baldry & Glazebrook (2003) IMF.

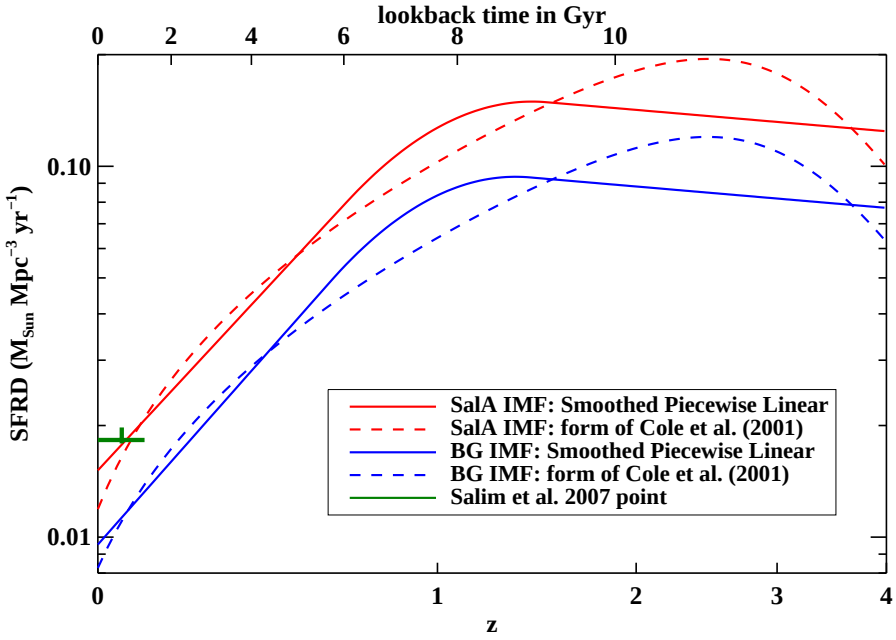

Figure 2.1: Comparison of forms of the SFRD. The solid curves show our smoothed version of the piecewise linear fits from Hopkins & Beacom (2006); the dashed curves show the fits to the Cole et al. (2001) form. Two IMFs are plotted: the modified Salpeter A IMF (SalA IMF; red) and the IMF from Baldry & Glazebrook (2003) (BG IMF; blue). The green symbol denotes the SFRD at $z = 0$ measured by Salim et al. (2007).

At $z = 0$, the SFRD fits from Hopkins & Beacom (2006) predict a local SFRD of $(0.8 - 1.5) \times 10^{-2}$ $M_\odot$ Mpc^{-3} yr^{-1}. In an extensive study of galaxies in the local universe (to $z = 0.1$), Salim et al. (2007) find that the SFRD is $1.828^{+0.148}_{-0.039} \times 10^{-2}$ h_{70} $M_\odot$ Mpc^{-3} yr^{-1} from UV observations (using the Chabrier 2003 IMF), a value they argue is the most accurate determination of this number to date. This value (shown as a data point in Figure 2.1) is indeed close to those found from other recent investigations (Houck et al. 2007; Hanish et al. 2006) and is also in reasonable agreement with the forms of Hopkins & Beacom (2006).

The agreement between the locally determined SFRD and extrapolation from studies at higher z (Hopkins & Beacom 2006; Steidel et al. 1999; Hippelein et al. 2003) is encouraging and provides some confidence that the star formation rates and their time variation are being measured reliably. While somewhat different functional forms for the decline of the SFRD with time have been proposed in the literature, e.g., log(SFRD) has been found to be linear in z (Steidel et al. 1999), in t (Hippelein et al. 2003), and in $\log(1 + z)$ (Hopkins & Beacom 2006), these differences have only a small quantitative effect in what follows.

2.2.2 MGDR

Measurements at z = 0

The star formation efficiency, SFE, is often defined as the star formation rate per comoving volume divided by the mass per comoving volume of gas; its units are yr^{-1} (Leroy et al. 2008 and references therein). Defined in this way, the SFE is not properly an efficiency, but a rate, and we drop this unfortunate usage even though it has become firmly entrenched in the observational literature. Since we are interested in SFE$_{\rm M}$, the star formation rate density divided by the density of *molecular* gas, ρ_{H_2}, we introduce the molecular gas depletion rate, MGDR, to replace the usage of SFE$_{\rm M}$. We define MGDR as SFRD divided by the density of molecular hydrogen, ρ_{H_2} (this does not include He). The inverse of MGDR is the molecular gas depletion time, $\tau_{\rm M}$, which represents the time it takes to consume all of the molecular gas at the current rate of star formation.

Recently, Leroy et al. (2008) have measured MGDR($z = 0$) from a comprehensive analysis of 23 nearby galaxies. The results are based on H I surface densities measured from the THINGS H I survey (Walter et al. 2008), H_2 surface densities inferred from the BIMA SONG (Helfer et al. 2003) and HERACLES (Leroy et al. 2008b) CO surveys, and star formation rates from both SINGS (Kennicutt et al. 2003) and GALEX (Gil de Paz et al. 2007) data. The galaxies surveyed include spiral and dwarf galaxies and the analysis was done on a pixel-by-pixel basis convolved to a common resolution, typically ∼800 pc. This comparison is the most extensive work done to date and the authors find a remarkable constancy of MGDR over a wide range of conditions: 0.525 ± 0.25 Gyr^{-1}, equivalent to a molecular gas depletion time of 1.9 Gyr. Their measured star formation rates and H_2 column densities vary by three orders of magnitude averaged over entire galaxies, and the pixel-by-pixel values vary even more. Thus the constancy of the MGDR occurs over a wide

range of conditions both within galaxies (including nuclei and disks) and from galaxy to galaxy.

Measurements at high z

The Leroy et al. (2008) study only applies to galaxies near $z = 0$. To extend the range of z we appeal to observations of the MGDR in normal, $z \gtrsim 1$ galaxies. Daddi et al. (2010) report the SFR and total gas mass for six, near-infrared selected BzK galaxies at $z \sim 1.5$. Using numerical simulations, they calculate a conversion factor $\alpha_{CO} = M_{gas}/L_{CO} = 3.6 \pm 0.8$ $M_\odot$ (K km s^{-1} pc^2)$^{-1}$. This value is close to a Milky Way-like value of $\alpha_{CO} \sim 4.6$ and excludes a typical ULIRG value of $\alpha_{CO} \sim 1$. This gas mass includes He, so we divide by 1.4 to calculate the MGDR, which we have defined to not include He. The MGDR values for these six galaxies in Daddi et al. (2010) vary between 1.9 and 4.7 Gyr^{-1}, three to nine times the Leroy et al. (2008) value for $z = 0$. Apparently, molecular gas is consumed by star formation at a much higher rate at high redshift than it is today.

Similarly, Tacconi et al. (2010) have made an extensive survey of normal, star forming galaxies at redshifts 1 and 2, measuring the MGDR for a sample of 19 galaxies. At each redshift locus, the selected galaxies sample the high mass end of the main sequence galaxy population in the M_*-SFR plane. The Tacconi et al. (2010) results use a Milky Way-like value for α_{CO}. They find MGDR values in agreement with the Daddi et al. (2010) values at $z \sim 1.5$. The data points from these studies are plotted in Figures 2.3 and 2.5: Daddi et al. (2010) as purple diamonds and Tacconi et al. (2010) as green squares.

In samples of galaxies selected by different optical and near-IR criteria, Reddy et al. (2005) find that BzK, BX/BM and DRG selected galaxies account for an SFRD of ~ 0.1 $M_\odot$ Mpc^{-3} yr^{-1} in the range $1.4 < z < 2.6$. This is most of the observed SFRD (see Figure 2.1). More recently, Reddy et al. (2008) find that galaxies with $L_{\rm IR} \approx L_{\rm bol} \lesssim 10^{12}$ $L_\odot$ account for $\approx 70\%$ of the SFRD at $1.9 \leq z < 2.7$. The BX/BM, BzK and DRG selection criteria sample luminous, star forming galaxies with L $\sim 10^{11} - 10^{12}$ L$_\odot$ and SFR $\sim 10 - 500$ $M_\odot$ yr^{-1} (Tacconi et al. 2008). Therefore, these systems sampled by Daddi et al. (2010) and Tacconi et al. (2010) account for most of the SFRD at these redshifts so that the MGDR value that typifies these galaxies should describe the average cosmic MGDR in Equation 2.2. This motivates us to use these samples to constrain our guessed forms of the MGDR at other redshifts.

Numerous other authors have estimated the MGDR from individual high redshift galaxies, or from starbursts or ULIRGS (e.g. Gao & Solomon 2004), and all have found that the MGDR is greater in these galaxies than is typical of galaxies at $z = 0$. In fact, there is no observational evidence for a declining MGDR with increasing redshift to at least $z \sim 4$. Taken together, all of these observations lead us to reject any model of gas consumption that *requires* lower MGDR values at redshifts significantly greater than zero.

2.2.3 ρ_{H_2}

Obreschkow & Rawlings (2009) used a combination of CO and H I measurements in the local universe to determine the density of H_2 at $z = 0$, $\rho_{H_2}(0)$. They find $\rho_{H_2}(0) = 1.9 - 2.8 \times 10^7$ h $M_\odot\,\mathrm{Mpc}^{-3}$. The range of values corresponds to different assumptions about how metallicity affects the CO-to-H_2 conversion ratio (the authors quote an error of $\pm 40\%$ on each individual calculated value). Using $h = 0.7$ gives $\rho_{H_2}(0) = (1.3 - 2.0) \times 10^7$ $M_\odot\,\mathrm{Mpc}^{-3}$, or an average value of 1.65×10^7 $M_\odot\,\mathrm{Mpc}^{-3}$. This value is within 50% of the estimate of $\rho_{H_2}(0) = 1.1 \times 10^7$ $M_\odot\,\mathrm{Mpc}^{-3}$ by Zwaan & Prochaska (2006) (no error quoted) using a different set of observations and should therefore be reasonably reliable.

2.2.4 ρ_{HI}

A number of recent studies have reported measurements of the mean H I comoving mass density in galaxies, $\rho_{HI}(z)$, from the local universe to $z \sim 6$. At $z = 0$, Zwaan et al. (2005) present a study of the H I mass function using the H I Parkes All Sky Survey (HIPASS) data. At low redshift, Lah et al. (2007) calculate ρ_{HI} by co-adding H I 21-cm emission from galaxies with known positions and redshifts. At higher redshifts, estimates of ρ_{HI} are mainly obtained from DLA studies (Rao et al. 2006; Prochaska & Wolfe 2009). We use these observations of H I to construct an analytical form for ρ_{HI} as a function of z. We

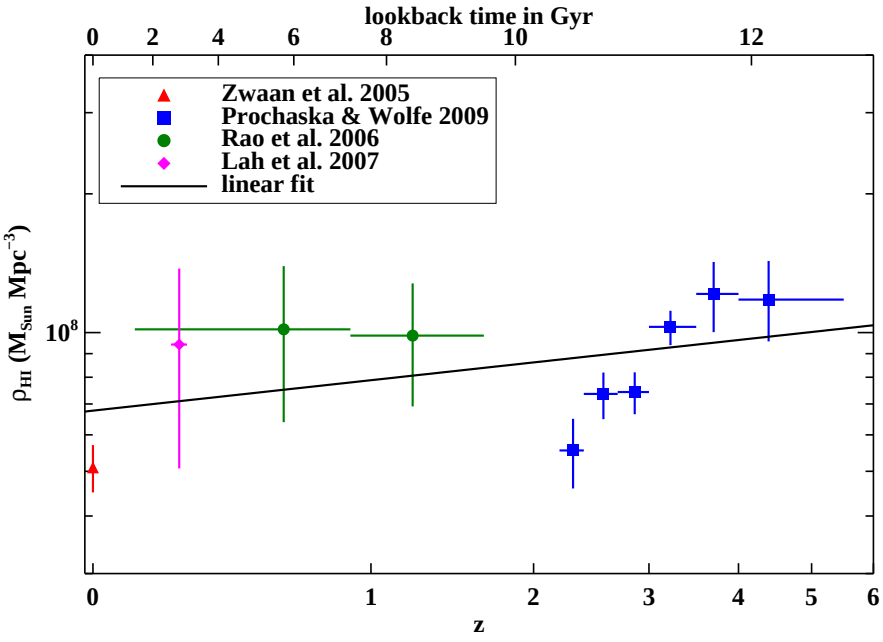

Figure 2.2: Data points for the comoving ρ_{HI} from Zwaan et al. (2005); Rao et al. (2006); Lah et al. (2007); and Prochaska & Wolfe (2009) with linear fit in $\log(1+z)$ vs $\log(\rho_{HI})$ space.

fit a straight line to these points in $\log(1+z)$ vs $\log(\rho_{HI})$ space. The data points and the fit are shown in Figure 2.2. The observations suggest very little evolution of ρ_{HI} , which increases by only a factor of 2-3 between $z = 0$ and $z = 6$. A more recent DLA study (Noterdaeme et al. 2009) using SDSS DR7 finds the values at $z \sim 2$ to 3 to be somewhat higher than the Prochaska & Wolfe (2009) points; this would make our linear fit in Figure 2.2 correspond even better to the observations.

2.3 Building a Model to Fit the Observations

The observations above allow us to compare the evolution of the SFRD and $d\rho_{H_2}/dt$. We start with the simplest model possible: a closed box of H_2 being turned into stars at the rate of $d\rho_{H_2}/dt$. In this closed box model, we initially assume that the MGDR is constant in time (the restricted closed box model; Section 2.3.1) and subsequently relax this condition (the general closed box model; Section 2.3.2). The failure of both models motivates us to consider an open box model (Section 2.3.3), where we allow the densities of all four phases of the IGM – stars, H_2, H I and H II – to vary to match the observational constraints.

We assume that the molecular gas is depleted only through star formation, and that any H_2 dissociated or ionized by star formation is instantaneously returned to the molecular state. Given the short timescales for the formation of molecular gas from its atomic form, $\sim 10^6$ yr at the relevant densities (Hollenbach & Salpeter 1971; Cazaux & Tielens 2004), this approximation should be a good one for the purposes of this work. In any event, if we define $d\rho_{H_2}/dt$ to be the *net* flow rate of molecular gas into stars, then there is no ambiguity.

We write the statement that star formation occurs only through the depletion of molecular gas:

$$SFRD = MGDR \times \rho_{H_2} \, . \tag{2.2}$$

This equation was used to infer the individual MGDR for a sample of nearby galaxies with a wide of range of SFRs and H_2 column densities, where it was found that $MGDR \approx 0.5$ Gyr^{-1} to a remarkable constancy (Leroy et al. 2008, see Section 2.2.2). We use this prescription for the SFRD for our models but we note that the form may change at higher redshift (see Section 2.4.1).

It is also interesting to note that if we divide the observed global star formation rate density SFRD$(z = 0) \sim (0.8 - 1.8) \times 10^{-2} M_\odot$ Mpc^{-3} yr^{-1} (Hopkins & Beacom 2006; Salim et al. 2007) by the observed molecular gas density, $\rho_{H_2}(0) = (1.3 - 2.0) \times 10^7 M_\odot$ Mpc^{-3} (Obreschkow & Rawlings 2009), we obtain a range of MGDR that is consistent with the values of Leroy et al. (2008). Given that stars must form from molecular gas, this result is not surprising. Nevertheless, the agreement is reassuring because it is based on different data sets and different methods of determining the relevant quantities. It also suggests, combined with the arguments in Section 2.1 that Equation 2.2 can be extrapolated to all z.

We use mass densities instead of mass surface densities, which are used by observers,

but note that these are roughly equivalent because for the most part, the stars, H I and H_2 are generally confined to thin disks within galaxies.

2.3.1 The Restricted Closed Box Model

In the closed box model, we consider only stars and H_2, and allow ρ_{H_2} to be converted into stars at the star formation rate density, SFRD:

$$\frac{d\rho_{H_2}}{dt} = -SFRD\,. \tag{2.3}$$

For the moment, we consider a restricted closed box model in which we take the MGDR to be constant as a function of redshift. To assess the ability of this model to fit observations, we first combine Equations 2.2 and 2.3 to obtain $d(SFRD)/dt = MGDR \times SFRD$. We then note that our piecewise linear fit to the observed SFRD as a function of time implies $d(SFRD)/dt \sim (.24\,\mathrm{Gyr}^{-1}) \times SFRD$, where the coefficient is about half of the observed MGDR (Leroy et al. 2008).

In other words, from the assumption of a constant MGDR at the present epoch in a closed box H_2 model, we find that the star formation rate is declining only half as fast as expected given our current reservoir of molecular gas. It is this discrepancy in the derivatives of the observed cosmic star formation rate and the rate at which we observe molecular gas being converted into stars that we call the cosmic molecular gas depletion problem. We note here that given the uncertainties in the observations, this factor of two in itself is not a strong argument against the closed box model, but we will show in general that observational constraints rule out *any* closed box model.

2.3.2 The General Closed Box Model

We now relax the assumption of a constant MGDR in the closed box model in Section 2.3.1. To study the predictions of this model, we calculate $\rho_{H_2}(z)$ by integrating Equation 2.3 and using the observed SFRD(z) as an input. We then divide SFRD(z) by $\rho_{H_2}(z)$ to obtain MGDR(z). The results are shown in Figure 2.3, where $\rho_{H_2}(0)$ is set to the mean value from Obreschkow & Rawlings (2009). The uncertainties in the SFRD (due to the IMF) discussed in Section 2.2.1 are seen to have only a minor effect on the resulting $\rho_{H_2}(z)$ and MGDR(z).

Figure 2.3 shows that $\rho_{H_2}(t)$ increases by a factor of ~ 10 from $z = 0$ to 1, and MGDR decreases with increasing redshift, *contrary to the observational results discussed in Section 2.2.2*. Thus, even the general closed box model is at odds with the observations, leading us to our next model.

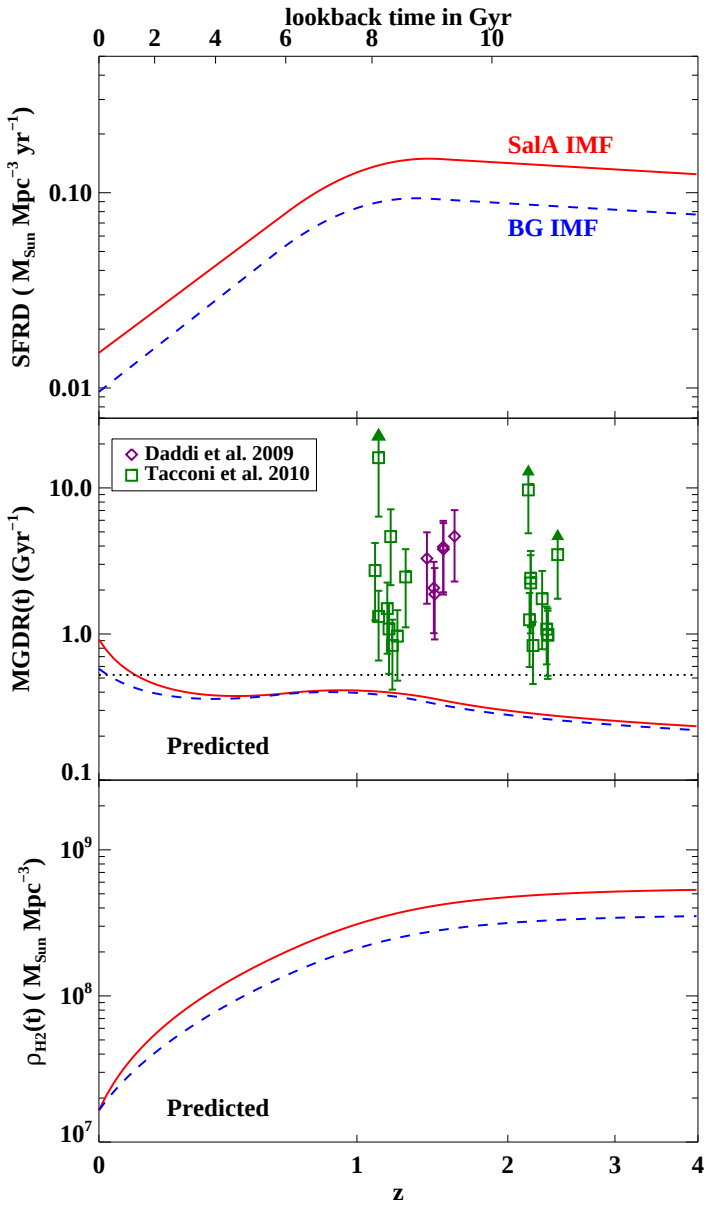

Figure 2.3: The predicted MGDR(t) and $\rho_{H_2}(t)$ in the closed box model. The top panel shows the input SFRD forms (the smoothed piecewise linear fits from Figure 2.1). The middle and bottom panels show the MGDR and $\rho_{H_2}(t)$, respectively, predicted by the general closed box model for these observed SFRD(t) forms. The points in the middle panel show the MGDR observations from Daddi et al. (2010) (purple diamonds) and from Tacconi et al. (2010) (green squares), discussed in Section 2.2.2. This model requires a lower MGDR in the past, contrary to observations.

2.3.3 The Open Box Model

Since a closed box model of only H_2 and stars is inconsistent with observations, we now allow additional components that can be converted into H_2 and then into stars. We consider separately the H I gas and an external source of gas that we call ρ_{ext}, and modify Equation 2.3 to

$$\frac{d\rho_{H_2}}{dt} = -SFRD - \frac{d\rho_{HI}}{dt} - \frac{d\rho_{ext}}{dt}\,. \tag{2.4}$$

Atomic Gas

For the H I gas, the observations discussed in Section 2.2.4 and Figure 2.2 suggest that $\rho_{HI}(z)$ is very slowly varying over cosmic timescales; therefore $d\rho_{HI}/dt$ is small. Figure 2.4 shows that the derivative of the observed ρ_{HI} (red curve) is an order of magnitude smaller than the observed SFRD (black curves). In the absence of ρ_{ext}, we have $|d\rho_{H_2}/dt|$ (blue curves) is approximately equal to $SFRD$, as in the failed closed box model. Thus the inclusion of H I *alone* in an open-box model is not enough to fit the model to the observations. This leads to a robust conclusion: *the reservoirs of* H I *and* H_2 *at all times*

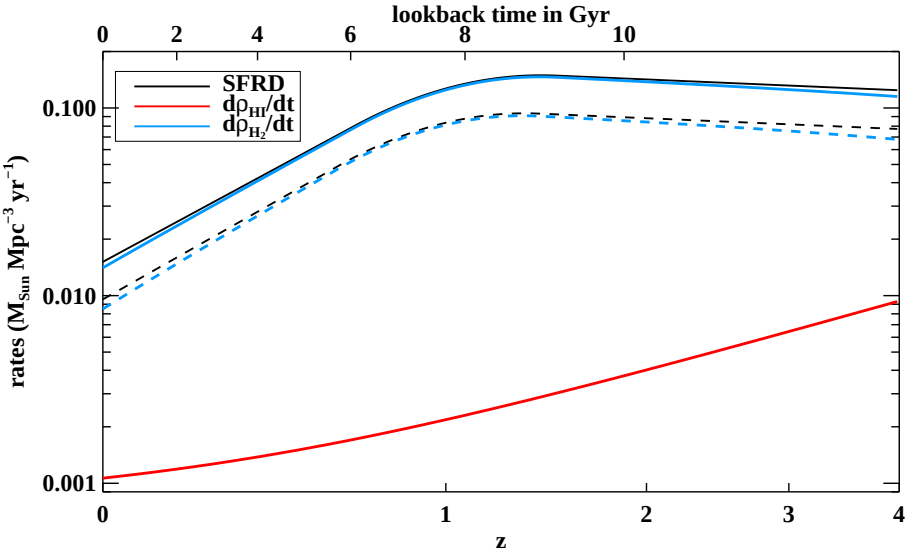

Figure 2.4: Rates of gas flowing from one phase to another in an open box model with only stars, H_2 and HI (ignoring ρ_{ext}). The SFRD (black curves) is an order of magnitude higher than $d\rho_{HI}/dt$ (red curve), forcing $d\rho_{H_2}/dt$ (blue curves) to be approximately equal to the SFRD, as in the closed box model. The two forms of the SFRD described in Section 2.2.1 are used: modified Sal A IMF (solid) and the Baldry & Glazebrook (2003) IMF (dashed). The derivatives of ρ_{HI} and ρ_{H_2} are negative, but the absolute values are plotted here.

in the past (at least as far back as $z = 4$) are insufficient to fuel the star formation over cosmic timescales.

It is important at this point to clarify that ρ_{HI} represents the reservoir of H I both in galaxies as well as the H I outside of galaxies. This is because the DLA observations of Prochaska and Wolfe (2009) include all of the high column density neutral H I (N(HI) $> 2\times 10^{20}$ cm^{-2}). This gas contains at least 85% of the neutral H I atoms for $z < 6$ (O'Meara et al 2007).

External Gas

We are therefore forced to include a nonzero $d\rho_{ext}/dt$ term in the open box model. This component represents the ionized intergalactic gas at all temperatures and densities that can recombine to form H I within a Hubble time. Effectively, it is the ionized gas in the filaments of the cosmic web.

Note that some of the H I can become ionized and redistributed to the intergalactic medium at high enough temperatures and low densities such that this gas does not recombine in a Hubble time. Such gas can be ejected by means of supernovae, galactic winds or AGN. However, if we define $d\rho_{ext}/dt$ to be the *net* flow out of the ionized phase, then the gas that is fed back into the ionized state is implicitly included in our accounting. That is, any H I fed back into the ionized phase is made up by an equivalent increase in $d\rho_{ext}/dt$. If the total amount of ionized gas available is represented by Ω_{baryon} minus the total amount of baryons in galaxies, we may consider the ionized phase to be a nearly infinite reservoir of gas available to fuel star formation. Any gas ionized and added to that reservoir by star-formation and active galaxies is negligible.

To compute the $d\rho_{ext}/dt(t)$ required in the open box model to match the observations in Section 2.2, we start with an observed SFRD(t) and $\rho_{HI}(t)$, and a guess for the form of the MGDR(t) that is compatible with the data points from Tacconi et al. (2010) and Daddi et al. (2010). From these inputs, we compute $\rho_{H_2}(t)$ and its time derivative using $\rho_{H_2}(t) =$ SFRD(t)/MGDR(t). Combining $d\rho_{H_2}/dt$ with the observed SFRD(t) and $d\rho_{HI}(t)/dt$ in Equation 2.4 then gives $d\rho_{ext}/dt$. The results of this procedure are shown in Figure 2.5.

To illustrate the expected range of possible values, we use two forms for the input MGDR (top panel) and two forms for the input SFRD (black dashed curves in the bottom panel). We bracket the possible values for the MGDR on one side as constant using the measured value at $z = 0$, and on the other as one that increases linearly to larger redshifts as suggested by the Tacconi et al. (2010) and Daddi et al. (2010) data points. For the SFRD, we use the smoothed piecewise fits from Hopkins & Beacom (2006) for the two extreme IMFs discussed in Section 2.2.1. We then calculate $d\rho_{H_2}/dt$, $d\rho_{ext}/dt$ and ρ_{H_2} for each of the four possible combinations of MGDR and SFRD. The range of calculated values is indicated in Figure 2.5 by plotting the minimum and maximum of the four curves for each calculated quantity.

In the middle panel of Figure 2.5, we note that the minimum ρ_{H_2} curve lies below ρ_{HI} at all times, and the maximum curve becomes larger than ρ_{HI} at $z \sim 0.35$. The difference

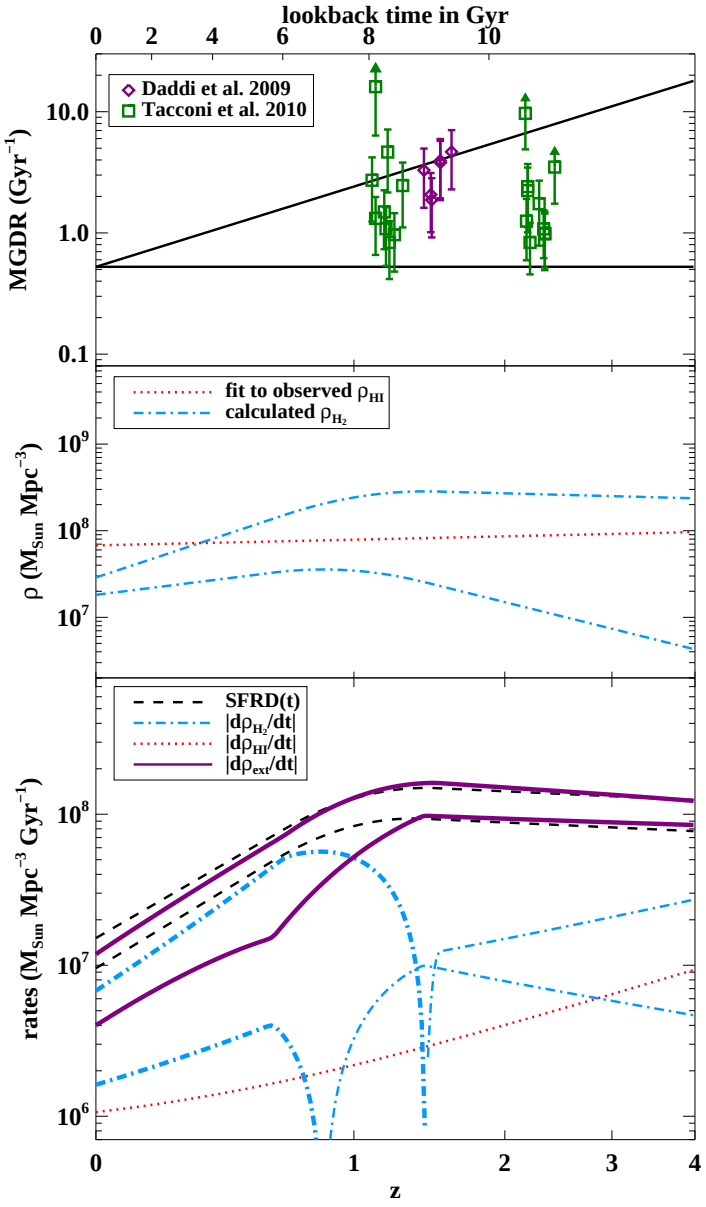

Figure 2.5: Predictions of the open box model, calculated from combinations of the inputs: two forms of the MGDR (solid black lines in top panel), two forms of the SFRD (dashed black lines in bottom panel) and the fit to the observations of ρ_{HI} (red dotted line in middle panel). In the top panel, we plot the MGDR points from Tacconi et al. (2010) (green squares) and Daddi et al. (2010) (purple diamonds) to constrain the guessed range of MGDR forms. The possible range of each of the calculated quantities, $d\rho_{H_2}/dt$, $d\rho_{ext}/dt$ and ρ_{H_2}, is shown by two lines illustrating the minimum and maximum curves from the four combinations of inputs. In the bottom panel, the absolute values of the rates are plotted: thicker lines indicate negative values.

between the two curves is mostly the MGDR choice: the maximum curve corresponds to the higher SFRD and the flat MGDR, while the minimum curve corresponds to the lower SFR and the increasing MGDR (as expected from Equation 2.2). All other combinations of MGDR and SFRD would lie between these two curves. *Because all of the molecular gas resides in galaxies, we require that the molecular gas mass in galaxies is larger, on average, at z = 1-2, than is typical at z = 0.* The change in ρ_{H_2} resulting from changing the SFRD is minor. Therefore, observations of ρ_{H_2} at $z > 0$ or the redshift at which $\rho_{H_2} = \rho_{HI}$ will constrain the form of the MGDR.

In the bottom panel of Figure 2.5, the absolute value of the rates is plotted, with a thicker line style used to indicate negative rates. The negative portions of the $d\rho_{H_2}/dt$ curves correspond to decreasing ρ_{H_2} as we move forward in time towards $z = 0$, as H_2 is converted into stars. The $d\rho_{ext}/dt$ curves are negative for the whole range of redshifts plotted, indicating a flow of external gas into the H I reservoir of galaxies. We note that the range of solutions for $d\rho_{ext}/dt$ does not deviate very much from the SFRD: roughly a factor of two at low redshifts for the minimum case. This is because the reservoirs of H_2 and H I are so small compared to what is required by the observed SFRD. *Therefore, we conclude that the amount of inflow needed from this external gas, $d\rho_{ext}/dt$, is approximately equal to the SFRD.* This observational conclusion is reinforced by cosmological simulations which find that star formation rates closely follow gas infall rates (Kereš et al. 2005; Dekel et al. 2009). Specifically, Kereš et al. (2009) calculate an upper limit on the external gas supply feeding galaxies that is only a factor of 2 higher than our predicted $d\rho_{ext}/dt$ curves and shows similar evolution with redshift.

2.4 Discussion

We have shown in Section 2.3.1 and Section 2.3.2 why the closed H_2 box model doesn't work. Here we discuss the open box model of Section 2.3.3 and what this model predicts.

2.4.1 Variations in the SFRD

For the models in Section 2.3, we have extended the star formation rate prescription from Leroy et al. (2008) to mass densities averaged over Mpc scales: SFRD $\propto \rho_{H_2}$. Some studies of galaxies with higher gas surface densities have found evidence for a steeper power law of SFRD $\propto \rho_{H_2}^{1.4}$ (Kennicutt 1998b; Wong & Blitz 2002; Bouché et al. 2007). The choice of SFRD prescription at a given redshift depends on what type of galaxies dominate the SFRD at that redshift. At the present epoch, regular spiral galaxies, such as those studied by Leroy et al. (2008), seem to dominate the SFRD: Salim et al. (2007) finds that galaxies in the mass range $10^{9.3} < M_* < 10^{10.6} M_\odot$ account for about half of the total SFRD. At higher redshifts, however, the BzK and BX/BM galaxies dominate the SFRD (see Section 2.2.2). These galaxies are more gas rich, and thus the $\rho_{H_2}^{1.4}$ prescription may be more appropriate.

In this work, we have assumed the Leroy et al. (2008) prescription for the SFRD, but note that the power law may change at higher redshift because the dominant mode of star formation may change. This is equivalent to a change in the MGDR with time, a case we consider explicitly and probably contributes to the values of the MGDR found by Tacconi et al. (2010) and Daddi et al. (2010). If, for example, $SFRD = MGDR(0)\rho_{H_2}^{1.4}$ at higher redshift, then we would find $MGDR(z) = MGDR(0)\rho_{H_2}^{0.4}$ by forcing our prescription of $SFRD = MGDR \times \rho_{H_2}$. Thus as ρ_{H_2} increases at higher redshift, an increase in the power law of the SFRD prescription will be manifested as an increase in the MGDR. An increase would tend to bring the MGDR closer to the upper bound in the top panel of Figure 2.5, with the result that $\rho_{H_2}(z)$ would lie closer to the lower blue curve in the bottom panel in Figure 2.5.

2.4.2 Stellar Recycling

Stellar recycling is an important component of any treatment of gas evolution in galaxies. Kennicutt et al. (1994), for example, suggest that gas returned to the ISM during stellar evolution can signficantly increase the gas depletion time in the Milky Way and in nearby galaxies. In the model presented here, we do not explicitly consider the effect of gas return to the ISM in Equations 2.2 and 2.4, but we argue that our formulation already accounts for stellar recycling due to the nature of the observed quantities we use as inputs. Most of the return of gas to the ISM comes from red giant stars (see e.g. Blitz 1997), and much of that is returned to the ISM in the form of molecules (Marengo 2009). Even gas that is returned in other phases becomes largely molecular after each spiral arm passage, the timescale for which is $\sim 10^8$ yr in most galaxies, a timescle short compared to the rather long timescales we consider in this work. Since the recycled gas is largely molecular, and any that isn't is quickly returned to the molecular phase, we argue that observations of molecular gas already include the gas returned via stellar recycling. Therefore, this recycled component is included in our initial condition, $\rho_{H_2}(z = 0)$, as well as the MGDR. Since we use the MGDR to relate SFRD and ρ_{H_2} at each time step, stellar recycling is built into our model through these observations, so we need not include an explicit recycling term in our equations.

2.4.3 Behavior of $\rho_{H_2}(z)$

Although the exact shape of ρ_{H_2} depends sensitively on the form of MGDR, we have bounded the behavior of ρ_{H_2} by calculating what we take to be limiting cases in our open box model (Figure 2.5). The ρ_{H_2} curves all rise with increasing redshift, peaking around $z \sim 1 - 1.5$ at 1.5 to 10 times the value of ρ_{H_2} today. After the peak, ρ_{H_2} may fall off toward higher redshift if the MGDR is rather constant, or stay close to constant if the MGDR remains high. The prediction is less well constrained at higher redshifts. It is noteworthy that Tacconi et al. (2010) find that the gas disks they observe at $z = 1$ and $z = 2$ have considerably more molecular gas relative to the stars, typically about 30-50%,

compared to $\sim 1-5\%$ for the Milky Way and nearby disk galaxies (Helfer et al. 2003). This trend is consistent with our estimates. Although there is some uncertainty in the H_2 masses of Tacconi et al. (2010) because of the uncertainty in the value of X_{CO}, there appears to be little doubt that the ratio of H_2 to stellar mass in the BzK and BX/BM galaxies is higher than typical values for similar galaxies at $z = 0$. Due to the sensitivity of ρ_{H_2} to the form of MGDR, future observations of ρ_{H_2} or the ratio ρ_{H_2}/ρ_{HI} at higher redshift would allow us to better constrain the evolution of MGDR, and reduce the area between the bounding curves of Figure 2.5.

2.4.4 The Nature of $d\rho_{ext}/dt$

In our open box model, the H I reservoir, ρ_{HI}, is augmented by an inflow of gas from ρ_{ext} at a rate of $10^7 - 10^8 M_\odot\,\mathrm{Mpc}^{-3}\,\mathrm{Gyr}^{-1}$, depending on z. This high rate of inflow means that the gas being accreted is mostly ionized since the fraction of neutral hydrogen outside of the ρ_{HI} reservoir is too small.

The ρ_{HI} inferred from observations of DLA systems accounts for the H I associated with galactic disks. As mentioned in Section 2.3.3, O'Meara et al. (2007) find that systems with column density $\Sigma_{HI} < 2 \times 10^{20}$ cm^{-2} account for $\approx 15\%$ of neutral hydrogen atoms at all $z < 6$. Therefore, the fraction of H I outside DLA systems is about 15%, corresponding to roughly 1.5×10^7 M$_\odot$ Mpc^{-3}. For an average inflow rate of a few times 10^7 M$_\odot$ Mpc^{-3} Gyr^{-1} for the past 10 Gyr, this intergalactic H I could only account for ten percent of the total, at most. Therefore, the inflow of gas needed for fueling ongoing star formation represented by $d\rho_{ext}/dt$ must be almost completely ionized.

Recently, cold flows have been suggested as an important source of gas for galaxy formation and evolution (Kereš et al. 2005; Dekel & Birnboim 2006). In these models, galactic disks in halos with $M \lesssim 10^{12} M_\odot$ are built up by direct accretion of cold gaseous streams from the cosmic web. For galaxies with larger masses, cold flows are also the dominant means of mass accretion, but different outcomes for individual galaxies depend on the epoch of inflow. If this picture is correct, our work implies that the cold flows must be almost entirely ionized.

The same is true if the gas needed to fuel star formation is brought in primarily through minor mergers. If this gas were in atomic form, it would be part of the inventory of atomic gas observed in the DLA systems, which we have shown in Section 2.3.3 to contribute negligibly to fueling the star formation at all redshifts up to $z = 4$.

2.4.5 Cooling Times

The open box model requires $d\rho_{ext}/dt \sim SFRD$, or about 10^7 to 10^8 M$_\odot$ Mpc^{-3} Gyr^{-1}. We use these numbers for $d\rho_{ext}/dt$ to calculate a cooling time for the gas in the context of two models for gas accretion onto galaxies: two-phase cooling of hot halo gas (Maller & Bullock 2004) and cold flow accretion (Kereš & Hernquist 2009).

We estimate the cooling time, t_{cool}, by taking

$$\frac{\rho_{gas}}{t_{cool}} \sim \dot{\rho}_{ext}\,, \tag{2.5}$$

where ρ_{gas} is the average mass density of the cooling ionized gas smoothed over the appropriate volume (to be specified for each cooling model individually). We set ρ_{gas} equal to $m_H n_e f$ where n_e is the local number density of electrons and f is the filling factor for the relevant volumes ($\bar{n}_e/n_e$). Combining this with the cooling time

$$t_{cool} \sim \frac{3k_bT}{2\Lambda(T)n_e}\,, \tag{2.6}$$

where $\Lambda(T)$ is the cooling function of the gas, gives

$$fn_e^2 \sim \frac{3k_bT\dot{\rho}_{ext}}{2\Lambda(T)m_H}\,. \tag{2.7}$$

As a basis for comparison, we first estimate the filling factor f for hot halos of L_* galaxies out to the virial radius. We make the simplistic assumption that the universe is made up of L_* galaxies with masses $M_{dyn} \sim 10^{12}$ $M_\odot$ and circular velocities of ~ 160 km s^{-1}. Therefore, the virial radius, $R_{vir} = GM_{dyn}/v^2 \sim 300$ kpc. We estimate the average number density in this simple universe composed of L_* galaxies by dividing the total luminosity density, $\mathcal{L}$, by L_*. We use the r band values from Blanton et al. (2003) which calculates the galaxy luminosity function at $z \sim 0.1$ from SDSS data: $\mathcal{L} \approx 1.84\times10^8$ h $M_\odot$ Mpc^{-3}, $L_* \approx 1.2\times10^{10}$ h^{-2} $M_\odot$. This yields $n_{L_*} \sim \mathcal{L}/L_* \sim 0.015$ h^3 Mpc^{-3} $\sim 5\times10^{-3}$ Mpc^{-3}. More recent work on the luminosity function using SDSS DR6 yields similar results (Montero-Dorta & Prada 2009). Therefore, in this simple universe, the filling factor for the L_* galaxy halos is

$$f \sim n_{L_*}\frac{4}{3}\pi R_{vir}^3 \sim 6\times10^{-4}\,. \tag{2.8}$$

Maller & Bullock (2004) consider gas within the cooling radius of a halo, R_c, cooling via cloud fragmentation. This results in the formation of warm ($\sim 10^4$ K) clouds within the hot gas halo. In this model for the two-phase cooling of the hot halo gas, the relevant temperature for the gas is the virial temperature of the halo, $\sim 10^6$ K for a Milky Way type halo.

Kereš & Hernquist (2009) find that the majority of cold clouds that form around Milky Way type galaxies are the result of filamentary "cold mode" accretion. Most of the gas does not reach the virial temperature of the halo, $\sim 10^6$ K, but rather cools from a maximum temperature of $\sim 10^4 - 10^5$ K.

We examine the possible values for n_e and f in these two models by calculating f as a function of n_e for three temperatures: 10^4 K and 10^5 K for cold flow accretion and 10^6 K for cooling from the hot halo. In Figure 2.6, we plot f versus n_e for these three temperatures for the range of $d\rho_{ext}/dt$ at $z = 0$ predicted by our open box model: $0.4 - 1.2\times10^7$ $M_\odot$

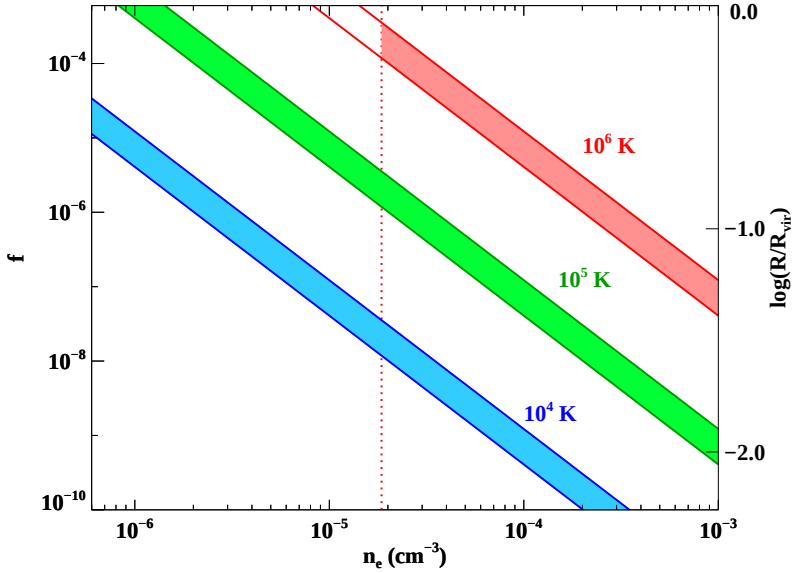

Figure 2.6: Shaded regions show the allowed filling fraction f and n_e for three temperatures: 10^4 K in blue, 10^5 K in green and 10^6 K in red. The axis on the right gives the radius of the relevant volumes as a fraction of the virial radius corresponding to the filling fraction f in a simple universe filled with L_* galaxies. At each temperature, the allowed region of n_e vs f space is calculated using the predicted range for the inflow rate at $z = 0$: $d\rho_{ext}/dt = 0.4 - 1.2 \times 10^7$ $M_\odot$ Mpc^{-3} Gyr^{-1}. The region is further bounded by the vertical dotted line at the value of n_e corresponding to a cooling time equal to the age of the universe. This line is only plotted for the 10^6 K gas: for the other two temperatures, the densities are very small and lie outside of the plotting range.

Mpc^{-3} Gyr^{-1}. The y-axis on the right side shows $\log(R/R_{virial})$ corresponding to f, where R is the radius of the relevant volume associated with an L_* galaxy. The vertical dotted line indicates the value of n_e at which the cooling time is equal to the age of the universe. We use the approximate form for $\Lambda(T)$ for mildly enriched gas ($Z = 0.1$) from Maller & Bullock (2004) :

$$\Lambda(T) \simeq 2.6 \times 10^{-23} \left(\frac{T}{10^6\ K}\right)^{-1}\ cm^{-3}\ erg\ s^{-1} \tag{2.9}$$

For the cold flow gas at 10^4 K and 10^5 K, the dotted lines where the cooling times equal the age of the universe are outside of the plotting range, so the minimum allowed value of n_e is where $R \sim R_{virial}$: about 8×10^{-7} cm^{-3} for the 10^5 K gas and even smaller for the 10^4 K gas. For the cooling hot halo gas at 10^6 K, the condition that the cooling time be less than the age of the universe forces n_e to be larger than about 2×10^{-5} cm^{-3}.

These calculations don't put strong constraints on the density of the halo gas since the cooling times are so rapid for a large range of temperatures and densities. How the gas gets

into the galaxies themselves will involve a more complete treatment including the effects of self-sheilding, which is beyond the scope of this work.

2.4.6 Comparing $d\rho_{ext}/dt$ to Dark Matter Accretion Rate

The rate $d\rho_{ext}/dt$ inferred from our open box model provides an estimate for the average rate at which the baryonic fuel is required to make its way to a galactic disk in order to sustain the observed star formation, which largely occurs in the disk. A comparison of this rate with the mean rate of baryon accretion at the virial radius of the host dark matter halo will provide an estimate for the efficiency of converting the cosmological infalling baryons into stars. Many cooling and feedback processes obviously affect the fate of baryons after their infall onto the halo and whether they will reach the disk. In fact, much of the current research in galaxy formation modeling is aimed at understanding this transition. Our goal here is to estimate an overall ratio, as a function of redshift, of the baryon accretion rates at the virial radius and at the disk scale.

We begin with the dark matter accretion rate. McBride et al. (2009) and Fakhouri et al. (2010) quantified the mass accretion histories of all dark matter halos with masses above $\sim 10^{10}$ $M_\odot$ in the two Millennium simulations of a ΛCDM universe (Springel et al. 2005; Boylan-Kolchin et al. 2009). Fakhouri et al. (2010) provides an approximate function for the average mass accretion rate as a function of redshift and halo mass:

$$\begin{aligned} \dot{M} &= \beta\, M_\odot \mathrm{yr}^{-1} \left(\frac{M}{10^{12} M_\odot}\right)^{1.1} \\ &\quad \times (1+\gamma\, z)\sqrt{\Omega_m (1+z)^3 + \Omega_\Lambda}\,. \end{aligned} \tag{2.10}$$

where $(\beta, \gamma) = (25.3, 1.65)$ for the median rate and (46.1, 1.11) for the mean rate, Ω_m and Ω_Λ are the present-day density parameters in matter and the cosmological constant, and $\Omega_m + \Omega_\Lambda$ is assumed to be unity (as in the Millennium simulation). The mean rate is $\sim 50\%$ higher than the median rate due to the long tail of halos with high accretion rates in the distribution. This $\dot{M}$ represents the average rate at which the mass in dark matter is being accreted through the virial radius of a halo. The mass growth comes in two forms in cosmological simulations: via mergers with other resolved halos (Fakhouri & Ma 2009), and via "diffuse" accretion of non-halo material that is a combination of unresolved halos and unbound dark matter particles (Fakhouri & Ma 2010).

We convert $\dot{M}$ above into a mean accretion rate for the baryons, $\dot{M}_b$, by assuming a cosmic baryon-to-dark matter ratio of $f_b = \Omega_b/\Omega_m = 1/6$. The result should provide a reasonable approximation for the mean rate of baryon mass that is entering the virial radius via mergers plus accretion of intergalactic gas. These infalling baryons are presumably in a mixture of forms: warm-hot ionized hydrogen gas of 10^5 to 10^7K, "cold" flows of $\sim 10^4$K (still ionized) gas, and H I, H_2, and stars brought in from merging galaxies. As discussed earlier, the majority of these baryons must be in the form of H II gas.

To compare $\dot{M}_b$ with the rate of external gas inflow, $\dot{\rho}_{ext}$ (Section 2.3.3), needed to account for the evolution of the observed star formation rates, we define

$$\alpha = \frac{d\rho_{ext}/dt}{f_b \dot{M} M(dn/dM)}, \tag{2.11}$$

where M is the mass of the dark matter halo under consideration, $\dot{M}$ is calculated using Equation 2.10, and dn/dM is the (comoving) number density of dark matter halos with mass in the range of M and $M + dM$. The parameter α represents the fraction of accreting baryons (at the virial radius) that must be converted into stars in our open box models.

The value of α can be estimated by combining the allowed range of $d\rho_{ext}/dt$ from Figure 2.5 with the halo abundance dn/dM from the Millennium simulation (Springel et al. 2005). Taking $f_b = 1/6$ and $M = 10^{12}$ M$_\odot$, we find the predicted α to be $\sim 70 - 100\%$ at $z \gtrsim 3$, $\sim 120 - 200\%$ at $z \sim 2$, and $\sim 30 - 90\%$ at $z = 0$. We note here that several factors may contribute to the uncertainty in the alpha values. First, the distribution of $\dot{M}$ is broad at a given halo mass (see, e.g., Figure 5 of Fakhouri et al. 2010), and we have simply used the mean value for a rough estimate of α here. Second, α depends on the halo mass appropriate for the population of galaxies that dominates the SFRD at a given redshift. Using a clustering analysis, Adelberger et al. (2005) find that BzK and BX/BM galaxies have halo masses of about 10^{12} M$_\odot$, but the average value appropriate to our analysis may vary. However, since $\dot{M} \propto M^{1.1}$ and Mdn/dm is approximately $\propto M^{-1}$, the mass dependence is weak, so alpha changes by a maximum of $\sim 20\%$ if we change the halo mass by a factor of 3. Third, since the $d\rho_{ext}/dt$ calculated in our open box model roughly traces the SFRD, the alpha values, especially around $z \sim 1 - 2$, will be affected by the exact form of the SFRD. Finally, the large alpha value at $z \sim 2$ may be reflecting a change in the fraction of baryons in the filaments at that redshift. Considering all the uncertainties, we make the conservative suggestion that *the open box model requires a large fraction ($\sim 30 - 90\%$) of the infalling baryons at the virial radius to be turned into stars from $z \sim 0 - 4$.* This is consistent with the work of Dekel et al. (2009), which finds that the star formation rates in the typical 'star-forming galaxies' at $z \sim 2$ are very close to the baryonic inflow rates from simulations.

Another way to estimate α is to compare the various $\dot{M}$ directly. At $z \sim 0$, the median baryon accretion rate from Equation 2.10 is $\dot{M}_b \sim 9$ M$_\odot$ yr^{-1} for 2×10^{12} M$_\odot$ halos, and the measured star formation rate in the Milky Way ranges from $\dot{M}_* \sim 2$ M$_\odot$ yr^{-1} to ~ 4 M$_\odot$ yr^{-1} (Miller & Scalo 1979; Diehl et al. 2006a). These rates imply $\alpha \sim \dot{M}_*/\dot{M}_b \sim 25$ to 50% at $z \sim 0$. In addition, we can use the predicted $\dot{\rho}_{ext}$ from our open box models to estimate a mean conversion rate of external H II gas into stars per galaxy, $\dot{M} \sim \dot{\rho}_{ext}/n_{L_*}$. Taking $\dot{\rho}_{ext} \sim 10^7$ M$_\odot$Mpc^{-3} Gyr^{-1} from Figure 2.5 and $n_{L_*} \sim 5 \times 10^{-3}$ Mpc^{-3} for the number density of L_* galaxies today, we obtain a rate of ~ 2 M$_\odot$ yr^{-1}, which is consistent with the star formation rate in the Milky Way.

2.5 Summary and Conclusions

In this chapter, we have built a quantitative model of gas consumption on cosmic scales based solely on observations. Using the observed the Star Formation Rate Density (SFRD), Molecular Gas Depletion Rate (MGDR), and volume averaged density of molecular hydrogen (ρ_{H_2}) and atomic hydrogen (ρ_{HI}) we have defined the cosmic molecular gas depletion problem and calculated the mass flow rates and densities of the star-forming gas back to $z \simeq 4$ needed to resolve it. Extrapolations further back in time are primarily limited by uncertainties in the SFRD. We find that:

- There are no models of gas consumption where the reservoir of gas is either only H_2 or both H I and H_2 that are compatible with the observations of molecular gas in the galaxies at $z \sim 2$ that produce the observed SFRD.
- Inflowing ionized intergalactic gas must provide most of the gas that turns into stars to times as early as $z \sim 4$. There is so little neutral gas inflow at all epochs, that the neutral gas ought to be considered more as a phase of cosmic gas flow than a reservoir of star forming gas.
- The rate of mass inflow from the ionized state to the atomic state roughly traces the star formation rate density. From $z \simeq 1 - 4$, the mass inflow rate is 1 - 2 $\times 10^8$ $M_\odot$ Mpc^{-3} Gyr^{-1}. At $z \lesssim 1$, the mass inflow rate varies linearly from about 0.5 $\times 10^7$ $M_\odot$ Mpc^{-3} Gyr^{-1} at $z = 0$ to about 1.5 $\times 10^8$ $M_\odot$ Mpc^{-3} Gyr^{-1}. At all redshifts, we find the mass inflow rate must be a significant fraction of the infalling rate at the virial radius, in agreement with simulations.
- For all models, the volume averaged density of H_2 increases from its present value by a factor of 1.5 to 10 at $z = 1$ – 2 depending mostly on MGDR(t).

Acknowledgements

This work has been partially supported by NSF grant AST-0838258. LB would also like to acknowledge Distinguished Visitor Awards from the University of Sydney and CSIRO as well as a visiting scholar award from the Center for Astrophysics, where much of the present work was done. We would like to thank Reinhard Genzel and Linda Tacconi for use of their results prior to publication, and conversations with many people including Robert Braun, Avi Loeb, Dušan Kereš, Norm Murray and Eliot Quataert.

Chapter 3

The Evolution of molecular Gas in Normal Galaxies Survey

We present the Evolution of molecular Gas in Normal Galaxies (EGNoG) survey, an observational study of molecular gas in 31 star-forming galaxies from $z = 0.05$ to $z = 0.5$, with stellar masses of $(4-30)\times10^{10}$ $M_\odot$ and star formation rates of $4-100$ $M_\odot$ yr^{-1}. This survey probes a relatively un-observed redshift range in which the molecular gas content of galaxies is expected to have evolved significantly. To trace the molecular gas in the EGNoG galaxies, we observe the CO($J = 1 \rightarrow 0$) and CO($J = 3 \rightarrow 2$) rotational lines using the Combined Array for Research in Millimeter-wave Astronomy (CARMA). We detect 24 of 31 galaxies and present resolved maps of 10 galaxies in the lower redshift portion of the survey. [1]

3.1 Introduction

In the past decade, molecular gas observations have begun probing the high redshift universe in a systematic way using increasingly powerful millimeter instruments. The picture that is emerging at redshifts $1-2$ is similar in some respects to what we see in the local universe. Sub-mm galaxies (SMGs) are observed to be undergoing extreme starbursts as a result of major mergers (e.g. Tacconi et al. 2008; Engel et al. 2010), equivalent to local ultra-luminous infrared galaxies (ULIRGs) (e.g. Sanders et al. 1986; Solomon et al. 1997; Downes & Solomon 1998). Normal star-forming galaxies (SFGs) at high redshifts, akin to local spirals, are becoming accessible as well. Recent works (Tacconi et al. 2010; Daddi et al. 2010) suggest that $z \sim 1-2$ star-forming galaxies (with star formation rates (SFRs) of $\approx 50-200$ $M_\odot$ yr^{-1}) are scaled up versions of local spirals, forming stars in a steady

[1] This chapter will be submitted to the Astrophysical Journal as part of *The EGNoG Survey: Molecular Gas in Intermediate-Redshift Star-Forming Galaxies* by Bauermeister, Blitz, Bolatto, Bureau, Leroy, Ostriker, Teuben, Wong & Wright and is reproduced with the permission of all coauthors.

mode (not triggered by interaction), despite hosting star formation rates at the level of typical local starburst systems like luminous infrared galaxies (LIRGs) and ULIRGS.

While galaxies classified as LIRGs or ULIRGs (by their infrared luminosities only) have typically been associated with starbursting and merging systems by analogy to galaxies in the local universe, it is becoming clear that this connection does not hold at high redshifts. Morphological studies find that while 50% of local LIRGs show evidence for major mergers (Wang et al. 2006), that fraction appears to decrease toward high redshifts: Bell et al. (2005) find that more than half of intensely star-forming galaxies at $z \approx 0.7$ have spiral morphologies and fewer than 30% show evidence of strong interaction. Further, the typical star formation rate of SFGs increases toward higher redshift. SFGs have been observed to obey a tight relation between stellar mass and star formation rate out to $z \sim 4$ (e.g. Brinchmann et al. 2004; Noeske et al. 2007; Elbaz et al. 2007; Daddi et al. 2007; Pannella et al. 2009; Daddi et al. 2009; Magdis et al. 2010). This 'main sequence' of SFGs evolves with redshift, shifting to higher star formation rates at higher redshifts.

The increase in the star formation rate is mirrored in the molecular gas fraction of these systems. While studies of local spirals (e.g. BIMA SONG, Helfer et al. 2003; HERACLES, Leroy et al. 2009) find average molecular gas fractions $f_{\rm mgas} = M_{\rm mgas}/(M_* + M_{\rm mgas}) \sim 5\%$ (where $M_{\rm mgas}$ is the molecular gas mass (including He) and M_* is the stellar mass), observations of high redshift SFGs suggest molecular gas fractions of 20-80%, an order of magnitude higher than local spirals. Unfortunately, the past 8 Gyr of the evolution of $f_{\rm mgas}$ remains relatively unprobed, with only one study of normal SFGs between $z = 1$ and $z = 0.05$ (Geach et al. 2011, at $z = 0.4$).

To fill in this observational gap in redshift, we have carried out the Evolution of molecular Gas in Normal Galaxies (EGNoG) survey, a key project at the Combined Array for Research in Millimeter-wave Astronomy (CARMA).[2] The EGNoG survey uses rotational transitions of the carbon monoxide (CO) molecule to trace the molecular gas content of 31 star-forming galaxies from $z = 0.05$ to 0.5 (the CO($J = 1 \rightarrow 0$) line for galaxies at $z = 0 - 0.3$ and the CO($J = 3 \rightarrow 2$) line for galaxies at $z = 0.3 - 0.5$). The survey includes four galaxies at $z \approx 0.3$ (the gas excitation sample) observed in both the CO($J = 1 \rightarrow 0$) and CO($J = 3 \rightarrow 2$) lines, more than doubling the number of normal SFGs at $z > 0.1$ in which CO line ratios have been measured.

In this chapter, we present the data for the entire EGNoG sample. The main results of the EGNoG sample are discussed separately: the evolution of the molecular gas fraction from $z \sim 1 - 2$ to today and the constraints at intermediate redshifts from the EGNoG survey are discussed in Chapter 4 and the excitation of the gas in four EGNoG galaxies at $z \approx 0.3$ is discussed in Chapter 5. This chapter is organized as follows. In Section 3.2 we describe the selection of the EGNoG survey galaxies and the properties of the sample. In Section 3.3 we briefly describe the observations and data reduction. Appedix A contains

[2]CARMA is a 3-band, 23-element millimeter interferometer jointly operated by the California Institute of Technology, University of California Berkeley, University of Chicago, University of Illinois at Urbana-Champaign, and University of Maryland.

a detailed description of the data reduction and flux measurement, including polarization measurements of calibrators 0854+201 and 1058+015. We present the CO maps, total CO luminosities, and derived molecular gas masses in Section 3.4 and discuss the morphologies of the low-redshift portion of the survey and the non-detections of the high-redshift portion of the survey.

Throughout this work, we use a ΛCDM cosmology with (h, Ω_M, Ω_Λ) = (0.7, 0.3, 0.7). We use the following terms for star-forming galaxies at low and high redshift according to the definitions below:

- **Star-forming galaxy** refers to any galaxy which is actively forming stars. Quantitatively, these galaxies lie on or above the main sequence of star-forming galaxies. This term encompasses both normal star-forming and starburst galaxies.
- **Normal star-forming galaxy or SFG** refers to star-forming galaxies that lie on the main sequence (within some scatter). While the acronym SFG stands for star-forming galaxy, we use it (in keeping with other authors) to refer to main sequence galaxies, which comprise the bulk of the star-forming galaxy population.
- **Starburst galaxy** refers to a galaxy undergoing a period of enhanced star formation. We give a quantitative definition in Section 3.2.1.
- **LIRG, ULIRG** (luminous Infrared galaxy, ultra-luminous Infrared galaxy) denotes a galaxy with a total infrared luminosity between 10^{11} and 10^{12} $L_\odot$ (LIRG) or $> 10^{12}$ $L_\odot$ (ULIRG). Local LIRGs and ULIRGs tend to be starbursts, but at high-redshift, normal star-forming galaxies would be classified as LIRGs or ULIRGs by the infrared luminosities.
- **SMG** (sub-mm galaxy) refers to the population of galaxies at $z \gtrsim 1$ which have 850-μm fluxes $\gtrsim 4$ mJy. SMGs tend to be starbursts (often as a result of a merger, akin to local ULIRGs).

3.2 The EGNoG Sample

The EGNoG survey observed 31 galaxies spanning the accessible redshift range in 4 redshift bins, A-D. The redshift range, sample size, parent sample and range of M_* and SFR are given for each redshift bin in Table 3.1.

Sample galaxies in redshift bins A-C are drawn from the main spectroscopic sample of the SDSS, Data Release 7 (York et al. 2000; Strauss et al. 2002; Abazajian et al. 2009). Spectroscopic redshifts are from David Schlegel's *spZbest* files produced by the Princeton-1D code, *specBS*[3]. The stellar masses and SFRs of galaxies in the SDSS DR7 are provided by the Max-Planck-Institute for Astrophysics - John Hopkins University group[4]. Stellar masses are derived by fitting SDSS ugriz photometry to a grid of models spanning a wide range of

[3]See http://spectro.princeton.edu/ for more information

[4]http://www.mpa-garching.mpg.de/SDSS

Redshift Bin	Redshift Range	Sample Size	Parent Sample	M_* Range ($M_\odot$)	SFR Range ($M_\odot$ yr^{-1})
A	0.05 - 0.10	13	SDSS	(4.0 - 16)$\times 10^{10}$	3.4 - 41
B	0.16 - 0.20	10	SDSS	(6.3 - 32)$\times 10^{10}$	47 - 106
C	0.28 - 0.32	4	SDSS	(16 - 32)$\times 10^{10}$	39 - 65
D	0.47 - 0.53	4	zCOSMOS	(4.0 - 5.5)$\times 10^{10}$	62 - 74

Table 3.1: Summary of the EGNoG sample.

star formation histories. This method is found to compare quite well with the Kauffmann et al. (2003) methodology using spectral features (more detail on this comparison is found on the website above). Star formation rates are derived by fitting the fluxes of no less than 5 emission lines using the method described in Brinchmann et al. (2004). Both stellar masses and star formation rates are derived using a Bayesian analysis, producing probability distributions of each quantity for each galaxy. We show the probability distributions of the stellar mass and SFR in Figure 3.1 for galaxies in redshift bins A-C. Data points give the 2.5, 16, 50, 84 and 97.5 percentiles of the distribution. The median, mean and mode are indicated by the vertical solid, dashed and dotted lines respectively. In cases where a duplicate exists (sources A1, B4 and C1), the duplicate values are plotted in red. For each of the quantities plotted in Figure 3.1 (stellar mass in the top panels, SFR in the bottom panels), the probability distribution function for each galaxy is plotted over the same range on the x-axis, centered at the median value for that galaxy.

We take the median of the distribution, with errors indicated by the 16th and 84th percentile points ($\pm 1\sigma$ for a Gaussian distribution). In cases where a duplicate SDSS source exists (as a result of SDSS automated source-finding), we take the average of the two median values and use the lowest(highest) 16th(84th) percentile value to indicate the negative(positive) error (average values and errors given in Table 3.2).

The higher redshift portion of our sample (redshift bin D) is drawn from the COSMOS survey (2 square degrees at RA $\approx$ 10 h, Dec $\approx$ 2; Scoville et al. (2007)) which has imaging and photometric redshifts for all the galaxies in the survey; with spectroscopic redshifts available for many sources (zCOSMOS; Lilly et al. (2009)). We did not use the SDSS for this redshift bin due to the poor coverage of star-forming galaxies at this redshift. Lilly et al. (2009) report an average accuracy of 110 km s^{-1}for the spectroscopic redshifts, independent of redshift. Stellar masses come from spectral energy distribution (SED) fitting by Bundy et al. (2010) and star formation rates are based on SED fits provided by Ilbert et al. (2010). Typical errors are 0.15 dex for the stellar masses and 0.3-0.4 dex for the star formation rates.

Basic information (RA, Dec, SDSS and COSMOS identification) for the EGNoG galaxies is listed in Table 3.2. The redshifts, stellar masses and star formation rates from the MPA-JHU group and the COSMOS survey are given in Table 3.3.

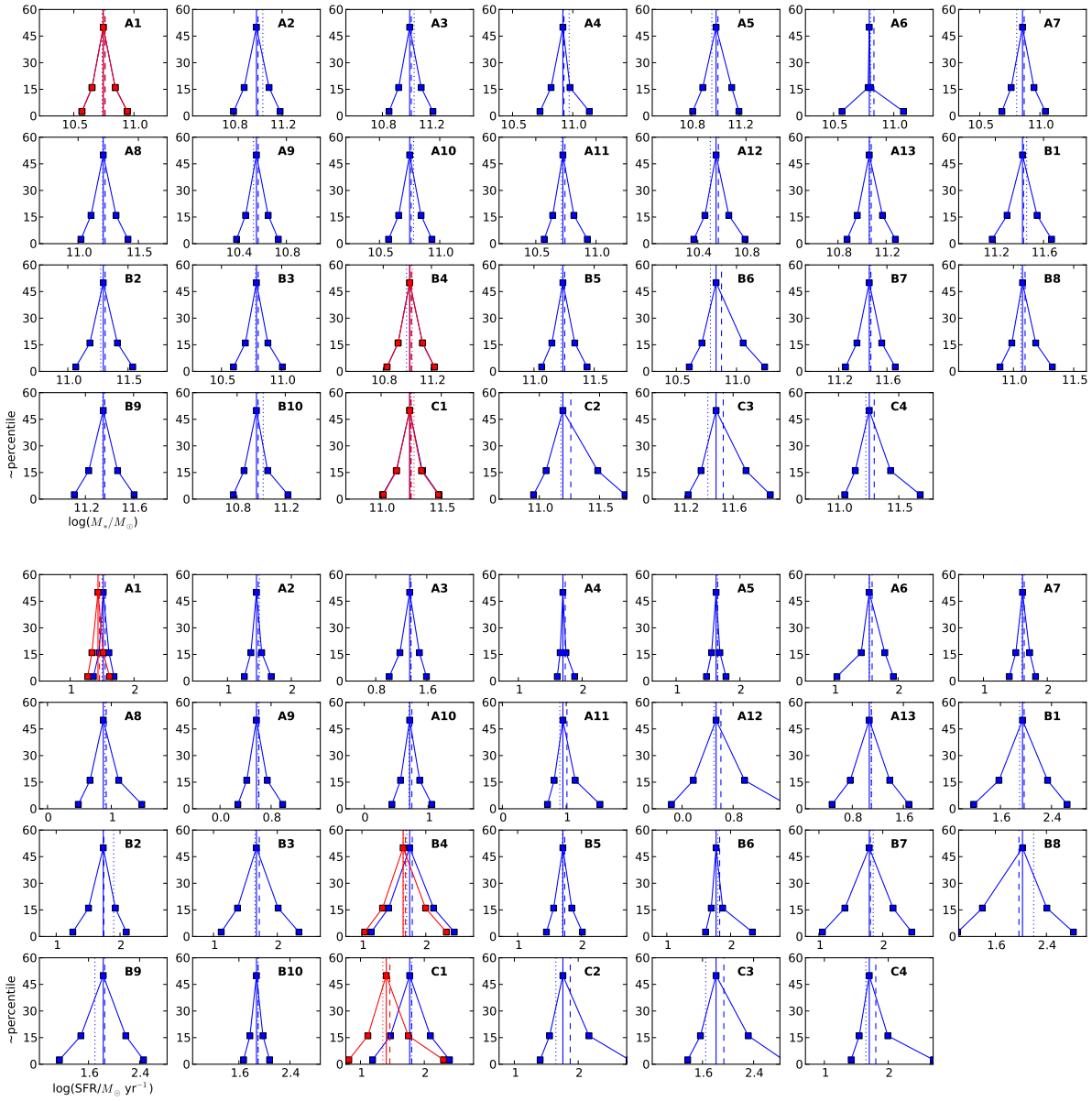

Figure 3.1: Stellar mass (top) and SFR (bottom) probability distribution functions of galaxies selected from SDSS (bins A, B and C). For galaxies A1, B4 and C1, a duplicate SDSS source exists, which is over-plotted in red.

EGNoG Name	RA	Dec	SDSS, COSMOS Identification
A1	23:43:11.257	+00:05:24.319	SDSS J234311.26+000524.3
A2	23:13:32.468	+13:38:45.301	SDSS J231332.46+133845.3
A3	23:34:55.239	+14:17:31.093	SDSS J233455.23+141731.0
A4	08:55:04.171	+52:52:48.320	SDSS J085504.16+525248.4
A5	08:53:07.258	+12:19:00.827	SDSS J085307.26+121900.8
A6	08:45:49.662	+57:32:39.329	SDSS J084549.66+573239.3
A7	21:15:27.817	-08:12:34.441	SDSS J211527.81-081234.4
A8	13:57:51.775	+14:05:27.317	SDSS J135751.77+140527.3
A9	10:57:33.589	+19:51:54.274	SDSS J105733.59+195154.2
A10	14:16:01.216	+18:34:34.171	SDSS J141601.21+183434.1
A11	10:05:59.890	+11:09:19.688	SDSS J100559.89+110919.6
A12	11:11:50.654	+28:11:47.767	SDSS J111150.65+281147.7
A13	22:19:38.115	+13:42:13.890	SDSS J221938.11+134213.9
B1	22:35:28.638	+13:58:12.619	SDSS J223528.63+135812.6
B2	00:23:53.973	+15:59:47.757	SDSS J002353.97+155947.8
B3	10:05:18.640	+05:25:44.225	SDSS J100518.63+052544.2
B4	10:55:27.188	+06:40:15.025	SDSS J105527.18+064015.0
B5	11:57:44.348	+12:07:50.792	SDSS J115744.35+120750.8
B6	12:42:52.548	+13:09:44.215	SDSS J124252.54+130944.2
B7	09:14:26.239	+10:24:09.649	SDSS J091426.24+102409.6
B8	11:46:49.182	+24:36:47.703	SDSS J114649.18+243647.7
B9	13:43:22.288	+18:11:14.135	SDSS J134322.28+181114.1
B10	13:05:29.304	+22:20:19.867	SDSS J130529.30+222019.8
C1	09:28:31.941	+25:23:13.925	SDSS J092831.94+252313.9
C2	09:06:36.694	+16:28:07.136	SDSS J090636.69+162807.1
C3	13:20:47.139	+16:06:43.720	SDSS J132047.13+160643.7
C4	13:38:49.189	+40:33:31.748	SDSS J133849.18+403331.7
D1	10:00:55.82	+01:57:03.84	SDSS J100055.81+015703.8, zCOSMOS 811469
D2	10:00:52.41	+01:48:32.92	SDSS J100052.41+014833.0, zCOSMOS 811543
D3	09:59:39.07	+02:22:49.94	SDSS J095939.07+022249.6, COSMOS 2019408
D4	09:59:00.62	+02:28:33.20	SDSS J095900.61+022833.0, zCOSMOS 840823

Table 3.2: Basic information.

EGNoG Name	z	$\log(M_*/M_\odot)$	SFR ($M_\odot$ yr^{-1})	sSFR (Gyr^{-1})
A1[a]	0.096941 ± 0.000007	$10.74^{+0.10}_{-0.09}$	$30.0^{+10.5}_{-8.1}$	0.54
A2	0.081196 ± 0.000008	$10.99^{+0.10}_{-0.10}$	$28.4^{+5.9}_{-5.2}$	0.29
A3	0.062168 ± 0.000010	$11.03^{+0.10}_{-0.09}$	$21.5^{+9.0}_{-6.4}$	0.20
A4	0.089592 ± 0.000028	$10.92^{+0.06}_{-0.10}$	$49.9^{+5.9}_{-4.6}$	0.60
A5	0.080978 ± 0.000011	$11.01^{+0.13}_{-0.11}$	$42.3^{+6.2}_{-6.3}$	0.42
A6	0.085259 ± 0.000005	$10.80^{+0.01}_{-0.01}$	$35.4^{+26.5}_{-9.0}$	0.56
A7	0.090469 ± 0.000006	$10.86^{+0.10}_{-0.09}$	$40.9^{+12.1}_{-8.7}$	0.57
A8	0.099188 ± 0.000027	$11.21^{+0.11}_{-0.10}$	$7.5^{+5.6}_{-2.8}$	0.05
A9	0.077338 ± 0.000007	$10.55^{+0.10}_{-0.09}$	$3.7^{+1.8}_{-1.1}$	0.10
A10	0.055121 ± 0.000008	$10.75^{+0.09}_{-0.09}$	$5.1^{+2.2}_{-1.4}$	0.09
A11	0.076055 ± 0.000006	$10.72^{+0.09}_{-0.08}$	$8.9^{+5.0}_{-2.4}$	0.17
A12	0.098171 ± 0.000012	$10.55^{+0.11}_{-0.09}$	$3.4^{+6.1}_{-1.9}$	0.10
A13	0.083503 ± 0.000012	$11.06^{+0.11}_{-0.10}$	$11.7^{+12.8}_{-5.8}$	0.10
B1	0.183193 ± 0.000017	$11.43^{+0.12}_{-0.13}$	$88.2^{+129.9}_{-50.5}$	0.33
B2	0.191773 ± 0.000020	$11.29^{+0.12}_{-0.11}$	$54.6^{+30.1}_{-22.5}$	0.28
B3	0.165737 ± 0.000012	$10.79^{+0.09}_{-0.09}$	$47.1^{+55.9}_{-23.3}$	0.76
B4[a]	0.173078 ± 0.000013	$11.02^{+0.11}_{-0.10}$	$49.7^{+82.8}_{-28.7}$	0.47
B5	0.182661 ± 0.000010	$11.24^{+0.10}_{-0.09}$	$51.1^{+19.3}_{-14.5}$	0.29
B6	0.174661 ± 0.000013	$10.83^{+0.23}_{-0.12}$	$59.2^{+15.9}_{-9.5}$	0.87
B7	0.176180 ± 0.000018	$11.45^{+0.10}_{-0.10}$	$61.5^{+83.6}_{-36.0}$	0.22
B8	0.176579 ± 0.000021	$11.07^{+0.11}_{-0.09}$	$106.1^{+149.5}_{-81.1}$	0.89
B9	0.178004 ± 0.000019	$11.35^{+0.12}_{-0.12}$	$67.7^{+84.8}_{-37.5}$	0.30
B10	0.190227 ± 0.000010	$10.96^{+0.09}_{-0.10}$	$75.0^{+19.7}_{-15.8}$	0.82
C1[a]	0.283020 ± 0.000022	$11.24^{+0.10}_{-0.11}$	$38.7^{+85.9}_{-25.6}$	0.22
C2	0.300622 ± 0.000010	$11.20^{+0.29}_{-0.14}$	$57.5^{+90.1}_{-21.9}$	0.37
C3	0.312361 ± 0.000014	$11.46^{+0.25}_{-0.12}$	$64.9^{+142.9}_{-28.0}$	0.23
C4	0.285380 ± 0.000015	$11.26^{+0.18}_{-0.12}$	$50.5^{+48.1}_{-15.4}$	0.28
D1	0.474100 ± 0.000367	$10.60^{+0.15}_{-0.15}$	$62.2^{+77.1}_{-34.4}$	1.55
D2	0.527900 ± 0.000367	$10.69^{+0.15}_{-0.15}$	$71.9^{+89.1}_{-39.8}$	1.47
D3	0.470800 ± 0.000367	$10.73^{+0.15}_{-0.15}$	$78.7^{+97.5}_{-43.5}$	1.47
D4	0.477800 ± 0.000367	$10.74^{+0.15}_{-0.15}$	$74.4^{+92.1}_{-41.2}$	1.36

Table 3.3: Derived quantities (z, M_*, SFR) from the MPA-JHU group (see text for details). Galaxies A1, B4 and C1 (marked by [a]) have duplicate SDSS sources: the average value is reported. The specific star formation rate (sSFR= SFR/M_*) is given in the last column.

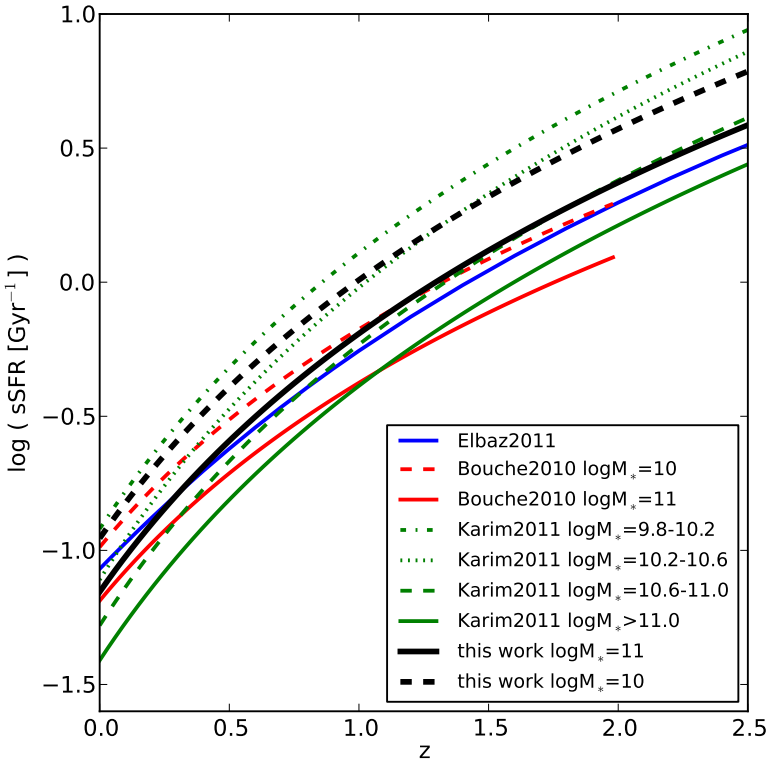

Figure 3.2: Specific star formation rate (sSFR) versus redshift for different stellar masses. Three published forms are shown (Elbaz et al. 2011 in blue, Bouché et al. 2010 in red, and Karim et al. 2011 in green) as well as the relation adopted for this work in black.

3.2.1 Sample Selection

The EGNoG galaxies were selected from the parent samples (SDSS and COSMOS) to be as representative as possible of the 'main sequence' (MS) of star-forming galaxies. The main sequence is the tight correlation between M_* and SFR that has been observed over a large range of redshifts: e.g. $z \sim 0$ (Brinchmann et al. 2004), $z \sim 0.2 - 1$ (Noeske et al. 2007), $z \sim 1 - 2$ (Elbaz et al. 2007; Daddi et al. 2007; Pannella et al. 2009), $z \sim 3 - 4$ (Daddi et al. 2009; Magdis et al. 2010) (see also the summary of recent results in Dutton et al. (2010)). Building on these observations, a few authors have attempted to describe the main sequence relation at all redshifts with one form. Figure 3.2 shows the functional forms of the specific star formation rate (sSFR= SFR/M_*) as a function of redshift reported by three papers: Bouché et al. (2010), Karim et al. (2011) and Elbaz et al. (2011). Bouché et al. (2010) suggest that existing literature data are well-fit by the form sSFR $\propto M_*^{-0.2}(1+z)^{2.7}$ for $z = 0 - 2$. Karim et al. (2011) use a deep 3.6 μm selected sample of galaxies from the COSMOS field, with average SFRs determined from stacked 1.4 GHz radio continuum

emission. Like Bouché et al. (2010), they find the sSFR to be a function of stellar mass, with galaxies with lower stellar masses having higher specific star formation rates. Specifically, the authors find sSFR $\propto M_*^{-0.4}(1+z)^{3.5}$ (on average) for star-forming galaxies at $z = 0-3$ (in Figure 3.2, we plot the fit sSFR for each of the Karim et al. (2011) mass bins individually). On the other hand, Elbaz et al. (2011) argue that observations at all redshifts are consistent with a sSFR independent of stellar mass. The authors use far-infrared observations from Herschel Space Observatory in conjunction with existing data on the GOODS-North and GOODS-South fields to fit the sSFR versus redshift, finding sSFR $(\mathrm{Gyr}^{-1}) = 26t_{\mathrm{cosmic}}^{-2.2}$ for $z = 0 = 3$ (where t_{cosmic} is the time since the Big Bang in Gyr). The sSFR forms from Bouché et al. (2010) (red) and Karim et al. (2011) (green) are shown for different stellar masses in Figure 3.2. As Elbaz et al. (2011) argues that the sSFR is independent of sSFR, only one curve (blue) is plotted.

For this work, we are only concerned with the behavior of sSFR(z) out to $z \sim 2.5$, but note that there is evidence for a flattening of this relation at $z > 2-2.5$ (e.g. Stark et al. 2009; González et al. 2010; Reddy et al. 2012). For $z < 2.5$, we adopt a sSFR relation which roughly agrees with the three forms described above. Specifically, we define

$$sSFR_{\mathrm{MS}}(\mathrm{Gyr}^{-1}) = 0.07(1+z)^{3.2}\left(\frac{M_*}{10^{11}\ \mathrm{M}_\odot}\right)^{-0.2} \tag{3.1}$$

In Figure 3.2, this is plotted in black for $M_* = 10^{10}$ $\mathrm{M}_\odot$ (dashed) and $M_* = 10^{11}$ $\mathrm{M}_\odot$ (solid). We use this representative form of the sSFR to describe the main sequence of star-forming galaxies throughout this work.

To differentiate 'starburst' (SB) galaxies from normal main sequence galaxies, we adopt the quantitative definition given by Rodighiero et al. (2011), a study of PACS/Herschel observations of COSMOS and GOODS-South galaxies at $z = 1.5-2.5$. Rodighiero et al. (2011) fit the main sequence population with a Gaussian distribution and define starbursts as outliers of this distribution. They find deviations from the Gaussian main sequence starting at a sSFR four times that of the main sequence. Therefore, we define starbursts as having

$$sSFR_{\mathrm{SB}} > 4 \times sSFR_{\mathrm{MS}} \tag{3.2}$$

In the selection of the EGNoG sample, we apply the following criteria in each redshift bin in order to identify non-interacting, star-forming galaxies lying as close to the main sequence as possible. At $z \lesssim 0.3$ (bins A-C), star-forming galaxies were selected (rejecting sources with AGN) using the cut from Kauffmann et al. (2003) in the BPT line-ratio diagram (Baldwin et al. 1981). We did not extend this criterion to bin D at $z \approx 0.5$ since the Kauffmann et al. (2003) dataset only covers $z = 0.02-0.3$. Obviously interacting galaxies were excluded via visual inspection of the SDSS or COSMOS optical images. However, some interacting galaxies may be in the sample due to the difficulty of identification at the modest resolution of the SDSS images.

Practical considerations imposed the following further constraints. From the SDSS dataset, we only used spectroscopically targeted galaxies, for which spectroscopic redshifts,

stellar masses and SFRs were available from the MPA-JHU group. We required a spectroscopic redshift so that the error in the redshift is small enough to ensure that CO emission would be captured within the observed bandwidth. We excluded galaxies with SFRs below a minimum value estimated from the instrument sensitivity in each redshift range, assuming a molecular gas depletion time ($\tau_{\rm mgas} = M_{\rm mgas}/{\rm SFR}$) of 2 Gyr (Leroy et al. 2008), a Milky Way-like CO conversion factor (e.g. Dame et al. 2001) and (for bins C and D) a CO($J = 3 \rightarrow 2$) to CO($J = 1 \rightarrow 0$) line ratio (r_{31}) of 0.6 (Aravena et al. 2010). Note that this is close to $r_{31} = 0.5$, found in the EGNoG bin C galaxies at $z \approx 0.3$ (see Chapter 5).

In each redshift bin, the EGNoG galaxies were selected randomly from the subset of the parent sample that satisfied the constraints discussed above. Figure 3.3 shows stellar mass versus SFR in each of the four redshift bins. EGNoG galaxies are indicated by the red points with error bars. The blue shading indicates the (logarithm of the) density of points in the M_* - SFR plane for all star-forming galaxies (spectroscopic targets only for the SDSS data, bins A-C) in the redshift range (indicated in the lower right of each panel. The redshift ranges plotted for bins B-D are slightly larger than the EGNoG redshift ranges so that more points may be included to better capture the behavior of the main sequence at each redshift. The blue shading corresponds to approximately 100,000 galaxies at $z = 0.05 - 0.1$, 15,000 galaxies at $z = 0.15 - 0.21$, 1300 galaxies at $z = 0.25 - 0.35$, and 14,000 galaxies at $z = 0.43 - 0.57$. The main sequence of star-forming galaxies at each redshift is indicated by the solid black line, with the starburst cutoff indicated by the dashed black line. From bin A to bin C, the low-mass, low-SFR end of the main sequence becomes sparsely sampled as the number of spectroscopically targeted, star-forming galaxies available in the SDSS decreases. This effect is most dramatic in the bin C panel, where the sample of spectroscopically-targeted star-forming galaxies in the SDSS is an order of magnitude smaller than in the bin B redshift range. Conversely, the small area covered by the COSMOS survey results in a sparsely sampled high-mass end of the main sequence in the bin D panel.

The result of our sample selection is that the EGNoG galaxies generally lie at the high-M_*, high-SFR end of the main sequence of star-forming galaxies. Our starburst criterion suggests that roughly half of the galaxies in each of bins A and B, and all of the bin D galaxies are starbursts. All four bin C galaxies lie below the starburst cut. In each redshift bin, the EGNoG galaxies lie roughly within the width of the scatter around the main sequence. The starburst classification of some of the EGNoG galaxies will be considered further in Chapter 4.

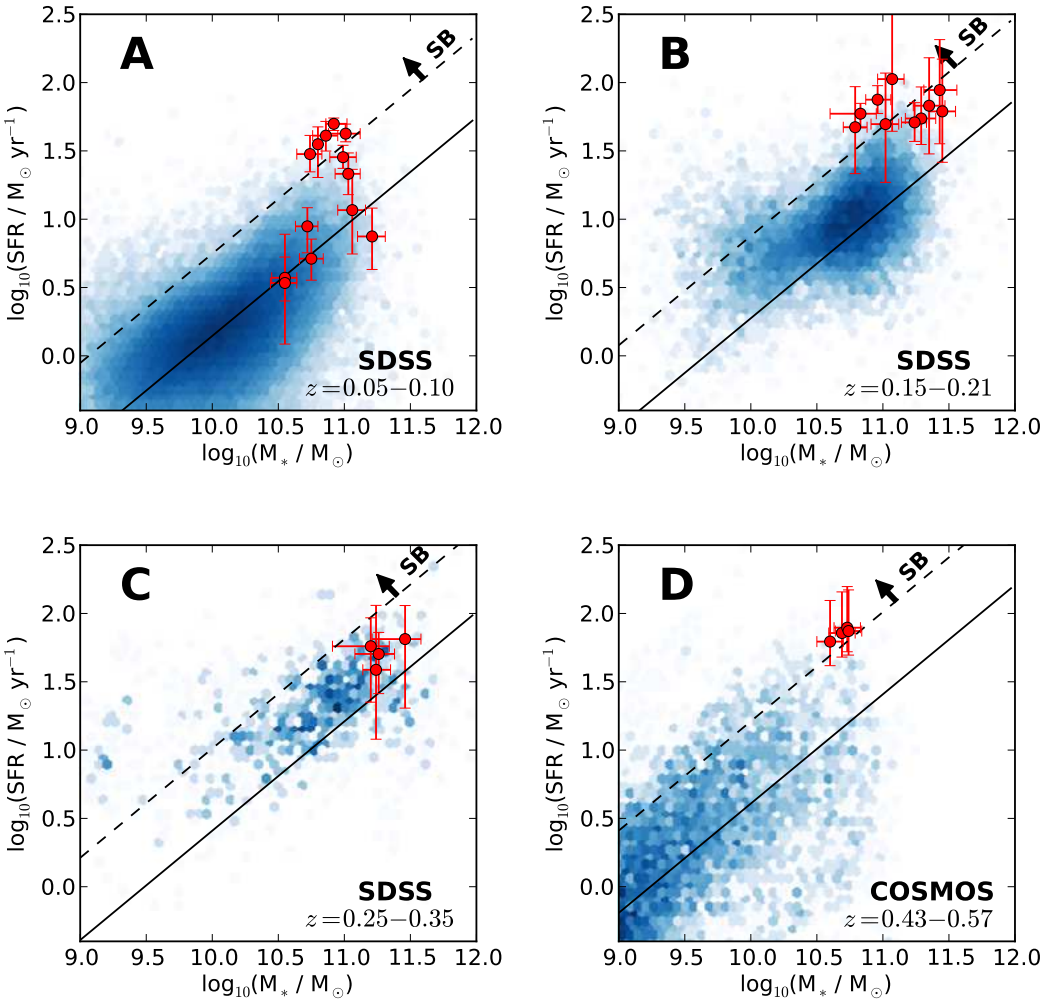

Figure 3.3: Stellar mass versus SFR in each redshift bin. The redshift bin is indicated in the upper left corner of each panel. Red points and error bars show EGNoG galaxies and blue shading shows the logarithm of the density (in the M_*-SFR plane) of star-forming galaxies from the parent dataset in the specified redshift range (given in the lower right corner). The redshift ranges plotted in bins B-D are slightly larger than the EGNoG redshift ranges so that more points may be included to better capture the behavior of the main sequence at each redshift. The solid black line indicates the main sequence (Equation 3.1) at the average redshift of the bin. The starburst criterion (Equation 3.2) is indicated by the black dashed line.

Redshift Bin	Redshift Range	Sample Size	Observed Transition	$\nu_{\rm obs}$ (GHz)	CARMA Configuration
A	0.05 - 0.10	13	CO($J = 1 \rightarrow 0$)	107	C
B	0.16 - 0.20	10	CO($J = 1 \rightarrow 0$)	98	D, some C
C	0.28 - 0.32	4	CO($J = 1 \rightarrow 0$)	88	D
			CO($J = 3 \rightarrow 2$)	266	D, E
D	0.47 - 0.53	4	CO($J = 3 \rightarrow 2$)	230	D, E

Table 3.4: Summary of the EGNoG survey observations with CARMA.

3.3 CARMA Observations

Each of the 31 EGNoG galaxies was observed in at least one rotational transition of the CO molecule: galaxies in bins A, B and C were observed in CO($J = 1 \rightarrow 0$) ($\nu_{\rm rest} = 115.3$ GHz, $\nu_{\rm obs} \sim 107$, 98 and 88 GHz respectively); galaxies in bins C and D were observed in CO($J = 3 \rightarrow 2$) ($\nu_{\rm rest} = 345.9$ GHz, $\nu_{\rm obs} \sim 266$ and 230 GHz respectively). At each frequency, each galaxy was observed over several different days. Each dataset includes observations of a nearby quasar for phase calibration (taken every 15-20 minutes), a bright quasar for passband calibration and either a planet (Uranus, Neptune or Mars) or MWC349 for flux calibration (in most cases).

The reduction of all observations for this survey was carried out within the EGN[5] data reduction infrastructure (based on the MIS pipeline; Pound & Teuben 2012) using the Multichannel Image Reconstruction, Image Analysis and Display (MIRIAD, Sault et al. 2011) package for radio interferometer data reduction. Our data analysis also used the `miriad-python` software package (Williams et al. 2012). The data were flagged, passband-calibrated and phase calibrated in the standard way. Final images were created using `invert` with `options=mosaic` in order to properly handle and correct for the three different primary beam patterns. All observations are single-pointing. We describe the CO($J = 1 \rightarrow 0$) and CO($J = 3 \rightarrow 2$) observations individually below. A full description of the data reduction and flux measurement is given in Appendix A.

3.3.1 CO($J = 1 \rightarrow 0$)

The CO($J = 1 \rightarrow 0$) transition lies in the 3 mm band of CARMA (single-polarization, linearly polarized feeds) for galaxies in bins A, B and C. The line was observed with at least three overlapping 500 MHz bands, covering $\approx$ 4200, 4600 and 5000 km s^{-1} total, at 35, 39 and 42 km s^{-1} resolution for galaxies in bins A, B and C. The details of the 3mm observations of bins A, B and C are given in Tables 3.5, 3.6 and 3.7 respectively. We describe the observations briefly below.

Bin A galaxies were observed during three time periods: October to November 2010,

[5] http://carma.astro.umd.edu/wiki/index.php/EGN

April to May 2011 and February 2012. All data were taken in CARMA's C configuration, with $26 - 370$ m baselines yielding a typical synthesized beam of $2.0'' \times 1.5''$ at 107 GHz. These observations are sensitive to spatial scales up to $\approx 22''$, which is sufficient for most galaxies in the sample but may resolve out some large scale structure in the largest galaxies. However, since molecular gas is centrally concentrated, we expect any under-estimation of the flux to be minimal. (In D and E configuration in the 3mm band, we are sensitive to sufficiently large spatial scales so that we expect to recover all of the flux.) Each galaxy was observed for 2-3 hours (time on-source), yielding final maps with a typical rms noise of $5 - 10$ mJy beam^{-1} in a 35 km s^{-1} channel.

Bin B sources were observed from August to November 2011 and April 2012 in CARMA's D configuration, with $11 - 150$ m baselines yielding a typical synthesized beam of $4.9'' \times 3.9''$ at 98 GHz. Supplementary observations were made of B1, B2, B3 and B7 in CARMA's C array in February 2012, which resulted in a synthesized beam of $3.0'' \times 2.3''$ in the final maps combining data from both array configurations. Each galaxy was observed in D configuration for approximately 7 hours (time on-source), resulting in a typical rms noise of 2.5 mJy beam^{-1} in a 39 km s^{-1} channel in the final map.

Bin C observations were made from August to November 2011 in CARMA's D configuration, with a typical synthesized beam of $4.8'' \times 3.9''$ at 88 GHz. Each galaxy was observed for 20 to 30 hours (time on-source), yielding final maps with a typical rms noise of 1.2 mJy beam^{-1} in a 42 km s^{-1} channel.

The flux scale in each dataset is set by the flux of the phase calibrator (given in Tables 3.5, 3.6 and 3.7), which is determined from the flux calibrator. See Appendix A for the details of the flux calibration of the data.

Of the 27 galaxies observed in the CO($J = 1 \rightarrow 0$) line, we detect 24 easily, with 3 non-detections in bin A. We show the *uv*-spectra for all detected galaxies in Figures 3.4 and 3.5. For each galaxy (indicated in the top left), the top (bottom) panel shows the vector-averaged *Real* and *Imaginary* amplitudes (phase) of the calibrated *uv* data versus velocity. In Figure 3.5, the CO($J = 1 \rightarrow 0$) line is shown in the top panels and the CO($J = 3 \rightarrow 2$) line in the bottom panels. For galaxy A8, the spectrum is calculated at a position offset from the SDSS position in order to coincide with the observed peak of the CO emission. For a compact source at the center of the field of view, the *Real* part shows the signal without a noise bias, and the *Imaginary* part shows the noise. In all cases (except CO($J = 3 \rightarrow 2$) in galaxy C1), we see coherent emission (larger *Real* amplitudes coincident with noise-like *Imaginary* amplitudes and phases of ≈ 0) over multiple velocity channels, indicative of a detection. The 3 non-detections in bin A are discussed further in Section 3.4.4.

3.3.2 CO($J = 3 \rightarrow 2$)

The CO($J = 3 \rightarrow 2$) transition lies in the CARMA 1 mm band (dual-polarization, circularly polarized feeds). for galaxies in bins C and D. We again observed the line with at least three overlapping 500 MHz bands, covering ≈ 1500 and 1700 km s^{-1} total, at 14 and

Summary of 3 mm Observations: Bin A										
src	trial	observation date	$t_{\rm int}$ (hr)	$l_{\rm rms}$ (μm)	τ_{230}	phase calibrator	flux (Jy)	passband calibrator	flux calibrator	3 ch rms
A1	C 1	31 Oct 2010	1.7	211	0.44	0006-063	1.6	3C454.3	MWC349	4.4
A2	C 1	23 Oct 2010	1.2	447	0.82	3C454.3	39.5	3C454.3	NEPTUNE	9.8
A2	C 2	01 Nov 2010	1.0	114	0.59	3C454.3	39.5	3C454.3	URANUS	5.1
A2	C 4	14 Nov 2010	1.0	266	0.38	3C454.3	39.5	3C454.3	URANUS	10
A3	C 1	06 Nov 2010	1.5	168	0.39	0010+109	0.23	3C454.3	URANUS	4.2
A4	C 1	10 Nov 2010	2.7	290	0.17	0920+446	1.8	0927+390	3C84	2.6
A4	C 2	15 Feb 2012	0.8	196	0.21	0920+446	1.0	0423-013	3C84	4.3
A5	C 2	12 Nov 2010	1.3	202	0.27	0854+201	5.15[1]	0927+390	3C84	3.2
A6	C 1	13 Nov 2010	1.1	194	0.19	0958+655	1.1	1058+015	3C273	3.2
A6	C 2	11 Feb 2012	5.4	287	0.36	0958+655	1.66	3C84	MWC349	2.4
A7	C 1	22 Apr 2011	2.5	297	0.42	2134-018	1.2	3C454.3	URANUS	3.9
A8	C 2	29 Apr 2011	3.3	-	0.16	1357+193	0.7	1357+193	MWC349	3.0
A9	C 3	30 Apr 2011	2.6	196	0.15	1159+292	1.35	1058+015	3C84	1.9
A10	C 2	08 May 2011	2.5	374	0.50	1357+193	0.65	3C279	MWC349	4.9
A11	C 3	01 May 2011	2.7	147	0.14	1058+015	4.55[1]	3C84	3C84	1.9
A12	C 1	02 May 2011	1.8	145	0.14	1159+292	1.35	1058+015	3C84	2.2
A12	C 3	05 May 2011	2.4	151	0.24	1159+292	1.35	3C273	3C273	2.0
A12	C 5	10 Feb 2012	3.9	227	0.17	1159+292	0.7	0854+201	MARS	1.7
A13	C 1	24 Apr 2011	0.8	200	0.18	2232+117	1.25	1733-130	MWC349	3.3
A13	C 2	30 Apr 2011	2.3	190	0.10	2232+117	1.25	3C454.3	MWC349	2.5

Table 3.5: Summary of 3 mm observations of the CO($J = 1 \rightarrow 0$) line in EGNoG bin A sources (src). Integration time ($t_{\rm int}$) is on-source, in hours. $l_{\rm rms}$ and τ_{230} are indicators of the weather conditions during the observations. Median values are given. $l_{\rm rms}$ is the standard deviation of the path length on a 100m baseline measured at an elevation close to 45 degrees over a period of 10 minutes. τ_{230}, the zenith optical depth at 230 GHz, (calculated from the tipper on-site). In the last column we give the typical image noise, averaging three velocity channels averaged together (3 ch rms), as in indication of data quality. For bin A and B observations, 3 velocity channels is roughly 105 km s^{-1} and 115 km s^{-1} respectively. [1] indicates the gain calibrator is polarized (see Appendix A.3).

Summary of 3 mm Observations: Bin B										
src	trial	observation date	$t_{\rm int}$ (hr)	$l_{\rm rms}$ (μm)	τ_{230}	phase calibrator	flux (Jy)	passband calibrator	flux calibrator	3 ch rms
B1	D 1	27 Aug 2011	5.0	211	2.5	2232+117	1.5	3C454.3	MWC349	2.7
B1	D 2	28 Aug 2011	3.9	245	2.1	2232+117	1.5	3C454.3	MWC349	2.8
B1	D 3	23 Sep 2011	2.6	268	0.57	2232+117	1.5	3C454.3	URANUS	2.6
B1	C 1	07 Feb 2012	3.8	147	0.58	2232+117	1.74	3C454.3	MWC349	2.0
B1	C 2	11 Feb 2012	2.4	295	0.29	2232+117	1.74	3C454.3	URANUS	3.6
B1	C 3	12 Feb 2012	3.8	459	0.25	2232+117	1.74	3C454.3	NEPTUNE	2.8
B1	C 5	14 Feb 2012	3.0	269	0.30	2232+117	1.74	3C343.3	MWC349	2.4
B2	D 2	25 Sep 2011	3.2	300	0.91	0108+015	2.0	3C454.3	URANUS	2.6
B2	D 3	25 Sep 2011	3.9	195	0.94	0108+015	2.0	3C454.3	NEPTUNE	2.5
B2	D 4	28 Sep 2011	1.3	120	0.44	0108+015	2.0	3C454.3	URANUS	2.6
B2	C 1	14 Feb 2012	2.7	295	0.21	0108+015	1.7	0108+015	URANUS	2.1
B2	C 7	17 Feb 2012	2.7	317	0.20	0108+015	1.7	0108+015	URANUS	2.1
B2	C 8	19 Feb 2012	4.4	278	0.13	0108+015	1.7	0108+015	URANUS	1.8
B3	D 1	12 Nov 2011	2.7	247	0.65	1058+015	4.06[1]	1058+015	MARS	5.6
B3	D 3	13 Nov 2011	2.3	510	0.49	1058+015	4.06[1]	1058+015	MARS	3.9
B3	D 4	14 Nov 2011	5.0	281	0.45	1058+015	4.06[1]	1058+015	MARS	1.9
B3	C 1	07 Feb 2012	3.0	203	0.59	1058+015	3.6	0854+201	MARS	2.7
B3	C 2	08 Feb 2012	3.3	77	0.63	1058+015	3.6	0854+201	MARS	2.3
B3	C 3	09 Feb 2012	2.6	119	0.27	1058+015	3.6	0854+201	MARS	1.8
B3	C 4	10 Feb 2012	2.5	186	0.20	1058+015	3.6	0854+201	MARS	1.8
B4	D 1	05 Apr 2012	4.7	149	0.09	1058+015	2.78[1]	0854+201	MARS	1.2
B4	D 2	08 Apr 2012	3.0	82	0.15	1058+015	2.78[1]	3C273	MARS	1.5
B5	D 1	11 Apr 2012	5.6	265	0.54	3C273	6.75	3C273	MARS	1.7
B5	D 2	12 Apr 2012	3.7	231	0.19	3C273	6.75	3C273	MARS	1.4
B6	D 2	12 Apr 2012	4.1	178	0.23	3C273	6.75	3C273	MARS	1.3
B6	D 3	14 Apr 2012	6.0	377	0.38	3C273	6.75	0854+201	MARS	1.7
B7	D 1	07 Nov 2011	4.1	298	0.30	0854+201	5.20[1]	0854+201	MARS	1.5
B7	D 2	08 Nov 2011	3.1	140	0.12	0854+201	5.20[1]	0854+201	MARS	1.3
B7	C 1	05 Feb 2012	3.0	80	0.18	0854+201	5.16[1]	0854+201	MARS	1.4
B7	C 2	06 Feb 2012	2.8	74	0.12	0854+201	5.16[1]	0854+201	MARS	1.4
B7	C 3	07 Feb 2012	2.4	204	0.31	0854+201	5.16[1]	3C84	MARS	2.0
B8	D 1	15 Apr 2012	6.7	229	0.38	1310+323	1.4	0927+390	MARS	1.2
B8	D 2	18 Apr 2012	2.9	171	0.58	1310+323	1.4	0927+390	MARS	1.9
B9	D 1	19 Apr 2012	2.9	178	0.83	1310+323	1.4	3C279	MARS	1.9
B9	D 2	21 Apr 2012	4.2	201	0.59	1310+323	1.4	3C273	MARS	1.6
B10	D 1	17 Apr 2012	5.6	232	0.45	1310+323	1.4	0854+201	MARS	1.5
B10	D 2	22 Apr 2012	3.7	345	0.45	1310+323	1.4	3C273	MARS	1.7

Table 3.6: Summary of 3 mm observations of the CO($J = 1 \rightarrow 0$) line in EGNoG bin B galaxies. Three velocity channels is roughly 115 km s^{-1}. See Table 3.5 for column description.

Summary of 3 mm Observations: Bin C										
src	trial	observation date	$t_{\rm int}$ (hr)	$l_{\rm rms}$ (μm)	τ_{230}	phase calibrator	flux (Jy)	passband calibrator	flux calibrator	3 ch rms
C1	D 1	28 Aug 2011	2.8	719	1.3	0854+201	4.0[1]	0854+201	MARS	4.7
C1	D 2	29 Aug 2011	2.6	466	0.88	0854+201	4.0[1]	0854+201	MARS	4.8
C1	D 3	30 Aug 2011	3.7	475	0.60	0854+201	4.0[1]	0854+201	MARS	2.4
C1	D 4	30 Aug 2011	3.6	370	0.26	0854+201	4.0[1]	0854+201	MARS	1.4
C1	D 5	03 Sep 2011	3.6	193	0.33	0854+201	4.0[1]	0854+201	MARS	1.4
C1	D 6	05 Sep 2011	2.2	643	0.47	0854+201	4.0[1]	0854+201	MARS	3.5
C1	D 7	07 Sep 2011	4.2	355	0.49	0854+201	4.0[1]	0854+201	MARS	1.6
C1	D 8	25 Sep 2011	3.1	290	0.51	0854+201	4.0[1]	0927+390	MARS	2.2
C1	D 9	26 Sep 2011	3.8	174	0.58	0854+201	4.0[1]	0927+390	MARS	1.9
C2	D 1	01 Sep 2011	4.0	270	0.25	0854+201	4.0[1]	0854+201	MARS	1.3
C2	D 2	02 Sep 2011	4.0	157	0.26	0854+201	4.0[1]	0854+201	MARS	1.2
C2	D 3	09 Sep 2011	0.6	161	0.65	0854+201	4.0[1]	0854+201	MARS	3.7
C2	D 8	09 Sep 2011	1.3	240	0.67	0854+201	4.0[1]	0854+201	MARS	3.0
C2	D 9	10 Sep 2011	2.8	173	0.69	0854+201	4.0[1]	0854+201	MARS	2.0
C2	D 10	28 Sep 2011	3.1	153	0.42	0854+201	4.0[1]	0854+201	MARS	1.6
C2	D 11	29 Sep 2011	3.3	318	0.48	0854+201	4.0[1]	0927+390	MARS	1.5
C2	D 12	01 Oct 2011	2.4	413	0.43	0854+201	4.0[1]	1058+015	MARS	2.2
C3	D 1	04 Sep 2011	4.7	399	0.33	1357+193	0.77	3C273	MARS	1.5
C3	D 2	05 Sep 2011	2.4	753	0.48	1357+193	0.77	3C279	MARS	3.0
C3	D 3	06 Sep 2011	2.3	411	0.45	1357+193	0.77	3C279	MWC349	2.2
C3	D 4	09 Sep 2011	2.2	447	0.67	1357+193	0.77	3C279	MARS	2.7
C3	D 5	10 Sep 2011	2.7	831	0.84	1357+193	0.77	3C279	MARS	3.0
C3	D 6	12 Sep 2011	2.7	674	0.83	1357+193	0.77	3C279	MARS	2.8
C3	D 7	15 Sep 2011	0.5	899	1.5	1357+193	0.77	3C279	MARS	4.0
C3	D 8	17 Sep 2011	2.3	387	0.48	1357+193	0.77	3C279	MWC349	2.3
C3	D 9	09 Oct 2011	2.3	496	0.38	1357+193	0.77	3C279	MARS	2.3
C3	D 10	21 Oct 2011	3.1	340	0.29	1357+193	0.77	3C279	MARS	1.9
C3	D 11	01 Nov 2011	4.5	522	0.18	1357+193	0.77	3C273	MARS	1.7
C3	D 13	04 Nov 2011	2.3	223	0.18	1357+193	0.77	3C273	MARS	2.6
C4	D 1	13 Sep 2011	2.0	517	0.74	1310+323	1.7	3C273	MARS	2.8
C4	D 2	13 Sep 2011	2.5	325	0.86	1310+323	1.7	0927+390	MARS	2.6
C4	D 3	16 Sep 2011	4.7	695	0.83	1310+323	1.7	1058+015	MARS	2.4
C4	D 4	17 Sep 2011	2.8	385	0.45	1310+323	1.7	0927+390	MARS	2.2
C4	D 6	20 Sep 2011	0.9	440	0.45	1310+323	1.7	3C273	-	3.5
C4	D 7	22 Sep 2011	2.3	176	0.49	1310+323	1.7	0927+390	MARS	2.4
C4	D 8	04 Nov 2011	2.6	306	0.34	1310+323	1.7	0927+390	MARS	2.1
C4	D 9	05 Nov 2011	2.1	224	0.29	1310+323	1.7	3C279	MARS	1.8
C4	D 10	06 Nov 2011	2.2	215	0.25	1310+323	1.7	1058+015	MARS	1.9

Table 3.7: Summary of 3 mm observations of the CO($J = 1 \rightarrow 0$) line in EGNoG bin C galaxies. Three velocity channels is roughly 126 km s^{-1}. See Table 3.5 for column description.

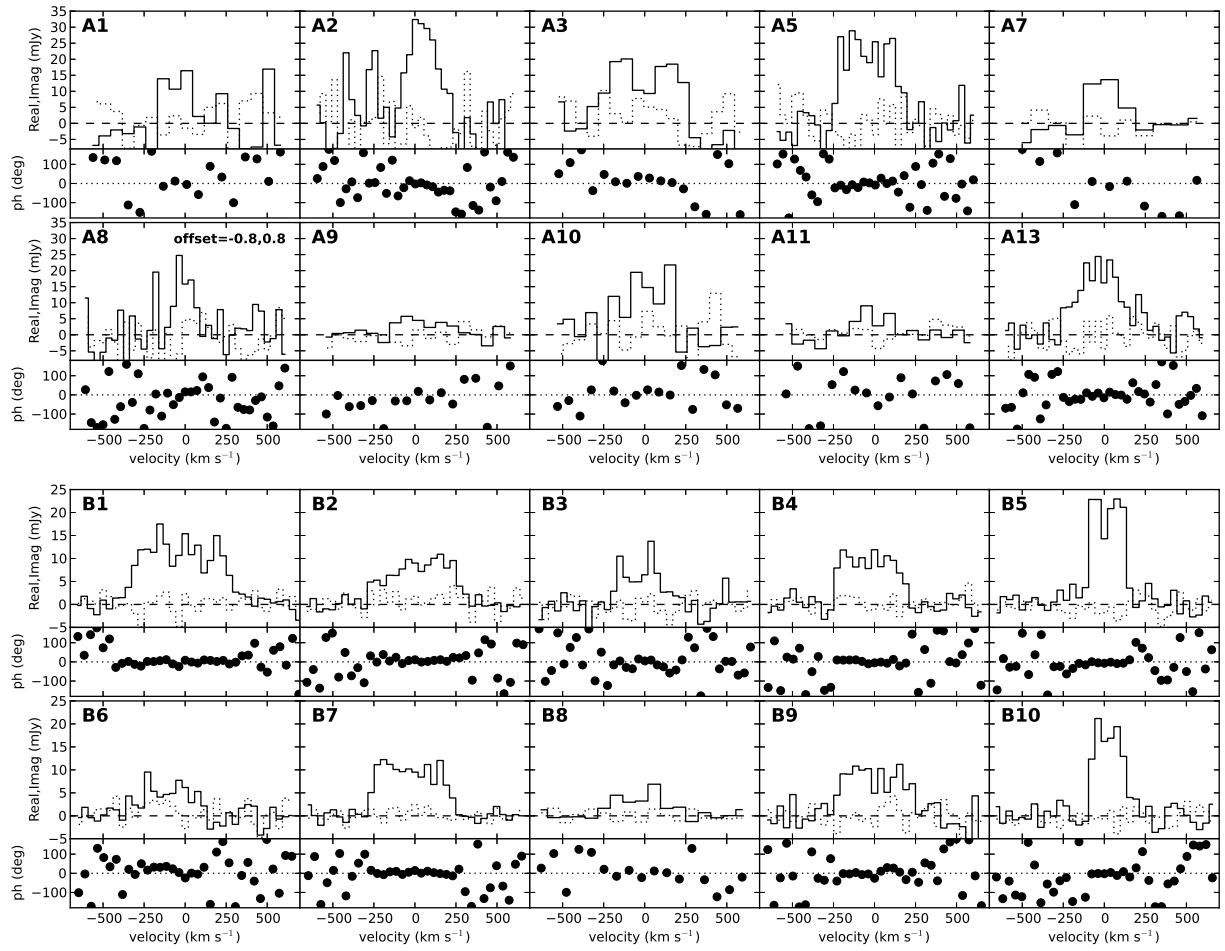

Figure 3.4: *uv*-spectra of bin A and B galaxies. The top panel shows the vector-averaged *Real* (solid) and *Imaginary* (dotted) amplitudes (Real,Imag in mJy beam^{-1}) and the bottom panel shows phase (ph, degrees) of the calibrated *uv* data versus velocity (km s^{-1}). For galaxy A8, the spectrum is calculated at $-0.8'', 0.8''$ offset from the SDSS position (indicated in the upper right corner of the A8 panel).

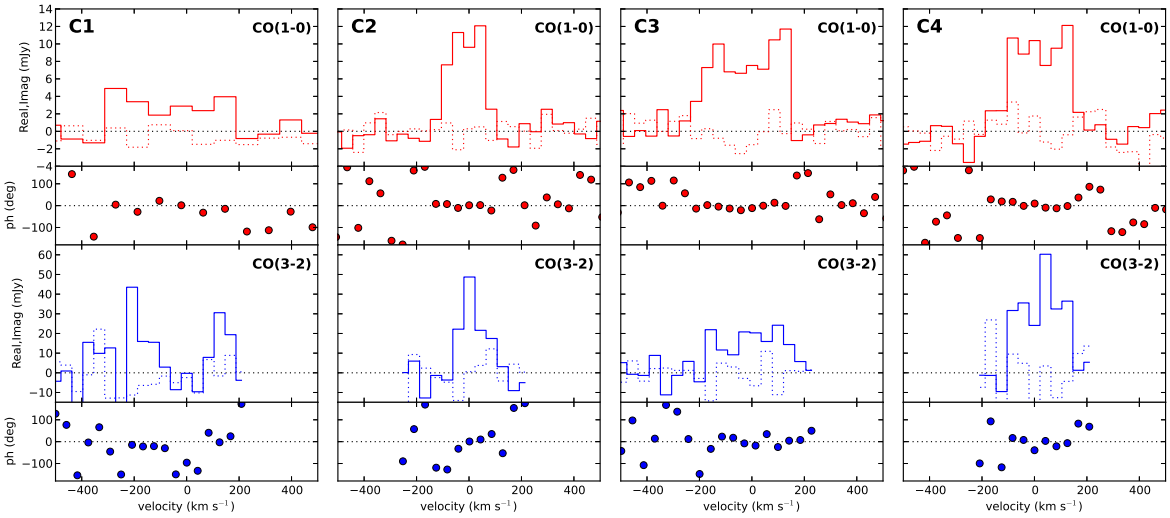

Figure 3.5: *uv*-spectra of bin C galaxies. The top row (red) shows the CO($J = 1 \rightarrow 0$) line and the bottom row (blue) shows the CO($J = 3 \rightarrow 2$) line. For each line, for each source, the top panel shows the vector-averaged *Real* (solid) and *Imaginary* (dotted) amplitudes (Real,Imag in mJy beam^{-1}) and the bottom panel shows phase (ph, degrees) of the calibrated *uv* data versus velocity (km s^{-1}). With the higher resolution of the CO($J = 3 \rightarrow 2$) data, we observe the peak of the CO($J = 3 \rightarrow 2$) emission to be offset ($< 1.5'' \sim 6$ kpc) from the centers of galaxies C1 and C2. In these cases, we calculate the *uv* spectra at the peak of the CO($J = 3 \rightarrow 2$) emission. For the CO($J = 1 \rightarrow 0$) line of galaxy C1, we average 2 channels together in order to increase the signal to noise ratio.

15 km s^{-1} resolution, for galaxies in bins C and D respectively. The details of the 1 mm observations of bins C and D are given in Table 3.8. We describe the observations briefly below.

Bin C observations were carried out in CARMA's E configuration during August 2011 and D configuration during April 2012. Source C4 was observed entirely in E configuration, while the other three sources were observed mostly in D configuration. The E configuration has $8 - 66$ m baselines yielding a typical synthesized beam of $3.2'' \times 2.5''$ at 266 GHz. The D configuration has $11 - 150$ m baselines yielding a typical synthesized beam of $1.7'' \times 1.5''$ at 266 GHz. Each galaxy was observed for 2 to 6.5 hours (time on-source), yielding final maps with rms noise of 5-10 mJy beam^{-1} in a 42 km s^{-1} channel.

Bin D observations were carried out in CARMA's E and D configuration during August 2011 and April to June 2012, respectively. In E configuration, a typical synthesized beam is $4.2'' \times 3.6''$ at 230 GHz. In D configuration, a typical synthesized beam is $2.5'' \times 1.7''$ at 230 GHz. Galaxies D1 and D2 were observed in both D and E configuration for approximately 10 hours (time on-source) total, yielding final maps with rms noise of ≈ 7 mJy beam^{-1} in a 48 km s^{-1} channel. Galaxies D3 and D4 were observed in D configuration for approximately

Summary of 1 mm Observations										
src	trial	observation date	$t_{\rm int}$ (hr)	$l_{\rm rms}$ (μm)	τ_{230}	phase calibrator	flux (Jy)	passband calibrator	flux calibrator	3 ch rms
C1	E 7	07 Aug 2011	2.6	232	0.29	0854+201	2.0	3C84	MARS	38
C1	D 1	07 Apr 2012	4.1	91	0.08	0854+201	4.0	3C279	MARS	5.0
C2	D 1	09 Apr 2012	2.0	114	0.18	0854+201	4.0	3C84	MARS	7.8
C3	D 1	06 Apr 2012	4.1	87	0.12	1224+213	0.6	1224+213	MARS	5.3
C4	E 1	05 Aug 2011	2.4	245	0.32	1310+323	0.55	3C273	MWC349	13
C4	E 2	17 Aug 2011	1.7	223	0.34	1310+323	0.55	3C273	MWC349	31
C4	E 4	22 Aug 2011	1.7	191	0.30	1310+323	0.55	3C279	MWC349	17
D1	E 1	17 Aug 2011	2.6	288	0.25	1058+015	2.6	1058+015	MARS	23.4
D1	E 3	21 Aug 2011	2.7	288	0.28	1058+015	2.6	1058+015	MARS	20.0
D1	D 1	05 May 2012	2.7	167	0.27	1058+015	2.0	1058+015	MARS	11.2
D1	D 2	06 Jun 2012	3.1	117	0.32	1058+015	2.0	1058+015	MARS	14.9
D2	E 1	17 Aug 2011	2.9	296	0.24	1058+015	2.6	3C273	MARS	12.3
D2	D 1	27 Apr 2012	2.3	88	0.32	1058+015	2.0	3C84	MARS	10.5
D2	D 2	06 May 2012	1.0	234	0.14	1058+015	2.0	3C273	MARS	12.1
D2	D 3	07 Jun 2012	4.8	169	0.38	1058+015	2.0	3C84	MARS	15.5
D3	D 1	08 May 2012	3.2	141	0.18	1058+015	2.0	3C279	MARS	9.0
D4	D 1	13 May 2012	3.4	159	0.26	1058+015	2.0	0854+201	MARS	12.0

Table 3.8: Summary of 1 mm observations of the CO($J = 3 \rightarrow 2$) line. For bin C and D observations, three velocity channels is roughly 42 km s^{-1} and 48 km s^{-1} respectively. See Table 3.5 for column description.

3 hours (time on-source), yielding final maps with rms noise of ≈ 10 mJy beam^{-1} in a 48 km s^{-1} channel.

In bin C, sources C2, C3 and C4 were detected at the $\approx 5\sigma$ level in the CO($J = 3 \rightarrow 2$) line. However, C1, with its wide velocity profile (observed in the CO($J = 1 \rightarrow 0$) line), was only marginally detected and we give an upper limit on the CO($J = 3 \rightarrow 2$) flux. We show the *uv*-spectra for all bin C galaxies in Figure 3.5. For each galaxy (indicated in the top left), the top (bottom) panel shows the vector-averaged *Real* and *Imaginary* amplitudes (phase) of the calibrated *uv* data versus velocity. The CO($J = 1 \rightarrow 0$) line is shown in the top panels and the CO($J = 3 \rightarrow 2$) line in the bottom panels. For the CO($J = 3 \rightarrow 2$) line in galaxies C1 and C2, the spectrum is calculated at a position offset from the SDSS position in order to coincide with the observed peak of the CO emission.

In bin D, we do not significantly detect any of the four galaxies, and give only upper limits. The bin D galaxies are discussed further in Section 3.4.5

3.4 Results

The results of these observations are presented in the following sections. Section 3.4.1 gives the measured CO fluxes and derived molecular gas masses, and shows the CO emission maps and spectra for all detected galaxies. In Section 3.4.2, we discuss the morphologies of the resolved bin A galaxies, comparing the observed CO emission maps to noise-added model data. Section 3.4.3 highlights two bin A galaxies (A3 and A8) with extraordinary CO emission features. We complete the description of the bin A galaxies with a brief presentation of the three bin A non-detections in Section 3.4.4. Finally, we discuss the non-detection of the bin D galaxies in Section 3.4.5. We estimate the expected CO flux as well as stack the spectra of the four galaxies to increase the signal-to-noise ratio.

3.4.1 CO Emission Maps and Molecular Gas Masses

Tables 3.9 and 3.10 present the quantities we derive from the CO observations. The CO line luminosity is calculated from the line flux ($S_{\rm CO}$ in Jy km s^{-1}, calculated as described in Appendix A.2) following

$$L'_{\rm CO} = 3.25 \times 10^7 \; S_{\rm CO} \; \nu_{\rm obs}^{-2} \; r_{\rm com}^2 (1+z)^{-1} \tag{3.3}$$

(see the review by Solomon & Vanden Bout 2005), where $\nu_{\rm obs}$ is in GHz and $r_{\rm com}$ is the comoving distance in Mpc. The units of $L'_{\rm CO}$ are K km s^{-1} pc^2. We report the measurement error for $S_{\rm CO}$. The error reported for $L'_{\rm CO}$ includes both the measurement error of $S_{\rm CO}$ and a 30% systematic error, added in quadrature (see Appendix A.2 for more details).

The center velocity, $v_{\rm center}$, is the flux-weighted average velocity of the galaxy-integrated spectrum ($v = 0$ at the redshift in Table 3.3). The error reported is the standard deviation of the v_{center} values found with the three flux measurement methods and different channel averaging described in Appendix A.2. The reported velocity width (ΔV) is the full width of the emission, where 'source' velocity channels are selected by eye. We give the velocity width of a single channel as the error.

In the case of a non-detection (galaxies A4, A6, A12, D1, D2, D3, and D4; indicated by ^{a} in Tables 3.9 and 3.10), we estimate a 3σ upper limit on $S_{\rm CO}$ from the noise in the channel maps and a maximum velocity width motivated by detections at that redshift: 600 km s^{-1} in bin A and 400 km s^{-1} in bin D. For the CO($J = 3 \rightarrow 2$) line in galaxy C1, while the CO($J = 3 \rightarrow 2$) channel maps did not show evidence of a source upon visual inspection, an integrated spectrum made of a circular region 4.5″ in radius at the center of the image suggests a 3σ detection. We calculate an upper limit on the line flux (and related quantities) from this spectrum, over the velocities of the CO($J = 1 \rightarrow 0$) line in C1.

Src	J_{upper}	S_{CO} (Jy km s^{-1})	v_{center} (km s^{-1})	ΔV (km s^{-1})	L'_{CO} (10^9 K km s^{-1} pc^2)	M_{mgas} ($10^9 M_\odot$)	f_{mgas}	τ_{dep} (Gyr)
A1	1	10.75 ± 2.99	33.7 ± 27.3	428.0 ± 71.3	4.76 ± 1.95	20.72 ± 8.47	$0.27^{+0.10}_{-0.09}$	$0.69^{+0.37}_{-0.34}$
A2	1	14.40 ± 2.55	30.5 ± 12.6	281.2 ± 35.2	4.44 ± 1.55	19.32 ± 6.73	$0.17^{+0.06}_{-0.06}$	$0.68^{+0.28}_{-0.27}$
A3	1	17.94 ± 2.07	22.8 ± 6.8	552.5 ± 34.5	3.22 ± 1.03	14.01 ± 4.50	$0.12^{+0.04}_{-0.04}$	$0.65^{+0.35}_{-0.29}$
A4[a]	1	5.98 ± 1.98	0.0 ± 0.0	600.0 ± 0.0	2.25 ± 1.01	9.79 ± 4.38	$0.11^{+0.04}_{-0.05}$	$0.20^{+0.09}_{-0.09}$
A5	1	23.22 ± 3.90	-60.3 ± 9.8	492.0 ± 35.1	7.12 ± 2.45	30.99 ± 10.65	$0.23^{+0.09}_{-0.07}$	$0.73^{+0.27}_{-0.27}$
A6[a]	1	3.65 ± 1.23	0.0 ± 0.0	600.0 ± 0.0	1.24 ± 0.56	5.40 ± 2.43	$0.08^{+0.03}_{-0.03}$	$0.15^{+0.13}_{-0.08}$
A7	1	6.72 ± 1.52	49.2 ± 31.9	319.0 ± 106.3	2.58 ± 0.97	11.23 ± 4.22	$0.13^{+0.05}_{-0.05}$	$0.27^{+0.13}_{-0.12}$
A8	1	4.52 ± 1.35	-61.0 ± 20.5	357.3 ± 71.5	2.10 ± 0.89	9.14 ± 3.87	$0.05^{+0.03}_{-0.02}$	$1.22^{+1.05}_{-0.70}$
A9	1	5.68 ± 1.42	-7.1 ± 17.7	420.3 ± 70.1	1.59 ± 0.62	6.92 ± 2.70	$0.16^{+0.06}_{-0.06}$	$1.86^{+1.15}_{-0.91}$
A10	1	7.88 ± 3.16	4.3 ± 17.0	274.4 ± 68.6	1.11 ± 0.56	4.83 ± 2.42	$0.08^{+0.04}_{-0.04}$	$0.94^{+0.62}_{-0.54}$
A11	1	6.89 ± 0.98	-10.5 ± 11.2	419.8 ± 70.0	1.86 ± 0.62	8.09 ± 2.69	$0.13^{+0.05}_{-0.04}$	$0.91^{+0.60}_{-0.39}$
A12[a]	1	3.50 ± 1.16	0.0 ± 0.0	600.0 ± 0.0	1.59 ± 0.71	6.92 ± 3.09	$0.16^{+0.07}_{-0.07}$	$2.03^{+3.76}_{-1.45}$
A13	1	21.89 ± 4.12	-27.3 ± 8.9	563.5 ± 35.2	7.15 ± 2.53	31.12 ± 11.02	$0.21^{+0.08}_{-0.07}$	$2.67^{+3.07}_{-1.63}$
B1	1	11.35 ± 0.62	-23.1 ± 4.0	615.4 ± 38.5	18.60 ± 5.67	80.95 ± 24.68	$0.23^{+0.08}_{-0.07}$	$0.92^{+1.38}_{-0.60}$
B2	1	7.32 ± 0.40	25.5 ± 11.7	581.1 ± 38.7	13.20 ± 4.03	57.45 ± 17.52	$0.23^{+0.08}_{-0.07}$	$1.05^{+0.66}_{-0.54}$
B3	1	4.49 ± 0.35	-23.1 ± 6.6	378.9 ± 37.9	5.97 ± 1.85	25.98 ± 8.05	$0.30^{+0.08}_{-0.08}$	$0.55^{+0.68}_{-0.32}$
B4	1	4.81 ± 0.20	-25.6 ± 5.2	457.6 ± 38.1	6.99 ± 2.12	30.42 ± 9.21	$0.23^{+0.07}_{-0.06}$	$0.61^{+1.04}_{-0.40}$
B5	1	6.61 ± 0.22	16.1 ± 2.5	307.6 ± 38.5	10.70 ± 3.23	46.57 ± 14.06	$0.21^{+0.07}_{-0.06}$	$0.91^{+0.44}_{-0.38}$
B6	1	3.52 ± 0.31	-133.6 ± 16.4	343.7 ± 38.2	5.22 ± 1.63	22.72 ± 7.10	$0.25^{+0.14}_{-0.07}$	$0.38^{+0.16}_{-0.13}$
B7	1	5.97 ± 0.30	-40.9 ± 4.9	497.0 ± 38.2	9.01 ± 2.74	39.21 ± 11.93	$0.12^{+0.04}_{-0.04}$	$0.64^{+0.89}_{-0.42}$
B8	1	2.25 ± 0.33	-34.8 ± 20.4	382.5 ± 76.5	3.41 ± 1.14	14.84 ± 4.96	$0.11^{+0.04}_{-0.04}$	$0.14^{+0.20}_{-0.12}$
B9	1	3.91 ± 0.27	-18.6 ± 5.9	459.5 ± 38.3	6.03 ± 1.86	26.24 ± 8.08	$0.10^{+0.04}_{-0.04}$	$0.39^{+0.50}_{-0.25}$
B10	1	5.25 ± 0.22	27.1 ± 2.6	270.9 ± 38.7	9.28 ± 2.81	40.39 ± 12.23	$0.31^{+0.08}_{-0.08}$	$0.54^{+0.22}_{-0.20}$

Table 3.9: Properties of the CO emission: bins A and B. (Described in Section 3.4.1). For sources marked by [a], we give an upper limit on the CO flux.

Src	J_{upper}	S_{CO} (Jy km s^{-1})	v_{center} (km s^{-1})	ΔV (km s^{-1})	L'_{CO} (10^9 K km s^{-1} pc^2)	M_{mgas} ($10^9 M_\odot$)	f_{mgas}	τ_{dep} (Gyr)
C1	1	2.05 ± 0.34	-84.9 ± 18.1	542.2 ± 41.7	8.25 ± 2.83	35.90 ± 12.31	$0.17^{+0.06}_{-0.06}$	$0.93^{+2.09}_{-0.69}$
C2	1	2.35 ± 0.10	-6.7 ± 1.2	253.7 ± 42.3	10.70 ± 3.24	46.57 ± 14.11	$0.23^{+0.18}_{-0.07}$	$0.81^{+0.39}_{-0.39}$
C3	1	4.39 ± 0.09	-24.7 ± 5.7	384.0 ± 42.3	21.70 ± 6.53	94.44 ± 28.40	$0.25^{+0.15}_{-0.07}$	$1.45^{+0.77}_{-0.77}$
C4	1	3.01 ± 0.11	17.3 ± 13.0	292.5 ± 41.8	12.30 ± 3.72	53.53 ± 16.18	$0.23^{+0.10}_{-0.07}$	$1.06^{+0.45}_{-0.45}$
C1[a]	3	9.02 ± 2.65	-49.9 ± 7.3	542.3 ± 23.4	4.03 ± 1.69	35.08 ± 14.73	$0.17^{+0.07}_{-0.07}$	$0.91^{+2.05}_{-0.71}$
C2	3	8.39 ± 1.12	19.5 ± 8.2	169.2 ± 42.3	4.25 ± 1.40	36.99 ± 12.15	$0.19^{+0.16}_{-0.07}$	$0.64^{+0.32}_{-0.32}$
C3	3	13.46 ± 1.56	-14.0 ± 7.8	426.7 ± 42.7	7.39 ± 2.38	64.32 ± 20.69	$0.18^{+0.12}_{-0.06}$	$0.99^{+0.53}_{-0.53}$
C4	3	11.88 ± 1.22	33.5 ± 5.0	250.7 ± 41.8	5.41 ± 1.72	47.09 ± 14.93	$0.21^{+0.10}_{-0.07}$	$0.93^{+0.41}_{-0.41}$
D1[a]	3	3.36 ± 1.12	0.0 ± 0.0	400.0 ± 0.0	4.38 ± 1.96	38.12 ± 17.10	$0.49^{+0.15}_{-0.13}$	$0.61^{+0.81}_{-0.44}$
D2[a]	3	2.73 ± 0.91	0.0 ± 0.0	400.0 ± 0.0	4.45 ± 2.00	38.73 ± 17.37	$0.44^{+0.15}_{-0.13}$	$0.54^{+0.71}_{-0.38}$
D3[a]	3	3.39 ± 1.13	0.0 ± 0.0	400.0 ± 0.0	4.36 ± 1.96	37.95 ± 17.02	$0.41^{+0.15}_{-0.13}$	$0.48^{+0.64}_{-0.34}$
D4[a]	3	5.19 ± 1.73	0.0 ± 0.0	400.0 ± 0.0	6.88 ± 3.09	59.88 ± 26.86	$0.52^{+0.15}_{-0.13}$	$0.81^{+1.06}_{-0.57}$

Table 3.10: Properties of the CO emission: bins C and D. (Described in Section 3.4.1). For sources marked by [a], we give an upper limit on the CO flux.

The molecular gas mass ($M_{\rm mgas}$) is calculated from $L'_{\rm CO}$ according to

$$M_{\rm mgas} = 1.36\alpha_{\rm CO}L'_{\rm CO} \tag{3.4}$$

where $\alpha_{\rm CO}$ is the CO luminosity to H_2 mass conversion factor (akin to $X_{\rm CO}$) and the factor of 1.36 accounts for Helium in order to give the total molecular gas mass. We use a Milky Way-like $\alpha_{\rm CO}$ value of 3.2 $M_\odot$ (K km s^{-1} pc^2)$^{-1}$ (e.g. Dame et al. 2001). There is of course considerable uncertainty in this value, but we do not reflect this uncertainty in the error in the molecular gas mass. The error in $M_{\rm mgas}$ is calculated by propogating the error in $L'_{\rm CO}$. We use a Milky Way-like conversion factor for all galaxies in Tables 3.9 and 3.10, but note that a starburst conversion factor may be more appropriate in some cases. This is discussed further in Chapter 4.

We report the molecular gas fraction and the molecular gas depletion time in the last two columns of Tables 3.9 and 3.10. In keeping with previous work, we define the molecular gas fraction ($f_{\rm mgas}$) as the fraction of baryonic matter (ignoring atomic and ionized hydrogen gas):

$$f_{\rm mgas} = \frac{M_{\rm mgas}}{M_* + M_{\rm mgas}} \tag{3.5}$$

The molecular gas depletion time (τ_{mgas}) represents the time it would take to consume all the available molecular gas at the current star formation rate, defined:

$$\tau_{\rm dep} = \frac{M_{\rm mgas}}{SFR} \tag{3.6}$$

The errors in both of these quantities include both the error in the CO luminosity and the error in the stellar mass or SFR.

The CO emission maps for all detected galaxies are presented in Figures 3.6 - 3.11. For each galaxy, the optical image (from SDSS) is in the left-most panel, the moment 0 (total intensity) map is in the left middle panel, the moment 1 (intensity-weighted mean velocity) map is in the right middle panel and the integrated spectrum is in the far right panel. The dotted white ellipse shows the region in which pixels were summed (un-masked pixels; see Appendix A.2 for details). The white bar in the moment 0 map shows the angular size of 10 kpc at the redshift of the galaxy. In the far right panel, the solid blue line shows the masked spectrum and the dotted green line shows the unmasked spectrum. Channels considered part of the source emission are shaded yellow.

The moment maps are produced using the 2σ clipped smooth mask (described in Appendix A.2). The moment 0 map is a simple sum of the masked image in the 'source' velocity channels. The moment 1 map is produced by summing the masked image multiplied by the velocity in each channel then normalizing by the moment 0 value. Thus, the color in the moment 1 map indicates the intensity-weighted mean velocity in each pixel. The moment 1 map is only calculated in pixels which have a positive moment 0 value.

In most of the bin A galaxies, we resolve the CO disk, illustrated by a velocity gradient across the emission region in the moment 1 map (indicative of a rotating disk). The

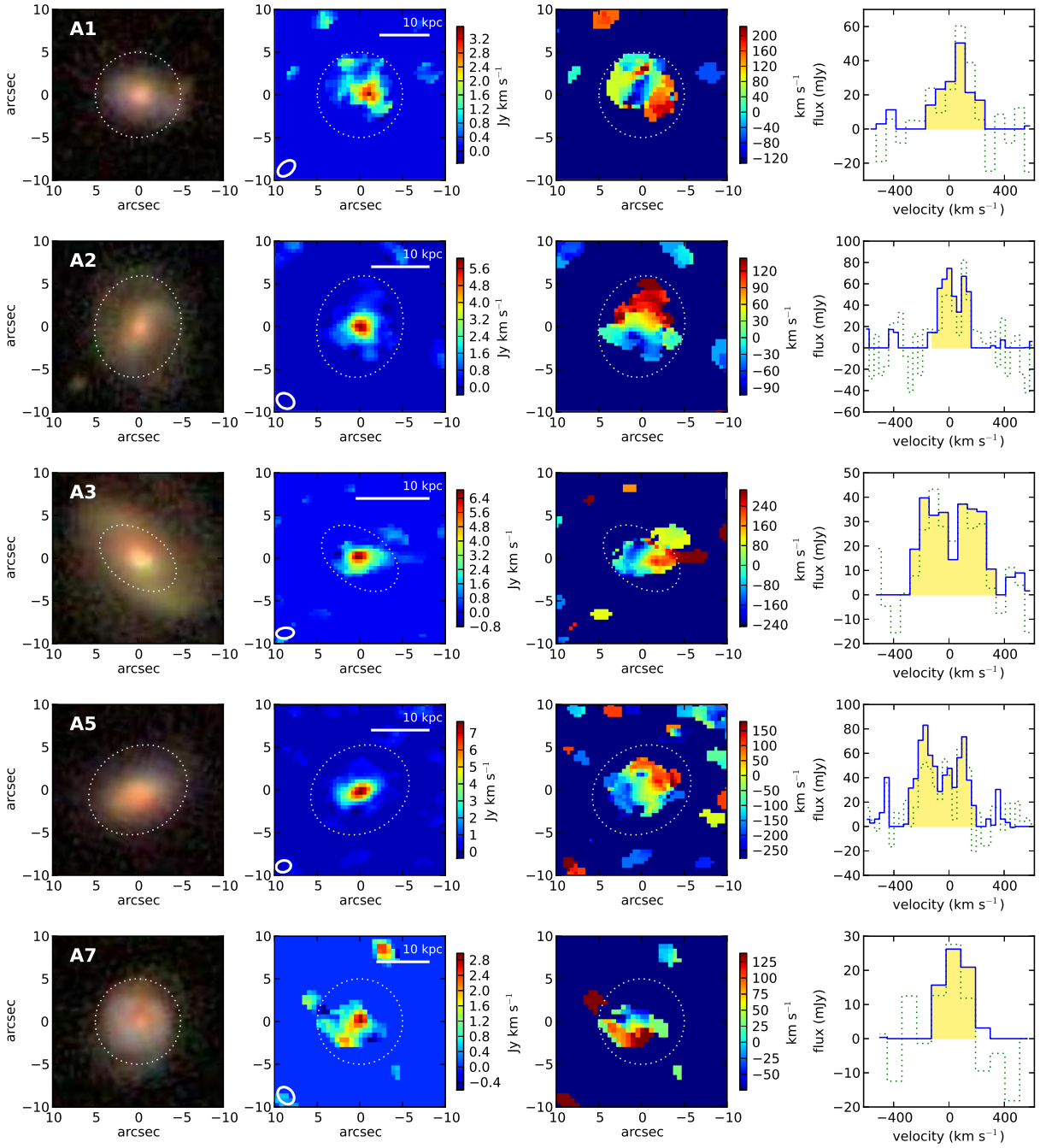

Figure 3.6: CO emission maps for detected bin A galaxies, part 1. For each galaxy (indicated in upper left), we show the optical image (left), moment 0 map (left middle) and moment 1 map (right middle). The dotted white ellipse indicates the source region. In the moment 0 map, the synthesized beam is indicated by the solid white ellipse in the lower left corner and a 10 kpc scale bar is given in the top right. The far right panel shows the spectrum of the galaxy, with (solid blue) and without (dotted green) masking.

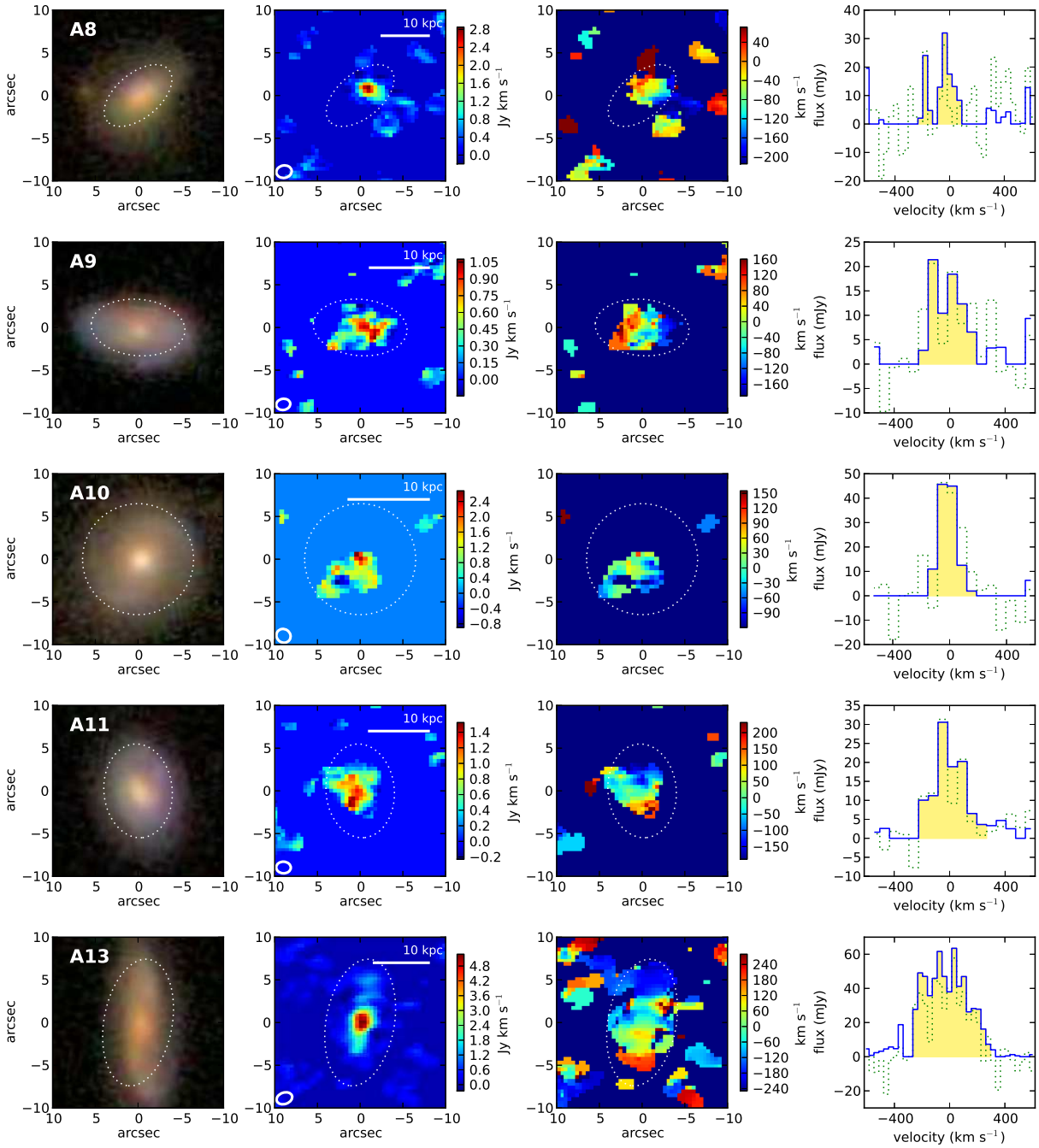

Figure 3.7: CO emission maps for detected bin A galaxies, part 2. Same as Figure 3.6.

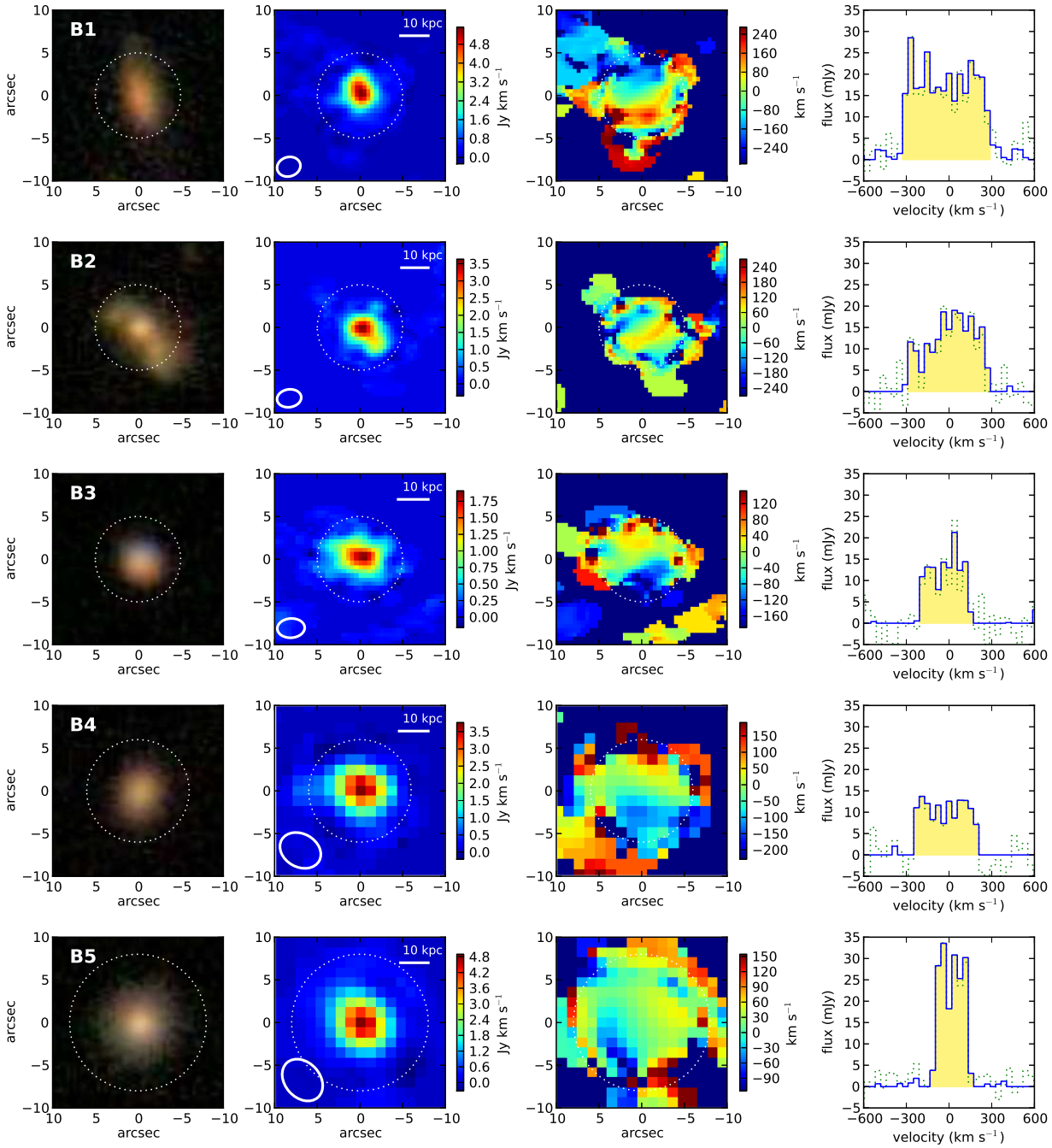

Figure 3.8: CO emission maps for bin B galaxies, part 1. Same as Figure 3.6.

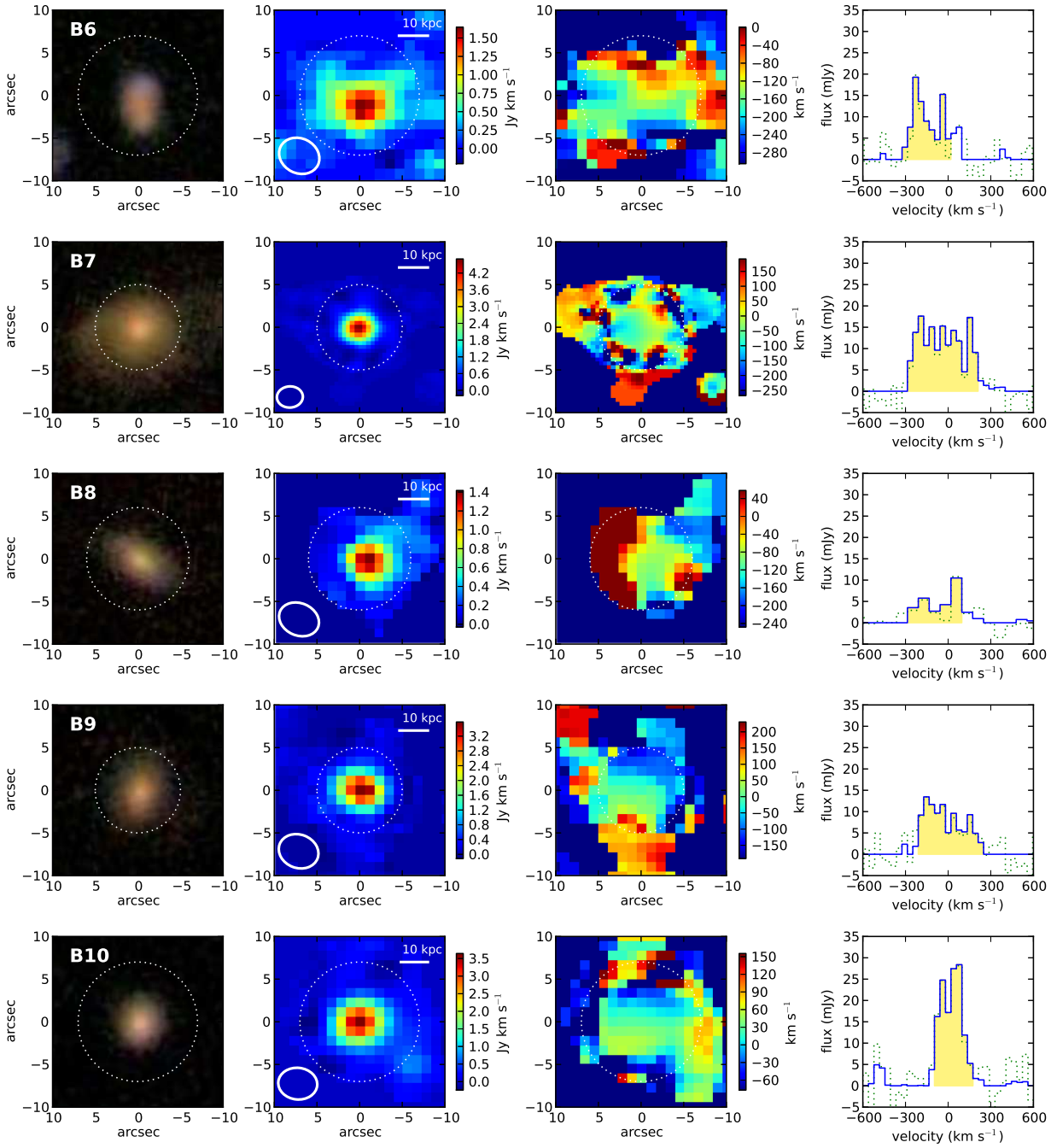

Figure 3.9: CO emission maps for bin B galaxies, part 2. Same as Figure 3.6.

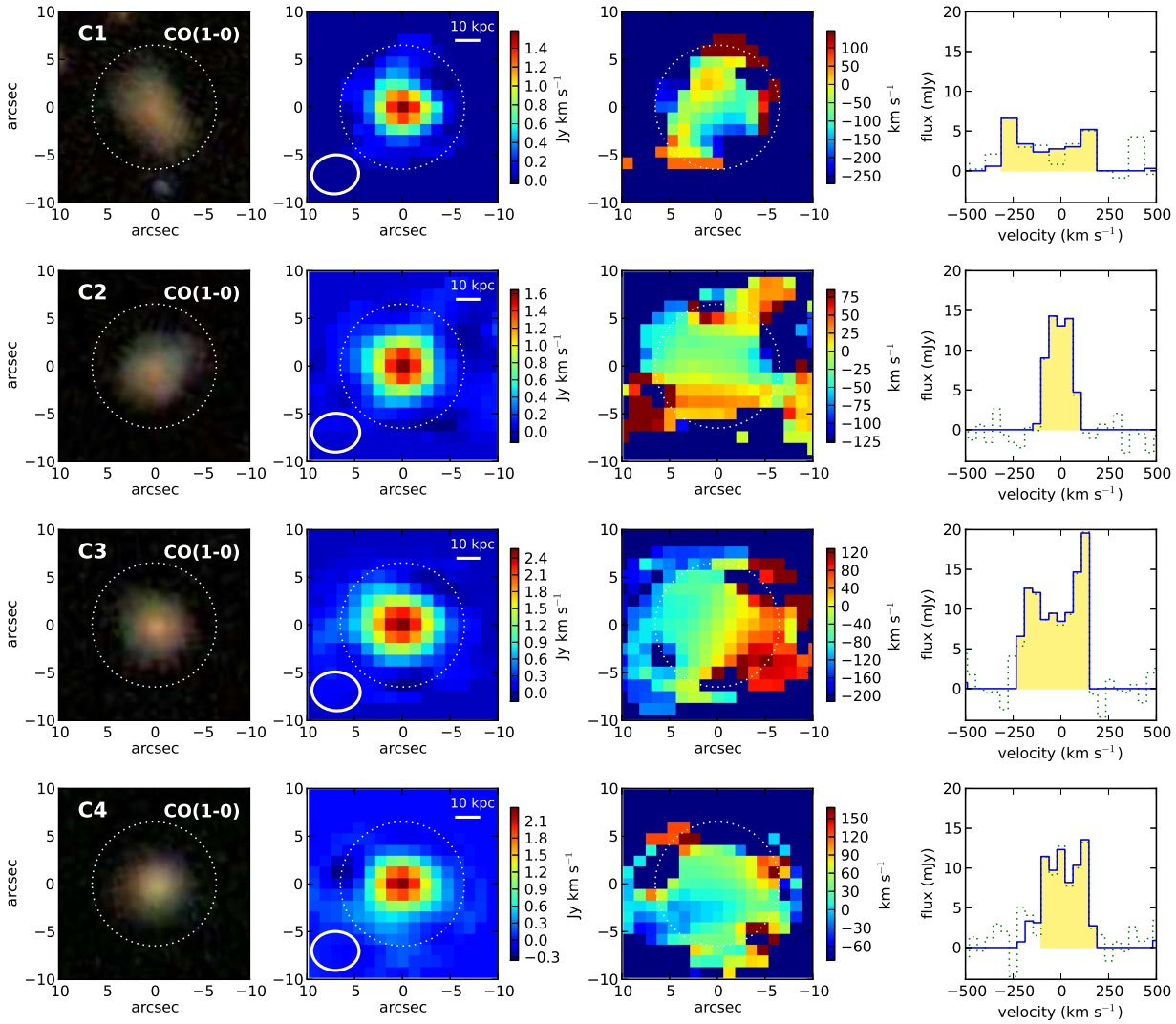

Figure 3.10: CO emission maps for bin C galaxies in the CO($J = 1 \rightarrow 0$) line. Same as Figure 3.6.

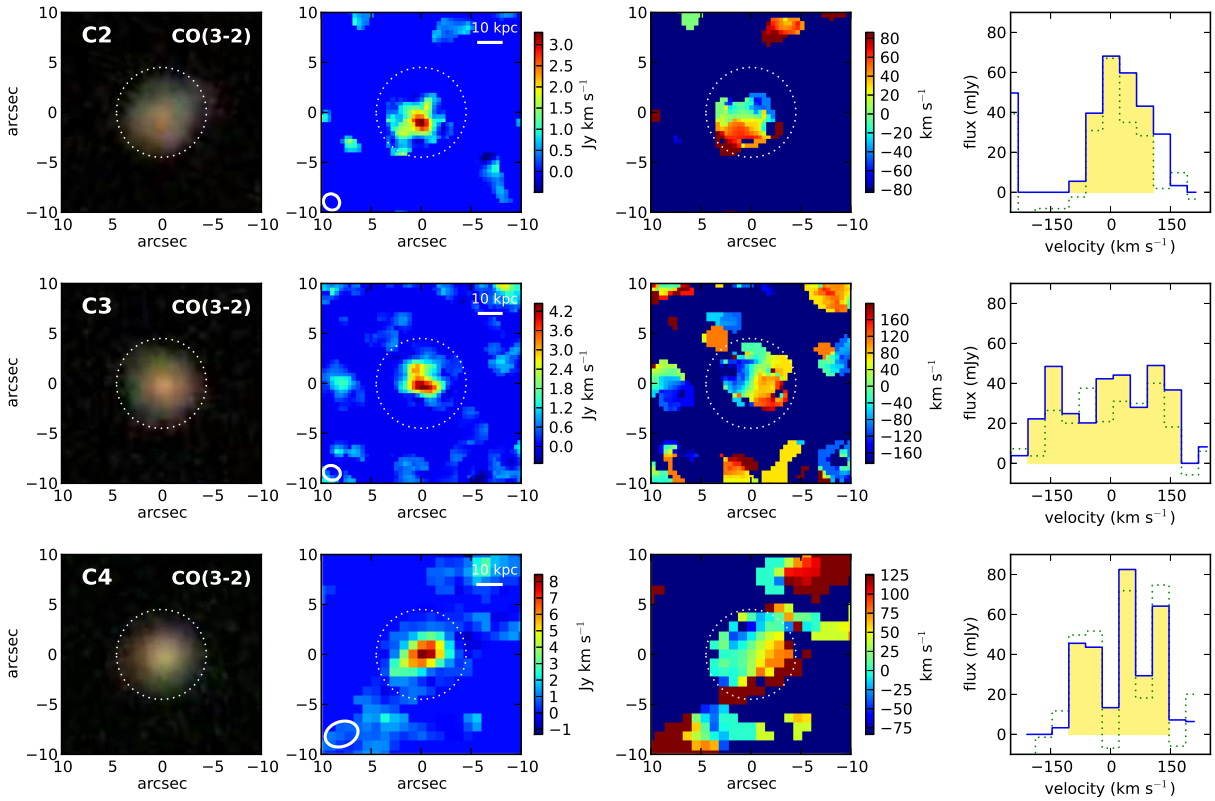

Figure 3.11: CO emission maps for detected bin C galaxies in the CO($J = 3 \rightarrow 2$) line. Same as Figure 3.6.

morphology of the bin A CO emission is discussed further in Section 3.4.2. The bin B galaxies which were observed only in D configuration are unresolved. However, galaxies B1, B2, B3 and B7 were observed in C configuration as well, increasing the resolution by roughly a factor of 2. Of these four, galaxies B1 and B3 show evidence for ordered rotation but are only marginally resolved. Bin C galaxies are unresolved in the CO($J = 1 \rightarrow 0$) line and marginally resolved in the CO($J = 3 \rightarrow 2$) line, The CO($J = 3 \rightarrow 2$) moment 1 maps of the galaxies C2, C3 and C4 are suggestive of a rotating disk of gas. Bin D galaxies are not detected, but would be unresolved based on the sizes of the stellar disks.

3.4.2 Morphology of the Low-Redshift Sample

For the EGNoG galaxies in redshift bin A, the resolution of the CO observations allows us to comment on the morphology of the molecular gas disk in these at $z = 0.05 - 0.1$. The CO intensity maps in Figures 3.6 and 3.7 are suggestive of irregular morphology at first glance. However, due to the modest signal to noise ratio of these observations, it is difficult to infer the true shape of the underlying CO emission.

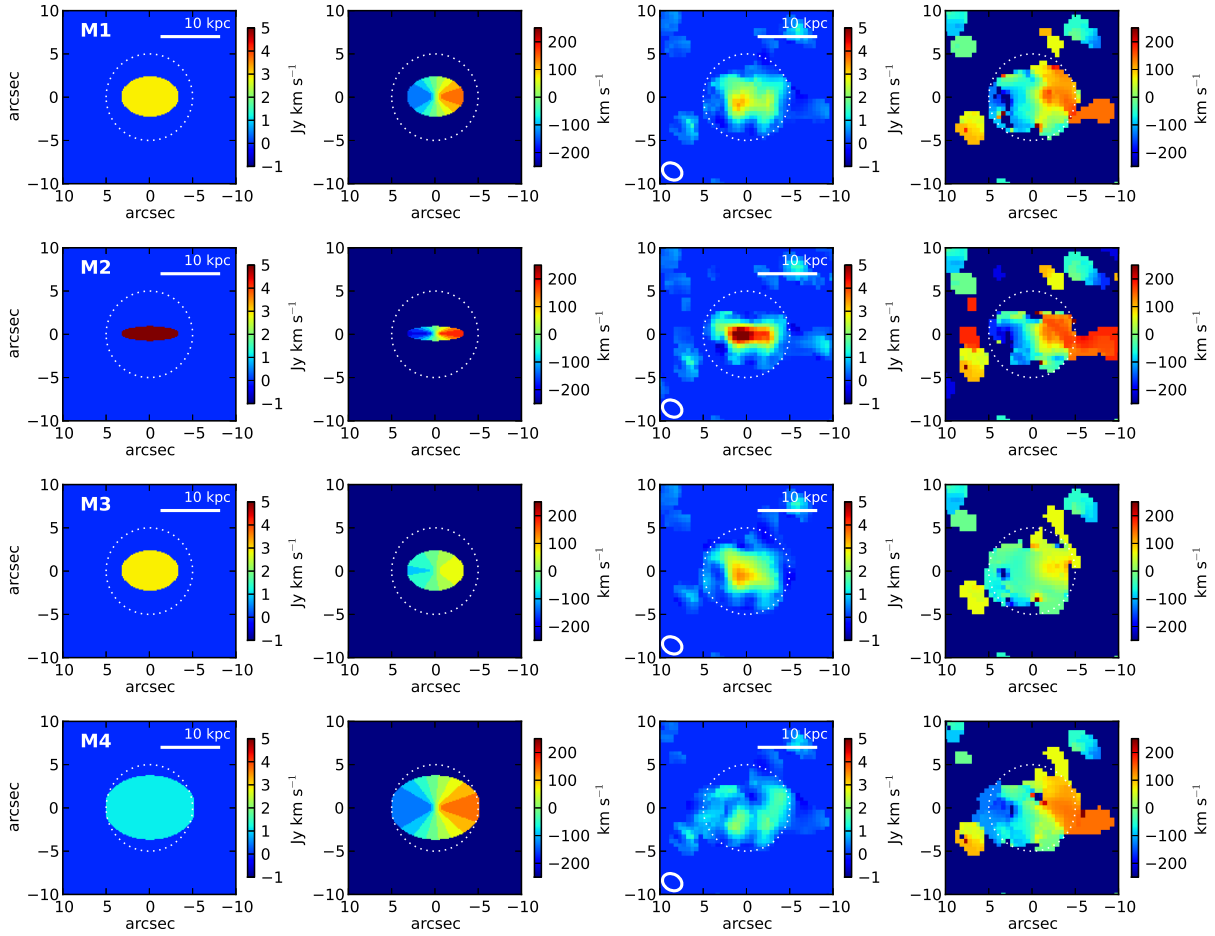

Figure 3.12: Model galaxy maps. For each model (M1 - M4, parameters given in Table 3.11), the far left and left middle panels show the model galaxy moment 0 and moment 1 maps respectively. In the right middle and far right panels are the moment 0 and moment 1 maps from normal processing of the model galaxy inserted into noise-only data.

To determine the effect of a modest signal to noise ratio on our CO emission maps, we produced a simple model galaxy at $z = 0.08$, inserted it into noise-only *uv* data channels and processed the data as we did the real data. We used a Milky-Way-like rotation curve, linear in the central 1 kpc, flat outside. We varied the total flux, velocity width, inclination angle (i) and physical radius of the molecular gas disk ($R_{\rm CO}$). Models M1 to M4, shown in Figure 3.12, are representative of the results of varying all four parameters within reasonable ranges. The parameters used in the four models are listed in Table 3.11.

The 'observed' model maps (right two panels in Figure 3.12) suggest that at the signal to noise level typical for our bin A data, irregularities in the CO emission maps do not necessarily indicate underlying irregular structure in the molecular gas disk. Therefore,

Model	i (deg)	ΔV (km s^{-1})	$R_{\rm CO}$ (kpc)	$S_{\rm CO}$ (Jy km s^{-1})
M1	45	400	5	14
M2	75	400	5	14
M3	45	200	5	14
M4	45	400	8	14

Table 3.11: Model parameters: inclination angle (i), velocity width (ΔV), radius of the CO disk ($R_{\rm CO}$) and total CO flux ($S_{\rm CO}$).

while our observations suggest that the CO in the bin A galaxies is typically ordered in a rotating disk, we conclude that deeper observations would be required to investigate the detailed morphology of the molecular gas disks in these systems.

Two exceptions are galaxies A3 and A8, which exhibit disturbed morphologies that are not likely a result of low signal to noise. Both galaxies show rotating molecular gas disks misaligned with the major axis of the optical disk as well as CO emission outside the optical disk. These two galaxies are discussed in detail in the next section.

3.4.3 Extraordinary CO Emission in Galaxies A3 and A8

The CO emission maps of galaxies A3 ($z = 0.06$) and A8 ($z = 0.10$) show evidence for disturbed morphologies. In both galaxies, we detect CO emission coincident with the optical disk which shows a velocity gradient misaligned with respect to the major axis of the optical disk. In galaxy A8 we detect CO emission outside of the optical disk. Our observations are suggestive of CO emission outside the optical disk of A3 as well, but are not conclusive. In this Appendix, we investigate these extraordinary emission components using *uv*-spectra calculated at various positions in the field to distinguish true emission from noise. We discuss the more compelling case of galaxy A8 first, then galaxy A3.

EGNoG A8

In Figure 3.13 we show the optical image, moment maps, integrated spectrum (as in Figure 3.6), and *uv*-spectra for galaxy A8. In the top right panel, the solid blue line shows the integrated spectrum of the disk of the galaxy (the central white dotted ellipse in the map panels) and the dashed red line shows the integrated spectrum of the emission component outside the disk of the galaxy (the offset white dotted ellipse in the map panels). The bottom three panels show the *uv*-spectra (amplitude and phase versus velocity) at 3 points, A, B and C, labeled on the map panels in the top row.

Point A is centered on the emission coinciding with the optical disk of the galaxy. We only detect CO emission corresponding to the upper right (north-west) half of the optical disk, at negative velocities (relative to the optical redshift from SDSS). The moment 1 map (intensity-weighted velocity) of this component shows a velocity gradient suggestive

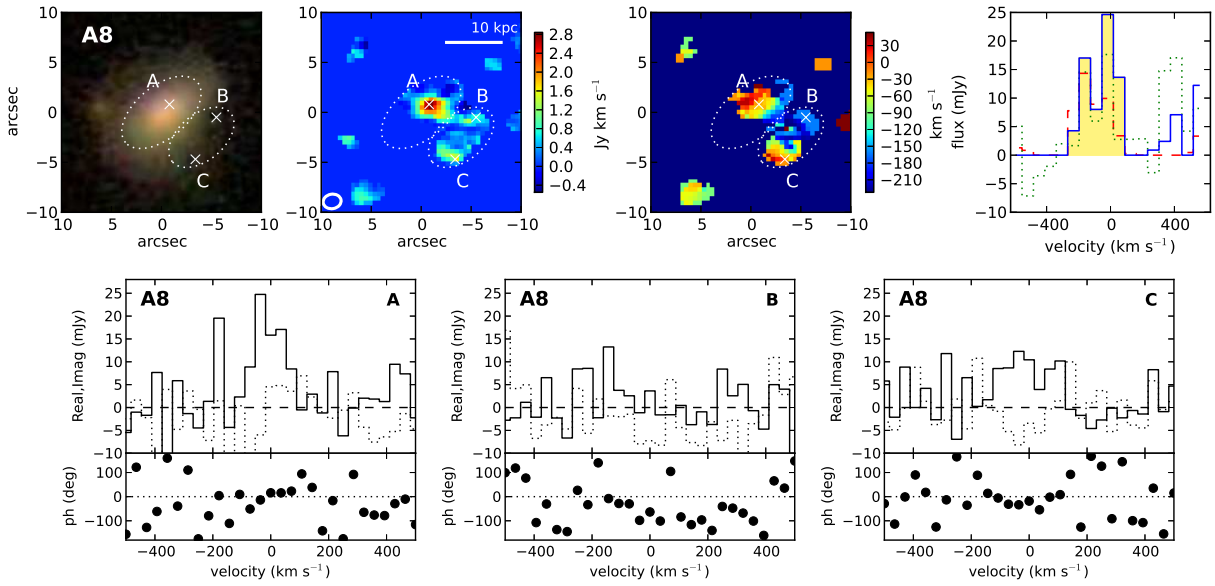

Figure 3.13: Optical image, moment maps, spectra and *uv*-spectra for EGNoG galaxy A8. The top four panels show (from left to right) the optical image, the moment 0 map, the moment 1 map and the integrated spectrum (as in Figure 3.6) of the main part of the galaxy. The spectrum of the external CO component is shown by the red dashed line. The bottom three panels show the *uv*-spectra (vector-averaged *Real* (solid) and *Imaginary* (dotted) amplitudes in the top panel, phases in the bottom panel) at each of the 3 points (A,B and C) marked in the maps in the top row.

of a rotating disk. However, this velocity gradient does not lie along the major axis of the optical image, but appears to be rotated 45 to 90 degrees from the major axis.

Points B and C are at two positions along the long axis of the component that lies outside the optical disk (following the velocity gradient). The optical image from the SDSS shows no optical counterpart to this component of the CO emission. While the *uv*-spectrum at point B appears dominated by noise, point C shows phases of ≈ 0 over several velocity channels, indicative of real emission. This component shows a velocity gradient parallel to the major axis of the optical disk and is therefore not aligned with the velocity gradient of the disk component. However, the two components become roughly spatially coincident at negative velocities.

In summary, we observed the molecular gas in galaxy A8 to be disturbed: CO emission is observed corresponding to the north-west half the optical disk but not in the south-east portion; the velocity gradient of the CO emission component of the disk is not aligned with the major axis of the optical disk; and we observe significant emission outside the optical disk, with no optical counterpart. The optical image does not indicate interaction. We note that there is another galaxy in the field (seen on the left side of the optical image), but

this galaxy is in the SDSS catalog with a photometric redshift of 0.28. The flux of emission component outside the disk is 3.2 Jy km s^{-1}, with $v_{\rm center} = -110$ km s^{-1} and $\Delta V = 357$ km s^{-1}. This is very similar to the CO emission of the disk: $S_{\rm CO} = 4.5$ Jy km s^{-1}, with $v_{\rm center} = -67$ km s^{-1} and $\Delta V = 357$ km s^{-1}. If the emission outside of the optical disk traces dense molecular gas, the molecular gas mass of this component (assuming a Milky Way-like conversion factor) would be 6.5×10^9 M$_\odot$, roughly 70% the molecular mass of the disk component.

EGNoG A3

In Figure 3.14 we show the optical image, moment maps, integrated spectrum (as in Figure 3.6), and *uv*-spectra for galaxy A3. The top row shows moment maps and spectra calculated in the velocity channels of the CO emission coinciding to the optical disk of the galaxy. In the top right panel, the solid blue line shows the integrated spectrum of the disk of the galaxy (the central white dotted ellipse in the map panels) and the dashed red line shows the integrated spectrum of the emission component outside the disk of the galaxy (the offset white dotted ellipse in the map panels). The middle row shows the same as the top row, but at the velocity channels of the negative velocity component of the emission lying outside of the optical disk. In the middle right panel, the solid blue line shows the integrated spectrum of the emission component outside the optical disk of the galaxy and the dashed red line shows the emission corresponding to the optical disk. The bottom three panels show the *uv*-spectra (amplitude and phase versus velocity) at 3 points, A, B and C, labeled on the map panels in the top row.

Point A is centered on the emission coinciding with the optical disk of the galaxy. The CO emission in this case is centered on the optical emission of the galaxy. The moment 1 map (intensity-weighted velocity) of this component shows a velocity gradient suggestive of a rotating disk, but misaligned with the major axis of the optical disk of the galaxy (rotated 45 to 90 degrees from the major axis, as in galaxy A8).

Points B and C are at two positions in the emission component that lies outside the optical disk: point B marks an area that is bright at positive velocities (93 km s^{-1}) and point C marks the area that is bright at negative velocities (-377 km s^{-1}). The optical image from the SDSS shows no optical counterpart to this component of the CO emission. The *uv*-spectra at points B and C (bottom row, middle and right panels) may be suggestive of real emission but do not show a strong signal. The flux from the positive (negative) velocity component is 2.6 Jy km s^{-1} (1.2 Jy km s^{-1}), with $v_{\rm center} = 93$ (-377) km s^{-1} and $\Delta V = 138$ (138) km s^{-1}. If the emission is real and tracing dens molecular gas, the positive velocity component has a molecular gas mass of 1.5×10^9 M$_\odot$ and the negative velocity component has 7.0×10^8 M$_\odot$. These masses are both small compared the molecular gas mass of the main disk, 1.4×10^{10} M$_\odot$.

Therefore, the misalignment (with respect to the optical disk) of the velocity gradient of the main component of the CO emission is suggestive of a disturbed morphology. Our observations are suggest there is CO emission outside of the optical disk, but we do not

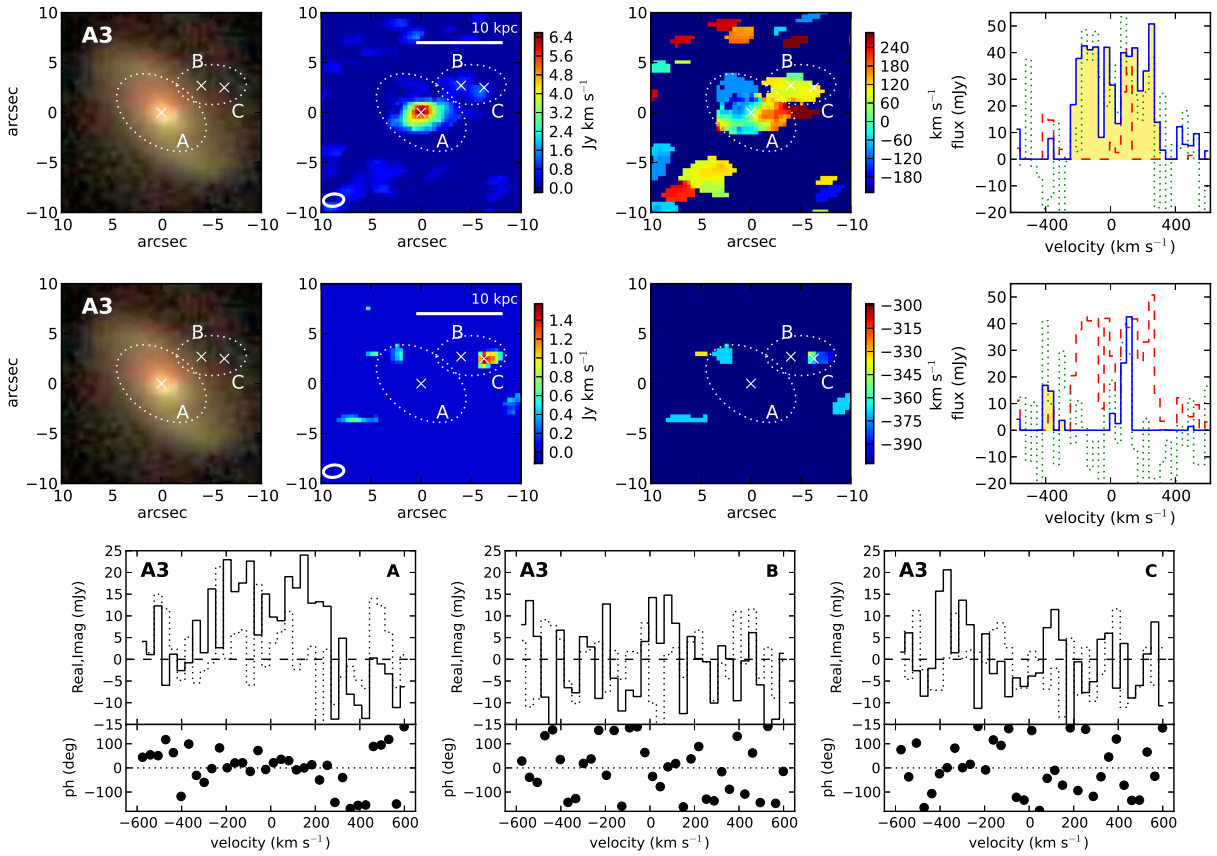

Figure 3.14: Optical image, moment maps, spectra and *uv*-spectra for EGNoG galaxy A3. The top four panels show (from left to right) the optical image, the moment 0 map, the moment 1 map and the integrated spectrum (as in Figure 3.6) of the main part of the galaxy. The spectrum of the external CO component is shown by the red dashed line. The middle four panels show the same as the top, but for the negative velocity component of the external CO emission. The red dashed line in the far right panel of the middle row shows the spectrum of the main part of the galaxy for reference. The bottom three panels show the *uv*-spectra (vector-averaged *Real* (solid) and *Imaginary* (dotted) amplitudes in the top panel, phases in the bottom panel) at each of the 3 points (A,B and C) marked in the maps in the top and middle rows.

detect this emission at a significant level.

3.4.4 Redshift Bin A Non-Detections

We report no detection for three of the thirteen galaxies in redshift bin A: galaxies A4, A6 and A12. In each case, we estimate an upper limit on the flux by assuming a full velocity width of 600 km s^{-1}(based on the Milky Way). From the moment 0 map, we calculate the noise and take 3σ as the upper limit in a beam. We then estimate the take the area of the expected CO emission to be the size of the optical disk (shown by the white dotted ellipse in Figures 3.15-3.17) and multiply the 3σ upper limit value by the number of beams equivalent to this area.

Figures 3.15-3.17 show the un-masked moment maps, spectra and *uv*-spectra for the three non-detections. We show the *uv*-spectra both at the center position and at the positions of peaks in the CO emission moment 0 maps.

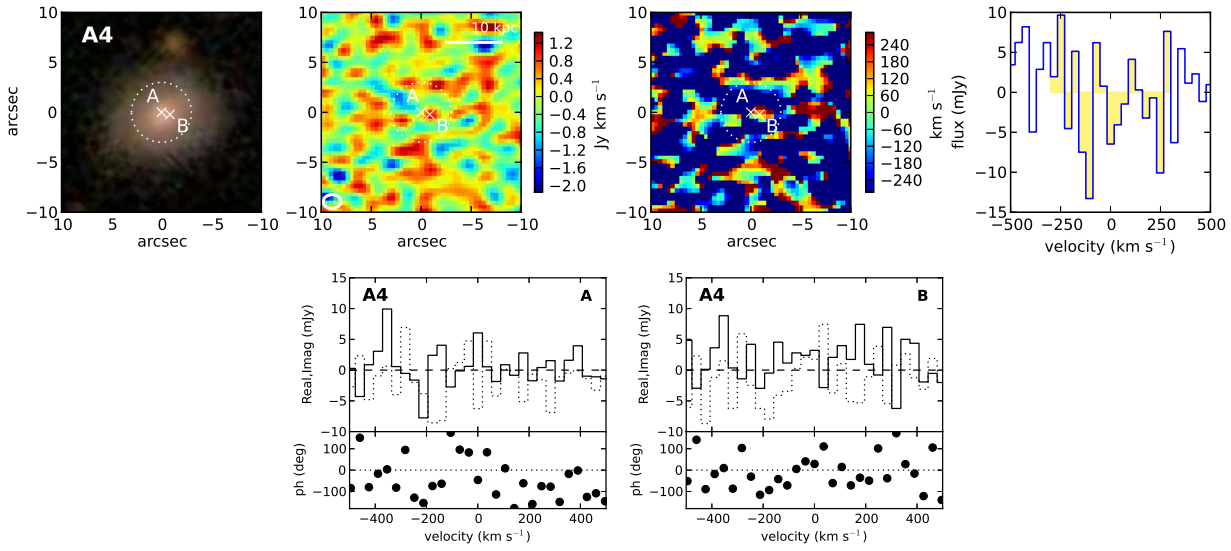

Figure 3.15: Galaxy A4: the top row shows the optical image, moment maps and spectrum as in Figure 3.6. The bottom row shows *uv*-spectra (vector-averaged *Real* (solid) and *Imaginary* (dotted) amplitudes in the top panel, phases in the bottom panel) at the center of the image (A) as well as at an offset position that shows a positive signal in the total intensity map (B).

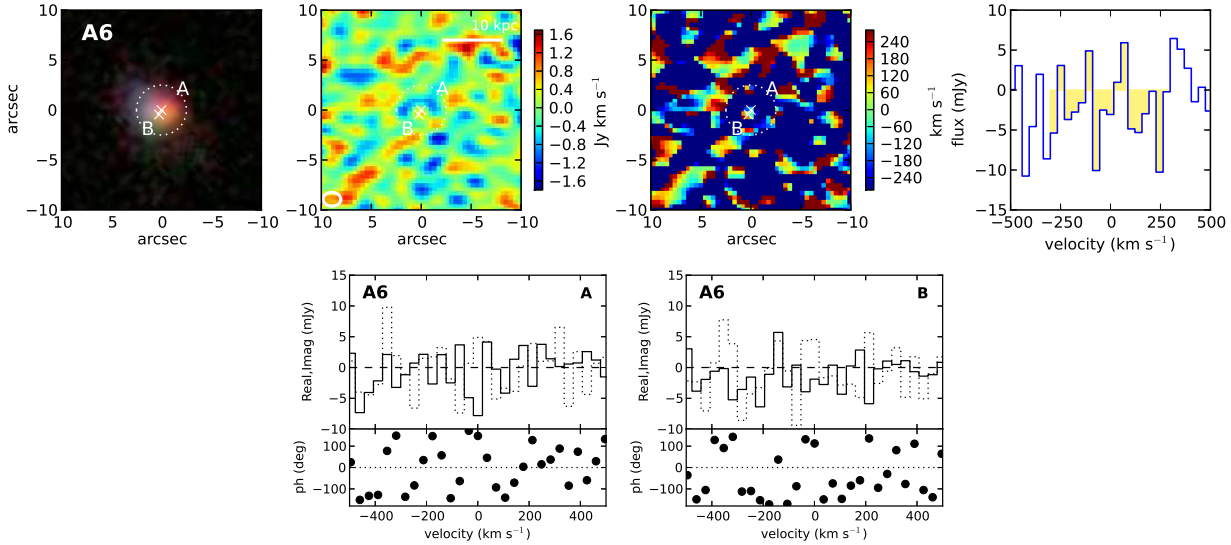

Figure 3.16: Galaxy A6: the top row shows the optical image, moment maps and spectrum as in Figure 3.6. The bottom row shows *uv*-spectra (vector-averaged *Real* (solid) and *Imaginary* (dotted) amplitudes in the top panel, phases in the bottom panel) at the center of the image (A) as well as at an offset position that shows a positive signal in the total intensity map (B).

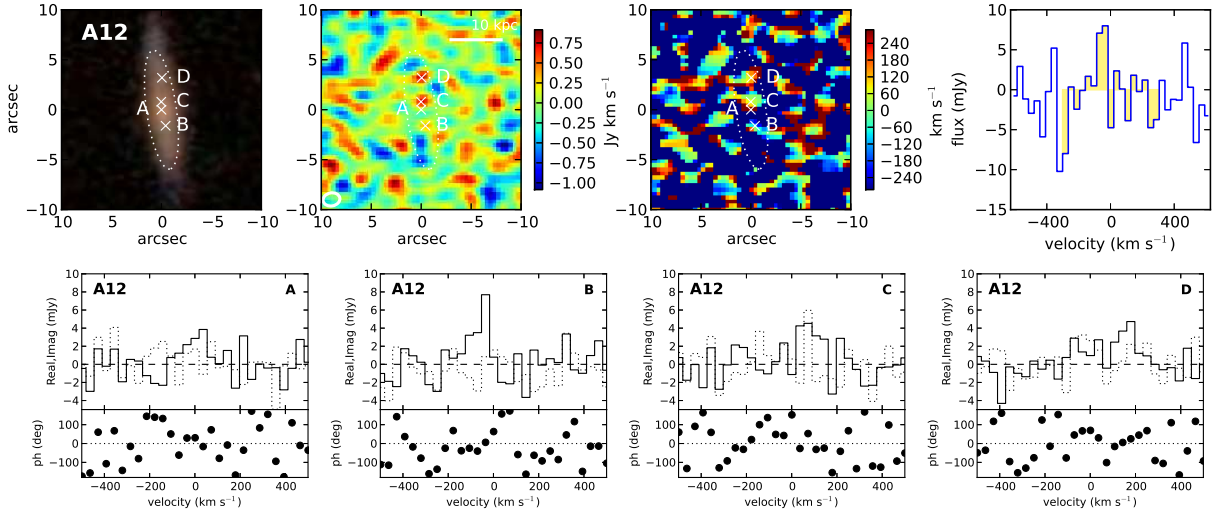

Figure 3.17: Galaxy A12: the top row shows the optical image, moment maps and spectrum as in Figure 3.6. The bottom row shows *uv*-spectra (vector-averaged *Real* (solid) and *Imaginary* (dotted) amplitudes in the top panel, phases in the bottom panel) at four points, labelled A-D. Position A marks the center of the image.

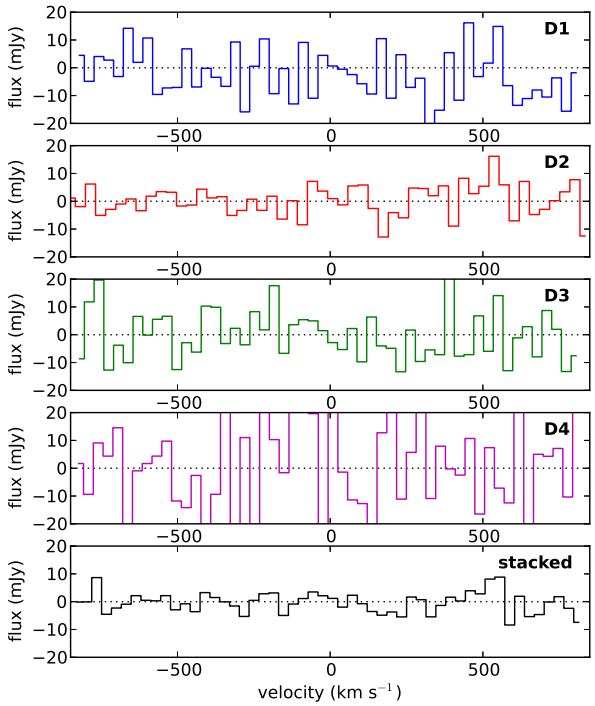

Figure 3.18: Spectra of the four bin D sources within a 2″ circular region (top four panels), plus the stacked (average) spectra, weighted by the variance, in the bottom panel.

3.4.5 Non-Detections of the Bin D Galaxies

We do not detect CO($J = 3 \rightarrow 2$) in any of the four bin D galaxies at $z \approx 0.5$. The 3σ upper limits on $S_{\rm CO}$ are between 2.7 and 5.2 Jy km s^{-1}, assuming a total velocity width of 400 km s^{-1}. The spectra of each of the four bin D galaxies are shown in the top four panels of Figure 3.18 at a velocity resolution of $\approx$ 32 km s^{-1}. The bottom panel shows the stacked spectrum, where each individual spectrum is weighted by the variance. Note that the spectra are stacked centered at the spectroscopic redshifts given in Table 3.10, which have a typical uncertainty of 110 km s^{-1}. The stacked spectrum does not indicate a detection; we calculate a 3σ upper limit of 1.5 Jy km s^{-1} for a 400 km s^{-1} wide signal.

To place these limits in context, we calculate the expected CO flux for a galaxy with SFR $\approx$ 70 M$_\odot$ yr^{-1}, typical for the bin D galaxies. First we consider these galaxies to be normal, using a Milky way-like $\alpha_{\rm CO}$ and $r_{31} = 0.5$. For $\tau_{\rm mgas} = 0.77 \pm 0.57$ Gyr (average from our literature sample; see Section 4.2.2), we expect a CO flux of $S_{\rm CO} = 1.2 - 8.4$ Jy km s^{-1} for normal galaxies. Performing the same calculation using a starburst $\alpha_{\rm CO}$ and the starburst average $\tau_{\rm mgas} = 0.07 \pm 0.04$ Gyr (Section 4.2.2), we expect $S_{\rm CO} = 0.76 - 2.7$ Jy km s^{-1}. We have used $r_{31} = 0.5$ in this calculation but note that a larger value may be appropriate in a starburst system. We can further constrain the expected CO flux using the typical stellar mass ($\log(M_*) = 10.7$) and the expected molecular gas fraction (see Section

4.2.3). For $f_{\rm mgas} = 0.03 - 0.4$, we expect $S_{\rm CO} = 0.13 - 2.6$ Jy km s^{-1}for normal galaxies or $S_{\rm CO} = 0.5 - 11.0$ Jy km s^{-1}for starburst galaxies. Note that these estimates have an uncertainty of a factor of 1.5-2.5 from the uncertainty in the SFR and M_* of the bin D galaxies in addition to further uncertainty in the r_{31} value.

Considering the range of expected CO fluxes, four non-detections at the depth of these observations is not unreasonable. Given the large, overlapping ranges of expected CO fluxes for starburst and normal galaxies detailed above, we do not draw any conclusions about the gas consumption properties of the bin D galaxies based on these upper limits.

3.5 Conclusions

In this chapter, we present the EGNoG survey: CO observations of 31 galaxies from $z = 0.05$ to $z = 0.5$. We detect 24 of the 31 observed galaxies, providing CO maps, spectra, and integrated CO luminosities for detections and 3σ upper limits for non-detections. The analysis of these data is presented in Chapters 4 and 5. In Chapter 4, we place the molecular gas fractions observed in the EGNoG galaxies in context with a sample of galaxies at low and high redshift from the literature. The observed evolution of the moleclar gas fraction from $z \sim 2$ to today agrees well with a simple empirically-based prescription for star formation in normal and starburst galaxies. In Chapter 5, we discuss the gas excitation sample, bin C, for which we have observed both the CO($J = 1 \rightarrow 0$) and CO($J = 3 \rightarrow 2$) lines. We use these data to constrain the line ratio appropriate for intermediate and high redshift star-forming galaxies.

Acknowledgements

We thank Kevin Bundy for useful discussions and assistance with the COSMOS dataset. A.B. thanks all the members of the EGNoG collaboration for their guidance and assistance. We thank the OVRO/CARMA staff and the CARMA observers for their assistance in obtaining the data. Support for CARMA construction was derived from the Gordon and Betty Moore Foundation, the Kenneth T. and Eileen L. Norris Foundation, the James S. McDonnell Foundation, the Associates of the California Institute of Technology, the University of Chicago, the states of California, Illinois, and Maryland, and the National Science Foundation. Ongoing CARMA development and operations are supported by the National Science Foundation under a cooperative agreement, and by the CARMA partner universities.

Chapter 4

Molecular Gas in Intermediate-Redshift Star-Forming Galaxies

In this chapter, we analyze the evolution of the molecular gas fraction in star-forming galaxies using the EGNoG dataset presented in Chapter 3. We use an empirically-motivated, bimodal prescription for the CO to molecular gas conversion factor based on specific star formation rate to compare the EGNoG galaxies to a large sample of galaxies assembled from the literature. We find an average molecular gas depletion time of 0.77 ± 0.57 Gyr for normal galaxies and 0.07 ± 0.04 Gyr for starburst galaxies. We calculate an average molecular gas fraction of 7-20% at the intermediate redshifts probed by the EGNoG survey. By expressing the molecular gas fraction in terms of the specific star formation rate and molecular gas depletion time (using typical values), we calculate the expected evolution of the molecular gas fraction with redshift. The predicted behavior agrees well with the significant evolution observed from $z \sim 2.5$ to today.[1]

4.1 Outline

In the previous chapter, we presented the results of the Evolution of molecular Gas in Normal Galaxies (EGNoG) Survey. In this chapter, we look at the EGNoG galaxies in the context of starburst and normal galaxies at low and high redshift from the literature. We present the literature sample in the following section (Section 4.2). The identification and treatment of starburst and normal galaxies in the literature dataset as well as the EGNoG dataset is described in Section 4.2.1. We then calculate the molecular gas depletion times in normal and starburst galaxies in Section 4.2.2 and investigate the evolution of the molecular gas fraction with redshift in Section 4.2.3.

[1]This chapter will be submitted to the Astrophysical Journal as part of *The EGNoG Survey: Molecular Gas in Intermediate-Redshift Star-Forming Galaxies* by Bauermeister, Blitz, Bolatto, Bureau, Leroy, Ostriker, Teuben, Wong & Wright and is reproduced with the permission of all coauthors.

4.2 Literature Data

The local galaxies of our literature data compilation include normal spiral galaxies, LIRGs and ULIRGs. We include 22 galaxies from Leroy et al. (2008), 10 of which are defined by the authors to be dwarf galaxies ($M_* < 10^{10}$ $M_\odot$). Leroy et al. (2008) present CO data from the HERACLES and BIMA SONG surveys, stellar masses estimated from the SINGS survey K-band luminosities and star formation rates calculated from a combination of GALEX FUV and Spitzer 24 μm. We augment this dataset with 47 galaxies (26 of which have $M_* < 10^{10}$ $M_\odot$) from the overlap of the Hα survey by (Kennicutt et al. 2008) and the CO sample (taken from the literature) of Obreschkow & Rawlings (2009). We estimate stellar masses, star formation rates and CO luminosities for these galaxies following Bothwell et al. (2009). For each galaxy, the stellar mass is calculated from the B-band luminosity using a mass-to-light ratio estimated using the B-V color (Bell & de Jong 2001). The SFR is calculated from the Hα flux via the relation given by Kennicutt (1998a), using an extinction correction calculated from the B-band luminosity following Lee et al. (2009). For more details, see Bothwell et al. (2009).

We include a sample of 56 local LIRGs and ULIRGs, with CO data compiled from Gao & Solomon (2004), Solomon et al. (1997) and Sanders et al. (1991). We use stellar masses and SFRs from the following: the GOALS survey (Howell et al. 2010), with stellar masses calculated from K-band luminosties and SFRs estimated from the combination of IRAS infrared and GALEX FUV luminosities; da Cunha et al. (2010), with stellar masses and SFRs from SED fitting of mid-IR Spitzer/IRS spectra and multi-band photometry available from the literature; and Hou et al. (2011) (table of values via private communication), with stellar masses from SED fitting of SDSS spectra. We estimate SFRs for Hou et al. (2011) galaxies (for which only stellar masses are given) from the total infrared luminosity ($L_{\rm IR}$; 8-1000 μm) using SFR $= 1.7\times10^{-10} L_{\rm FIR}$ (Kennicutt 1998a; $L_{\rm FIR}$ is the far infrared luminosity in $L_\odot$) and $L_{\rm IR}/L_{\rm FIR} = 1.3$ (Graciá-Carpio et al. 2008).

At intermediate redshifts ($z = 0.05 - 1$), the EGNoG sample is augmented by the CO($J = 1 \rightarrow 0$) observations of 7 galaxies (2 are upper limits) at $z \approx 0.4$ by Geach et al. (2011). The stellar masses are from the K-band luminosity using a mass-to-light ratio determined from SED fitting using BVRIJK imaging. SFRs are from the total infrared luminosities, which are estimated from the PAH 7.7 μm line (see Geach et al. 2009).

At high redshifts ($z > 1$), we include 21 SFGs presented in Genzel et al. (2010) (from Tacconi et al. 2010), 6 SFGs from Daddi et al. (2010), and 26 SMGs from Bothwell et al. (2012) (table of values via private communication). The SFGs are observed in the CO($J = 3 \rightarrow 2$) (Tacconi et al. 2010) and CO($J = 2 \rightarrow 1$) lines (Daddi et al. 2010) and converted to CO($J = 1 \rightarrow 0$) luminosities using $r_{31} = 0.5$ and $r_{21} = 0.83$ (where $r_{J1} = L'_{\rm CO}(J \rightarrow J-1)/L'_{\rm CO}(1 \rightarrow 0)$). The SMGs from Bothwell et al. (2012) are observed in various rotational transitions of the CO molecule ($J_{\rm upper}$ = 2-7) and converted to CO($J = 1 \rightarrow 0$) luminosity using the excitation model calculated from the entire sample, normalized to a common far-IR luminosity. The stellar masses and SFRs for the Tacconi et al. (2010) SFGs

are calculated from stellar population synthesis fitting to rest-frame UV to optical/near-IR SEDs and Hα luminosities. Daddi et al. (2010) use the average of 3 estimators for the SFR (dust-corrected UV luminosities, mid-IR continuum luminosities from 24 μm Spitzer imaging and VLA 1.4 GHz radio continuum) and derive stellar masses from stellar template fitting to multicolor photometry in the rest-frame UV, optical, and near-IR bands. Bothwell et al. (2012) use stellar masses from Hainline et al. (2011) (not available for all Bothwell et al. (2012) galaxies), which come from stellar population synthesis fitting to observed-frame optical to mid-IR SEDs. We estimate SFRs for the SMG sample from the Bothwell et al. (2012) far-IR luminosities using the conversion from Kennicutt (1998b), as described above for a few of the LIRGs and ULIRGs.

4.2.1 Identifying Starburst Galaxies

In Figure 4.1, we present the stellar mass and star formation properties of the literature sample and the EGNoG survey. The color indicates approximate redshift ($z \sim 0$ in blue, $z \sim 0.05 - 0.5$ in green, and $z > 1$ in red) and the symbol indicates galaxy type: normal galaxies (local spirals, Geach et al. (2011) galaxies at $z = 0.4$ and high-redshift SFGs) are marked with circles, local LIRGs with triangles and starbursts (local ULIRGs and high-redshift SMGs) with squares. The EGNoG galaxies are plotted with a unique symbol (green diamonds) for emphasis. This color and symbol scheme will be used for the rest of this work.

The left panel of Figure 4.1 shows the SFR versus M_*, with the main sequence at three representative redshifts indicated by the blue ($z = 0$), green ($z = 0.3$), and red ($z = 1.5$) lines. The main sequence correlation is apparent, with normal galaxies lying near the main sequence curve at the corresponding redshift. In order to more precisely discern starburst galaxies from normal galaxies, in the right panel of Figure 4.1 we plot the sSFR of each galaxy normalized by the main sequence sSFR ($\mathrm{sSFR_{MS}}$; Equation 3.1) at the redshift and stellar mass of the galaxy. The horizontal black line indicates the main sequence relation, with the dashed lines showing a spread of 0.6 dex. Starburst galaxies lie above the higher dashed line, with sSFRs larger than 4 times the main sequence sSFR (as defined in Equation 3.2).

Using this starburst criterion, we standardize the conversion of CO luminosity to molecular gas mass in our literature and EGNoG samples. For galaxies that are classified as starburst based on their specific star formation rates, we use the value observed in starburst systems: $\alpha_{\mathrm{CO}}(\mathrm{ULIRG}) = 0.8\ \mathrm{M_\odot}\ (\mathrm{K\ km\ s^{-1}\ pc^2})^{-1}$ (local ULIRGs: Scoville et al. 1997, Downes & Solomon 1998; high-redshift SMGs: Tacconi et al. 2008). For all other galaxies, we use a Milky Way-like conversion factor, $\alpha_{\mathrm{CO}}(\mathrm{MilkyWay}) = 3.2\ \mathrm{M_\odot}\ (\mathrm{K\ km\ s^{-1}\ pc^2})^{-1}$ (e.g. Dame et al. 2001). (These conversion factors do not explicitly include He; see Equation 3.4.) This bimodal prescription for the conversion factor is discussed further in Section 4.2.4.

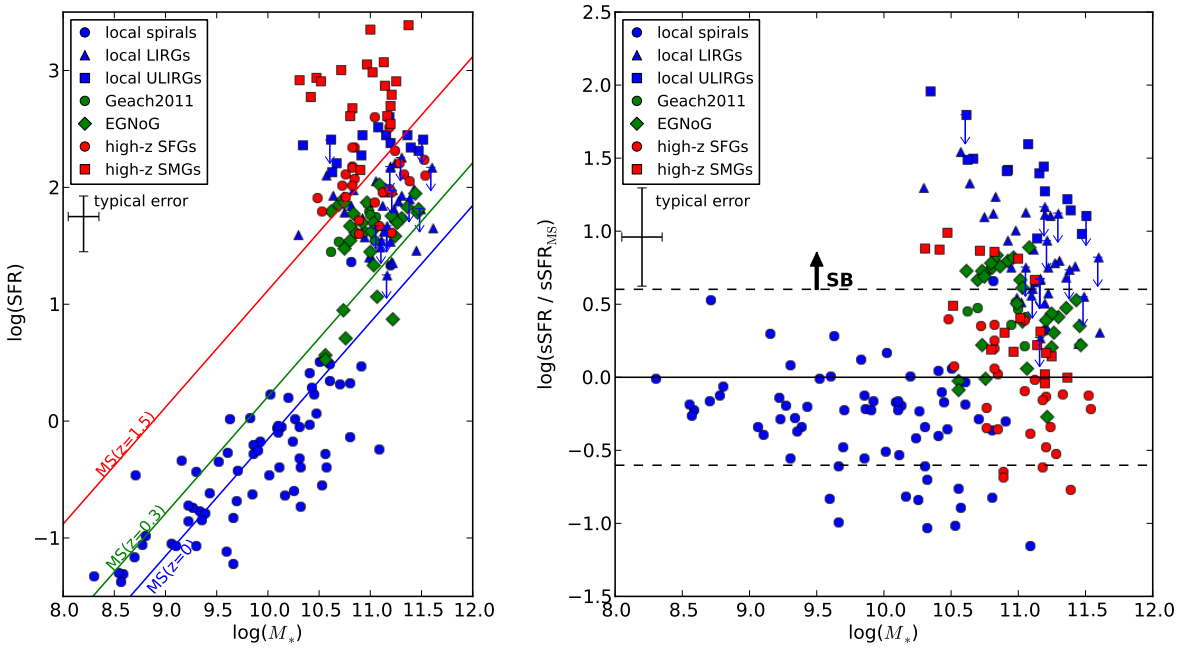

Figure 4.1: Star formation rate (left panel) and normalized specific star formation rate (right panel) versus stellar mass for our literature sample and the EGNoG galaxies. Color indicates approximate redshift and plotting symbol shows galaxy type (see text for full description). In the left panel, the main sequence at three representative redshifts is indicated by the blue, green and red lines. In the right panel, the sSFR is normalized by the main sequence sSFR (for the relevant z and M_*). Starburst (SB) galaxies lie above the higher dashed line.

4.2.2 Gas Depletion Time

Using our compilation of data, we investigate the molecular gas depletion time ($\tau_{\rm mgas}$) for starburst and normal galaxies. Excluding dwarf galaxies, the average molecular gas depletion time for the normal (non-starburst) galaxies is 0.77 ± 0.57 Gyr. The average for the starburst galaxies is 0.07 ± 0.04 Gyr. These averages generally agree with previous work (see references for the literature sample in Section 4.2). However, we note that a depletion time calculated from molecular gas and SFR surface densities may differ from our calculated value (from the total molecular gas mass and total SFR) due to different scale lengths of the CO and SFR distributions and trends in gas depletion time with galaxy size (larger galaxies will dominate an area-weighted average gas depletion time). This is the case for the sample from Leroy et al. (2008), in which the authors calculate an average molecular gas depletion time of 1.9 Gyr using surface densities, while the average depletion time using total quantities would be 1.3 Gyr (which lies within the error of our average value for normal galaxies).

In the left panel of Figure 4.2, we plot CO luminosity versus SFR to illustrate that

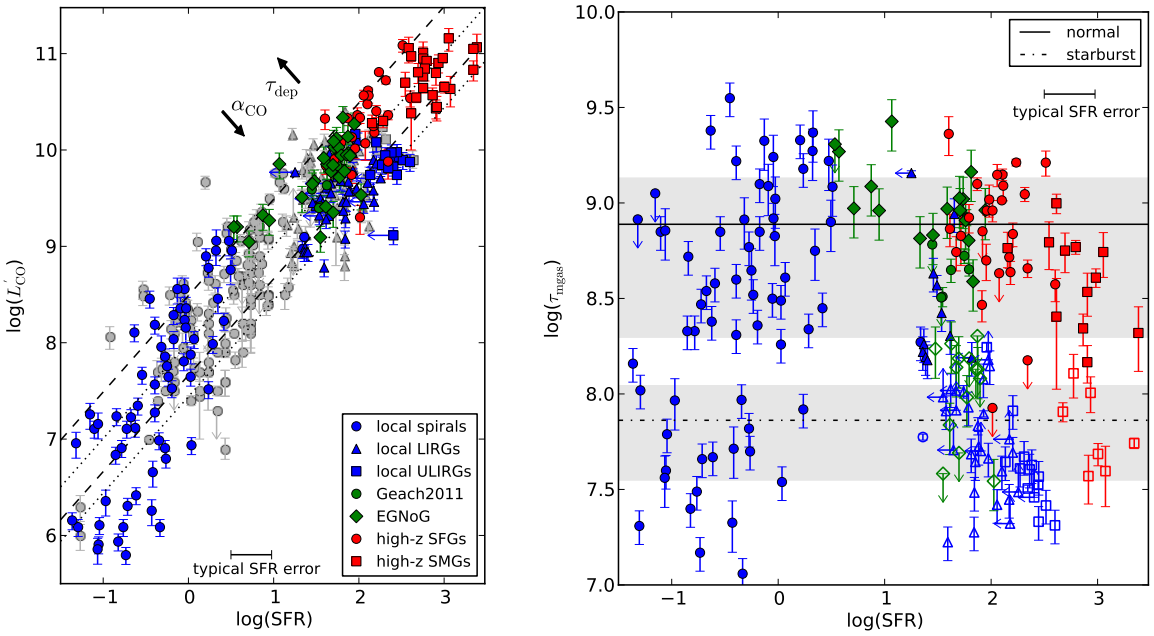

Figure 4.2: CO luminosity (L'_{CO}; left panel) and molecular gas depletion time (τ_{mgas}; right panel) versus SFR. In the left panel, galaxies from Yao et al. (2003); Mao et al. (2010); Papadopoulos et al. (2011) are plotted (gray points) in addition to the literature sample. Dashed (dotted) lines show the expected region in L'_{CO}-SFR space occupied by normal (starburst) galaxies. In the right panel, the horizontal solid (dot-dashed) line indicated the average τ_{mgas} value for normal (starburst) galaxies, with the gray region indicating $\pm 1\sigma$. Starburst galaxies are plotted as un-filled symbols in the right panel.

starburst and normal galaxies fill the same space in this plane, making the differentiation of starburst from normal galaxies impossible using only CO luminosity and SFR. In addition to the literature sample described in Section 4.2, we include local spirals, LIRGs and ULIRGs from Yao et al. (2003), Mao et al. (2010) and Papadopoulos et al. (2011) as gray circles, triangles and squares. These datasets do not include stellar masses and thus are only included in this plot for illustrative purposes (we estimate SFRs from the far-IR luminosities using the Kennicutt 1998b conversion). The dashed lines indicate the area of the plane occupied by normal galaxies using α_{CO}(MilkyWay) and the average τ_{mgas} for normal galaxies given above. The dotted lines indicate the area occupied by starburst galaxies (using α_{CO}(ULIRG) and the starburst τ_{mgas}), which overlaps the normal galaxy area significantly. This overlap occurs because the differences in α_{CO} and τ_{mgas} between starburst and normal galaxies cancel each other out in this plane: as the effective α_{CO} increases, a galaxy moves toward the lower right and as the effective τ_{mgas} increases, a galaxy moves toward the upper left.

In the right panel of Figure 4.2, molecular gas depletion time is plotted against SFR,

with the average value for normal (starburst) galaxies indicated by the solid (dot-dashed) line. 1σ error bars on the averages are indicated by the gray shaded regions. The conversion factor used for each data point is indicated by the fill of the symbol: filled symbols are normal and un-filled symbols are starburst according to the sSFR criterion in Equation 3.2 (plotted in the right panel of 4.1. Only galaxies that can be classified this way (galaxies for which the M_* and SFR have been estimated) are included in this plot. Note that the $\tau_{\rm mgas}$ error bars plotted only represent the error associated with the CO measurement and not the SFR error since we do not have errors on all the SFR measurements in the literature sample. We estimate that the typical SFR error is $\pm 50\%$. The population of galaxies in the lower left are dwarfs ($M_* < 10^{10}$), for which a larger conversion factor may become appropriate due to decreasing metallicity. Leroy et al. (2011) find that the conversion factor begins to increase significantly as the metallicity falls below $12 + \log({\rm O/H}) = 8.2 - 8.4$, which is expected for $M_* \lesssim 10^9$ M$_\odot$ (Tremonti et al. 2004). This change in conversion factor would shift the dwarf galaxy points to higher $\tau_{\rm mgas}$. Therefore, we do not include dwarf galaxies in the calculation of the average $\tau_{\rm mgas}$ values.

4.2.3 Evolution of the Molecular Gas Fraction

In order to calculate the expected evolution of the molecular gas fraction, we first consider the ratio of the molecular gas mass to the stellar mass ($r_{\rm mgas}$), which can be written as the product of the molecular gas depletion time and the specific star formation rate:

$$r_{\rm mgas} = \frac{M_{\rm mgas}}{M_*} = \frac{M_{\rm mgas}}{\rm SFR}\frac{\rm SFR}{M_*} = \tau_{\rm mgas} \times {\rm sSFR} \tag{4.1}$$

In Section 3.2.1, we motivated and defined the sSFR of the main sequence as a function of redshift and stellar mass. As illustrated in the right panel of Figure 4.1, main sequence galaxies lie roughly within a factor of 4 (± 0.6 dex) of the main sequence relation and starburst galaxies lie at sSFRs 4-30 times larger than the main sequence value. In the previous section, we found an average $\tau_{\rm mgas}$ of 0.77 ± 0.57 Gyr for normal galaxies and 0.07 ± 0.04 Gyr for starburst galaxies. Using these typical $\tau_{\rm mgas}$ values and sSFR ranges (relative to the sSFR$_{\rm MS}$), we get:

$$r_{\rm mgas}({\rm normal}) = (0.05 \pm 0.04)\left[\frac{1}{4} - 4\right](1+z)^{3.2} M_{*,11}^{-0.2} \tag{4.2}$$

$$r_{\rm mgas}({\rm starburst}) = (0.05 \pm 0.03)\left(\frac{[4-30]}{10}\right)(1+z)^{3.2} M_{*,11}^{-0.2} \tag{4.3}$$

where $M_{*,11} = M_*/(10^{11}$ M$_\odot)$. In each of Equations 4.2 and 4.3, the scatter in $\tau_{\rm mgas}$ is reflected in the error in the first term (± 0.04 and ± 0.03) and the appropriate range of sSFR values (relative to sSFR$_{\rm MS}$) is given in square brackets. The corresponding molecular gas fraction may be calculated from $r_{\rm mgas}$: $f_{\rm mgas} = (1 + r_{\rm mgas}^{-1})^{-1}$.

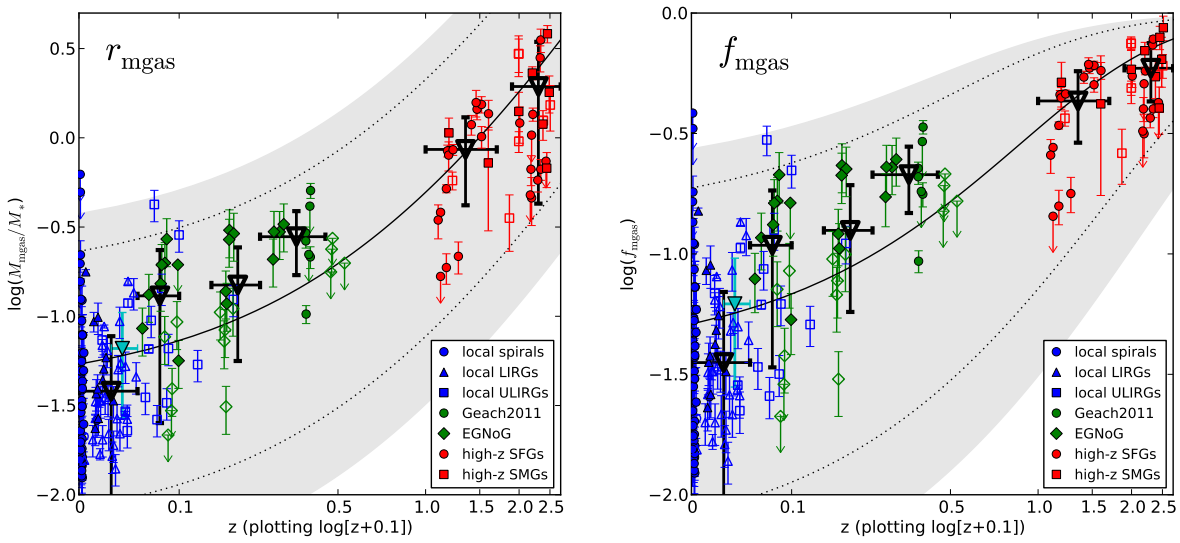

Figure 4.3: Molecular gas ratio ($r_{\rm mgas}$) and molecular gas fraction ($f_{\rm mgas}$) versus redshift. We plot $log(z + 0.1)$ on the x-axis. The average value from the COLDGASS survey is plotted as a cyan upside-down triangle. Starburst galaxies are plotted as un-filled symbols. Average values (with 1σ errors) for each of 6 redshift bins are plotted as un-filled black upside-down triangles. The shaded gray area shows the expected behavior for normal galaxies, with the solid black curve indicating the average. The dotted black lines bound the expected behavior for starburst galaxies.

Figure 4.3 shows the data and expectation for $r_{\rm mgas}$ (left panel) and $f_{\rm mgas}$ (right panel) versus redshift, plotting $log(z + 0.1)$ on the x-axis in order to spread out the low to intermediate redshifts for clarity. As in the right panel of Figure 4.2, the starburst galaxies (identified using Equation 3.2) are plotted as un-filled symbols. Note that the error bars plotted only represent the error associated with the CO measurement (and not the stellar mass error) since we do not have errors on all the stellar mass measurements in the literature sample. We estimate that a typical stellar mass error is 0.1-0.2 dex. We also plot the average value at $z = 0.025 - 0.05$ reported by the COLDGASS survey (Saintonge et al. 2011) as a cyan upside-down triangle. We plot the expected $r_{\rm mgas}$ and $f_{\rm mgas}$ versus redshift for normal galaxies (Equation 4.2) as the solid black curve with the gray shaded area indicating the range of values (we take a nominal M_* of 10^{11} $M_\odot$). The range for starburst galaxies (Equation 4.3) is indicated by the dotted black curves.

The data points are binned into 6 redshift ranges (number of detected galaxies in parenthesis): $z = 0 - 0.05$ (110), $z = 0.05 - 0.1$ (19), $z = 0.15 - 0.25$ (11), $z = 0.25 - 0.45$ (9), $z = 1.0 - 1.7$ (18), $z = 1.9 - 2.7$ (20). The average values (for all detections) are plotted as un-filled black upside-down triangles with vertical lines showing the standard deviations. All redshift bin averages lie within the expected range for both normal galaxies

(gray shaded region) and starburst galaxies (dotted lines). For all but one average point ($z = 0.25 - 0.45$), the average expectation curve ($r_{\rm mgas} = {\rm sSFR_{MS}} \times (0.77\ {\rm Gyr})$) lies within the dispersion (vertical black lines).

We note that the three intermediate redshift bins ($z = 0.05 - 0.01$, $0.15 - 0.25$, and $0.25 - 0.45$) lie systematically higher than the average expectation curve. However, the number of galaxies in each of these bins is small and dominated by EGNoG galaxies, which we have shown to lie close to the starburst cutoff (see Figure 4.1). Therefore, these points are sensitive to the exact starburst criterion used (which determines $\alpha_{\rm CO}$). For example, if we consider galaxies with ${\rm sSFR} > 2\ {\rm sSFR_{MS}}$ to be starbursts, the three intermediate redshift bin average values decrease by ≈ 0.3 dex, falling in line with the average expectation curve.

In summary, while the EGNoG galaxy redshift bins lie systematically higher than the average expectation curve for the starburst criterion (and resulting $\alpha_{\rm CO}$ choices) used in this work, reasonable variation of this criterion results in a decrease of ≈ 0.3 dex, bringing the averages in line with expectation. We therefore conclude that the data agree well with the behavior of $r_{\rm mgas}$ and $f_{\rm mgas}$ expected from a simple prescription for the sSFR and $\tau_{\rm mgas}$ in star-forming galaxies. While the EGNoG bin D galaxies (non-detections) have not been included in the redshift bin averages discussed above, we note that the four upper limits are included in Figure 4.3 and agree with expectations as well.

4.2.4 A Bimodal Conversion Factor Prescription

In this work, we have used a bimodal prescription for the conversion factor $\alpha_{\rm CO}$ in normal and starburst galaxies. We have included some local low-mass galaxies in our literature sample, but we do not include these systems in the calculation of average values since a different $\alpha_{\rm CO}$ is likely appropriate due to decreasing metallicity (Leroy et al. 2011; Narayanan et al. 2012). While our bimodal prescription (excluding low-mass galaxies) likely does not describe the true conversion factor in all of these galaxies (e.g. simulations by Narayanan et al. 2012 suggest a continuous variation of $\alpha_{\rm CO}$ from normal to starburst galaxies), it appears to capture the typical behavior. A recent study by Magnelli et al. (2012) using observed dust masses to calculate the conversion factor in $z > 1$ star-forming galaxies found smaller conversion factors in starburst galaxies (classified by sSFR, as in this work) but was unable to distinguish between a step function and continuous variation for $\alpha_{\rm CO}$ as a function of ${\rm sSFR/sSFR_{MS}}$.

Independent of the issue of bimodal or continuous conversion factor is the question of whether the local values for normal and starburst conversion factors may be extended to high redshift. Both simulations by Narayanan et al. (2012) and observations by Daddi et al. (2010) suggest that the conversion factor is lower than the Milky Way value in normal star-forming galaxies at high redshift. We cannot answer these questions with this dataset, but note that using a reduced $\alpha_{\rm CO}$ in high-redshift SFGs or a continuous variation of $\alpha_{\rm CO}$ from normal to starburst galaxies would not change the general conclusions of this work.

4.3 Conclusions

We place the EGNoG galaxies in context with a sample of 185 normal and starburst galaxies at low and high redshift collected from the literature. We standardize the comparison of the EGNoG and literature galaxies using a simple prescription for molecular gas mass calculation. Each galaxy is classified as normal or starburst based on sSFR relative to the sSFR of the main sequence of star-forming galaxies (see Equations 3.1 and 3.2). We then use a bimodal prescription for $\alpha_{\rm CO}$ based on this classification (a Milky Way-like value for normal galaxies, a ULIRG-like value for starbursts) to calculate the molecular gas mass, molecular gas depletion time, and molecular gas fraction for each galaxy.

Using this prescription, we find an average molecular gas depletion time of 0.77 ± 0.57 Gyr for normal galaxies and 0.07 ± 0.04 Gyr for starburst galaxies. We calculate an average molecular gas fraction of 7-20% at the intermediate redshifts probed by the EGNoG survey ($z = 0.05 - 0.5$). By expressing the molecular gas fraction in terms of the sSFR and molecular gas depletion time ($f_{\rm mgas} = (1 + [\tau_{\rm mgas} \times {\rm sSFR}]^{-1})^{-1}$), we use typical ranges of sSFR and $\tau_{\rm mgas}$ for starburst and normal galaxies to calculate the expected evolution of the molecular gas fraction with redshift. The expected behavior agrees well with the EGNoG and literature data from $z = 0$ out to $z \sim 2.5$.

Acknowledgements

We thank Kevin Bundy for useful discussions and assistance with the COSMOS dataset. A.B. thanks all the members of the EGNoG collaboration for their guidance and assistance. We thank the OVRO/CARMA staff and the CARMA observers for their assistance in obtaining the data. Support for CARMA construction was derived from the Gordon and Betty Moore Foundation, the Kenneth T. and Eileen L. Norris Foundation, the James S. McDonnell Foundation, the Associates of the California Institute of Technology, the University of Chicago, the states of California, Illinois, and Maryland, and the National Science Foundation. Ongoing CARMA development and operations are supported by the National Science Foundation under a cooperative agreement, and by the CARMA partner universities.

Chapter 5

Gas Excitation in Normal Galaxies at $z \approx 0.3$

As observations of molecular gas in galaxies are pushed to lower star formation rate galaxies at higher redshifts, it is becoming increasingly important to understand the conditions of the gas in these systems to properly infer their molecular gas content. The rotational transitions of the carbon monoxide (CO) molecule provide an excellent probe of the gas excitation conditions in these galaxies. In this chapter we present the results from the gas excitation sample of the Evolution of molecular Gas in Normal Galaxies (EGNoG) survey at the Combined Array for Research in Millimeter-wave Astronomy (CARMA). This subset of the full EGNoG sample consists of four galaxies at $z \approx 0.3$ with star formation rates of $40 - 65$ $M_\odot$ yr^{-1} and stellar masses of $\approx 2 \times 10^{11}$ $M_\odot$. Using the 3 mm and 1 mm bands at CARMA, we observe both the CO($J = 1 \rightarrow 0$) and CO($J = 3 \rightarrow 2$) transitions in these four galaxies in order to probe the excitation of the molecular gas. We report robust detections of both lines in three galaxies (and an upper limit on the fourth), with an average line ratio, $r_{31} = L'_{\rm CO(3-2)}/L'_{\rm CO(1-0)}$, of 0.46 ± 0.07 (with systematic errors $\lesssim 40\%$), which implies sub-thermal excitation of the CO($J = 3 \rightarrow 2$) line. We conclude that the excitation of the gas in these massive, highly star-forming galaxies is consistent with normal star-forming galaxies such as local spirals, not starbursting systems like local ultra-luminous infrared galaxies. Since the EGNoG gas excitation sample galaxies are selected from the main sequence of star-forming galaxies, we suggest that this result is applicable to studies of main sequence galaxies at intermediate and high redshifts, supporting the assumptions made in studies that find molecular gas fractions in star forming galaxies at $z \sim 1 - 2$ to be an order of magnitude larger than what is observed locally.[1]

[1]This chapter has been accepted for publication in the Astrophysical Journal as *The EGNoG Survey: Gas Excitation in Normal Galaxies at $z \approx 0.3$* by Bauermeister, Blitz, Bolatto, Bureau, Teuben, Wong & Wright and is reproduced with the permission of all coauthors and the copyright holder. Copyright American Astronomical Society.

5.1 Introduction

While studies of local spirals (e.g. BIMA SONG, Helfer et al. 2003; HERACLES, Leroy et al. 2009) find average molecular gas fractions $f_{\rm mgas} = M_{\rm mgas}/(M_* + M_{\rm mgas}) \sim 5\%$ (where $M_{\rm mgas}$ is the molecular gas mass (including He) and M_* is the stellar mass), observations of high redshift SFGs suggest molecular gas fractions of 20-80%, an order of magnitude higher than local spirals. It is clear that in order to understand these SFGs at $z \sim 1-2$, we must investigate the condition of the molecular gas which is forming stars at such an enhanced rate. Do these systems truly hold massive reservoirs of molecular gas or is enhanced excitation of the gas misleading the interpretation of the observations?

The rotational transitions of the carbon monoxide (CO) molecule provide a direct probe of the excitation of the molecular gas in galaxies. Local starburst galaxies and ULIRGs (e.g. Bayet et al. 2004; Weiß et al. 2005b; Papadopoulos et al. 2007; Greve et al. 2009) and high redshift SMGs and quasars (e.g. Weiß et al. 2005a; Riechers et al. 2006; Weiß et al. 2007; Riechers 2011; Riechers et al. 2011) show signatures of excited molecular gas: observed CO line spectral energy distributions peak at $\rm J_{upper} > 5$ with thermalized lines up to $\rm J_{upper} > 3$. In contrast, studies of the Milky Way (Fixsen et al. 1999) and local SFGs (e.g. Mauersberger et al. 1999; Yao et al. 2003; Mao et al. 2010) find a wide spread of excitation conditions, with an average that implies less-excited gas, where the $\rm J_{upper} = 3$ line is already subthermal. This suggests that the CO($J = 3 \rightarrow 2$) line in particular is an indicator of the star formation character of a galaxy: 'starburst' versus 'normal'.

More important still, the ratio of higher rotational lines of CO to the CO($J = 1 \rightarrow 0$) line is *necessary* to translate the observed CO line luminosity to a molecular gas mass using $X_{\rm CO}$ or $\alpha_{\rm CO}$, since this conversion factor is calibrated for the CO($J = 1 \rightarrow 0$) luminosity. Therefore, the measurement of $r_{J1} = L'_{\rm CO(J-(J-1))}/L'_{\rm CO(1-0)}$ not only informs our interpretation of the current intermediate and high redshift CO line studies, but is critical in the era of ALMA, which provides an order of magnitude increase in sensitivity, making the CO lines in high redshift galaxies more accessible. The CO($J = 3 \rightarrow 2$) line in particular, observed in the 1mm, 2mm and 3mm bands, probes the molecular gas in galaxies at z$\sim 0.3-3$. This redshift range is of particular interest since it includes the peak of the star formation rate density of the universe ($z \sim 1-2$) and therefore the height of galaxy building.

While several studies have measured r_{31} in the local universe (Mauersberger et al. 1999; Yao et al. 2003; Mao et al. 2010; Papadopoulos et al. 2011), the measurement of line ratios in intermediate and high redshift galaxies has mostly been limited to SMGs and quasars (see the review by Solomon & Vanden Bout 2005). Our knowledge of CO line ratios in SFGs at $z \sim 1-2$ is limited to one study at $z = 1.5$ (presented in two papers: Dannerbauer et al. 2009 and Aravena et al. 2010) which measures r_{21} in three galaxies and r_{31} in one galaxy. It is clear that more work is needed to better constrain the line ratios in intermediate and high redshift SFGs to interpret existing and future data and better understand the state of the molecular gas in these systems.

EGNoG Name	SDSS identification	RA	Dec
C1	SDSS J092831.94+252313.9	09:28:31.941	+25:23:13.925
C2	SDSS J090636.69+162807.1	09:06:36.694	+16:28:07.136
C3	SDSS J132047.13+160643.7	13:20:47.139	+16:06:43.720
C4	SDSS J133849.18+403331.7	13:38:49.189	+40:33:31.748

Table 5.1: Basic information.

As part of the Evolution of molecular Gas in Normal Galaxies (EGNoG) survey (presented in Chapters 3 and 4), we observe both the CO($J = 1 \rightarrow 0$) and CO($J = 3 \rightarrow 2$) lines in four galaxies at $z \approx 0.3$ (the gas excitation sample), more than doubling the number of SFGs at $z > 0.1$ in which CO line ratios have been measured. In this paper, we present the r_{31} values for the EGNoG gas excitation sample and compare to previous work at low and high redshifts. We discuss the implications of this measurement for the excitation of the molecular gas in the observed galaxies as well as for high-redshift SFGs.

This chapter is organized as follows: in Section 5.2 we give a brief description of the gas excitation sample of the EGNoG survey (see Chapter 3 for a complete description); in Section 5.3 we summarize the observations and data reduction; in Section 5.4 we present the analysis of r_{31} in these galaxies; in Section 5.5 we discuss the implications of this work; and we give some concluding remarks in Section 5.6. The data reduction and measurement of fluxes is discussed in detail in Appendix A. Throughout this work, we use a ΛCDM cosmology with (h, Ω_M, Ω_Λ) = (0.7, 0.3, 0.7).

5.2 The EGNoG Gas Excitation Sample

In the present chapter, we discuss the gas excitation sample (bin C) of the EGNoG survey, the subset of the full survey sample for which we observe both the CO($J = 1 \rightarrow 0$) and CO($J = 3 \rightarrow 2$) lines. Table 5.1 gives the RA, Dec and SDSS identification of the EGNoG bin C galaxies discussed in this chapter. Observations were made using the CARMA 15-element array with the 3mm band (single-polarization) for the CO($J = 1 \rightarrow 0$) observations and the 1mm band (dual-polarization) for the CO($J = 3 \rightarrow 2$) observations. The redshifts, stellar masses and star formation rates (with errors) are given in Table 5.2. For a complete description of the selection of the sample and the stellar masses and star formation rates from the MPA-JHU catalog, please see Chapter 3, Sections 3.2 and 3.2.1.

5.3 CARMA Observations

The four bin C galaxies were observed in two rotational transitions of the CO molecule: CO($J = 1 \rightarrow 0$) $\nu_{\rm rest} = 115.3$ GHz, $\nu_{\rm obs} \sim 88$ GHz and CO($J = 3 \rightarrow 2$) $\nu_{\rm rest} = 345.9$ GHz,

EGNoG Name	z	$\log(M_*/M_\odot)$	SFR ($M_\odot$ yr^{-1})
C1[a]	0.283020 ± 0.000022	$11.24^{+0.10}_{-0.11}$	$38.7^{+85.9}_{-25.6}$
C2	0.300622 ± 0.000010	$11.20^{+0.29}_{-0.14}$	$57.5^{+90.1}_{-21.9}$
C3	0.312361 ± 0.000014	$11.46^{+0.25}_{-0.12}$	$64.9^{+142.9}_{-28.0}$
C4	0.285380 ± 0.000015	$11.26^{+0.18}_{-0.12}$	$50.5^{+48.1}_{-15.4}$

Table 5.2: Derived quantities (z, M_*, SFR) from the MPA-JHU group (see text for details). C1 (marked with [a]) is a duplicate source in SDSS: the average value is reported for z, M_* and SFR.

$\nu_{\rm obs} \sim 266$ GHz. At each frequency, each galaxy was observed over several different days. Each dataset includes observations of a nearby quasar for phase calibration (taken every 15-20 minutes), a bright quasar for passband calibration and either Mars or MWC349 for flux calibration (in most cases).

The reduction of all observations for this survey was carried out within the EGN[2] data reduction infrastructure (based on the MIS pipeline; Pound & Teuben 2012) using the Multichannel Image Reconstruction, Image Analysis and Display (MIRIAD; Sault et al. 2011) package for radio interferometer data reduction. Our data analysis also used the `miriad-python` software package (Williams et al. 2012). The data were flagged, passband-calibrated and phase calibrated in the standard way. Final images were created using `invert` with `options=mosaic` in order to properly handle and correct for the three different primary beam patterns. All observations are single-pointing. We describe the CO($J = 1 \rightarrow 0$) and CO($J = 3 \rightarrow 2$) observations individually below. A full description of the data reduction and flux measurement is given in Appendix A.

5.3.1 CO($J = 1 \rightarrow 0$)

The CO($J = 1 \rightarrow 0$) transition for the galaxies presented here lies in the 3 mm band of CARMA (single-polarization, linearly polarized feeds). The wide bandwidth of the CARMA correlator allowed us to observe both the ^{12}CO($J = 1 \rightarrow 0$) and the ^{13}CO($J = 1 \rightarrow 0$) lines simultaneously. The ^{12}CO (^{13}CO) line was observed with five (three) overlapping 500 MHz bands, covering $\approx$ 7000 (5000) km s^{-1} total, at 42 km s^{-1} resolution, with 3-bit sampling. These observations were carried out from August to November 2011 in CARMA's D configuration, with $11-150$ m baselines yielding a typical synthesized beam of $4.8'' \times 3.9''$ at 88 GHz. Each galaxy was observed for 20 to 30 hours (time on-source) in moderate to good weather conditions for 3mm observation, yielding final images with rms noise of ≈ 1.2 mJy beam^{-1} in a 42 km s^{-1} channel. The flux scale in each dataset is set by the flux of the phase calibrator, which is determined from the flux calibrator. For these data, we use phase calibrators 0854+201 (4 Jy, 9% linearly polarized), 1357+193 (0.8 Jy) and 1310+323 (1.7 Jy).

All four galaxies were clearly detected in the CO($J = 1 \rightarrow 0$) line, as shown in Figure

[2] http://carma.astro.umd.edu/wiki/index.php/EGN

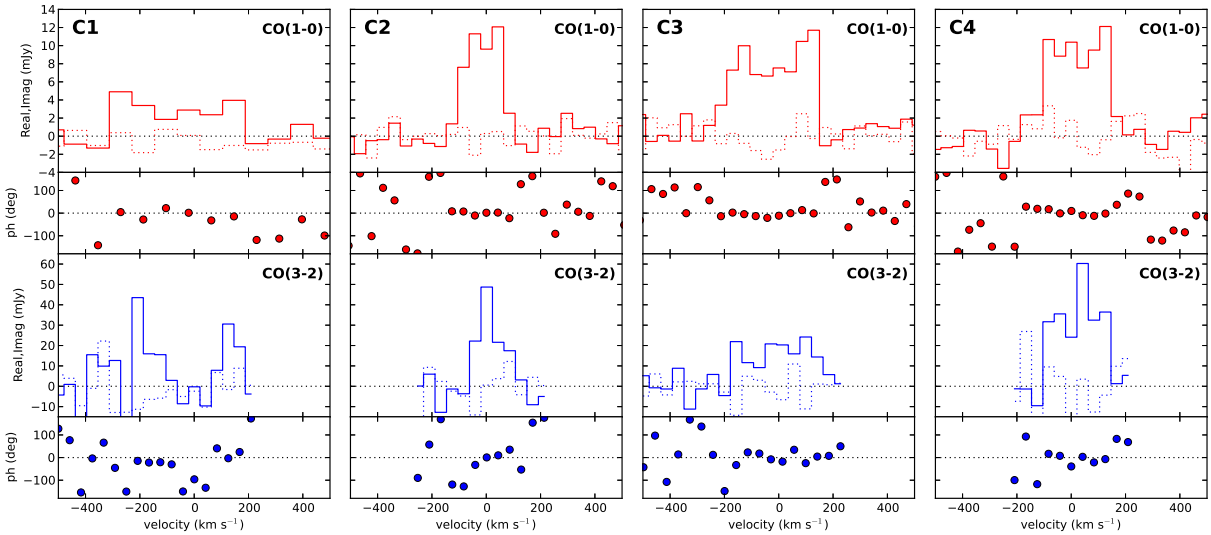

Figure 5.1: Vector-averaged *Real* (solid) and *Imaginary* (dotted) amplitudes (Real,Imag in mJy beam^{-1}) and phase (ph, degrees) of the calibrated *uv* data versus velocity (km s^{-1}) for the CO($J = 1 \rightarrow 0$) (red, top panel) and CO($J = 3 \rightarrow 2$) (blue, bottom panel) transitions in each of the four sources (indicated in upper left corner). With the higher resolution of the CO($J = 3 \rightarrow 2$) data, we observe the peak of the CO($J = 3 \rightarrow 2$) emission to be offset ($< 1.5'' \sim 6$ kpc) from the centers of galaxies C1 and C2. In these cases, we calculate the *uv* spectra at the peak of the CO($J = 3 \rightarrow 2$) emission. For the CO($J = 1 \rightarrow 0$) line of galaxy C1, we average 2 channels together in order to increase the signal to noise ratio. Large *Real* amplitudes (the *Imaginary* part shows the noise) coincident with phases of ≈ 0 over multiple velocity channels indicate a detection.

5.1. The top panels show the vector-averaged *Real* and *Imaginary* amplitudes and phase of the calibrated *uv* data versus velocity for the CO($J = 1 \rightarrow 0$) line. For a compact source at the center of the field of view, the *Real* part shows the signal without a noise bias, and the *Imaginary* part shows the noise. In all four cases, we see coherent emission (larger *Real amplitudes* coincident with noise-like *Imaginary* amplitudes and phases of ≈ 0) over multiple velocity channels, indicative of a detection. We report no detection of the ^{13}CO($J = 1 \rightarrow 0$) line, which is expected to be weaker than the ^{12}CO($J = 1 \rightarrow 0$) line by a factor of 7 to 17 (Rickard & Blitz 1985).

5.3.2 CO($J = 3 \rightarrow 2$)

The CO($J = 3 \rightarrow 2$) transition at the redshift of the galaxies discussed here lies in the CARMA 1 mm band (dual-polarization, circularly polarized feeds). We again observed both the ^{12}CO($J = 3 \rightarrow 2$) and the ^{13}CO($J = 3 \rightarrow 2$) lines simultaneously. The ^{12}CO (^{13}CO) line was observed with three (one) overlapping 500 MHz bands, covering ≈ 1500 (550) km s^{-1} total, at 14 km s^{-1} resolution, with 3-bit sampling. These observations

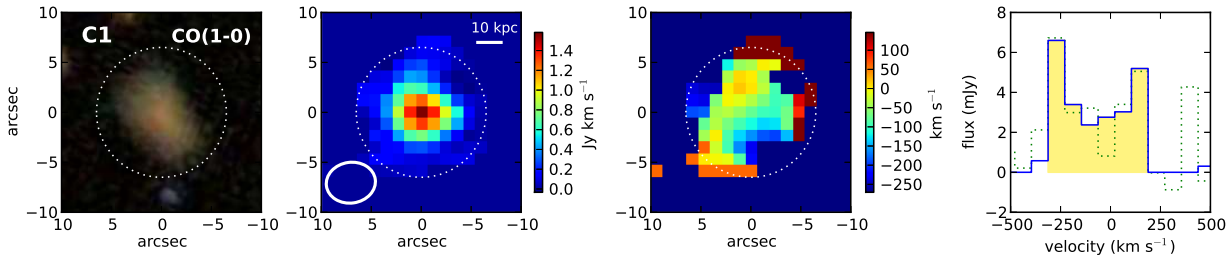

Figure 5.2: CO($J = 1 \rightarrow 0$) emission in source C1. The left panel shows the optical image. The moment 0 and moment 1 maps are displayed in the left middle and right middle panels respectively. The dotted white ellipse indicates the source region (6.5″radius). In the moment 0 map, the beam size is indicated by the solid white ellipse in the lower left corner and a 10 kpc scale bar is given in the top right. The far right panel shows the spectrum of the galaxy: the solid blue line is calculated with masking, the dotted green line is without.

were carried out in CARMA's E and D configuration during August 2011 and April 2012, respectively. Source C4 was observed entirely in E configuration, while the other three sources were observed mostly in D configuration. The E configuration has 8−66 m baselines yielding a typical synthesized beam of $3.2'' \times 2.5''$ at 266 GHz. The D configuration has $11 - 150$ m baselines yielding a typical synthesized beam of $1.7'' \times 1.5''$ at 266 GHz. Each galaxy was observed for 2 to 6.5 hours (time on-source) in good weather conditions for 1mm observation, yielding final images with rms noise of 5-10 mJy beam^{-1} in a 42 km s^{-1} channel. For these data, we use phase calibrators 0854+201 (2 Jy in August 2011, 4 Jy in April 2012), 1224+213 (0.6 Jy) and 1310+323 (0.6 Jy).

Sources C2, C3 and C4 were detected at the $\approx 5\sigma$ level in the CO($J = 3 \rightarrow 2$) line. However, C1, with its wide velocity profile (observed in the CO($J = 1 \rightarrow 0$) line), was only marginally detected and we give only an upper limit on the CO($J = 3 \rightarrow 2$) flux. The vector-averaged *Real* and *Imaginary* amplitudes and phase of the calibrated *uv* data versus velocity for the CO($J = 3 \rightarrow 2$) line are shown in the bottom panels of Figure 5.1. The peak of the CO($J = 3 \rightarrow 2$) emission in galaxies C1 and C2 is offset from the nominal center of each galaxy, so the *uv* spectra are calculated at this slightly offset ($< 1.5'' \sim 6$ kpc)) position. We report no detection in the ^{13}CO($J = 3 \rightarrow 2$) line for any galaxy.

Source C1 Upper Limit

While we detect the CO($J = 1 \rightarrow 0$) line in galaxy C1 (see Figure 5.2), the CO($J = 3 \rightarrow 2$) line was only marginally detected, likely due to the wide integrated velocity profile of source C1 (apparent in Figure 5.2). The channel maps did not show evidence of a source upon visual inspection, but an integrated spectrum made of a circular region 4.5″ in radius at the center of the image suggests a 3σ detection. The line flux and other quantities are calculated from this spectrum, over the velocities of the CO($J = 1 \rightarrow 0$) line for this

Name	Transition	$S_{\rm CO}$ (Jy km s^{-1})	$L'_{\rm CO}$ (10^9 K km s^{-1} pc^2)	$v_{\rm center}$ (km s^{-1})	ΔV (km s^{-1})	Non-matched r_{31}^b
C1	CO(1-0)	2.05± 0.34	8.25±2.83	−84.9±18.1	542.2±41.7	0.49^a± 0.26
	CO(3-2)	9.02^a± 2.65	4.03^a±1.69	−49.9± 7.3	542.3±23.4	
C2	CO(1-0)	2.35± 0.10	10.70±3.24	−6.7± 1.2	253.7±42.3	0.40± 0.18
	CO(3-2)	8.39± 1.12	4.25±1.40	19.5± 8.2	169.2±42.3	
C3	CO(1-0)	4.39± 0.09	21.70±6.53	−24.7± 5.7	384.0±42.3	0.34± 0.15
	CO(3-2)	13.46± 1.56	7.39±2.38	−14.0± 7.8	426.7±42.7	
C4	CO(1-0)	3.01± 0.11	12.30±3.72	17.3±13.0	292.5±41.8	0.44± 0.19
	CO(3-2)	11.88± 1.22	5.41±1.72	33.5± 5.0	250.7±41.8	

Table 5.3: Properties of the CO emission (described in Section 5.3.3). For each galaxy, the CO line flux ($S_{\rm CO}$), luminosity ($L'_{\rm CO}$, see Equation 5.1), central velocity ($v_{\rm center}$) and full velocity width (ΔV) are given for the CO($J = 1 \rightarrow 0$) and CO($J = 3 \rightarrow 2$) lines. The ratio of the line luminosities (r_{31}) for each galaxy is given in the last column.
[a] CO($J = 3 \rightarrow 2$) values for source C1 are upper limits.
[b] r_{31} reported here is calculated from the total line luminosities (see Section 5.4.1). We perform a more careful calculation, matching the 1 and 3mm data, in Section 5.4.3.

galaxy. These values should be taken as an upper limit on the true flux. The error in the flux measurement ($S_{\rm CO}$, Jy km s^{-1}) is calculated from the pixel noise, $\sigma_{\rm p}$ (Jy beam^{-1}): $\sigma_{S_{\rm CO}} = \sigma_{\rm p}\ \delta V \sqrt{N_{\rm p}/N_{\rm eq}}$ where δV is the channel width (km s^{-1}), $N_{\rm p}$ is the number of pixels summed and $N_{\rm eq}$ is the number of pixels equivalent to the beam.

5.3.3 Derived Properties of the CO Emission

Table 5.3 presents the quantities we derive from the CO emission images. The CO line luminosity is calculated from the line flux ($S_{\rm CO}$ in Jy km s^{-1}, calculated as described in Appendix A.2) following

$$L'_{\rm CO} = 3.25 \times 10^7\ S_{\rm CO}\ \nu_{\rm obs}^{-2}\ r_{\rm com}^2 (1+z)^{-1} \tag{5.1}$$

(see the review by Solomon & Vanden Bout 2005), where $\nu_{\rm obs}$ is in GHz and $r_{\rm com}$ is the comoving distance in Mpc. The units of $L'_{\rm CO}$ are K km s^{-1} pc^2. We report the measurement error for $S_{\rm CO}$. The error reported for $L'_{\rm CO}$ includes both the measurement error of $S_{\rm CO}$ and a 30% systematic error, added in quadrature (see Appendix A.2 for more details).

The center velocity, $v_{\rm center}$, is the flux-weighted average velocity of the galaxy-integrated spectrum ($v = 0$ at the redshift in Table 5.2). The error reported is the standard deviation of the v_{center} values found with the three flux measurement methods and different channel averaging described in Appendix A.2. The reported velocity width (ΔV) is the full width of the emission, where 'source' velocity channels are selected by eye. We give the velocity width of a single channel as the error. The line ratio r_{31} is given by

$$r_{31} = L'_{\rm CO(3-2)} / L'_{\rm CO(1-0)} \tag{5.2}$$

and the error is calculated by propagating the errors of the individual line luminosities.

Moment maps (discussed in Section 5.4.2) are created from the 2σ clip smooth mask (see Appendix A.2). Moment 0 (total intensity) maps are a simple sum of the masked images in the 'source' velocity channels. Moment 1 (intensity-weighted mean velocity) maps are produced by summing the masked image multiplied by the velocity in each channel then normalizing by the moment 0 value.

5.4 Analysis

We first present our total r_{31} measurements (using the total flux observed in each line) in Section 5.4.1. All four observed galaxies are discussed. However, the total r_{31} values use line luminosities calculated completely independently of one another, making no attempt at matching the spectral or spatial resolution. In Section 5.4.2, we carefully match the CO($J = 1 \rightarrow 0$) and CO($J = 3 \rightarrow 2$) data to each other as well as possible, in both spectral and spatial resolution. In Section 5.4.3 we re-calculate r_{31} using both the natural and adjusted spatial resolution, with matched spectral resolution in both cases. In Section 5.4.4 we investigate the radial dependence of r_{31} by fitting two-dimensional Gaussians to the total intensity maps in order to derive peak intensities, which are independent of spatial resolution. The analysis in Sections 5.4.2 to 5.4.4 is performed only for the three galaxies that are detected significantly in both lines (C1 is excluded due to marginal detection of the CO($J = 3 \rightarrow 2$) line).

5.4.1 Total r_{31}

As a first step, we calculate r_{31} in the simplest way possible, taking the ratio of the total line luminosities. Of the four galaxies observed, we detect three in both lines, yielding r_{31} values (see Table 5.3) of 0.34 to 0.44 with an average value of 0.39. For source C1 we derive an upper limit on r_{31} of 0.49, which is consistent with the other values.

These r_{31} values carry the caveat that they are determined from line luminosities that are calculated independently of one another. The 'source' velocity channels for each line are selected by eye for the most convincing detection. Further, the CO($J = 1 \rightarrow 0$) and CO($J = 3 \rightarrow 2$) lines are observed at different frequencies in the same configuration (except source C4). This yields different sampling of the uv-plane, which means that the two maps are sensitive to slightly different spatial scales. We re-calculate r_{31} more carefully for C2, C3 and C4 in the following sections.

5.4.2 Matching the 1 and 3 mm Data

In this section, we attempt to standardize the flux calculated for each line as much as possible by matching both spatial and spectral resolution. First, we use the same spectral

resolution in both the CO($J = 1 \rightarrow 0$) and CO($J = 3 \rightarrow 2$) data, selecting the starting channel so that the image velocity channels line up exactly.

Next, to investigate the effect of the different *uv* sampling of the two lines, we re-create the images using only data at *uv* distances present in both the 1 and 3 mm data (matched *uv* data): 8-44 kλ, which corresponds to spatial scales of $\approx 2.5''$-$13''$. Further, we force all the images to have a standard pixel size ($0.99''$for all except the CO($J = 3 \rightarrow 2$) line for C2 and C3 using all *uv* data, for which we use $0.33''$pixels since these images have higher resolution). Figures 5.3 - 5.5 show images and spectra calculated within the standard source regions (discussed in Appendix A.2) using all *uv* data (top panel) and using matched *uv* data (bottom panel).

This *uv*-distance restriction makes the beam sizes more similar, but not necessarily the same due to different sampling within the allowed *uv*-distance range. Table 5.4 compares the measured fluxes and beam sizes using all *uv* data and matched *uv* data. The change in the measured flux is $\lesssim 6\%$ for sources C2 and C4, which is less than the expected measurement error in the total flux. However, the change in flux is more significant for source C3 in both lines. For the CO($J = 1 \rightarrow 0$) line, the matched *uv*-coverage excludes the short *uv* spacings, which are sensitive to large-scale structure. Therefore, the presence of extended emission in source C3 would explain the decrease in flux in the matched *uv* data. This is supported by the radial profile of the CO($J = 1 \rightarrow 0$) cumulative flux in Figure A.1 in Appendix A, which shows the matched *uv* data agreeing with the all *uv* data at small radii and diverging at larger radii. The CO($J = 3 \rightarrow 2$) line, on the other hand, looses long *uv* spacings (sensitive to small-scale structure) in the matched *uv* data. However, the *uv*-distance restriction excludes a sizeable fraction of the *uv* data, which decreases the signal to noise in the image so that less flux is recovered using the masking technique. A comparison of the unmasked CO($J = 3 \rightarrow 2$) line fluxes in the all *uv* and matched *uv* datasets for source C3 shows a drop of only 7.2%, which is within the expected measurement error.

In the rest of our analysis, we consider the emission measured in both cases of *uv*

Name,	All *uv* data		Matched *uv* data		Flux
Trans.	$S_{\rm CO}$	Beam	$S_{\rm CO}$	Beam	% Diff.
C2 1-0	2.30	$4.90'' \times 4.08''$	2.15	$4.54'' \times 3.75''$	-6.5%
3-2	7.06	$1.70'' \times 1.56''$	7.00	$3.20'' \times 2.84''$	-0.8%
C3 1-0	4.29	$4.97'' \times 4.06''$	3.71	$4.62'' \times 3.77''$	-13.5%
3-2	13.75	$1.71'' \times 1.46''$	11.61	$3.12'' \times 3.02''$	-15.6%
C4 1-0	2.95	$4.99'' \times 4.02''$	2.76	$4.62'' \times 3.83''$	-6.4%
3-2	12.79	$3.33'' \times 2.41''$	12.01	$3.55'' \times 3.08''$	-6.1%

Table 5.4: Comparison of *uv* data selections. Measured CO line fluxes ($S_{\rm CO}$ in Jy km s^{-1}) and beam sizes for images made using all *uv* data and matched *uv* data. The fluxes reported here are calculated using the 2σ smooth masking technique discussed in Appendix A.2. The percent difference in the measured flux is defined as $100(S_{\rm CO,match} - S_{\rm CO,all})/S_{\rm CO,all}$.

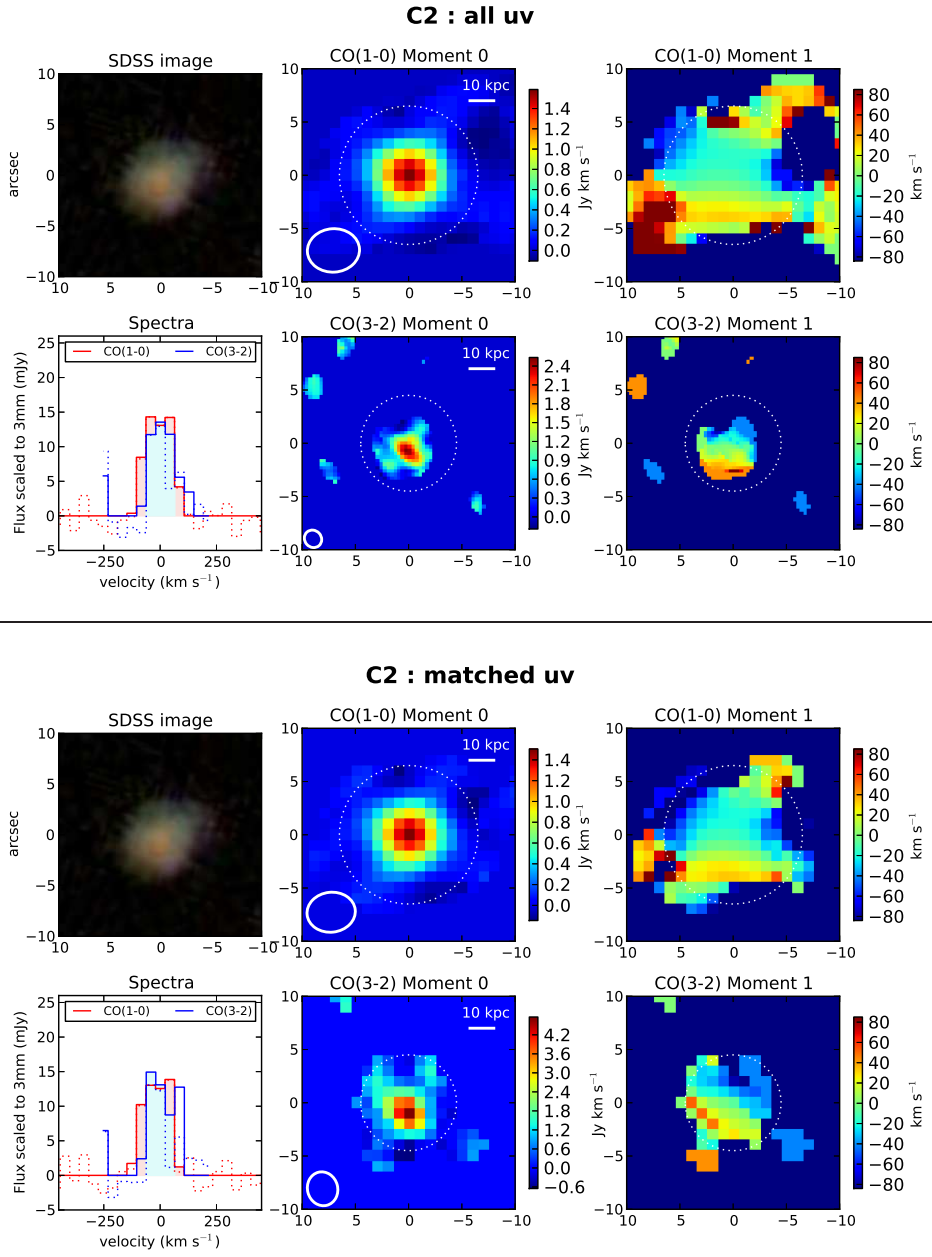

Figure 5.3: Two sets of 6 panels showing the optical image (top left), moment maps (middle and right panels) and spectra (bottom left) for source C2: the top set uses all *uv* data, the bottom set uses matched *uv* data. In each set, the top middle and right panels show the moment 0 (total intensity) and moment 1 (intensity-weighted mean velocity) maps, respectively, for the CO($J = 1 \rightarrow 0$) line. The bottom middle and right panels show the same, but for the CO($J = 3 \rightarrow 2$) line. The synthesized beam (solid white ellipse) and 10 kpc scale (white bar) are indicated. The dotted white circles (middle, right) show the source regions in which flux is summed. The bottom left panels show the spectra in mJy, with the CO($J = 3 \rightarrow 2$) spectrum reduced by a factor of 4.5 to match the scale of the CO($J = 1 \rightarrow 0$) spectrum.

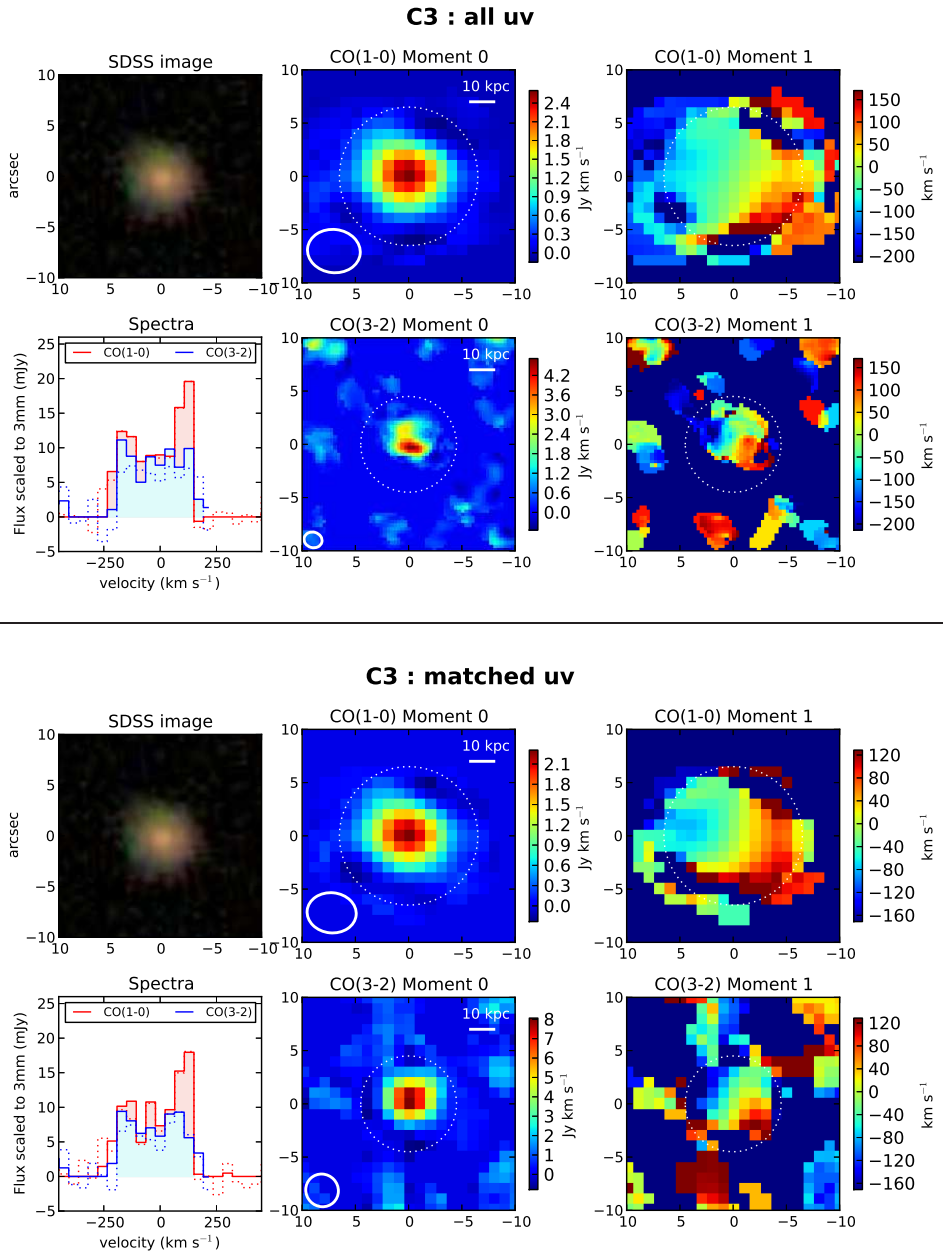

Figure 5.4: Same as Figure 5.3, but for source C3.

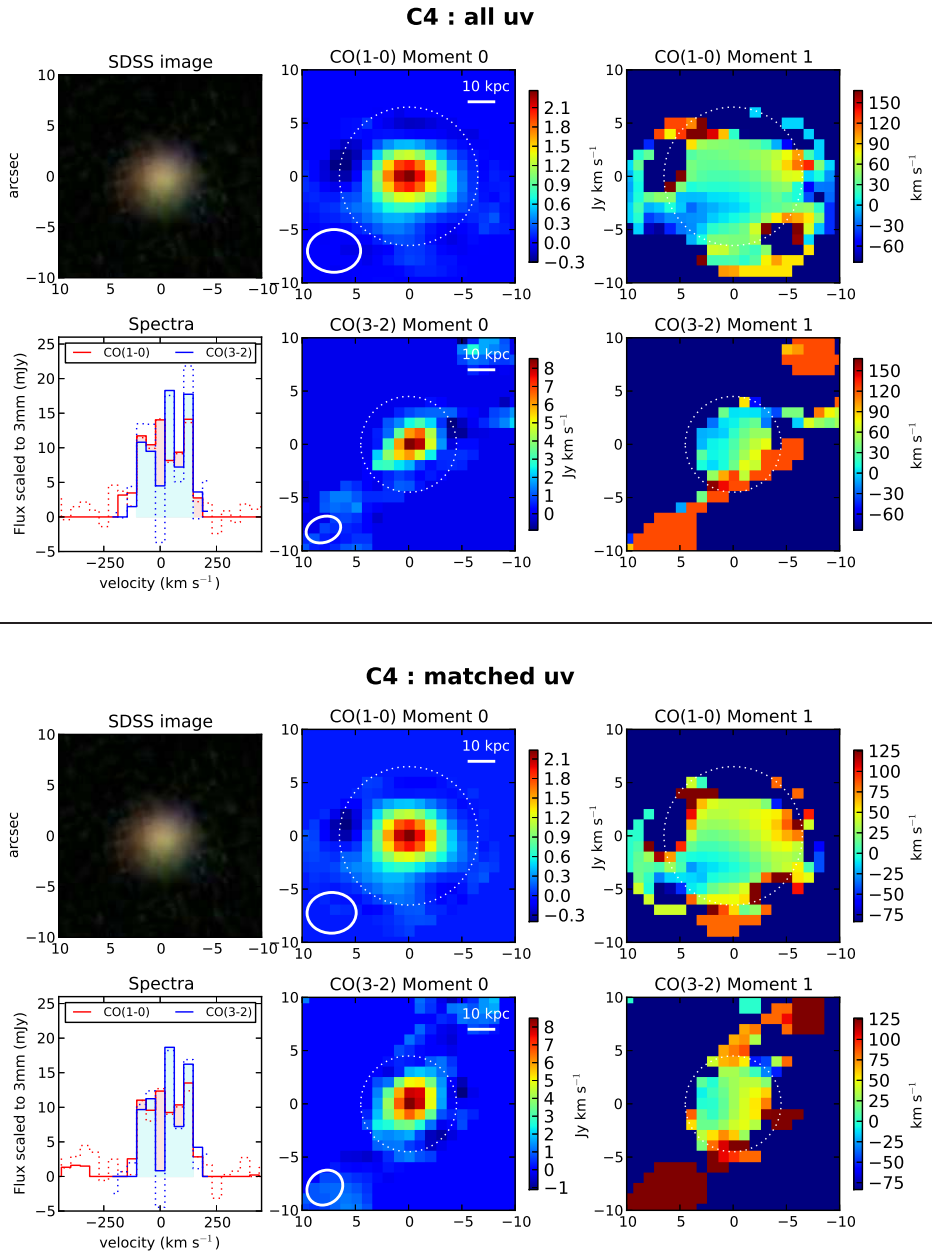

Figure 5.5: Same as Figure 5.3, but for source C4.

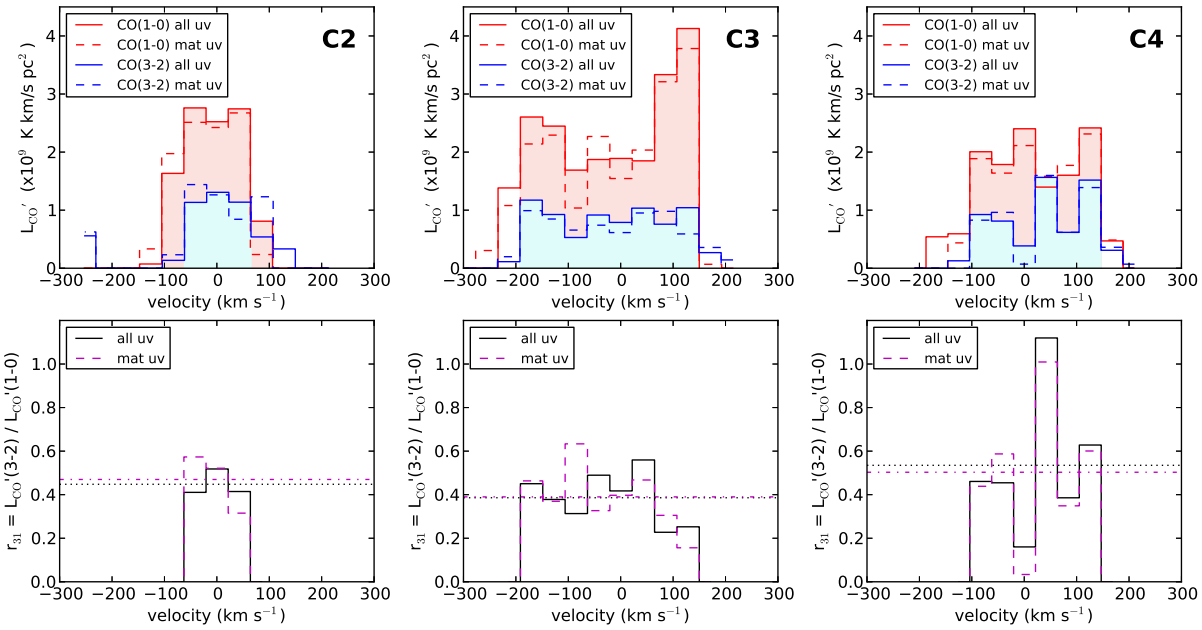

Figure 5.6: $L'_{\rm CO}$ and r_{31} profiles for the three detected sources. The top panels show the $L'_{\rm CO}$ profiles for the CO($J = 1 \rightarrow 0$) (red) and CO($J = 3 \rightarrow 2$) (blue) transitions using all uv data (all uv, solid lines) and matched uv data (mat uv, dashed lines). The shading under each profile indicates which velocity channels are considered part of the source emission for each transition. The r_{31} profile is plotted in the bottom panel for both uv selections (all uv in solid black, matched uv in dashed magenta). The average r_{31} value for each profile is plotted as a horizontal black dotted (all uv data) or magenta dash-dotted (matched uv data) line.

coverage.

5.4.3 Integrated r_{31} Velocity Profiles

We now make a more careful measurement of r_{31}, with the CO($J = 1 \rightarrow 0$) and CO($J = 3 \rightarrow 2$) flux measurements as well-matched to one another as possible. For each uv data selection (all uv, matched uv), we calculate r_{31} in each channel where flux is measured in both lines.

Figure 5.6 shows the integrated $L'_{\rm CO}$ and r_{31} velocity profiles for each of the three significantly detected galaxies. $L'_{\rm CO}$ as a function of velocity is plotted in the top panels for each transition (CO($J = 1 \rightarrow 0$) in red, CO($J = 3 \rightarrow 2$) in blue), for all uv data (solid lines) and matched uv data (dashed lines). Source velocity channels for each line (chosen by eye) are indicated by shading in the corresponding color. The bottom panels show the r_{31} profiles for all uv data (solid black line, with the average value indicated by the horizontal black dotted line) and the matched uv data (dashed magenta line, with average value shown by the horizontal magenta dash-dotted line). For galaxy C2, we have excluded

Name	$N_{\rm ch}$	All uv		Matched uv		Galaxy	Meas.
		Mean	σ	Mean	σ	Mean	Error
C2	3	0.45	0.06	0.47	0.14	0.46	0.08
C3	8	0.39	0.12	0.39	0.14	0.39	0.04
C4	6	0.54	0.32	0.50	0.32	0.52	0.06
					Sample Mean	0.46	
					Sample σ	0.07	

Table 5.5: Summary of EGNoG galaxy r_{31} values. For each source, we give the number of velocity channels in which r_{31} is calculated ($N_{\rm ch}$), the mean and standard deviation (σ) of r_{31} using all uv data and the matched uv data, and the average r_{31} value for each galaxy, with the expected measurement error. In the bottom rows we give the mean and standard deviation of r_{31} in this sample of three galaxies. The expected measurement error for the average r_{31} in each galaxy is the expected measurement error in each channel (30%) divided by $\sqrt{N_{\rm ch}}$.

the velocity channels at ± 86 km s^{-1} from this analysis. At -86 km s^{-1}, we do not detect the CO($J = 3 \rightarrow 2$) line despite a 3σ detection in the CO($J = 1 \rightarrow 0$) line. At $+86$ km s^{-1}, the CO($J = 3 \rightarrow 2$) image suggests a weak (2σ) detection at the center, but the measured flux is dominated by a 3σ noise spike close to this emission. Therefore, we use only the central three velocity channels in the CO($J = 3 \rightarrow 2$) transition.

In galaxies C2 and C3, the r_{31} profiles appear well behaved, remaining roughly constant in all velocity channels. On the other hand, galaxy C4 shows significant deviations from a flat profile, with a very low r_{31} at ≈ 0 km s^{-1} and a very high value at ≈ 40 km s^{-1}. Due to the modest signal to noise ratio at which the CO($J = 3 \rightarrow 2$) line is detected in each channel, we cannot draw any definitive conclusions, but note that if the enhanced r_{31} is real, it may indicate a region of enhanced gas excitation (at a velocity close to 0, it is likely to be physically near the center of the galaxy), such as a starbursting clump, in which a higher r_{31} would be expected.

For each galaxy, Table 5.5 gives the number of velocity channels in which r_{31} is calculated, the mean and standard deviation (σ) of r_{31} for each uv data selection and the the average r_{31} value for the two uv data selections (galaxy mean), with the expected measurement error (meas. error). We expect a 20% measurement error in the flux of each line, in each channel (Appendix A.2), which gives a 30% error in r_{31} in each channel, and a $30\%(N_{\rm ch})^{-1/2}$ error in the average r_{31}. This value is reported in the last column of Table 5.5 for each galaxy. The bottom rows give the mean and standard deviation of the average r_{31} values for the three sample galaxies. In this paper, the standard deviation given is the square root of the unbiased sample variance.

The average values for each uv selection are consistent with each other within each galaxy and roughly consistent across the three galaxies. While the uv selection appears to have a small effect on the average r_{31} value, it is not in a systematic direction. The standard deviation of r_{31} we observe in galaxies C2 and C3 is consistent with the expected 30% measurement errors in each channel. The standard deviation for galaxy C4 is roughly

twice the expected 30% error due to the two outlier channels discussed above. Overall, in the three EGNoG galaxies discussed here, we find a mean r_{31} of 0.46 with a standard deviation of 0.07. Since we estimate each line flux has systematic errors of of up to $\approx 30\%$ (see Appendix A.2), the systematic errors in the ratio r_{31} will be $\lesssim 40\%$.

5.4.4 Radial Dependence of r_{31}

Since r_{31} traces the local excitation conditions of the molecular gas of a galaxy, it is expected to vary within the disk of the galaxy. In fact, Dumke et al. (2001) found CO($J = 3 \rightarrow 2$) emission to be more centrally concentrated than CO($J = 1 \rightarrow 0$) emission in nearby galaxies, so that r_{31} decreased with radius. To look for radial variation in r_{31} in the EGNoG data, we cannot compare the emission maps directly due to the marginal resolution of the galaxies and the different uv coverage of the two transitions. We emphasize that the uv coverage (and thus different spatial resolution) of each transition determines the shape of the radial profile of the enclosed flux (see Figure A.1 in Appendix A), making a direct ratio of the two radial profiles meaningless without perfectly matched uv sampling (even our matched uv data do not meet this criterion due to different sampling within the allowed uv-distance range).

In order to disentangle the true emission distribution from the uv sampling, we fit a two-dimensional Gaussian to the total intensity (moment 0) map of each CO transition using the MIRIAD program `imfit`. The program fits for the position, peak intensity, total flux, size, and deconvolved source size. We perform the Gaussian fit on four versions of the moment 0 map for each transition in each galaxy: for each uv data selection (all and matched), we use moment 0 maps produced with and without 2σ smooth masking. The fit position offsets, deconvolved size and total flux for each case are presented in Table 5.6 along with the total flux calculated by a simple summing of pixels within the source region. The last column gives the percentage difference between the fit total flux and the summed total flux ((fit − summed)/summed)). In two cases, `imfit` found the deconvolved source to be consistent with a point source: this is indicated by a '-' in Table 5.6. In order to derive a good fit to the source emission, we restrict the Gaussian fit to the standard source region (Appendix A.2). The error in the fit total flux is calculated by propogating the errors on the fit peak intensity and (not deconvolved) size. Since these parameters are not independent, this error is likely an overestimate of the true error in the fit total flux.

The residual of each fit is inspected. We note that in general, the emission is fairly well fit by a Gaussian except for the CO($J = 3 \rightarrow 2$) transition in galaxies C2 and C3, which are observed at higher resolution. The structure present it in these higher resolution images is not well-fit by a Gaussian, which is reflected in the large deviations of the fit total flux from the summed flux, especially when no masking is used.

Name	CO Transition	uv Selection	Masking	FIT					Summed Total Flux (Jy km s^{-1})	Flux Percent Diff.
				RA Offset ($''$)	Dec Offset ($''$)	Deconvolved Size FWHM	Deconvolved Size PA	Total Flux (Jy km s^{-1})		
C2	1-0	all uv	no mask	-0.04 ± 0.13	-0.18 ± 0.12	$3.4'' \times 3.1''$	1.3	1.82 ± 0.95	1.76 ± 0.19	3.4%
			masked	-0.04 ± 0.13	-0.18 ± 0.12	$3.4'' \times 3.1''$	1.3	1.82 ± 0.95	1.76 ± 0.19	3.4%
		mat uv	no mask	-0.03 ± 0.12	-0.21 ± 0.12	$3.3'' \times 2.6''$	7.7	1.73 ± 0.17	1.66 ± 0.23	3.9%
			masked	-0.02 ± 0.12	-0.19 ± 0.11	$3.3'' \times 2.6''$	8.2	1.75 ± 0.30	1.67 ± 0.23	4.6%
	3-2	all uv	no mask	0.17 ± 0.25	-0.78 ± 0.23	$2.8'' \times 2.0''$	59.0	6.77 ± 2.51	5.44 ± 2.80	24.4%
			masked	0.16 ± 0.22	-0.74 ± 0.20	$2.8'' \times 2.6''$	-74.2	7.90 ± 2.43	7.06 ± 1.40	11.9%
		mat uv	no mask	0.33 ± 0.23	-0.81 ± 0.22	-	-	5.69 ± 1.92	5.03 ± 2.44	13.1%
			masked	0.35 ± 0.33	-0.77 ± 0.37	$2.4'' \times 2.2''$	36.2	6.67 ± 2.96	7.00 ± 2.02	-4.7%
C3	1-0	all uv	no mask	0.33 ± 0.23	0.13 ± 0.17	$4.8'' \times 1.9''$	65.8	3.84 ± 0.70	3.98 ± 0.37	-3.6%
			masked	0.35 ± 0.22	0.10 ± 0.19	$3.8'' \times 3.2''$	-56.5	4.04 ± 0.68	4.01 ± 0.36	0.8%
		mat uv	no mask	0.32 ± 0.14	0.13 ± 0.11	$4.4'' \times 2.5''$	62.2	3.89 ± 0.58	3.49 ± 0.42	11.4%
			masked	0.30 ± 0.18	0.12 ± 0.15	$3.7'' \times 3.1''$	-86.9	3.87 ± 0.53	3.71 ± 0.39	4.4%
	3-2	all uv	no mask	0.10 ± 0.17	0.22 ± 0.18	$2.8'' \times 2.7''$	12.9	15.03 ± 3.89	10.00 ± 3.21	50.3%
			masked	0.07 ± 0.16	0.23 ± 0.16	$2.6'' \times 2.4''$	7.8	13.76 ± 7.77	13.06 ± 1.70	5.4%
		mat uv	no mask	-0.18 ± 0.13	0.54 ± 0.13	$2.2'' \times 1.9''$	-48.2	12.37 ± 1.87	9.98 ± 2.58	23.9%
			masked	-0.20 ± 0.12	0.54 ± 0.12	$2.3'' \times 2.1''$	-64.6	12.65 ± 3.22	11.61 ± 2.28	9.0%
C4	1-0	all uv	no mask	0.06 ± 0.27	-0.21 ± 0.24	$3.3'' \times 1.7''$	33.1	2.77 ± 2.10	2.77 ± 0.33	-0.1%
			masked	0.07 ± 0.21	-0.28 ± 0.20	$2.9'' \times 1.9''$	-5.3	2.92 ± 0.54	2.83 ± 0.32	3.2%
		mat uv	no mask	0.12 ± 0.18	-0.23 ± 0.16	$2.5'' \times 2.1''$	-10.5	2.83 ± 0.73	2.64 ± 0.38	7.3%
			masked	0.09 ± 0.19	-0.19 ± 0.18	$2.9'' \times 1.5''$	-30.3	2.87 ± 0.46	2.76 ± 0.36	4.0%
	3-2	all uv	no mask	-0.20 ± 0.23	0.15 ± 0.21	$2.2'' \times 1.6''$	-21.7	11.94 ± 3.12	12.73 ± 2.91	-6.2%
			masked	-0.23 ± 0.23	0.09 ± 0.20	$2.3'' \times 1.5''$	-22.5	11.77 ± 3.63	12.79 ± 2.20	-8.0%
		mat uv	no mask	-0.14 ± 0.15	0.25 ± 0.15	$2.4'' \times 1.9''$	29.1	12.69 ± 2.17	11.35 ± 2.77	11.8%
			masked	-0.13 ± 0.26	0.20 ± 0.20	-	-	11.73 ± 4.55	12.01 ± 2.34	-2.3%

Table 5.6: Parameters of the two-dimensional Gaussian fits using `imfit`. For each galaxy, for each CO transition, the fit is performed on the moment 0 map made with and without masking, using two uv selections: all (all uv) and matched (mat uv). For each case, the fit position (RA offset and dec offset), total flux and deconvolved size ($\mathrm{FWHM_{major}} \times \mathrm{FWHM_{minor}}$) and position angle (PA) are reported in columns 5-8. Errors are given on these quantities when available from `imfit`. Columns 9 and 10 give the total flux calculated by a simple summing of pixels within the source region and the percent difference between the fit total flux and the summed total flux ((fit − summed)/summed)).

We look for a radial dependence in r_{31} by comparing the ratio calculated from the fit total fluxes to the ratio calculated from the deconvolved peak intensities. The results are presented in Table 5.7. For each galaxy, for each combination of uv data selection (all, matched) and masking (no mask, masked), we derive the deconvolved peak brightness temperature ($T_{\rm b}$) for each CO transition and calculate r_{31} from the deconvolved peak intensities as well as the fit total fluxes (all values and errors are derived from the parameters of the Gaussian fitting), given in Table 5.6). The rest-frame peak brightness temperature (in K) is given by

$$T_{\rm b} = \frac{h\nu_0}{k_{\rm B} \ln\left[\frac{2h\nu_0^3}{c^2(1+z)^3 I_{\rm peak}} + 1\right]} \tag{5.3}$$

where ν_0 is the rest frequency of the transition and $I_{\rm peak}$ is the observed peak specific intensity (erg s^{-1} cm^{-2} Hz^{-1} Sr^{-1}). We calculate $I_{\rm peak}$ from the velocity width (ΔV in km s^{-1}), fit total flux ($S_{\rm CO}$ in Jy km s^{-1}) and fit deconvolved size (FWHM$_{\rm major}$ and FWHM$_{\rm minor}$ in arcseconds):

$$I_{\rm peak} = \frac{4(\ln 2)(206265^2) S_{\rm CO}}{\pi(10^{23})\Delta V {\rm FWHM}_{\rm major}{\rm FWHM}_{\rm minor}} \tag{5.4}$$

The ratio of the lines, r_{31}, is calculated from the line flux (total or peak) according to Equations 5.1 and 5.2. Note that this ratio is not equivalent to the ratio of the brightness temperatures as defined here (see discussion in Section 5.5).

The errors in the quantities given in Table 5.7 are calculated from the errors in the relevant fit parameters reported by `imfit`. We estimate the error in the deconvolved source sizes (FWHM$_{\rm major}$ and FWHM$_{\rm minor}$) from the spread in the four estimates (all and matched uv, with and without masking) for each transition, for each galaxy. For each quantity, we report the average value for each galaxy, taking the error to be the average fractional error. From the average values, we report the mean (with an uncertainty from the errors in the average values) and standard deviation for the sample as a whole.

We find peak brightness temperatures of approximately 2 K and 4 K for CO($J = 1 \rightarrow 0$) and CO($J = 3 \rightarrow 2$) respectively. This is lower than the excitation temperature observed in Giant Molecular Clouds (GMCs) in the Milky Way (e.g. 10-30 K, Polychroni et al. 2012), as expected since the filling factor for GMCs in the molecular gas disk is less than unity.

While the value of r_{31} is a complex problem (discussed in detail in Section 5.5), the larger brightness temperature of the CO($J = 3 \rightarrow 2$) line (relative to the CO($J = 1 \rightarrow 0$) line) may be explained simply by differing excitation temperatures or filling factors. For instance, if the CO($J = 1 \rightarrow 0$) traces an additional diffuse, lower-excitation gas component not traced by the CO($J = 3 \rightarrow 2$) line (as observed in SMGs by Carilli et al. 2010; Riechers et al. 2011), the average brightness temperature of the CO($J = 3 \rightarrow 2$) line will be higher than the CO($J = 1 \rightarrow 0$) line. On the other hand, a larger brightness temperature in the CO($J = 3 \rightarrow 2$) line may be due to a larger filling factor for the CO($J = 3 \rightarrow 2$) emission. Our Gaussian fits find systematically smaller sizes for the CO($J = 3 \rightarrow 2$) emission relative to the CO($J = 1 \rightarrow 0$) sizes, which is consistent with the results of Dumke et al. (2001), who

Name	*uv*	Gaussian Fit Peak T_b		Gaussian Fit r_{31}	
	Sel.	CO(1-0)	CO(3-2)	Peak	Total
C2	all	1.83 ± 0.32	3.79 ± 0.40	0.75 ± 0.54	0.41 ± 0.26
		1.83 ± 0.32	3.71 ± 0.34	0.68 ± 0.47	0.48 ± 0.29
	mat	1.91 ± 0.13	-	-	0.37 ± 0.13
		1.90 ± 0.15	3.86 ± 0.47	0.72 ± 0.42	0.42 ± 0.20
	avg	1.87 ± 0.23	3.79 ± 0.40	0.72 ± 0.48	0.42 ± 0.22
C3	all	1.78 ± 0.32	3.45 ± 0.35	0.53 ± 0.40	0.44 ± 0.14
		1.65 ± 0.27	3.51 ± 0.51	0.74 ± 0.67	0.38 ± 0.22
	mat	1.68 ± 0.28	3.75 ± 0.37	0.94 ± 0.67	0.35 ± 0.07
		1.65 ± 0.27	3.65 ± 0.38	0.88 ± 0.66	0.36 ± 0.11
	avg	1.69 ± 0.28	3.59 ± 0.40	0.77 ± 0.60	0.38 ± 0.13
C4	all	2.03 ± 0.60	4.10 ± 0.40	0.76 ± 0.72	0.48 ± 0.38
		2.09 ± 0.33	4.16 ± 0.44	0.74 ± 0.46	0.45 ± 0.16
	mat	2.08 ± 0.36	3.89 ± 0.31	0.57 ± 0.34	0.50 ± 0.15
		2.23 ± 0.37	-	-	0.45 ± 0.19
	avg	2.11 ± 0.42	4.05 ± 0.38	0.69 ± 0.50	0.47 ± 0.22
	mean	1.89 ± 0.19	3.81 ± 0.23	0.73 ± 0.31	0.42 ± 0.11
	σ	0.21	0.23	0.04	0.04

Table 5.7: Gaussian fit T_b and r_{31}. Deconvolved, rest-frame peak brightness temperatures (peak T_b) and r_{31} calculated from the deconvolved peak intensities (r_{31} peak) and from the total fluxes (r_{31} total). All values are calculated using the parameters obtained from the Gaussian fitting. For each galaxy, we report five values in each column: one for each of the four data selections used (all *uv* (all) and matched *uv* (mat), with or without masking; presented in the same order as Table 5.6) and the average value with a typical error. From the average values for each galaxy, we calculate the mean (with an uncertainty from the errors in the average values) and the standard deviation for each quantity, presented in the bottom rows.

found CO($J = 3 \rightarrow 2$) emission to be more centrally concentrated than CO($J = 1 \rightarrow 0$) emission in nearby galaxies. Since the molecular gas disks of galaxies tend to have an exponential radial profile (e.g. Regan et al. 2001; Leroy et al. 2009), the gas-rich central region of the galaxy will account for a larger fraction of the CO($J = 3 \rightarrow 2$) emission area, increasing the effective filling factor of the CO($J = 3 \rightarrow 2$) emission relative to that of the CO($J = 1 \rightarrow 0$) emission. Assuming a constant excitation temperature for both transitions, the larger effective filling factor of CO($J = 3 \rightarrow 2$) emission would produce a higher brightness temperature, as we observe.

While the error bars are large, we do find the ratio of the deconvolved peak intensities (representative of the conditions in the central region of the galaxy) to be systematically

higher than the ratio of the total fluxes. In our sample, we find $r_{31}(\mathrm{peak}) = 0.73 \pm 0.31$, with a standard deviation across the three galaxies of 0.04. We compare this to the ratio calculated from total fluxes: 0.42 ± 0.11, with a standard deviation of 0.04. While the small standard deviations in our r_{31} values show consistency between the three galaxies, these results are plagued by sizable uncertainties as a result of fitting data with only modest signal to noise (note that our error estimates are conservative and may in fact be overestimating the true error). Therefore, we conclude (but not robustly) that r_{31} is higher in the center of the EGNoG galaxies than in the molecular disk as a whole (consistent with Dumke et al. 2001).

5.5 Discussion

The observed r_{31} is a function of many parameters, including the excitation temperature (T_{ex}), optical depth (τ_ν) and filling factor of each line (e.g. Hurt et al. 1993). For each line, the rest-frame intensity is

$$\begin{aligned} I_\nu &= \eta_{\mathrm{f}} \left(1 - \exp^{-\tau_\nu}\right) \left[B_\nu(T_{\mathrm{ex}}) - B_\nu(T_{\mathrm{CMB}})\right] \\ &\equiv B_\nu(T_{\mathrm{b}}) \equiv \frac{2k\nu^2 T_{\mathrm{b,RJ}}}{c^2} \end{aligned} \tag{5.5}$$

where $B_\nu(T)$ is the specific intensity of a blackbody at temperature T, T_{b} is the brightness temperature of the line, $T_{\mathrm{b,RJ}}$ is the Rayleigh-Jeans definition brightness temperature of the line and η_{f} is the efficiency of the coupling between the beam and source emission, which is determined by the beam size, the molecular gas disk size and the fraction of the disk that is emitting in the line (the filling factor). Note that Equation 5.5 is in the rest frame. The observed line intensity would be redshifted so that the corresponding observed brightness temperature (for both definitions) is reduced by a factor of $(1 + z)$.

For equal velocity widths in both lines (as we have enforced in Sections 5.4.3 and 5.4.4), r_{31}, as defined in Equations 5.1 and 5.2, reduces to the ratio of the Rayleigh-Jeans brightness temperatures. Following Equation 5.5, we can write r_{31} as

$$r_{31} = \frac{T_{\mathrm{b,RJ}}(3-2)}{T_{\mathrm{b,RJ}}(1-0)} = \frac{\left[\eta_{\mathrm{RJ}}\eta_{\mathrm{f}}\eta_\tau\eta_{\mathrm{CMB}}T_{\mathrm{ex}}\right]_{(3-2)}}{\left[\eta_{\mathrm{RJ}}\eta_{\mathrm{f}}\eta_\tau\eta_{\mathrm{CMB}}T_{\mathrm{ex}}\right]_{(1-0)}} \tag{5.6}$$

where each term in Equation 5.5 is represented as a correction factor η so that we can express r_{31} more directly in terms of the line excitation temperatures. Specifically, η_{CMB} gives the correction from T_{ex} to the effective excitation temperature ($T_{\mathrm{ex,eff}}$, where $B_\nu(T_{\mathrm{ex,eff}}) = B_\nu(T_{\mathrm{ex}}) - B_\nu(T_{\mathrm{CMB}})$) due to the CMB term. At $z = 0.3$, the temperature of the cosmic microwave background (T_{CMB}) is ≈ 3.5 K, so that for $T_{\mathrm{ex}} = 10$ - 30 K, $\eta_{\mathrm{CMB}} \approx 0.85$ - 0.95 for the CO($J = 1 \rightarrow 0$) line and 0.98 - 1.00 for the CO($J = 3 \rightarrow 2$) line. The term accounting for the optical depth of each line is $\eta_\tau = (1 - e^{-\tau_\nu})$. The filling factor term, η_{f} (defined above) is expected to be < 1 and may be different for the two lines. Finally, we

represent the difference between $T_{\rm b}$ and $T_{\rm b,RJ}$ by $\eta_{\rm RJ}$, which, for $T_{\rm b}$ = 10 - 30 K, is 0.75 - 0.91 for the CO($J = 1 \rightarrow 0$) line and 0.39 - 0.75 for the CO($J = 3 \rightarrow 2$) line. Therefore, for $T_{\rm ex}$ = 10 - 30 K for each line, we expect

$$r_{31} \quad = \quad (0.4 - 1.2)\frac{[\eta_{\rm f}\eta_{\tau}T_{\rm ex}]_{3-2}}{[\eta_{\rm f}\eta_{\tau}T_{\rm ex}]_{1-0}} \tag{5.7}$$

The excitation temperature of a given emission line will fall between the radiation temperature ($T_{\rm CMB}$) and the kinetic temperature, depending on the density of the gas. Where the molecular gas density is larger than the critical density (for 20 K gas, $n_{\rm crit} \approx 10^3$ cm^{-3} for CO($J = 1 \rightarrow 0$) and $\approx 10^5$ cm^{-3} for CO($J = 3 \rightarrow 2$)), the excitation temperature is equal to the kinetic temperature of the gas. Thus we see that optically thick gas with equal excitation temperature in both lines will have $r_{31} \approx 1.0 \pm 0.5$ for $T_{\rm ex} \approx 10 - 30$ K (depending on the relative filling factors and optical depths of the two lines). This is consistent with the general criterion that gas with $r_{31} < 1$ is sub-thermal and $r_{31} > 1$ is thermalized. Note that deviation from $r_{31} = 1$ in thermalized gas is a strong function of excitation temperature (due to $\eta_{\rm CMB}$ and $\eta_{\rm RJ}$): higher excitation temperature gas will have r_{31} closer to unity when thermalized. More generally, if one considers various optical depths (assuming local thermodynamic equilibrium (LTE) with equal excitation temperatures), r_{31} greater than unity is indicative of warm, optically thin gas and a ratio less than unity is indicative of optically thick gas (e.g. Meier et al. 2001).

Therefore, while we can comment on whether the excitation of the CO $J_{\rm upper}$ state is likely to be sub-thermal or thermalized, determining the conditions of the gas more accurately requires modeling of multiple transitions (e.g. using Large Velocity Gradient (LVG) models). Since one line ratio does not provide strong constraints, we do not perform LVG modeling as part of this work. In the following sections we compare the r_{31} values found in the EGNoG galaxies to previous studies at low and high redshift and we discuss the implications of this work for the interpretation of CO measurements in intermediate and high redshift galaxies.

5.5.1 Comparison with Previous Work

To date, the study of CO line ratios in intermediate and high redshift galaxies has been dominated by work on extreme starbursting systems: SMGs and quasars. The CO lines from ($J = 1 \rightarrow 0$) up to ($J = 9 \rightarrow 8$) in quasars at $z \approx 2 - 4$ are well-fit by a single component of highly excited gas (Riechers et al. 2006; Weiß et al. 2007; Riechers 2011). In contrast, while the high-J CO transitions in $z \approx 2 - 4$ SMGs are fit by similar highly excited gas, recent observations of the CO($J = 1 \rightarrow 0$) line in these systems reveal a diffuse, low-excitation component in addition to the highly excited component (Carilli et al. 2010; Riechers et al. 2011), similar to what has been observed in local ULIRGS (Papadopoulos et al. 2007; Greve et al. 2009). In contrast, the limited work on $z \approx 1 - 2$ SFGs suggests low-excitation gas similar to the Milky Way (Dannerbauer et al. 2009; Aravena et al. 2010).

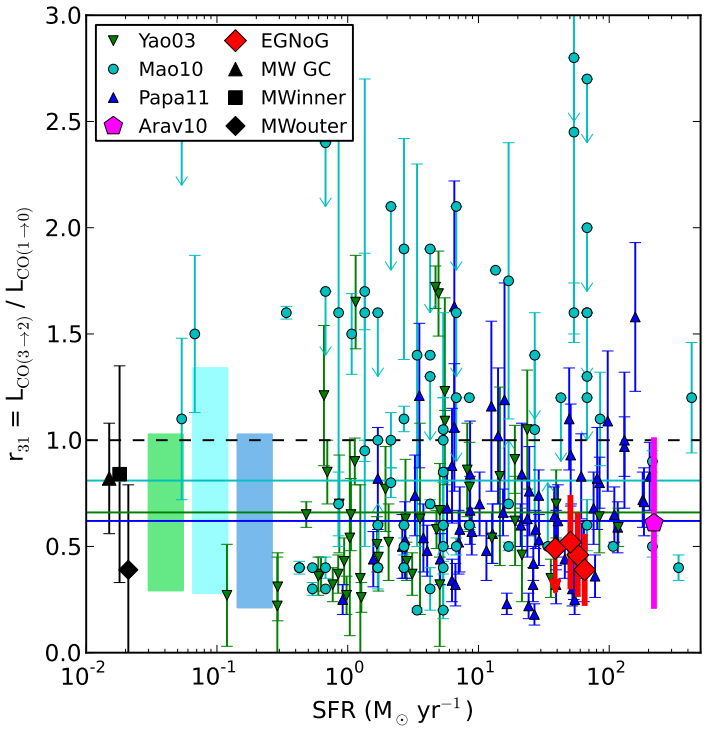

Figure 5.7: Compilation of r_{31} literature data. r_{31} is plotted against approximate SFR ($1.7 \times 10^{-10} L_{\rm FIR}$ when a SFR is not available) for the following datasets: Yao et al. (2003) (Yao03), Mao et al. (2010) (Mao10), Papadopoulos et al. (2011) (Papa11), Aravena et al. (2010) (Arav10), this paper (EGNoG) and Fixsen et al. (1999) (MW GC, inner and outer). Milky Way points are shown at the left side of the plot for clarity. The black horizontal dashed line shows $r_{31} = 1$ and the horizontal solid lines indicate the average values for Yao03, Mao10 and Papa11 (the corresponding shaded rectangles show the standard deviation around the average values).

Since the EGNoG galaxies are SFGs (lying on the main sequence), we restrict the rest of this discussion to SFGs (normal star-forming galaxies) at low and high redshift.

To place the r_{31} values we measure at $z \approx 0.3$ in the context of previous work on normal SFGs, Figure 5.7 shows r_{31} versus approximate SFR for the EGNoG galaxies (red diamonds) and a compilation of literature data, which includes three large surveys of r_{31} in nearby galaxies (Yao et al. 2003; Mao et al. 2010; Papadopoulos et al. 2011) as well as the study at $z = 1.5$ (Aravena et al. 2010). We plot r_{31} from our matched analysis (Section 5.4.3) for sources C2, C3 and C4 (values from Table 5.5, with 40% error bars to indicate potential systematic errors) and the upper limit for source C1 derived from the total line luminosities (Section 5.4.1, Table 5.3). While SFRs are available for the present survey and Aravena et al. (2010), the other three surveys only provide total infrared luminosities ($L_{\rm IR}$) or far infrared luminosities ($L_{\rm FIR}$) calculated from IRAS (the Infrared Astronomical

Satellite) fluxes. We use approximate SFRs of $1.7 \times 10^{-10} L_{\rm FIR}$ $M_\odot$ yr^{-1} ($L_{\rm FIR}$ in $L_\odot$; Kennicutt 1998a) and $LIR/L_{\rm FIR} = 1.3$ (Graciá-Carpio et al. 2008) in Figure 5.7. Values for the Milky Way are plotted as well: the galactic center (MW GC), inner disk (MWinner), and outer disk (MWouter) values, all in black, are taken from Fixsen et al. (1999) and plotted (slightly offset from one another) for illustrative purposes at the left side of the plot. The average r_{31} values of the Yao et al. (2003), Mao et al. (2010) and Papadopoulos et al. (2011) datasets are indicated by the horizontal lines of the corresponding color, with the corresponding shaded rectangles indicating the standard deviation around the average values. To guide the eye, the black dashed line shows $r_{31} = 1$.

Despite the large range of values observed, we find general agreement between our values, that of Aravena et al. (2010) and the average values of the local surveys, with the EGNoG galaxies showing slightly lower r_{31} values than the other studies. Note that the Mao et al. (2010) survey found an average value of 0.81 for the entire sample, but a lower average of 0.61 for galaxies classified as 'normal', based on SFR surface density as indicated by the far infrared luminosity and optical diameter. The range and average r_{31} values for the points plotted (including number of galaxies, redshift and SFR ranges) are given in Table 5.8.

In order to compare our values to the literature data, we first discuss the nature of the observations presented. Yao et al. (2003) observe 60 IR-luminous galaxies (most sources have $L_{\rm FIR} > 10^{10}$ $L_\odot$) selected from the SCUBA Local Universe Galaxy Survey (SLUGS). Each line is measured with a single pointing of a single-dish telescope: CO($J = 1 \rightarrow 0$) at the Nobeyama Radio Observatory (NRO), CO($J = 3 \rightarrow 2$) at the James Clerk Maxwell Telescope (JCMT). For both measurements, the beam size is $\approx 15''$, corresponding to physical sizes of $\approx 0.5 - 13$ kpc for their sample galaxies ($\approx 0.5 - 5$ kpc for most of the sample).

Mao et al. (2010) measure the CO($J = 3 \rightarrow 2$) line for 125 nearby galaxies of various types (e.g. normal, starburst, LIRG, ULIRG) using the Heinrich Hertz Telescope (HHT; beam size $\approx 22''$). This beam size corresponds to a physical size of $\approx 0.25 - 17$ kpc for the sample galaxies (1.7 kpc on average). The CO($J = 1 \rightarrow 0$) data for their sample were taken from the literature and therefore the beam size depends on the telescope used. In their analysis, Mao et al. (2010) only use those galaxies for which they found IRAM 30m CO($J = 1 \rightarrow 0$) data (61), which have a beam size matching the HHT CO($J = 3 \rightarrow 2$) data. These measurements are plotted with error bars in Figure 5.7. Galaxies with CO($J = 1 \rightarrow 0$) data from other sources are reported as upper or lower limits.

Papadopoulos et al. (2011) examine a composite sample of 70 LIRGs in the nearby universe ($z \leq 0.1$) spanning a wide range of morphologies. They present new measurements of 36 galaxies and data from the literature for 34 more. The new measurements use the IRAM 30m telescope for CO($J = 1 \rightarrow 0$) (beam size $\approx 22''$) and the JCMT for CO($J = 3 \rightarrow 2$) (beam size $\approx 14''$), and therefore are not observed with the same beam size. The authors do not comment on matching beam sizes in the new measurements or those from the literature.

The galaxy in which Aravena et al. (2010) measure r_{31}, BzK-21000 at $z = 1.5$, was

Dataset	N	Redshift Range	SFR[1] ($M_\odot$ yr^{-1})	r_{31}	
				Range	Mean
Milky Way	3			0.4 - 0.9	0.68
Mao 2010	61	0.0 - 0.04	0.03 - 200	0.2 - 1.9	0.81
normal	7			0.3 - 1.5	0.61
starburst	25			0.3 - 1.9	0.89
Yao 2003	60	0.007 - 0.05	0.1 - 100	0.2 - 1.7	0.66
Papa 2011	70	0.006 - 0.08	0.7 - 150	0.1 - 1.9	0.67
EGNoG	3	0.28 - 0.31	39 - 65	0.39 - 0.52	0.46
Arav 2010	1	1.52	220		0.61

Table 5.8: Summary of r_{31} from the literature. The range and mean values are given for the following datasets: Fixsen et al. (1999) (Milky Way), Mao et al. (2010) (Mao 2010), Yao et al. (2003) (Yao 2003), Papadopoulos et al. (2011) (Papa 2011), this paper (EGNoG) and Aravena et al. (2010) (Arav 2010). Columns 2 to 4 give the number of galaxies, redshift and SFR ranges for each dataset. For Mao 2010, we also report the r_{31} range and average for the 'normal' and 'starburst' subsets. [1] SFR values are approximate (see Section 5.5.1).

observed in the CO($J = 3 \rightarrow 2$) line with the Plateau de Bure Interferometer (PdBI) by Dannerbauer et al. (2009) and in the CO($J = 1 \rightarrow 0$) line with the Very Large Array (VLA) in C and D configurations (Aravena et al. 2010). In both cases, the source is unresolved or marginally resolved, so the measured fluxes should represent the total emission of the galaxy.

The three samples of nearby galaxies are observed with single-dish instruments, typically sampling the inner portion of the molecular gas disk of the observed galaxies. This is different from the r_{31} measurements for the EGNoG galaxies (Table 5.5) and the galaxy at $z = 1.5$ (Aravena et al. 2010), for which the emission from the entire gas disk is observed. We note that a gradient in r_{31} has been observed in nearby galaxies (Dumke et al. 2001), with higher values measured in the centers. This can be inferred from the Milky Way measurements (Fixsen et al. 1999) as well. This effect may well account for the EGNoG and Aravena et al. (2010) measurements appearing systematically lower than the average values reported by the surveys observing the central regions of nearby galaxies. Supporting this explanation, our analysis in Section 5.4.4 suggests r_{31} is higher in the centers of the EGNoG galaxies (more in line with the average values of the local surveys) compared to r_{31} averaged over the entire disk. However, with such a large spread in values and inhomogeneous datasets, it is difficult to draw any robust conclusions on this point.

5.5.2 Implications

We have measured $r_{31} = 0.46 \pm 0.07$ (with systematic errors of up to 40%) in three galaxies at $z \approx 0.3$, suggestive of optically thick, sub-thermal gas. Despite being massive and highly star-forming (with SFRs of 50-65 $M_\odot$ yr^{-1} and stellar masses of $\approx 2 \times 10^{11}$ $M_\odot$),

the excitation of the gas in these galaxies is consistent with SFGs like local spirals, not star-bursting systems like ULIRGS, SMGs and quasars. Since the EGNoG galaxies have been selected from the main sequence of star-forming galaxies at $z = 0.3$, our findings suggest that galaxies on the main sequence, over a range of star formation activity, harbor sub-thermally excited gas. Therefore, we suggest that CO line ratios similar to those observed in local spiral galaxies are appropriate for main-sequence star-forming galaxies.

The extension of the EGNoG results to main-sequence star-forming galaxies means that sub-thermal line ratios are appropriate for the $z \sim 1-2$ SFGs in which Tacconi et al. (2010) and Daddi et al. (2010) report high molecular gas fractions (20-80%). Tacconi et al. and Daddi et al. estimated the molecular gas mass associated with the observed $J_{upper} > 1$ CO luminosity assuming sub-thermal r_{J1} line ratios and a Milky Way-like α_{CO} (Daddi et al. 2010 used a slightly smaller value for α_{CO}). As the conversion factor is a complex problem, expected to vary as a function of gas excitation, density, metallicity and radiation field (Shetty et al. 2011; Leroy et al. 2011), the results of this work do not directly inform the choice of conversion factor. However, the r_{31} line ratios of the EGNoG gas excitation sample support the assumption of a sub-thermal line ratio in these studies. Specifically, Tacconi et al. (2010) use $r_{31} = 0.5$ to calculate molecular gas masses, which is consistent with our results (Daddi et al. 2010 observed the CO($J = 2 \rightarrow 1$) line and assume a sub-thermal r_{21}).

5.6 Conclusions

This paper presents the gas excitation sample of the EGNoG survey. We report robust detections of the CO($J = 3 \rightarrow 2$) and CO($J = 1 \rightarrow 0$) lines in three galaxies at $z \approx 0.3$, and an upper limit for the fourth galaxy. The average r_{31} value for this sample is 0.46 ± 0.07, with systematic errors of up to 40%. This value is consistent with published r_{31} values for main-sequence star-forming galaxies at $z \approx 0$ as well as the single measurement of at $z > 0.3$ (Aravena et al. 2010). The sub-thermal excitation of the CO($J = 3 \rightarrow 2$) line suggests the excitation state of the molecular gas in these galaxies is similar to local spirals, and is not indicative of a starburst. We conclude that the galaxies in our sample (and by extension, the main sequence galaxies at $z \sim 1 - 2$ studied by Tacconi et al. 2010 and Daddi et al. 2010) harbor cold, optically thick molecular gas despite being massive and highly star-forming.

Acknowledgements

The authors thank the anonymous referee for helpful comments and Eve Ostriker and Adam Leroy for useful discussions. A. Bauermeister thanks Statia Cook, Dick Plambeck and Peter Williams for useful discussions on the reduction and analysis of the EGNoG data. A. Bolatto wishes to acknowledge partial support from grants CAREER NSF AST-0955836, NSF AST-1139998, as well as a Cottrell Scholar award from the Research Corporation for

Science Advancement. We thank the OVRO/CARMA staff and the CARMA observers for their assistance in obtaining the data. Support for CARMA construction was derived from the Gordon and Betty Moore Foundation, the Kenneth T. and Eileen L. Norris Foundation, the James S. McDonnell Foundation, the Associates of the California Institute of Technology, the University of Chicago, the states of California, Illinois, and Maryland, and the National Science Foundation. Ongoing CARMA development and operations are supported by the National Science Foundation under a cooperative agreement, and by the CARMA partner universities.

Chapter 6

HI in Galaxy Groups with the Allen Telescope Array

With only the current reservoir of molecular gas, galactic star formation will cease much sooner than the decline of the observed star formation rate suggests. This is the molecular gas depletion problem. One aspect of the solution to this problem is including atomic hydrogen in the reservoir of gas for star formation. However, to form stars, the gas must be transported to the inner regions of galaxy disks. We have carried out a pilot study of H I gas in groups of galaxies to investigate the importance of tidal interactions between group members as a mechanism for moving H I gas inward to fuel star formation. We image three groups of galaxies in the 21 cm line of H I with the Allen Telescope Array (ATA), taking advantage of the ATA's large field of view and wide bandwidth. We detect many galaxies not previously observed in H I and four previously undetected clouds of H I between galaxies. In one group, we find no inter-galaxy gas. In the two other groups, we detect inter-galaxy gas that accounts for up to 3% of the H I reservoir of the groups. Estimates of the star formation rates of group members suggest group H I gas depletion times of 5-10 Gyr. Thus, the H I reservoir could serve to fuel ongoing star formation if it can be transported inwards to the star-forming centers of galaxies. While these observations have demonstrated the presence of inter-galaxy gas, further modeling will be required to interpret these observations and derive the rate at which star formation is being fueled by tidal interactions.

6.1 Motivation

In the local universe, galaxies harbor insufficient molecular gas to maintain star formation at the current rate for more than a few Gyr (Kennicutt et al. 1994; Wong & Blitz 2002; Leroy et al. 2008). On cosmic scales, we find a similar discrepancy between the star formation rate density and the molecular gas density of the universe : the average star formation rate (SFR) is declining only half as fast as expected given the current reservoir

of molecular gas (Bauermeister et al. 2010; see Chapter 2). This is the molecular gas depletion problem: the current molecular gas reservoir alone cannot be the only fuel for ongoing star formation. It is therefore necessary that the molecular gas reservoir be replenished. The three types of refueling (all of which are likely important) are: return of gas to the inter-stellar medium (ISM) through stellar evolution, infall of gas from an external source, and inflow of gas from the outskirts of the galaxy.

Gas returned to the ISM through stellar evolution may significantly extend the gas depletion time ($\tau_{\rm dep} = M_{\rm gas}/SFR$) in local galaxies, depending on the adopted prescription (Kennicutt et al. 1994). However, chemical evolution modeling suggests that the addition of fresh, un-enriched gas in necessary to match the observed metallicity gradient in the Milky Way (e.g. Lacey & Fall 1985; Chiappini et al. 1997), so stellar recycling alone is insufficient to maintain star formation.

The required un-enriched gas may come from the atomic gas (H I) in the outskirts of the disk or from infall of gas from outside the galaxy. Infall of gas has long been observed in the form of high velocity H I clouds (HVCs; see Wakker & van Woerden 1997 for a review) around the Milky Way and other local galaxies (Thilker et al. 2004; Westmeier et al. 2005). The source of these clouds may be the hot gaseous halo around galaxies like the Milky Way (see Putman et al. 2012 for a review): Peek et al. (2008) found the observed properties of HVCs to be consistent with the cool, overdense clouds predicted by Maller & Bullock (2004) to fall onto the disk via multiphase cooling of the hot gaseous halo. However, the gas accretion rate from this extra-planar gas around the Milky Way and other nearby spirals is estimated to be $0.1 - 0.2$ M$_\odot$ yr^{-1} (Wakker et al. 2007; Peek et al. 2008; Sancisi et al. 2008), which accounts for only about 10% of the star formation rate (in the Milky Way, the star formation rate is $\sim 1 - 4$ M$_\odot$ yr^{-1}; Diehl et al. 2006b; Murray & Rahman 2010; Robitaille & Whitney 2010.) Further, Fraternali & Binney (2008) argue that much of the extraplanar gas observed in nearby spiral galaxies comes from stellar feedback (the galactic fountain) and is thus not a supply of un-enriched gas.

Therefore, atomic gas in the outskirts of the disk may be an important reservoir of un-enriched gas for star formation. H I surveys like THINGS (The H I Nearby Galaxy Survey; Walter et al. 2008) have shown local galaxies to have large atomic gas disks, extending well beyond their star-forming disks. However, this gas may only fuel ongoing star formation if it is transported inwards (via radial inflows), where it may be converted to molecular gas and form stars. Inflow is important in the case of infalling external gas as well, as simple area and angular momentum arguments suggest that infalling gas will be deposited mostly in the outskirts of the galaxy and thus still need to be transported inwards (Peek 2009).

In this chapter, we focus on the role of interactions between galaxies in moving gas from the outskirts of galaxies inward. Close encounters and other interactions have long been known to disrupt the extended H I disk of nearby galaxies: the "H I Rogues Gallery" (Hibbard et al. 2001) presents a wide array of H I morphologies resulting from galaxy interactions. Interactions like these can be an effective way to move gas to the centers of galaxies. Numerical modeling of interacting galaxy NGC 7252 by Hibbard & Mihos (1995)

showed that most of the material drawn out into tidal tails remained bound and returned to the galaxy on Gyr time scales. The authors found that only a fraction of the gas was drawn into the tidal tail; in fact, much of the gas moved inward. On the observational side, evidence for radial gas inflows in interacting galaxies has been seen directly in both ionized (Rampazzo et al. 2005) and neutral gas (Iono et al. 2005; Cullen et al. 2007). Further, Kewley et al. (2010) find flattened metallicity gradients in close pairs of galaxies, indirect evidence of radial gas inflows as a result of tidal interactions.

In order to ascertain the importance of interactions in typical groups of galaxies, we undertook a pilot study of H I in local galaxy groups at the Allen Telescope Array (ATA; Welch et al. 2009), a cm-wave interferometer at the Hat Creek Radio Observatory in Hat Creek, California. Using the large field of view of the ATA, we looked for inter-galaxy H I in three loose groups of galaxies (similar to the Local Group) to constrain the amount of inter-galaxy gas in groups due tidal interactions between group members. We describe the properties of the ATA and the observations in Section 6.2 and the data reduction in Section 6.3. The results of this pilot program are detailed in Section 6.4. We discuss the implications of this work in Section 6.5.

6.2 Project Description

From its construction through mid-2011, the ATA was operated jointly by the UC Berkeley Radio Astronomy Laboratory and the SETI[1] Institute. The ATA is a "large number of small dishes" (LNSD) telescope, designed to be highly effective for surveys. The array consists of forty-two 6.1 meter offset Gregorian dishes (the full vision for the ATA comprised 350 dishes) with log-periodic, dual-linear-polarization feeds capable of continuous frequency coverage from 500 MHz to 10 GHz. The large primary beam (2.5° at L-band (1.42 GHz)) and large bandwidth (up to 104 GHz) made the ATA ideal for surveying local groups of galaxies, which cover a large area of the sky.

Our pilot program at the ATA consisted of observations of three loose groups of galaxies: the M106, NGC 262 and NGC 2403 groups. We started by observing the NGC 262 group, selected from the H I Rogues Gallery (Hibbard et al. 2001) for showing evidence of interaction in H I, and, at 65 Mpc, fitting easily within the primary beam of the ATA. The two nearby groups (M106 and NGC 2403) were selected from the catalog of galaxies in the local volume ($\lesssim$ 10 Mpc; Karachentsev et al. 2004). In this catalog, groups are distinguished by a common 'main disturber' (the neighboring galaxy producing the largest tidal force on a galaxy) with a positive tidal index. The tidal index from Karachentsev et al. (2004) quantifies the tidal action on the galaxy due to the main disturber: positive values indicate group members. All groups were selected to be outside of the area of the sky observable by Arecibo in order to be complimentary to the Arecibo Legacy Fast ALFA (ALFALFA) survey (Giovanelli et al. 2005), a blind H I survey out to $z \sim 0.06$.

[1]Search for Extraterrestrial Intelligence

Group Name	Dist. (Mpc)	Pointing	Dates Observed	Obs. Time (hrs)	3σ $N_{\rm HI}$ Limit ($\rm cm^{-2}$)
NGC 262	64		Sep - Nov 2008	75	1.5×10^{19}
NGC 2403/2366	3.5	NGC 2403	Dec 2008 - Feb 2009	54	1.5×10^{19}
		NGC 2366	Jan - Feb 2009	46	1.4×10^{19}
M106	7.5		Mar - Apr 2009	51	1.5×10^{19}

Table 6.1: Summary of galaxy group observations.

The M106 and NGC 262 groups required only one pointing each to capture the group. For the NGC 2403 group, we observed one pointing centered on NGC 2403 and one on group member NGC 2366. Each pointing was observed for approximately 40 hours in order to achieve an $\rm N_{HI}$ sensitivity of a few $\times 10^{19}$ $\rm cm^{-2}$. This limit was selected as the expected minimum H I column density of inter-galaxy gas due to ionization by the extra-galactic radiation field (Maloney 1993). While this H I cutoff has been observed by some authors (ie., van Gorkum 1993; Corbelli et al. 1989), we note that some more recent studies like Hunter et al. (2011) find no evidence for truncation of the H I disk at some cutoff. Thus it is not certain whether more, lower column density atomic gas may be present between galaxies. Observations were made using the maximum bandwidth of 104 GHz centered on the rest frequency of the 21 cm H I transition. This resulted in velocity coverage out to 9000 km $\rm s^{-1}$ with a channel width of 21.6 km $\rm s^{-1}$. A summary of observations is given in Table 6.1.

6.3 Data Reduction

All data were reduced using the Multichannel Image Reconstruction, Image Analysis and Display (MIRIAD; Sault et al. 2011) package for radio interferometer data reduction. Radio frequency interference (RFI) excision and calibration are performed using the Automated Real Time Imaging System (ARTIS) for the ATA (Keating et al. 2010), discussed in Section 6.3.1. Continuum subtraction and imaging are described in Section 6.3.2. Source identification is discussed in Section 6.3.3.

6.3.1 RFI Excision and Calibration

The ARTIS package was used to remove radio frequency interference (RFI) from the data and subsequently calibrate the data. ARTIS identifies RFI by spectral occupancy: each spectrum (calculated over an adjustable time window) is analyzed for 4σ outliers, then channels showing a high occupancy rate (4σ above the median occupancy rate) are flagged on all baselines. This procedure is first performed on each antenna individually in order to identify antenna-specific RFI. The flagging criteria are then expanded to consider

Group Name	Calibrator	Flux (Jy)	Freq (GHz)	Spectral Index
M106	3C286	15.0	1.5	-0.46
NGC 262	3C48	16.0[a]	1.43	0.0
NGC 2403/2366	3C147	22.5	1.5	-0.70

Table 6.2: Summary of calibrators. For each galaxy group, the same calibrator was used for all observations. The flux information is taken from the VLA Calibrator Manual, except for 3C48 (marked by [a]), for which we use the flux from an internal ATA calibrator flux table.

all baselines together. Multiple time windows are used in order to catch both strong RFI over short time-spans and weaker RFI over longer time-spans.

For the calibration of each dataset, a strong quasar was observed approximately every half hour in order to track the gain variations over the course of the observation. ARTIS calibrates the amplitude, phase and bandpass gains in an iterative fashion. A point source model for the calibrator is used to derive gain solutions. Baselines which exceed phase rms limits and closure limits are removed. This process is repeated until all data lie within the allowed limits. Baselines which retain less than 20% of their data and antennas which retain less than 20% of their baselines are removed entirely.

The flux scale of each dataset is set in the calibration step by giving ARTIS the flux of the calibrator. We use flux and spectral index values based on the VLA calibrator manual fluxes [2]. Flux values for each calibrator used are given in Table 6.1. Note that for calibrator 3C48, we use a flux of 16 Jy at 1.43 GHz from an internal ATA flux table. This value is 9% larger than that reported in the VLA Calibrator Manual.

As a check of the flux calibration of the data, we compared the fluxes of continuum sources in the field with the fluxes reported by the NRAO VLA Sky Survey (NVSS; Condon et al. 1998). We use MIRIAD program `sfind` to find and extract the fluxes of continuum sources in the cleaned continuum map (produced using `invert` with multi-frequency synthesis, deconvolved using `clean`, and corrected for primary beam attenuation using `linmos`). We then match these continuum sources to the NVSS catalog and compare the fluxes. Figure 6.1 shows the results, plotting our observed flux (after calibration) versus the NVSS flux. The black dashed line indicates perfect agreement. In general, the fluxes agree well. We tend to slightly over-predict the fluxes of less bright sources. Restricting the comparison to fluxes > 50 mJy, the median ratio of our extracted flux to the NVSS flux for the three galaxy groups is 1.04, 1.00 and 1.08 for M106, NGC 262 and NGC 2403/NGC 2366. Thus, the flux scale of our data appears to be correct to roughly 10%.

[2]The VLA calibrator manual can be found online at `http://www.vla.nrao.edu/astro/calib/manual/`

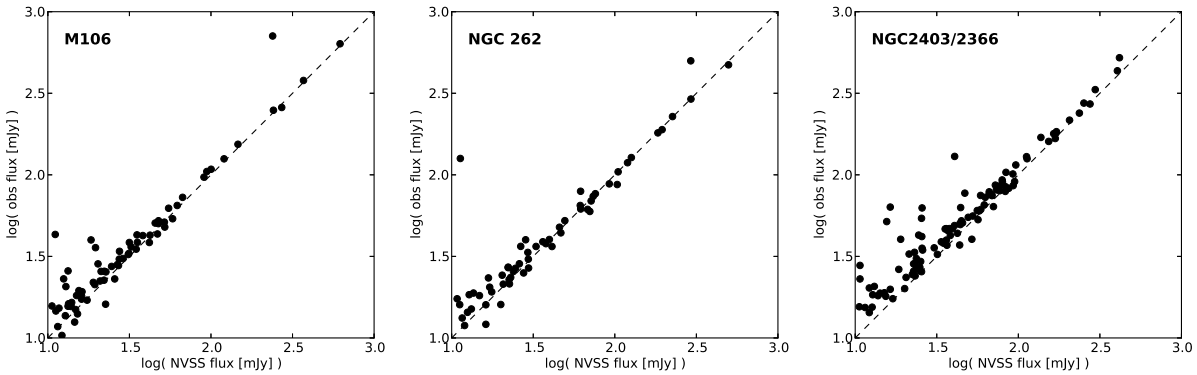

Figure 6.1: Comparison of fluxes of continuum sources matched to the NVSS catalog. The dashed black line indicates perfect agreement.

6.3.2 Continuum Subtraction and Imaging

For each pointing, all *uv* datasets are combined for continuum subtraction and imaging. The continuum emission is subtracted from the *uv* data using `uvlin`. This program performs a low-order polynomial fit to the *uv* data in line-free channels and subtracts the result. The data are imaged channel by channel using `invert` with a Briggs robustness parameter of 0.5 (Briggs 1995) and deconvolved using `clean` down to a cutoff of 3 times the rms noise in the dirty map. For the relatively empty fields of NGC 2403 and NGC 2366, cleaning was restricted to a polygon enclosing the HI emission from the detected galaxies. Finally, the cleaned, continuum-subtracted image cube (RA, Dec, H I velocity) is corrected for primary beam attenuation using `linmos`.

6.3.3 Source Identification

Each image cube is searched for H I emission both programmatically and by eye. We first run `sfind` on each plane of the image cube to identify all point-like sources, which does well at identifying the H I emission of marginally resolved sources. For large galaxies, `sfind` is not as reliable, but the larger galaxies are obvious upon visual inspection. The resulting list of detections is then passed to the `srcsort` program (written by A.B.) which goes through the `sfind` source list and determines which sources are actually the source appearing in multiple velocity channels. The program then displays the image cube channel by channel, with overlays showing the sources found by `sfind` and `srcsort` so that the user may inspect each potential detection by eye.

The potential sources which pass visual scrutiny (having 3σ signal continuous over at least two adjacent velocity channels) are accepted as detections. For each pointing, we use the NASA/IPAC Extragalactic Database (NED[3]) to match our H I detections to optical

[3] http://ned.ipac.caltech.edu/

Name	LGG14 Member	Major (arcmin)	Minor (arcmin)	Type	Distance (Mpc)
NGC 262	y	1.1	1.1	S0/a	63.9 ± 4.5 (H)
NGC 266	y	3.0	2.9	SBab	66.0 ± 4.6 (H)
UGC 484	y	2.8	0.8	Sb	62.2 ± 2.8 (TF)
UGC 509	y	1.4	0.5	Sc	68.2 ± 6.2 (TF)
UGC 511	y	1.8	0.4	Sc	67.0 ± 9.5 (TF)
CGCG 500-095	y	0.9	0.6	Sbc	71.7 ± 5.0 (H)
KUG 0044+324B	y	0.6	0.4	Sbc	71.1 ± 5.0 (H)
MAPS P0295-0699736	n	-	-	LSB	69.3 ± 5.1 (H)
UGC 479	n	1.1	0.6	Sa	96.2 ± 8.7 (TF)

Table 6.3: Properties of the NGC 262 group galaxies. Membership in the galaxy group LGG14 comes from Garcia (1993). The blue major and minor diameters (in arcmin) and the galaxy morphological type come from NED (for NGC 262 and NGC 266) or Springob et al. (2005). Galaxy type LSB stands for low surface brightness galaxy (see discussion for more detail). Galactocentric (GSR) distances are from NED, with the method is given in parentheses: Hubble flow (H), Tully-Fisher relation (TF).

counterparts. The flux, average velocity and velocity width is calculated for each detection using the Interactive Data Language (IDL) program `src_stats.pro` (written by A.B.). In each plane, pixels are considered part of the source if they are $> 3\sigma$ or are $> 2\sigma$ and adjacent to source pixels (along a spatial or velocity axis). This calculation is done in a very restricted region around the emission so as to limit the inclusion of noise peaks.

For each source, moment 0 (total intensity) and moment 1 (intensity-weighted velocity) maps are created using MIRIAD program `moment` excluding pixels below 2.5σ. For the moment maps of large fields, we make the moment map of each detected source individually, restricted to the area immediately around each source. The individual maps are then combined by re-gridding the maps with `regrid` and adding them together with `maths`.

6.4 Results

6.4.1 NGC 262

Group Membership

We have observed what we refer to as the NGC 262 group, centered on the interacting galaxies NGC 262, a large spiral galaxy with AGN activity, and NGC 266, a nearby barred spiral. The Lyon Group of Galaxies (LGG) catalog of nearby (recession velocities < 5500 km s^{-1}) groups (Garcia 1993) lists NGC 262 and its neighboring galaxies as part of the LGG 14 group. The LGG 14 group consists of 18 galaxies, 7 of which lie within the

Name	Prev Obs	v_{sys} (km s^{-1}) Prev	v_{sys} (km s^{-1}) ATA	Δv (km s^{-1}) Prev	Δv (km s^{-1}) ATA	S_{HI} (Jy km s^{-1}) Prev	S_{HI} (Jy km s^{-1}) ATA
NGC 262	Noor05	4534	4537	65	62	23.9	18.8
NGC 266	Noor05	4647	4646	453	418	7.7	4.0
UGC 484	Spr05	4864	4849	427	402	14.5	13.6
UGC 509	Spr05	5134	5203	212	151	2.1	1.1
UGC 511	Spr05	4595	4597	277	253	2.9	1.7
CGCG ...	Spr05	5072	5031	176	37	2.5	0.9
KUG ...	Spr05	4995	5003	162	99	3.6	1.9
MAPS ...	Spr05	4899	4919	124	92	1.5	1.7
IGC1	-	-	5367	-	52	-	1.4
UGC 479[b]	Spr05	6259	6127	367	49	3.5	2.0

Table 6.4: H I properties of the NGC 262 group. The average velocity, velocity width and integrated H I flux (S_{HI}) are reported for this work (ATA) and previous (Prev) observations: Springob et al. 2005 (Spr05) or Noordermeer et al. 2005 (Noor05).
[a] UGC 479 is only observed to the upper left of the NED position. We are likely only detecting the lower velocity half of the galaxy.

observed field: NGC 262, NGC 266, UGC 484, UGC 509, UGC 511, CGCG 500-095 and KUG 0044+324B. We detect two more galaxies in the field, UGC 479 and MAPS P0295-0699736, which are not listed as part of the LGG 14. However, MAPS P0295-0699736, is a low-surface brightness (LSB) galaxy (Cabanela & Dickey 2002) with an apparent blue magnitude of ~ 18 and would thus not have been included in the Garcia (1993) study, which had a limiting apparent blue magnitude of 14. Without a redshift-independent distance measurement for MAPS P0295-0699736, we choose to include it in the NGC 262 group since it is only separated from NGC 266 in recessional velocity by less than 300 km s^{-1}, a reasonable relative velocity between group members). Table 6.3 lists properties of the observed galaxies, with LGG 14 group membership indicated in the second column.

H I Detections and Previous Observations

We observed a field (2.5° diameter) centered between NGC 262 and NGC 266 down to a 3σ limit of 1.8×10^{19} cm^{-2} of H I. The synthesized beam was $2.9' \times 1.8'$, yielding a mass sensitivity of 4×10^8 M$_\odot$ of H I (requiring signal in 2 adjacent velocity channels). Figures 6.2 and 6.3 show the moment 0 (total intensity) and moment 1 (intensity-weighted average velocity) maps of the entire group. Table 6.4 gives the H I properties for all galaxies in the ATA field within 2000 km s^{-1} of the systemic velocity of NGC 262. We report the systemic velocity (v_{sys}), velocity width (Δv), and H I flux (S_{HI}) observed by the ATA in this work as well as by previous H I studies (Noordermeer et al. 2005; Springob et al. 2005). We discuss each detection individually below.

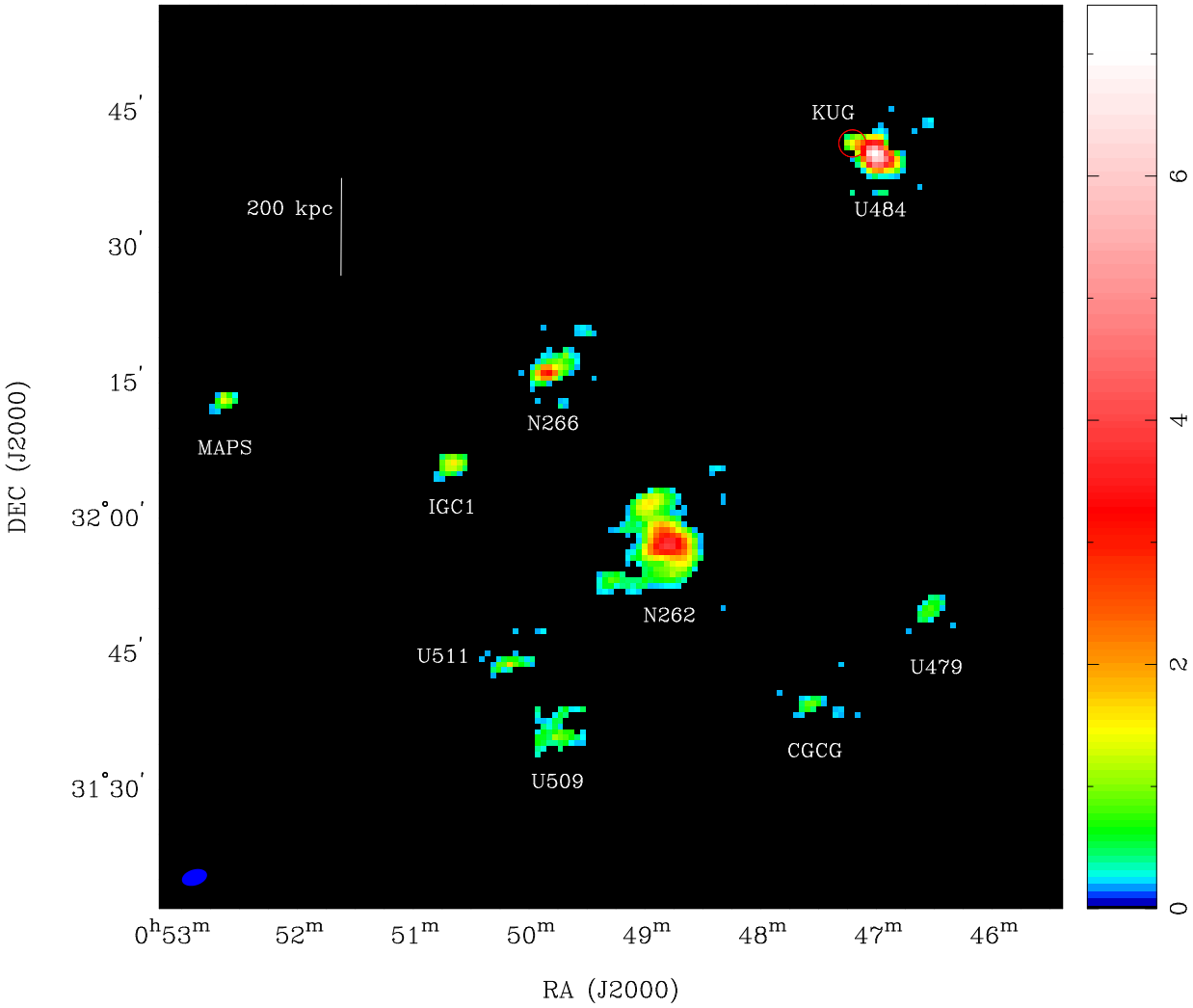

Figure 6.2: Moment 0 (total intensity) map of NGC 262 group. Each galaxy is labelled. The color scale shows intensity in Jy km s^{-1} on a logarithmic scale. The observed emission of KUG 0044+324B and UGC 484 overlap, so a red circle is drawn to indicate the position of the smaller galaxy, KUG 0044+324B (labelled KUG). The beam is shown in the lower left. The angular size corresponding to 200 kpc at the distance to NGC 262 (64 Mpc) is shown by the vertical bar in the upper left.

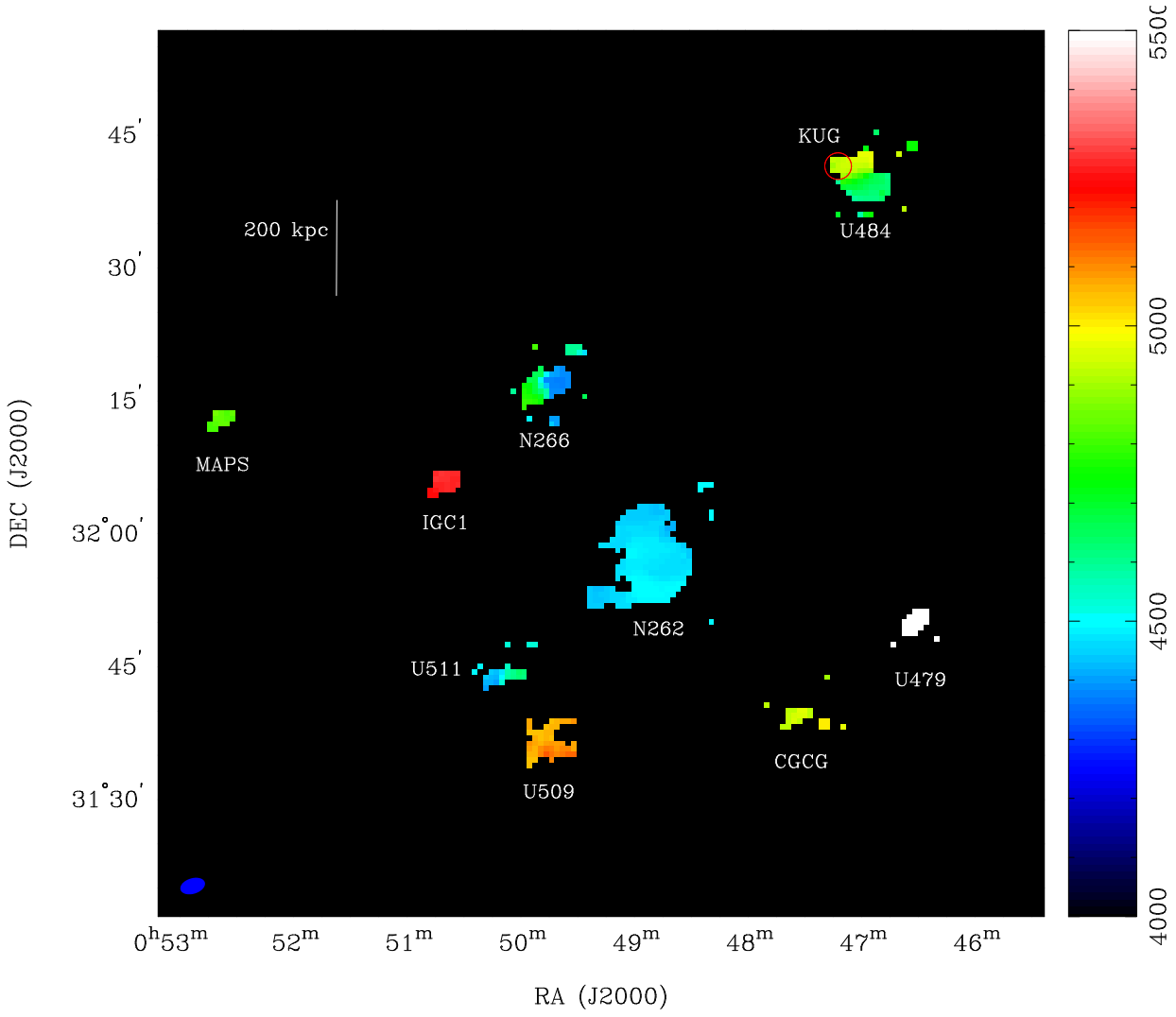

Figure 6.3: Moment 1 (intensity-weighted average velocity) map of NGC 262 group. Each galaxy is labelled. The color scale shows radio-definition velocity in km s^{-1} ($v_{\rm optical} = v_{\rm radio}(1-v_{\rm radio}/c)^{-1}$). UGC 479 lies at an average velocity of 6217 km s^{-1}, off of the plotted scale. Annotation is as in Figure 6.2.

NGC 262 is the central galaxy of the group. NGC 262 (Mrk 348, UGC 499) and was previously observed in the H I line by Simkin et al. (1987). The H I morphology showed evidence of tidal perturbation: a large H I envelope and tail-like extension to the south-east. Both features are present in our observations. Our observed flux (18.8 Jy km s^{-1}) is a little low, but not unreasonable compared to the spread in previous observed values: 21.5 Jy km s^{-1} by Simkin et al. (1987) and 23.9 Jy km s^{-1} by Noordermeer et al. (2005). The observed systemic velocity and velocity width are consistent across studies. We report the Noordermeer et al. (2005) results in Table 6.4.

NGC 266 (UGC 508) has been observed in H I by both Noordermeer et al. (2005) and Springob et al. (2005). The ATA observed flux (4.02 Jy km s^{-1}) is again a little low but not unreasonable compared the spread of previous observations: 5.24 Jy km s^{-1} and 7.71 Jy km s^{-1} from Springob et al. (2005) and Noordermeer et al. (2005) respectively. The observed systemic velocity is consistent across studies, but we observe a smaller velocity width, which may explain the lower flux. We give the Noordermeer et al. (2005) results in Table 6.4.

For the other UGC galaxies (484, 509, 511 and 479) and galaxies CGCG 500-095 and KUG 0044+324B, we compare to previous observations by Springob et al. (2005). In general, the fluxes and velocity widths observed by the ATA are smaller, which is likely because the ATA detections are generally lower signal to noise than those reported by Springob et al. (2005). Three of these galaxies are special cases: UGC 479, UGC 484, and KUG 0044+324B.

UGC 479: We only detect H I north-east of the NED position for UGC 479, at a lower systemic velocity with smaller velocity width than Springob et al. (2005). This suggests that we have only detected one half of the galaxy, explaining the discrepancy between our detection and previous work.

UGC 484 and KUG 0044+324B are separated on the sky by only 3.3′, with H I emission at the same velocities. Therefore, the H I emission of the two galaxies is blended in our images. Figure 6.4 shows the moment 0 (total intensity) H I contours overlaid on the optical image from the Digital Sky Survey (DSS[4]). The two galaxies are labelled. By changing the weighting of the *uv* data to produce a smaller beam, we can resolve the H I into two separate sources, but doing so results in a significant decrease in the the signal-to-noise ratio. Therefore, we calculate the flux of the merged H I emission, then separate it into the two galaxy components by fitting a Gaussian to the H I spectrum in the region of KUG 0044+324B. The resulting systematic velocities, velocity widths and total fluxes of the two galaxies are given in Table 6.4.

MAPS P0295-0699736 was previously observed by Cabanela & Dickey (2002) as part of an H I survey of low surface brightness (LSB) galaxies at Arecibo. Our observations agree fairly well with the values from Cabanela & Dickey (2002).

Inter-galaxy H I: We detect one inter-galaxy cloud of H I at RA 00:50:40.6, Dec +32:06:13 (J2000), which we have labelled IGC1. We detect IGC1 at the 7σ level in

[4] http://archive.stsci.edu/cgi-bin/dss_form

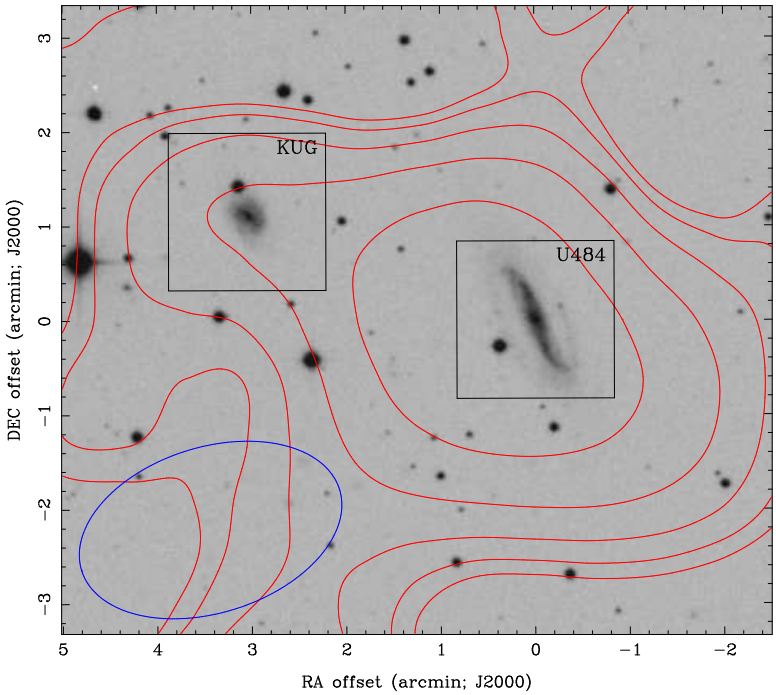

Figure 6.4: Integrated H I contours overlaid on the DSS image of UGC 484 and KUG 0044+324B. Each galaxy is labeled in black. The red H I contours show $2^n \times (2 \times 10^{19})$ cm^{-2} of H I, for $n = 0, 1, 2, ...$ The blue ellipse in the lower left shows the beam.

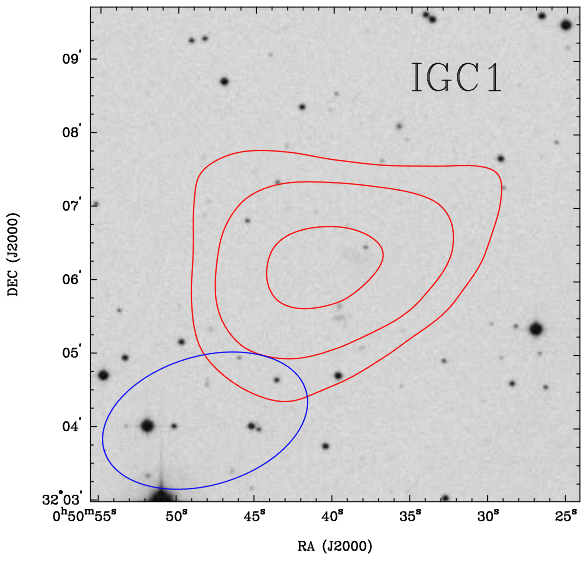

Figure 6.5: Integrated H I contours overlaid on DSS image of IGC1. The H I contours show $2^n \times (2 \times 10^{19})$ cm^{-2} of H I, for $n = 0, 1$. The blue ellipse in the lower left shows the beam.

	M_{HI} (10^9 $M_\odot$)		SFR ($M_\odot$ yr^{-1})				τ_{dep} (Gyr)	
Name	Prev	ATA	FIR	1.4GHz	Src	Avg	Prev	ATA
NGC 262	23.0	18.1	1.9	79.8	A	1.9	12.2	9.6
NGC 266	7.9	4.1	2.5	2.6	S	2.6	3.1	1.6
UGC 484	13.3	12.4	2.0	1.6	S	1.8	7.2	6.8
UGC 509	2.3	1.2	-	-	-	-	-	-
UGC 511	3.1	1.8	-	-	-	-	-	-
CGCG ...	3.0	1.1	-	-	-	-	-	-
KUG ...	4.3	2.2	-	-	-	-	-	-
MAPS ...	1.7	1.9	-	-	-	-	-	-
IGC1	-	1.4	-	-	-	-	-	-
UGC 479[b]	7.6	4.5	-	2.1	S	2.1	3.6	2.1

Table 6.5: H I masses and star formation properties of the NGC 262 group. H I masses are calculated from the H I fluxes reported in Table 6.4 using the distances given in Table 6.3. We assume IGC1 is at the distance of NGC 262. Star formation rates (SFR) are calculated from far infrared (FIR) fluxes and 1.4 GHz luminosities when available. For the 1.4 GHz SFR, we list the source of the 1.4 GHz luminosity as given in Condon et al. (2002): S for star formation, A for AGN. The average SFR is reported in the 'Avg' column. The H I gas depletion time (τ_{dep}) is calculated in the last two columns using the average SFR.

two consecutive channels with 3σ signal in the adjacent channels on either side. Figure 6.5 shows the moment 0 contours overlaid on the optical image from the DSS. No optical counterpart is visible in the DSS image. Similarly, NED lists no sources within $3'$ of IGC1's position. If the cloud is at 64 Mpc (the distance to NGC 262), the observed emission implies 1.4×10^9 $M_\odot$ of H I, somewhat less than the H I mass of the Milky Way (Dame 1993).

H I Gas Mass and Star Formation Properties

In Table 6.5, we compute the H I gas mass associated with the observed emission, using the distance to the galaxy given in Table 6.3. For IGC1, we use the distance to NGC 262 in computing the H I mass. In Table 6.5, we also give star formation rates (SFR) estimated from far infrared (FIR) fluxes and 1.4 GHz continuum emission when available. The FIR star formation rate is computed from IRAS (Infrared Astronomical Satellite) 60μm and 100μm fluxes (from the IRAS Point Source Catalog). We calculate the FIR luminosity following Sanders & Mirabel (1996) and convert this to a star formation rate using the Kennicutt (1998a) relation. The 1.4 GHz fluxes come from Condon et al. (2002). We calculate the star formation rate from the 1.4 GHz flux following Bell (2003). In Table 6.5 we also give the source of the 1.4 GHz emission reported by Condon et al. (2002): S for star formation, A for active galactic nucleus (AGN). Since the 1.4 GHz emission of NGC 262 is dominated by an AGN, we use only the FIR star formation rate.

Name	Major (arcmin)	Minor (arcmin)	Type	Distance (Mpc)
NGC 2403	21.9	12.3	Scd	3.54 ± 0.7 (M)
NGC 2366	8.1	3.3	IrDw	3.44 ± 1 (C)
UGCA 133	3.0	2.0	Im	-

Table 6.6: Properties of the NGC 2403 group. The blue major and minor diameters (in arcmin) and the galaxy morphological type come from NED. Galactocentric (GSR) distances are from NED, with the method is given in parentheses: Cepheids (C), or the average of multiple methods (M).

In order to gauge how much fuel for star formation is provided by the observed H I gas, we calculate the H I gas depletion time ($\tau_{\rm dep} = M_{\rm HI}{\rm SFR}^{-1}$) in the last columns of Table 6.5. In the galaxies for which we can estimate the SFR, the gas depletion times range from 2 to 12 Gyr. If we consider only the galaxies with estimated SFRs (NGC 262, NGC 266 and UGC 484) as part of the group, the gas depletion time of the group is $6-7$ Gyr. The inter-galaxy gas detected in IGC1 accounts for only $2-3\%$ of the atomic gas reservoir of all the galaxies in the group.

6.4.2 NGC 2403 / NGC 2366

Group Membership

Using the major disturber and tidal index given by Karachentsev et al. (2004), we find NGC 2403 to be the main disturber of two galaxies: NGC 2366 and UGCA 133. Our ATA observations of this group consist of two pointings: one centered on NGC 2403 and one centered on NGC 2366. UGCA 133 lies 1.3 degrees away from NGC 2403, and thus lies at the half power point of the ATA primary beam for the NGC 2403 pointing.

H I Detections and Previous Observations

We observed two pointings (2.5° in diameter): one centered on NGC 2403, the other on NGC 2366. The resulting images have a 3σ column density sensitivity of 1.3×10^{19} cm^{-2} of H I. The synthesized beam is $3.0' \times 1.9'$, yielding a mass sensitivity of 1.2×10^6 M$_\odot$ of H I(requiring signal in 2 adjacent velocity channels). Figure 6.6 shows the moment 0 (total intensity, left panel) and moment 1 (intensity-weighted average velocity, right panel) for the group. Note that Figure 6.6 shows a larger area than was mapped by our observations. We imaged the area of UGCA 133 (at the half-power point of the ATA beam) but did not detect H I. Chynoweth et al. (2009) also report no detection for UGCA 133. Table 6.7 gives the properties of the H I detections.

In addition to the two detected group members, we detect a third H I source at RA 07:29:50.8, Dec +69:24:13.5, which we refer to as unidentified H I cloud 1 (UHC1). This

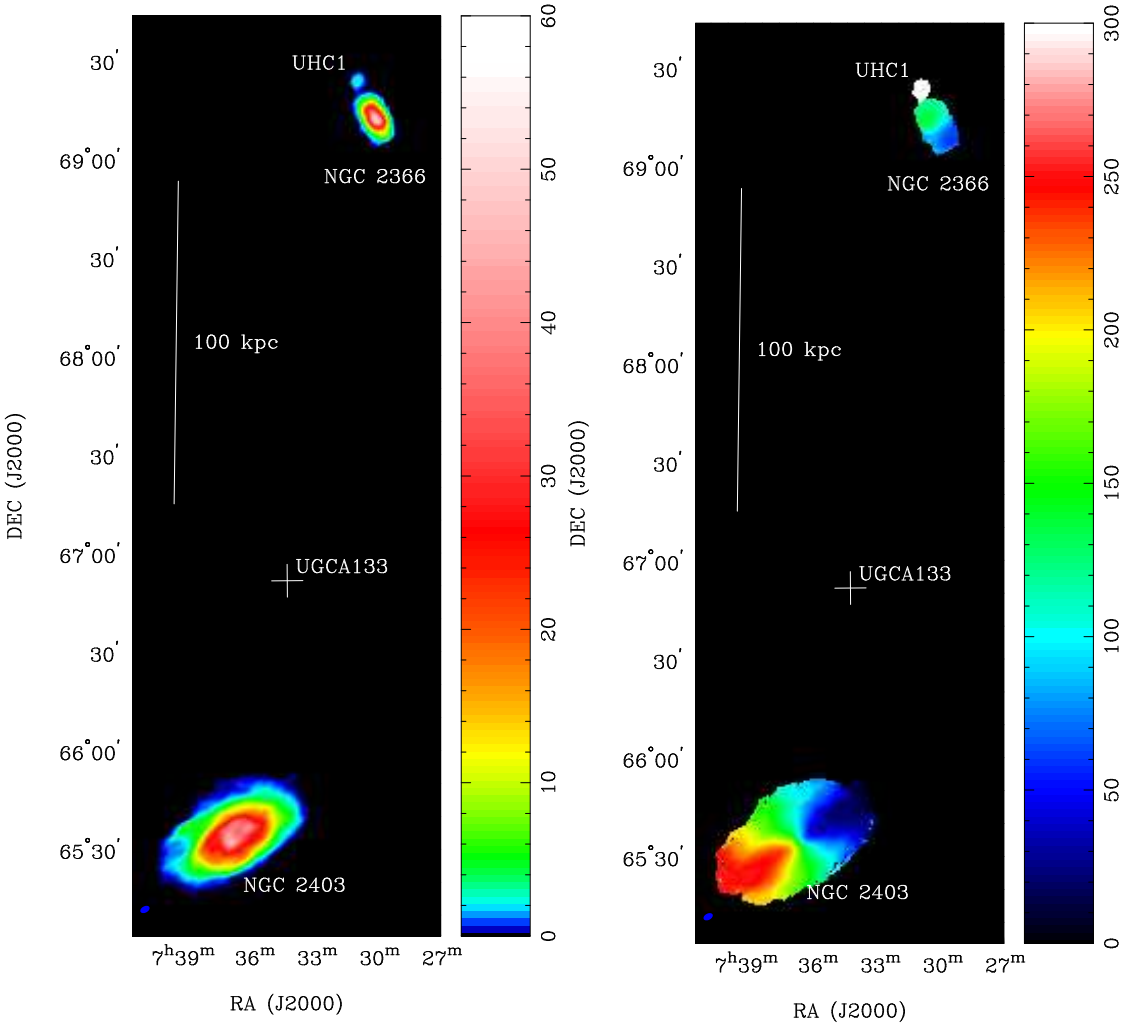

Figure 6.6: Moment 0 (total intensity) map (left) and moment 1 (intensity-weighted average velocity) map (right) of the NGC 2403 group. Each galaxy is labelled. The position of UGCA 133 (not detected) is marked by the cross. The color scale in the left panel shows intensity in Jy km s^{-1} on a logarithmic scale. The color scale in the right panel shows radio-definition velocity in km s^{-1} ($v_{\rm optical} = v_{\rm radio}(1 - v_{\rm radio}/c)^{-1}$). UHC1 lies at an average velocity of 901 km s^{-1}, off the plotted scale. The beam is shown in the lower left. The angular size corresponding to 100 kpc at the distance to NGC 2403 (3.5 Mpc) is shown by the vertical bar at the left.

Name	Prev Obs	v_{sys} (km s^{-1}) Prev	ATA	Δv (km s^{-1}) Prev	ATA	S_{HI} (Jy km s^{-1}) Prev	ATA
NGC 2403	Wal08	133	136	241	242	1054	1450
NGC 2366	Wal08	100	101	101	97	233	271
UHC1	-	-	901	-	82	-	6.7

Table 6.7: H I properties of the NGC 2403 group. The average velocity, velocity width and integrated H I flux (S_{HI}) are reported for this work (ATA) and previous (Prev) observations by the THINGS survey (Walter et al. 2008 (Wal08)).

source is very close to NGC 2366, but separated in recessional velocity by 800 km s^{-1}. A thorough search of intermediate velocity channels revealed no H I emission connecting the two galaxies. If we assume Hubble flow (with $H_0 = 70$ km s^{-1} Mpc^{-1}), the recession velocity of UHC1 (901 km s^{-1}) places it at 12.9 Mpc, 9.5 Mpc further than NGC 2366. Figure 6.7 shows the optical image (left), moment 0 contours (all panels) and moment 1 map (middle and right) of both NGC 2366 and UHC1. As the moment 1 map of UHC1 shows a velocity gradient suggestive of a rotating disk, we conclude that the emission is associated with a distant galaxy, and is merely spatially coincident with NGC 2366. A search of the NED database in the vicinity of UHC1 returns two potential matches, galaxy KUG 0724+695 (12″ away from the H I position) and 2MASX J07295446+6924093 (68″ away). Both galaxies lie within the observed H I emission. Neither galaxy has redshift information, so we are unable to determine which may host the observed H I gas.

The H I emission detected with the ATA agrees well with previous observations. Specifically, our observed H I masses for NGC 2403 and NGC 2366 agree roughly with the results from other authors: THINGS data (Walter et al. 2008; values given in Table 6.7), the work of Chynoweth et al. (2009) (3.4×10^9 M$_\odot$ for NGC 2403; 6.8×10^8 M$_\odot$ for NGC 2366), and Hunter et al. (2011) (7.4×10^8 for NGC 2366).

Aside from UHC1, we detect no H I emission outside NGC 2403 and NGC 2366. In a similar study, Chynoweth et al. (2009) used the Green Bank Telescope (GBT) to search for inter-galaxy H I clouds, finding evidence for three separate clouds. We attempt to look for these three clouds in our own data, but the first two clouds are at the level of the noise in our images and the third lies outside the field of view of our observations. Therefore, we neither confirm nor refute the H I clouds reported by Chynoweth et al. (2009).

H I Gas Mass and Star Formation Properties

In Table 6.8, we compute the H I gas mass associated with the measured emission, using the distance to the galaxy given in Table 6.6. For UHC1, we report the H I mass calculated at the Hubble flow distance as well as the distance to NGC 2366. In Table 6.8, we also give star formation rates (SFR) estimated from far infrared (FIR) fluxes, 1.4 GHz continuum emission and Hα luminosities when available. The derivation of FIR and 1.4 GHz star formation rates is given in Section 6.4.1. Hα luminosities are from the Hα Imaging Survey

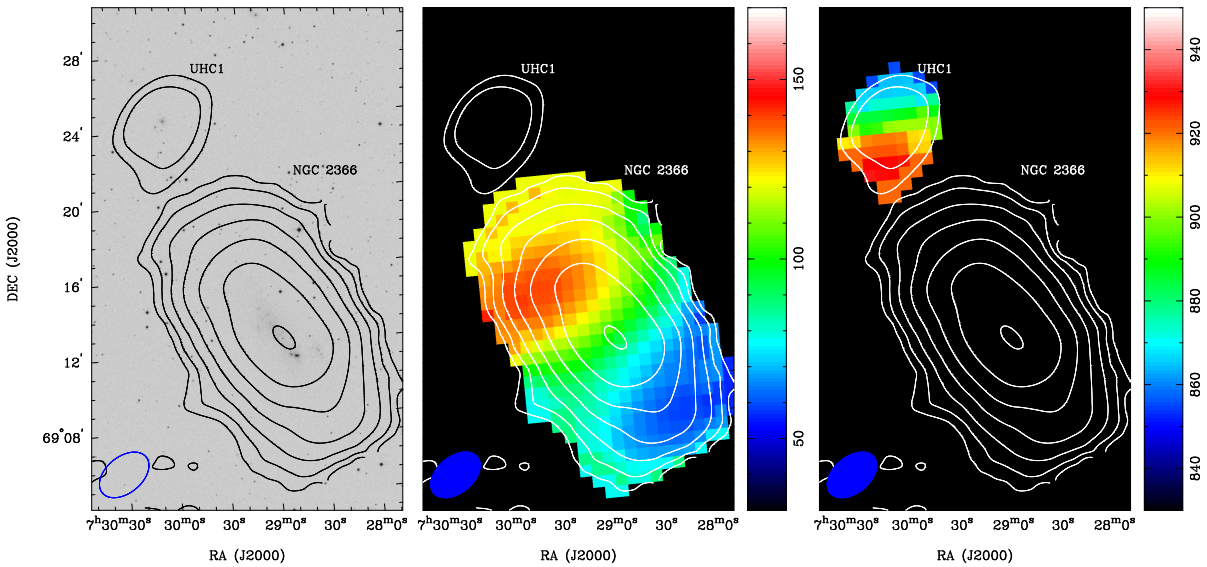

Figure 6.7: Optical image from the DSS (left panel), moment 0 (total intensity) contours (all panels) and moment 1 maps (middle and right panels) of NGC2366 and UHC1. Each galaxy is labelled. The moment 0 contours show H I column densities of $2^n \times (2 \times 10^{19}$ cm$^{-2})$ for $n = 1, 2, 3, ...$ The color scales in the middle and right panels show intensity-weighted average velocity (radio definition) in km s^{-1} for NGC 2366 (middle) and UHC1 (right). The beam is shown in the lower left.

	$M_{\rm HI}$ (10^8 $M_\odot$)		SFR ($M_\odot$ yr^{-1})					$\tau_{\rm dep}$ (Gyr)	
Name	Prev	ATA	FIR	1.4GHz	Src	Hα	Avg	Prev	ATA
NGC 2403	30.5	41.9	0.2	0.6	S	0.5	0.5	6.7	9.3
NGC 2366	6.4	7.4	0.0	0.1	S	0.1	0.1	9.7	11.3
UHC1	-	2.5 (0.2)	-	-	-	-	-	-	-

Table 6.8: H I masses and star formation properties of the NGC 2403 group. H I masses are calculated from the H I fluxes reported in Table 6.7 using the distances given in Table 6.6. The H I mass of UHC1 is calculated at the Hubble-flow distance (12.9 Mpc) and the distance of NGC 2403 (3.5 Mpc; mass given in parentheses). Star formation rates (SFR) are calculated from far infrared (FIR) fluxes, 1.4 GHz emission and Hα luminosities when available. For the 1.4 GHz SFR, we give the source of the 1.4 GHz luminosity as listed in Condon et al. (2002): S for star formation, A for AGN. The average SFR is reported in the 'Avg' column. The H I gas depletion time ($\tau_{\rm dep}$) is calculated in the last two columns using the average SFR.

by Kennicutt et al. (2008). We calculate the SFR from the Hα luminosity by applying the relation from Kennicutt (1998a), using the extinction correction based on the B-band luminosity from Lee et al. (2009). The average of the three methods is reported in Table 6.8.

The H I gas depletion time ($\tau_{\rm dep} = M_{\rm HI}{\rm SFR}^{-1}$) is given in the last columns of Table 6.8. The gas depletion times of NGC 2403 and NGC 2366 range from 6 to 11 Gyr, with a group average of 6-8 Gyr. We have not detected any H I gas between the galaxies that could serve as additional fuel for star formation.

6.4.3 M106 Group

Group Membership

For the M106 group of galaxies, we have observed one pointing, centered on M106. This galaxy was targeted for being the major disturber of several nearby galaxies according to the Karachentsev et al. (2004) catalog. However, all galaxies listed as part of the group by the Karachentsev et al. (2004) catalog lie outside of the field of view and are thus not included in the observations presented here. Table 6.9 lists the properties of the observed galaxies in the M106 field. As M106 is listed as part of the LGG 290 group by Garcia (1993), the second column indicates whether each galaxy is part of LGG 290 (NGC 4248 is listed as a possible member of the LGG290 group). Since the LGG 290 group includes many of the galaxies in the observed field, so we use this member list to inform the selection of the M106 group members.

For the purposes of this discussion, we define the M106 group to include any galaxies in the field of view which lie within 1.5 Mpc of M106 in the line of sight direction in cases where a redshift-independent distance to the galaxy is available. When only a Hubble flow distance is available, we relax this criterion in order to allow for relative velocity between

Name	LGG290 Group	Major (arcmin)	Minor (arcmin)	Type	Distance (Mpc)
M106	y	18.6	7.2	Sbc	7.4 ± 0.8 (M)
NGC 4144	y	6.9	1.7	Scd	6.6 ± 1.6 (TF)
NGC 4242	y	5.7	3.8	Scd	7.9 ± 2.3 (TF)
NGC 4248	y*	2.9[a]	0.9	Sa	7.3 ± 0.2 (TF)
NGC 4288	n	3.0	1.8	Sc	9.2 ± 1.0 (TF)
SDSS J121811.04+465501.2	n	0.5[a]	0.1	LSB	7.3 ± 0.5 (H)
2MASX J12173195+4759420	n	0.6[a]	0.5	-	10.4 ± 0.9 (H)
UGC 7391	n	1.1[a]	0.3	dblsys	9.1 ± 1.0 (H)
UGC 7392	n	1.0[a]	0.3	SBcd	11.8 ± 1.3 (H)
UGC 7401	n	0.8[a]	0.4	Im	11.3 ± 0.8 (H)
UGC 7408	y	2.6[a]	1.2	Im	6.7 ± 0.1 (H)
UGCA 281	n	0.8	0.6	Sm	5.4 ± 0.6 (M)
NGC 4217	n	5.5	1.6	Sb	19.6 ± 1.7 (TF)
NGC 4218	n	1.0	0.6	Sb	21.3 ± 5.7 (TF)
NGC 4220	n	3.8	1.4	Sa	17.9 ± 1.3 (TF)
UGC 7301	n	2.1	0.3	Sc	21.6 ± 8.3 (TF)

Table 6.9: Properties of the M106 group. Membership in the LGG290 group of galaxies is indicated in the second column (NGC 4248 is a possible member). The blue major and minor diameters and the galaxy morphological type come from Springob et al. (2005) or NED (marked by [a]). The SDSS galaxy is a low-surface brightness (LSB) galaxy (Liang et al. 2007); UGC 7391 is listed as a double system. Galactocentric (GSR) distances are from NED, with the method is given in parentheses: Tully-Fisher (TF), Cepheids (C), Hubble-flow (H), or the average of multiple methods (M).

group members. Galaxies lying above the horizontal line in Table 6.9 are considered part of the M106 group for this work.

H I Detections and Previous Observations

We observed a 2.5° diameter field centered on M106 down to a 3σ limit of 1.8×10^{19} cm^{-2} of H I with a velocity resolution of 21.6 km s^{-1}. The synthesized beam is $3.1' \times 1.8'$, yielding a mass sensitivity of 8×10^6 M$_\odot$ of H I(requiring signal in 2 adjacent velocity channels). Figures 6.8 and 6.9 show the moment 0 (total intensity) and moment 1 (intensity-weighted average velocity) maps of the entire group. The primary beam of the ATA is indicated by the red circle. Table 6.10 gives the H I properties for all detected galaxies within 2000 km s^{-1} of the systemic velocity of M106. We report the observed systemic velocity ($v_{\rm sys}$), velocity width (Δv), and H I flux ($S_{\rm HI}$). Table 6.10 also gives the H I parameters reported by previous studies: Rots 1980 (Rots80), Kovač et al. 2009 (Kov09), Schneider et al. 1992 (Sch92), or Springob et al. 2005 (Spr05).

For most of the galaxies with previous H I measurements, we find general agreement

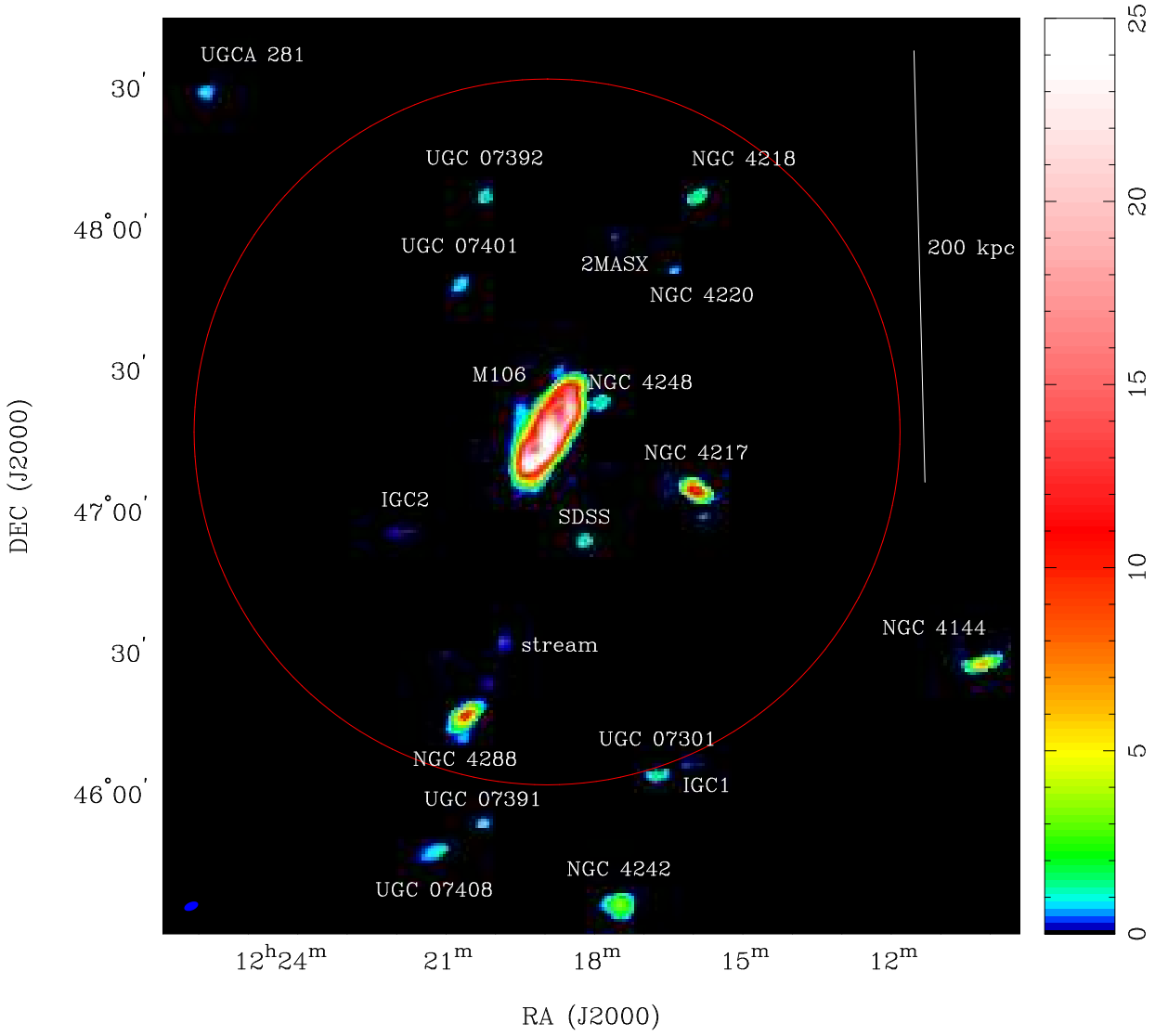

Figure 6.8: Moment 0 (total intensity) map of the M106 group. Each galaxy is labelled. The color scale shows intensity in Jy km s^{-1} on a logarithmic scale. The red circle indicates the size of the ATA primary beam. The synthesized beam is shown in the lower left. The angular size corresponding to 200 kpc at the distance to M106 (7.4 Mpc) is shown by the vertical bar at the right.

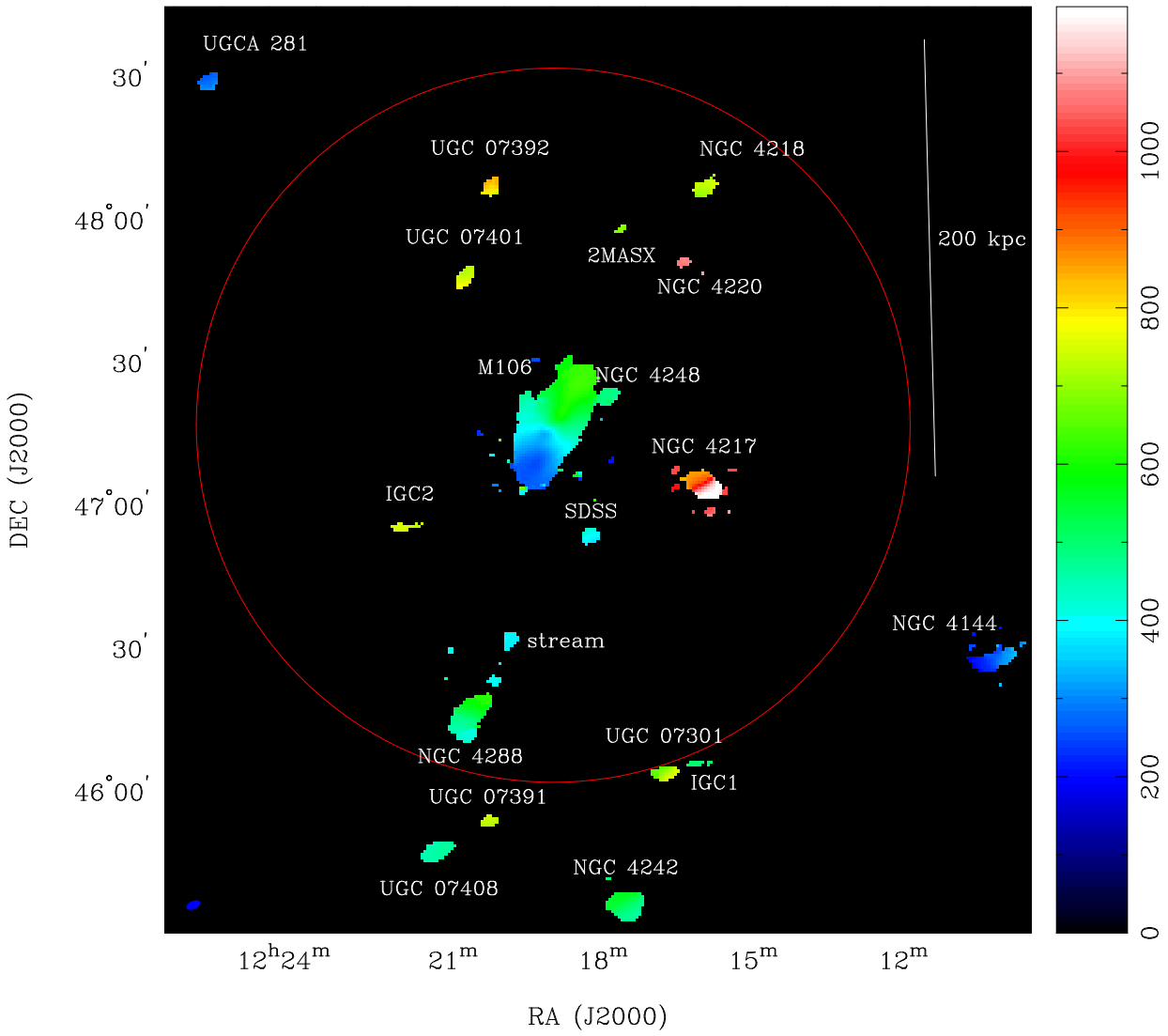

Figure 6.9: Moment 1 (intensity-weighted average velocity) map of the M106 group. Each galaxy is labelled. The color scale shows radio-definition velocity in km s^{-1} ($v_{\rm optical} = v_{\rm radio}(1-v_{\rm radio}/c)^{-1}$). Annotation is as in Figure 6.8.

Name	Prev Obs	v_{sys} (km s^{-1}) Prev	ATA	Δv (km s^{-1}) Prev	ATA	S_{HI} (Jy km s^{-1}) Prev	ATA
M106	Rots80	451	447	435	415	417.8	470.5
NGC 4144[b]	Spr05	265	266	156	151	45.3	45.8
NGC 4242[b]	Spr05	515	516	121	115	40.8	34.2
NGC 4248	-	-	486	-	55	-	2.7
NGC 4288	Spr05	535	524	177	170	36.8	38.3
SDSS	-	-	397	-	65	-	1.9
2MASX	-	-	691	-	65	-	0.5
UGC 7391[b]	Kov09	736	732	58	43	2.3	1.9
UGC 7392	-	-	807	-	110	-	2.9
UGC 7401	Sch92	741	746	57	65	1.7	2.1
UGC 7408[b]	Kov09	461	461	25	45	3.7	7.3
stream	-	-	391	-	43	-	3.0
IGC2[b]	-	-	501	-	43	-	0.9
IGC3	-	-	742	-	43	-	0.8
UGCA 281[b]	-	-	283	-	43	-	5.0
NGC 4217	Spr05	1028	1031	384	390	25.1	28.8
NGC 4218	Spr05	713	725	110	92	8.0	5.4
NGC 4220[a]	Spr05	929	1083	350	47	2.0	1.0
UGC 7301[b]	Spr05	706	710	150	130	8.5	5.5

Table 6.10: H I properties of the M106 group. The average velocity, velocity width and integrated H I flux (S_{HI}) values are reported for this work (ATA) and previous (Prev) observations: Rots 1980 (Rots80), Kovač et al. 2009 (Kov09), Schneider et al. 1992 (Sch92) or Springob et al. 2005 (Spr05).

[a] RFI interfered with the H I signal of NGC 4220, resulting in an offset systemic velocity and smaller velocity width and H I flux.

[b] These sources lie outside the half-power point of the primary beam.

between our observations and previous work. For five of the detected galaxies, we did not find a previous H I observation: NGC 4248, SDSS J121811.04+465501.2, 2MASX J12173195+4759420, UGC 7392 and UGCA 281. We further detect H I emission in three regions with no optical counterpart: a stream of H I extending to the north-west from NGC 4288 and two inter-galaxy clouds, labelled IGC1 and IGC2. We compare our findings with the recent deep optical study of the M106 group by Kim et al. (2011), but our inter-galaxy H I clouds do not match the dwarf galaxies found by that study. We discuss specific detections individually below.

NGC 4144, NGC 4242, UGCA 281, UGC 7301, UGC 7391, UGC 7408 and IGC1 are observed outside of the half power point of the primary beam of the ATA. Therefore, the measured H I fluxes are subject to increased uncertainty due to errors in the ATA primary

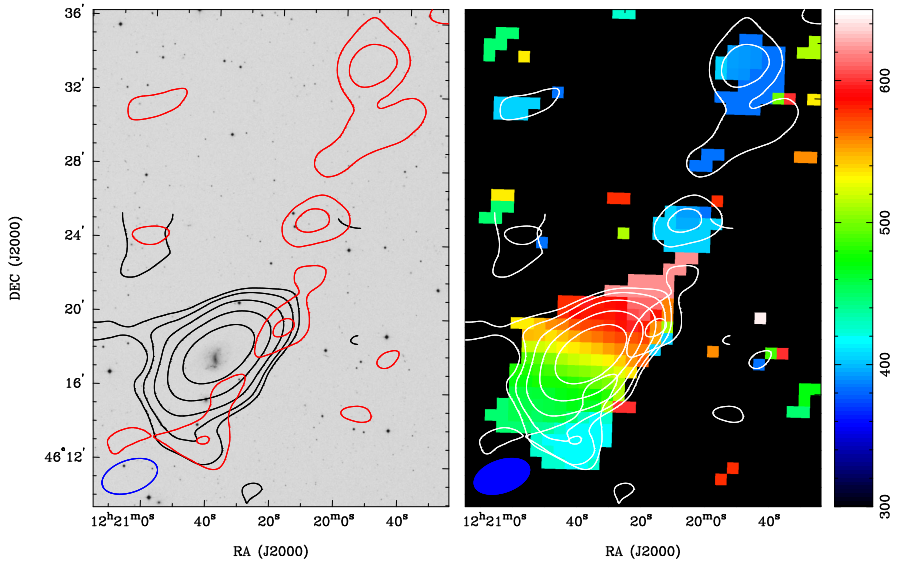

Figure 6.10: Optical image from the DSS (left panel), moment 0 (total intensity) contours (both panels) and moment 1 map (right panel) of NGC4288 and it's associated stream of H I. The moment 0 contours show H I column densities of $2^n \times (2 \times 10^{19}$ cm$^{-2})$ for $n = 0, 1, 2, 3, ...$ for the NGC2488 contours (black in left panel). The H I stream contours (red in left panel) are the same except for an additional contour at $n = -1$. The color scale in the right panel shows the intensity-weighted average velocity in km s^{-1}. The beam is shown in the lower left.

beam model.

NGC 4220: The H I velocity width and flux we observed with the ATA is lower than that reported by Springob et al. (2005). This is due to a low-significance detection of NGC 4220 which was further impeded by strong RFI in three velocity channels that should show NGC 4220 H I emission. As a result, our reported systemic velocity is offset from the Springob et al. (2005) value and our measured velocity width and flux are smaller.

Stream: We detect a stream of H I from NGC 4288 pointing in the direction of M106. Figure 6.10 shows the H I moment 0 contours overlaid on the optical image from the DSS (left panel) and the moment 1 map (right panel). The stream consists of a line of 3 to 5σ H I emission peaks consistent between two adjacent velocity channels. This stream of emission appears to emanate from the south-east, lower velocity portion of the galaxy, which shows an extension of the H I disk coincident with the south-east end of the stream. The velocity structure is consistent with the stream originating from the south-east tip of the H I disk of NGC 4288 and extending 24′ to the north-west, approximately 64 kpc at the distance to NGC 4288 (9.2 Mpc). No optical counterpart is apparent. The observed flux (assuming a distance of 9.2 Mpc) corresponds to 6×10^7 M$_\odot$ of H I, roughly 8% of the mass of the H I disk of NGC 4288.

IGC2 and IGC3: Each of the inter-galaxy H I clouds is detected at the 3σ level in two adjacent velocity channels, equivalent to a 5 sigma detection overall. Figure 6.11 shows the

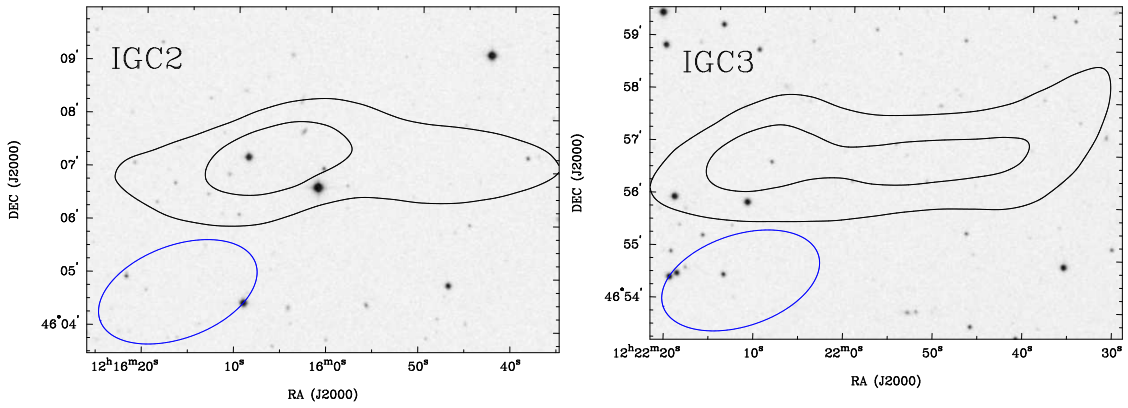

Figure 6.11: Optical images from the DSS with moment 0 (total intensity) contours overlaid for IGC2 (left) and IGC3 (right). The moment 0 contours show H I column densities of $2^n \times (2 \times 10^{19}$ cm^{-2}) for $n = -1, 0, 1, 2, 3, ...$ The beam is shown in the lower left.

moment 0 contours overlaid on the optical image from the DSS for IGC2 (left) and IGC3 (right). Assuming both clouds lie at the distance to M106, we calculate each contains 10^7 $M_\odot$ of H I.

H I Gas Mass and Star Formation Properties

In Table 6.11, we compute the H I gas mass associated with the measured emission, using the distance to the galaxy given in Table 6.9. For IGC2 and IGC3, we use the distance to M106 and for the stream, we use the distance to NGC 4288. In Table 6.11, we also give star formation rates (SFR) estimated from far infrared (FIR) fluxes, 1.4 GHz continuum emission and Hα luminosities when available. The derivation of FIR and 1.4 GHz star formation rates is given in Section 6.4.1 and the derivation of the Hα star formation rates is given in Section 6.4.2. The average of the three methods is reported in the eighth column of Table 6.11.

The H I gas depletion time ($\tau_{\rm dep} = M_{\rm HI}{\rm SFR}^{-1}$) is given in the last columns of Table 6.11. The gas depletion times of the detected galaxies are typically $3-10$ Gyr. Exceptions to this trend include the exceptionally long gas depletion time for UGC 7408 (for which we estimate a very low SFR) and the gas depletion times of less than 1 Gyr estimated in UGCA 281, NGC 4217, and NGC 4220. Including only the group members for which we have estimated a SFR, the gas depletion time of the group is ~ 4 Gyr. The H I gas detected between galaxies (IGC2, IGC3 and the stream associated with NGC 4288) account for 8×10^7 $M_\odot$ of H I, roughly 1% of the total H I gas in the group.

	$M_{\rm HI}$ (10^8 M$_\odot$)		SFR (M$_\odot$ yr^{-1})					$\tau_{\rm dep}$ (Gyr)	
Name	Prev	ATA	FIR	1.4GHz	Src	Hα	Avg	Prev	ATA
M106	54.0	60.8	0.8	2.5	SA	1.5	1.6	3.4	3.8
NGC 4144	4.7	4.7	0.0	0.0	S	0.2	0.1	5.2	5.3
NGC 4242	6.0	5.0	-	-	-	0.1	0.1	8.6	7.2
NGC 4248	-	0.3	-	-	-	0.01	0.01	-	3.3
NGC 4288	7.4	7.7	-	0.1	S?	0.04	0.1	8.7	9.0
SDSS	-	0.2	-	-	-	-	-	-	-
2MASX	-	0.0	-	-	-	-	-	-	-
UGC 7391	0.4	0.4	-	-	-	-	-	-	-
UGC 7392	-	1.0	-	-	-	-	-	-	-
UGC 7401	0.5	0.6	-	-	-	-	-	-	-
UGC 7408	0.4	0.8	-	-	-	7e-5	7e-5	585.1	1154.5
stream	-	0.6	-	-	-	-	-	-	-
IGC2	-	0.1	-	-	-	-	-	-	-
IGC3	-	0.1	-	-	-	-	-	-	-
UGCA 281	-	0.3	-	-	-	0.04	0.04	-	0.8
NGC 4217	22.8	26.1	3.0	3.6	S	-	3.3	0.7	0.8
NGC 4218	8.6	5.8	0.3	0.2	S	-	0.2	3.9	2.6
NGC 4220	1.5	0.8	0.3	0.2	S	-	0.3	0.5	0.3
UGC 7301	9.4	6.1	-	-	-	-	-	-	-

Table 6.11: H I masses and star formation properties of the M106 group. H I masses are calculated from the H I fluxes reported in Table 6.10 using the distances given in Table 6.9. The H I masses of IGC2 and IGC3 are calculated at the distance to M106; the mass of the stream is calculated at the distance to NGC 4288. Star formation rates (SFR) are calculated from far infrared (FIR) fluxes, 1.4 GHz emission and Hα luminosities when available. For the 1.4 GHz SFR, we give the source of the 1.4 GHz luminosity as listed in Condon et al. (2002): S for star formation, A for AGN. The average SFR is reported in the 'Avg' column. The H I gas depletion time ($\tau_{\rm dep}$) is calculated in the last two columns using the average SFR.

6.5 Conclusions

We have observed the H I in 3 loose groups down to a column density of 1.5×10^{19}. Given the distance to the groups and the beam size, this column density limit corresponds to a mass sensitivity limit of 4×10^8, 10^6 and 8×10^6 M$_\odot$ in the NGC 262, NGC 2403 and M106 groups respectively. In the the nearby groups, NGC 2403 and M106, this mass limit just begins to probe analogs of the high mass HVCs (Sancisi et al. 2008). We find evidence for three inter-galaxy H I clouds with masses of 10^7, 10^7 and 10^9 M$_\odot$ and a stream of H I extending from NGC 4288 containing approximately 6×10^7 M$_\odot$. This inter-galaxy gas makes up 0 to 3% of the H I gas in the group as a whole. Thus, the inter-galaxy gas with

$N_{\rm HI} \gtrsim 2 \times 10^{19}$ is insufficient to significantly increase the gas depletion time.

This result is in agreement with previous studies of H I gas between galaxies in groups. Pisano et al. (2007) observed six nearby loose groups down to $4 - 10 \times 10^5$ $M_\odot$ and found no inter-galaxy gas without an optical counterpart. In an H I survey of 5 nearby groups, Chynoweth et al. (2011) found some inter-galaxy clouds (down to a mass limit of $10^6 - 10^7$ $M_\odot$), but only in cases of strong interaction between group members. Chynoweth et al. concluded that the majority of the $M_{\rm HI} > 10^6$ $M_\odot$ inter-galaxy H I cloud population was generated by tidal stripping in interactions between group members and is not consistent with the dark matter halo population predicted by ΛCDM cosmological simulations.

The average gas depletion time of the groups in this work is $\sim 5 - 10$ Gyr, showing that the H I gas could maintain star formation for a significant amount of time if it can be transported inwards. This work and other studies (Pisano et al. 2007; Chynoweth et al. 2011) suggest H I clouds between galaxies are observed as a result of tidal interactions. While this is an important first step in constraining the importance of tidal interactions in fueling ongoing star formation, modeling of gas inflow rates and the lifetimes of inter-galaxy gas is needed to constrain the rate of fueling from the observed tidal debris. However, given the small amount of gas present and the low detection rate of inter-galaxy gas in this and previous studies, we conclude that H I disruption by tidal interactions between group members likely does not play a dominant role in replenishing the molecular gas reservoir to fuel ongoing star formation. As we found in Chapter 2, the molecular gas may be replenished by the infall and condensation of ionized gas from the hot gas halo (Maller & Bullock 2004) or from cosmological cold mode accretion (Kereš et al. 2009).

Acknowledgements

A.B. would like to thank the MMM group of the Radio Astronomy Lab at UC Berkeley for their mentoring and help with all things radio, especially Peter Williams, Garrett Keating, Melvyn Wright, Steve Croft and Casey Law. A.B. further thanks all the staff at the Allen Telescope Array for their guidance in running the array and troubleshooting problems, with special thanks to Samantha Blair and Rick Forster. This research has made use of the NASA/IPAC Extragalactic Database (NED) and the Digitized Sky Survey. NED is operated by the Jet Propulsion Laboratory, California Institute of Technology, under contract with the National Aeronautics and Space Administration. The Digitized Sky Surveys were produced at the Space Telescope Science Institute under U.S. Government grant NAG W-2166. The images of these surveys are based on photographic data obtained using the Oschin Schmidt Telescope on Palomar Mountain and the UK Schmidt Telescope. The plates were processed into the present compressed digital form with the permission of these institutions.

Chapter 7

Conclusions

In this dissertation, I have investigated several facets of the molecular gas depletion problem. I defined the problem in terms of cosmic averages, observationally constrained the molecular gas content of galaxies as a function of redshift, and finally explored a potential mechanism for making the extended atomic gas reservoir of galaxies available for star formation. I briefly review the conclusions of each of these studies below.

In Chapter 2, I derived the history of gas consumption by star formation on cosmic scales, from $z = 0$ to $z \sim 4$, using the observed cosmic densities of the star formation rate, H I and H_2 combined with measurements of the molecular gas depletion time in local galaxies. I found that closed-box models in which H_2 is not replenished by other gas require improbably large increases (with lookback time) in the density of H_2 and the gas depletion time that are inconsistent with observations. Allowing for replenishment of the molecular gas by atomic gas did not alleviate the problem because observations show very little evolution of the H I density from $z = 0$ to $z = 4$. I showed that to be consistent with observational constraints, star formation on cosmic timescales must be fueled by intergalactic ionized gas, which may come from either accretion of gas through cold (but ionized) flows, or from ionized gas associated with accretion of dark matter halos. I constrained the rate at which the extragalactic ionized gas must be converted into H I and ultimately into H_2. The ionized gas inflow rate roughly traces the star formation rate density: about $1 - 2 \times 10^8$ $M_\odot$ Gyr^{-1} Mpc^{-3} from $z \simeq 1 - 4$, decreasing by about an order of magnitude from $z = 1$ to $z = 0$. All models considered require the volume averaged density of H_2 to increase by a factor of 1.5 – 10 to $z \sim 1.5$ over the currently measured value. Because the molecular gas must reside in galaxies, this implies that galaxies at high redshift must, on average, be more molecule rich than they are at the present epoch, which is consistent with observations. These quantitative results, derived solely from observations, agree well with cosmological simulations.

As illustrated in Chapter 2, the molecular gas content of galaxies as a function of redshift is central to understanding the consumption of gas by star formation in galaxies over time. In light of the dearth of molecular gas observations at intermediate redshifts (during which time an order of magnitude decline in molecular gas fraction is expected to occur), I carried

out the Evolution of molecular Gas in Normal Galaxies (EGNoG) survey, an observational study of the molecular gas in 31 star-forming galaxies from $z = 0.05$ to $z = 0.5$. With stellar masses of $(4 - 30) \times 10^{10}$ $M_\odot$ and star formation rates of $4 - 100$ $M_\odot$ yr^{-1}, the EGNoG galaxies represent the high-mass, highly star-forming end of the main sequence of star-forming galaxies and some starburst systems, depending on the starburst criterion. To trace the molecular gas in the EGNoG galaxies, I observed the CO($J = 1 \rightarrow 0$) and CO($J = 3 \rightarrow 2$) rotational lines using the Combined Array for Research in Millimeter-wave Astronomy (CARMA). I described the details of the EGNoG survey in Chapter 3, and presented the two main results of the survey separately, in Chapters 4 and 5.

In Chapter 4, I investigated the molecular gas depletion time in normal and starburst galaxies, and the evolution of the molecular gas fraction from $z \sim 2$ to today. Using an empirically-motivated, bimodal (normal or starburst) prescription for the CO to molecular gas conversion factor based on specific star formation rate, I combined the EGNoG observations with a large sample of galaxies from the literature. I found an average molecular gas depletion time of 0.77 ± 0.57 Gyr for normal galaxies and 0.07 ± 0.04 Gyr for starburst galaxies. With 24 detections of 31 observed galaxies, I calculated an average molecular gas fraction of 7-20% at the intermediate redshifts probed by this survey, $z \sim 0.05 - 0.5$. By expressing the molecular gas fraction in terms of the specific star formation rate and molecular gas depletion time, I used the observed behavior of these two quantities to calculate the expected evolution of the molecular gas fraction with redshift and found the predicted behavior to agree well with current observations from $z \sim 2.5$ to today. In the upcoming era of the Atacama Large Millimeter/submillimeter Array (ALMA), I expect the explosion of molecular gas observations of normal star-forming galaxies at intermediate and high redshifts will vastly improve the current constraints on the evolution of the molecular gas fraction.

In Chapter 5, I used observations of the CO($J = 1 \rightarrow 0$) and CO($J = 3 \rightarrow 2$) lines in the gas excitation subsample of the EGNoG survey (four galaxies at $z \approx 0.3$) to constrain the excitation of the gas in intermediate-redshift star-forming galaxies. With robust detections of both lines in three galaxies (and an upper limit on the fourth), I calculated an average line ratio, $r_{31} = L'_{CO(3-2)}/L'_{CO(1-0)}$, of 0.46 ± 0.07 (with systematic errors $\lesssim 40\%$), which implies sub-thermal excitation of the CO($J = 3 \rightarrow 2$) line. I concluded that the excitation of the gas in these massive, highly star-forming galaxies is consistent with normal star-forming galaxies such as local spirals, not starbursting systems like local ultra-luminous infrared galaxies. Since the EGNoG gas excitation sample galaxies are representative of the main sequence of star-forming galaxies, I suggested that this result is applicable to studies of main sequence galaxies at intermediate and high redshifts, supporting the assumptions made in studies that find molecular gas fractions in star forming galaxies at $z \sim 1 - 2$ to be an order of magnitude larger than what is observed locally. This result is particularly important for the interpretation of observations of high redshift galaxies (a field expected to grow significantly in the era of ALMA), which use high-J lines to trace molecular gas.

Finally, I returned to the gas depletion problem in the local universe in Chapter 6,

investigating the role of tidal interactions in transporting atomic gas from the outskirts of galaxy disks to the central regions so that it may replenish the molecular gas and fuel ongoing star formation. I described the pilot study of H I gas in three groups of galaxies, carried out at the Allen Telescope Array (ATA), to look for inter-galaxy gas as evidence of tidal interactions between group members. I detected many galaxies not previously observed in H I as well as four previously undetected clouds of H I between galaxies. In one group, I found no inter-galaxy gas, but in the two other groups, I detected inter-galaxy gas that accounts for up to 3% of the H I reservoir of the groups. Comparing the observed H I gas masses to estimates of the star formation rates of group members, I found group H I gas depletion times of 5-10 Gyr, which implies that the H I reservoir could serve to fuel ongoing star formation if it can be transported inwards to the star-forming centers of galaxies. While the observations presented in Chapter 6 have demonstrated the presence of inter-galaxy gas, further modeling will be required to interpret these observations and derive the rate at which star formation is being fueled by tidal interactions.

Appendix A

EGNoG Data Reduction and Flux Measurement

In this appendix, we describe the reduction of the CARMA data taken as part of the Evolution of molecular Gas in Normal Galaxies (EGNoG) survey that was presented in Chapters 3, 4 and 5. Section A.1 describes the steps of the data reduction, gives the calibrator fluxes used to set the flux scale of the data, and explains the derivation of those fluxes. In Section A.2, we describe how the CO flux of each EGNoG source was calculated and estimate the error in the derived flux. Finally, Section A.3 explains the challenge of using linearly polarized calibrators to calibrate the 3mm CARMA data, which uses single, linear-polarization feeds. We present the observed polarization of calibrators 0854+201 and 1058+015 over the course of the EGNoG observations, in four epochs from November 2010 to April 2012.[1]

A.1 Data Reduction

Each dataset is reduced and calibrated as follows. The data are flagged for antenna - antenna shadowing and any other issues present during the observation (ie. high system temperature, high gains, tracking problems, etc.). The instrument bandpass is calibrated with `mfcal` on a bright passband calibrator. The time-dependent antenna gains (from atmospheric variation) are derived by performing a `selfcal` on the phase calibrator with an averaging interval of 18 minutes (the timescale of switching between the source and phase calibrator). For galaxies A5, A11, B3, B4, B7, C1 and C2, the phase calibrator (0854+201 or 1058+015), was up to 10% polarized, which required additional steps in the reduction of the 3mm data (observed with linearly polarized feeds). This is described in detail in Appendix A.3.

[1]This appendix will be submitted to the Astrophysical Journal as part of *The EGNoG Survey: Molecular Gas in Intermediate-Redshift Star-Forming Galaxies* by Bauermeister, Blitz, Bolatto, Bureau, Leroy, Ostriker, Teuben, Wong & Wright and is reproduced with the permission of all coauthors.

For each dataset, the flux of the phase calibrator is set during the antenna gain calibration in order to properly set the flux scale of the data. The flux of each phase calibrator is assumed to be constant over timescales of weeks, and is therefore determined from the best datasets of the survey using `bootflux` on bandpass-calibrated, phase-only gain-calibrated data using a planet (Uranus, Neptune or Mars) or MWC349 as a primary flux calibrator. In some cases, none of these flux calibrators was available so a bright quasar (3C84 or 3C273) was used instead, with the flux estimated using historical flux monitoring data at CARMA[2]. Table A.1 provides the flux used for each phase calibrator and the primary calibrator used. For non-planet primary calibrators, the flux used is given in parenthesis. The flux of MWC349 is calculated assuming 1.2 Jy at 92 GHz with a spectral index of 0.5, the typical value from historical flux monitoring at CARMA[2,3]. The brightness temperature (T_b) of the planets is set by the CARMA system. The brightness temperature of Mars comes from the Caltech thermal model of Mars (courtesy of Mark Gurwell), which includes seasonal variations in temperature. This model can be accessed in MIRIAD using `marstb`. For Uranus and Neptune, the CARMA system uses the following power laws:

$$T_b(\text{Uranus}) = 134.7 \left(\frac{\nu}{100\text{GHz}}\right)^{-0.337} \tag{A.1}$$

$$T_b(\text{Neptune}) = 129.8 \left(\frac{\nu}{100\text{GHz}}\right)^{-0.350} \tag{A.2}$$

Images are produced combining all fully calibrated datasets for each source. We used `invert`, weighting the visibilities by the system temperature as well as using a Briggs' visibility weighting robustness parameter (Briggs 1995) of 0.5. Since CARMA is an inhomogeneous array (these data use both the 10m and 6m dishes), we also use `options=mosaic` in the `invert` step in order to properly handle the three different primary beams patterns (10m-10m, 10m-6m and 6m-6m). All observations are single-pointing. The resulting maps are primary-beam-corrected. If channel averaging is required (based on the strength of the CO line), it is done in the `invert` step.

We deconvolve each image with `mossdi` (the mosaic version of `clean`), cleaning down to the rms noise within a single image channel, within a cleaning box selected by eye to include only source emission. We clean only channels which contain visible source emission. Cleaning down to a specified noise level is preferred to using a set number of clean iterations due to the nature of the spectral line emission: some channels will contain more flux and therefore require more clean iterations. In tests using a model source of known flux inserted into real data (emission-free channels), we found a 1σ cutoff to best extract the true source emission without overestimating the flux over a range of detection significance levels, with a 10-30% uncertainty in the recovered flux (depending on the significance of the signal). The final clean maps are produced by `restor`, which convolves the clean component map

[2]See CARMA Memo #59 (Bauermeister et al. 2012) for a description of flux monitoring at CARMA

[3]A history of MWC349 fluxes measured at CARMA is maintained at http://cedarflat.mmarray.org/fluxcal/primary_sp_index.htm

Calibrator Name	Obs. Band	Freq. (GHz)	Date Range	Flux (Jy)	Primary Calibrator (Flux in Jy)
0006–063	3mm	105	Oct 2010	1.6	MWC349 (1.28 Jy)
0010+109	3mm	109	Nov 2010	0.2	Uranus
0108+015	3mm	97	Sep 2011	2.0	Uranus; Neptune
0108+015	3mm	97	Feb 2012	1.7	Uranus
0854+201^p	3mm	107	Nov 2010	5.2	3C84 (11 Jy)
0854+201^p	3mm	98	Aug-Oct 2011	4.0	Mars
0854+201^p	3mm	98	Nov 2011	5.2	Mars
0854+201^p	3mm	98	Feb 2012	5.2	Mars
0854+201	1mm	258	Aug 2011	2.0	Mars
0854+201	1mm	254	Apr 2012	4.0	Mars
0920+446	3mm	106	Nov 2010	1.9	3C84 (11 Jy)
0920+446	3mm	106	Feb 2012	1.0	3C84 (15 Jy)
0958+655	3mm	105	Nov 2010	1.1	3C273 (12 Jy)
0958+655	3mm	105	Feb 2012	1.7	MWC349 (1.28 Jy)
1058+015^p	3mm	107	May 2011	4.6	3C84 (10 Jy)
1058+015^p	3mm	99	Nov 2011	4.1	Mars
1058+015^p	3mm	99	Feb 2012	3.6	Mars
1058+015^p	3mm	99	Apr 2012	2.8	Mars
1058+015	1mm	266	Aug 2011	2.6	Mars
1058+015	1mm	226	Apr 2012	2.0	Mars
1159+292	3mm	105	Apr-May 2011	1.4	3C84 (10 Jy); 3C273 (10 Jy)
1159+292	3mm	105	Feb 2012	0.7	Mars
1224+213	1mm	252	Apr 2012	0.6	Mars
1310+323	3mm	90	Sep-Nov 2011	1.7	Mars
1310+323	3mm	98	Apr 2012	1.4	Mars
1310+323	1mm	266	Aug 2011	0.6	MWC349 (2.0 Jy)
1357+193	3mm	105	Apr-May 2011	0.7	MWC349 (1.28 Jy)
1357+193	3mm	105	Sep-Nov 2011	0.8	Mars; MWC349 (1.28 Jy)
2134–018	3mm	106	Apr 2011	1.2	Uranus
2232+117	3mm	106	Apr 2011	1.3	MWC349 (1.28 Jy)
2232+117	3mm	97	Aug-Sep 2011	1.5	Uranus; MWC349 (1.23 Jy)
2232+117	3mm	97	Feb 2012	1.7	Uranus; Neptune; MWC349 (1.23 Jy)
3C273	3mm	98	Apr 2012	6.8	Mars
3C454.3	3mm	107	Oct 2010	39.5	Uranus

Table A.1: Summary of calibrator fluxes used to set the flux scale of EGNoG data. For each flux, the observing band (1 mm or 3 mm), frequency and date range are given. The last column gives the primary calibrator used to set the flux. For non-planet calibrators, the flux used (at the frequency given in the third column) is given in parentheses. ^{p} indicates the calibrator is linearly polarized, requiring additional reduction steps (only applicable for 3 mm data).

with the clean beam (calculated by fitting a Gaussian to the combined mosaic beam given by `mospsf`), and adds the residuals from the cleaning process.

A.2 Flux Estimation

Total source fluxes in the CO lines are calculated by summing 'source' pixels in each 'source' velocity plane of the image. The source velocity planes are selected by eye. The source pixels are those within the 'source' region which are not masked by our smooth mask, which is adapted from the masked moment method of Dame (2011). The smooth mask is created by applying a 2σ clip to a smoothed version of the image: Hanning smoothing is done along the velocity axis, and each velocity plane is convolved with a Gaussian beam twice the size of the original synthesized beam. This smoothed mask is used in order to exclude noise pixels but still capture low-level emission that a simple clip would miss. In our own testing (using a model source of known flux inserted into real data), we found a 2σ clip to best reproduce the true flux over a range of detection significance levels.

The appropriate source region size is selected to recover all of the flux without including the negative bowl. Since we do not have single dish data to complement the interferometric data presented here, our datasets are missing the shortest uv spacings. As a result, the emission in the clean maps sits in a negative bowl, which will affect the measured flux (calculated by summing pixels within a given radius). The bin A galaxies are observed with sufficiently small beam so that the galaxies are resolved. In this case, we use an elliptical source region selected by eye to enclose the spatial extent of the CO emission of each galaxy. In the case of the bins B and C galaxies, the molecular gas disks are unresolved, so we use a circular source region with the radius set to the radius at which the radial profile of the enclosed flux first peaks, thereby excluding the negative bowl. The radial profiles of the enclosed flux for bin B and C sources are shown in Figure A.1. The negative bowl is most evident in the unmasked profiles (dotted lines in Figure A.1), in which the enclosed flux peaks and then decreases with radius. We have selected the following source region radii by eye (approximately the radius at which the enclosed flux first peaks): $4.5''$ for bin C sources in the CO($J = 3 \rightarrow 2$) line (1 mm data); $5''$ for sources B1, B2, B3, B7 and B9; $6''$ for B4 and B8; $6.5''$ for bin C sources in the CO($J = 1 \rightarrow 0$) line (3 mm data); $7''$ for B6 and B10; $8''$ for B5. The source region radius for each galaxy in bins B and C is indicated by the vertical dashed line in each panel of Figure A.1. For all galaxies, the source region is indicated by the dotted white ellipse in the moment 0 and moment 1 maps of Figures 3.6 - 3.11.

The error in the flux measurement is estimated from the standard deviation of the measured fluxes using different velocity channel averaging and starting channel, using three different methods of calculating the flux in each case. The three methods are: the 2σ masking technique described above, the same masking technique with a 3σ clip, and the simple addition of all pixels (no mask) within the source region.

We performed extensive testing of our analysis technique in order to choose the param-

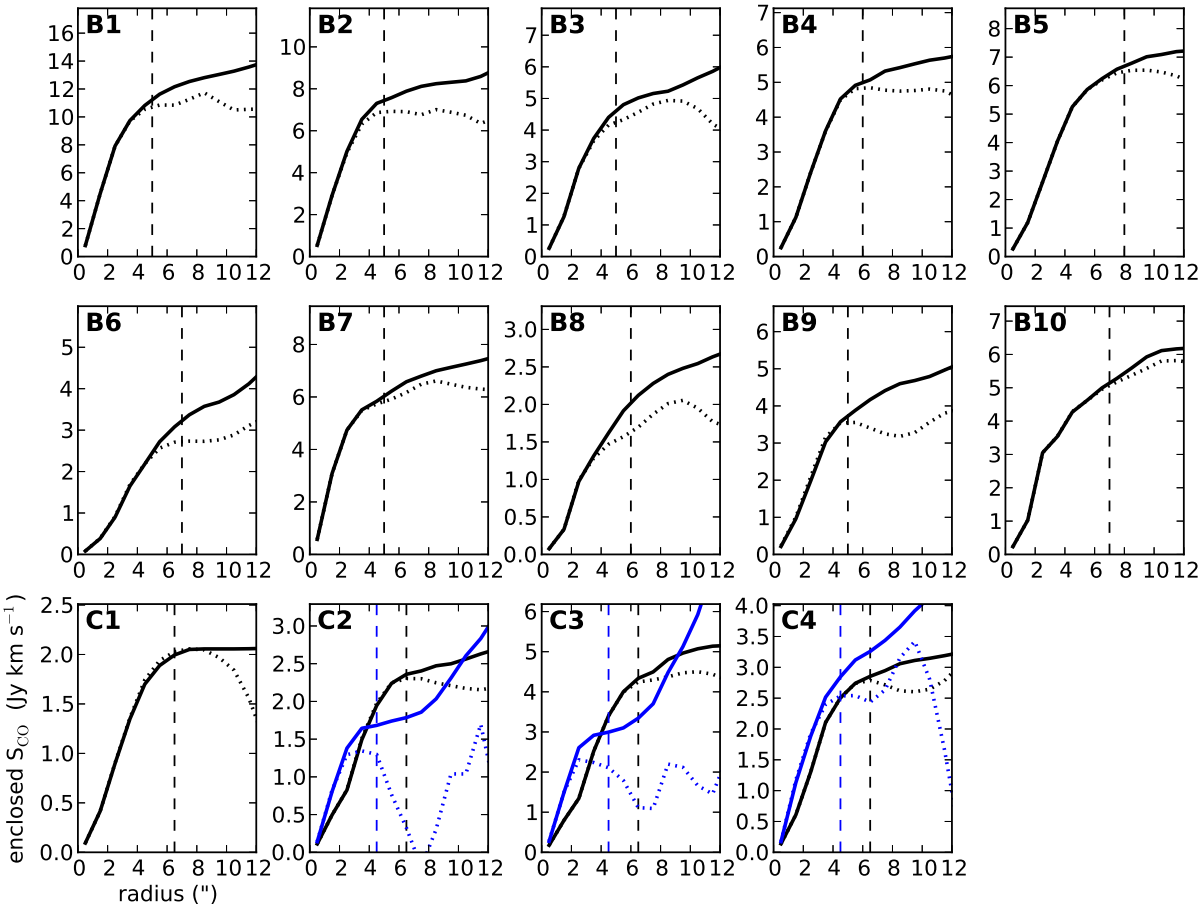

Figure A.1: Enclosed flux versus radius for bin B and C sources. The masked (unmasked) data are shown by the solid (dotted) line. The vertical dashed line indicates the source region radius used for each galaxy. For galaxies C2, C3 and C4, the CO($J = 1 \rightarrow 0$) line is in black and the CO($J = 3 \rightarrow 2$) line is in blue.

eters of the reduction to eliminate systematic offsets and minimize the uncertainty due to noise (as described above). We find a 10-30% error in the flux measurement coming from noise in the data reduction and analysis steps. From this, we take an average uncertainty of 20% in the flux estimated in each channel, which results in a uncertainty in the total flux of $20\%(N_{\rm ch})^{-0.5}$ ($N_{\rm ch}$ is the number of velocity channels in which the flux is summed). For the total flux values reported in Tables 3.9, 3.10 and 5.3, we estimate the error from the variation in the flux calculated using different channel averaging, flux measurement method, etc. (described above), which is consistent with the $20\%(N_{\rm ch})^{-0.5}$ we expect.

Further, these data suffer from systematic errors due to absolute flux calibration and primary beam correction. We set the flux scale in our dataset based on a primary flux calibrator, the flux of which is only known to $\approx 20\%$. In the primary beam correction of the dataset, pointing and focus errors at the time of the observations as well as errors in the primary beam model can significantly reduce image fidelity, leading to errors in the measured fluxes of $\approx 20\%$ (see SKA Memo #103, Wright & Corder 2008). Combining these systematic errors in quadrature, we estimate that our flux measurements suffer from systematic uncertainties of up to $\approx 30\%$. We consider all these factors in the presentation of our data in Tables 3.9, 3.10 and 5.3: for the line flux ($S_{\rm CO}$), we report the measured error; for $L'_{\rm CO}$, we include a 30% systematic error (added in quadrature to the measured error in $S_{\rm CO}$).

A.3 Polarized Calibrators

In this section we describe how we calibrated datasets which observed a strongly polarized source for gain calibration. This is for the 3mm data only, which are taken using single-polarization, linearly polarized receivers. The 1mm data uses dual-polarization, circularly polarized feeds and is thus not affected by the strong linear polarization present in some calibrators.

For Stokes I intensity I, linear polarization fraction p_{qu}, and polarization angle PA, the observed YY intensity as a function of parallactic angle χ is described by

$$YY = I\{1 - p_{qu}\cos[2(PA - \chi)]\} \tag{A.3}$$

Thus, the observed YY amplitude varies sinusoidally with parallactic angle in a dataset. Any amplitude self-calibration on the gain calibrator would assume constant amplitude with time and yield higher or lower gains according to this amplitude variation. Since this effect can be as large as 10% in some cases, we correct for it in the following way. After a phase-only `selfcal`, we use a modified version of `uvcal` to remove the known polarization effect from the calibrator data and then perform an amplitude `selfcal`. The resulting gains should represent the atmospheric variations during the track, with the influence of the polarization of the calibrator removed.

This procedure was used for two calibrators: 0854+201 and 1058+015. We do not assume stability over time in the polarization parameters of the calibrators (and in fact find

Calibrator	Epoch	$\nu_{\rm obs}$ (GHz)	Stokes I Flux (Jy)	$p_{\rm qu}$	Angle (deg)
0854+201	Nov 2010	106.6	5.2	0.10	70
	Sep 2011	98.1	4.0	0.10	67
	Nov 2011	98.0	5.2	0.10	67
	Feb 2012	98.0	5.2	0.08	54
1058+015	May 2011	107.0	4.6	0.08	19
	Nov 2011	98.9	4.1	0.09	19
	Feb 2012	98.9	3.6	-	-
	Apr 2012	98.3	2.8	0.08	94

Table A.2: Polarized calibrator parameters. The values given in the table are those that were used in the reduction of the relevant datasets. In some cases, these are not the same as the fit values. See text for discussion.

evidence for significant variation with time), so the polarization parameters for each source are derived in each epoch from the best datasets. The flux scale in most of the datasets was calibrated using MARS, with brightness temperatures from the Caltech thermal model by Mark Gurwell, which includes seasonal variations. Datasets from November 2010 and May 2011 use 3C84 as the flux calibrator. Based on flux monitoring at CARMA[4], we assumed a flux of 11 Jy in November 2010 and 10 Jy in May 2011 (both at 107 GHz).

The fits in the different epochs are shown in Figure A.2, with 0854+201 on the left and 1058+015 on the right. Flux versus parallactic angle is plotted, with data points for each dataset marked with a different symbol (indicated in the legend) and the fit line in solid black. The dotted black line shows the fit Stokes I flux. The observing frequency and fit parameters are given in the upper right corner of each panel. The polarization parameters used for each calibrator, in each epoch are given in Table A.2.

While the fit for 0854+201 in November 2010 is not well constrained due to limited parallactic angle coverage, it agrees with subsequent epochs, so we use it. The fit for 0854+201 in September 2011 is not very good due to noisy data, but the good fit from November 2011 (scaled to the average flux in September 2011; black dashed line) appears to match the September 2011 data well. Therefore, we use the November 2011 polarization fraction and angle, with an average Stokes I flux of 4.0 Jy for September 2011 (0854+201).

The data for 1058+015 from November 2011 to April 2012 suggest a radical change in polarization, from 9% polarized at 19 degrees to 8% polarized at 94 degrees over the course of 6 months. The data from February 2012 show no indication of polarization (in fact, the best fit is a negative polarization fraction). This disappearance and (rotated) reappearance of the linear polarization component of 1058+015 is coupled with a significant decrease in flux.

[4]See CARMA Memo #59 (Bauermeister et al. 2012) for a description of flux monitoring at CARMA

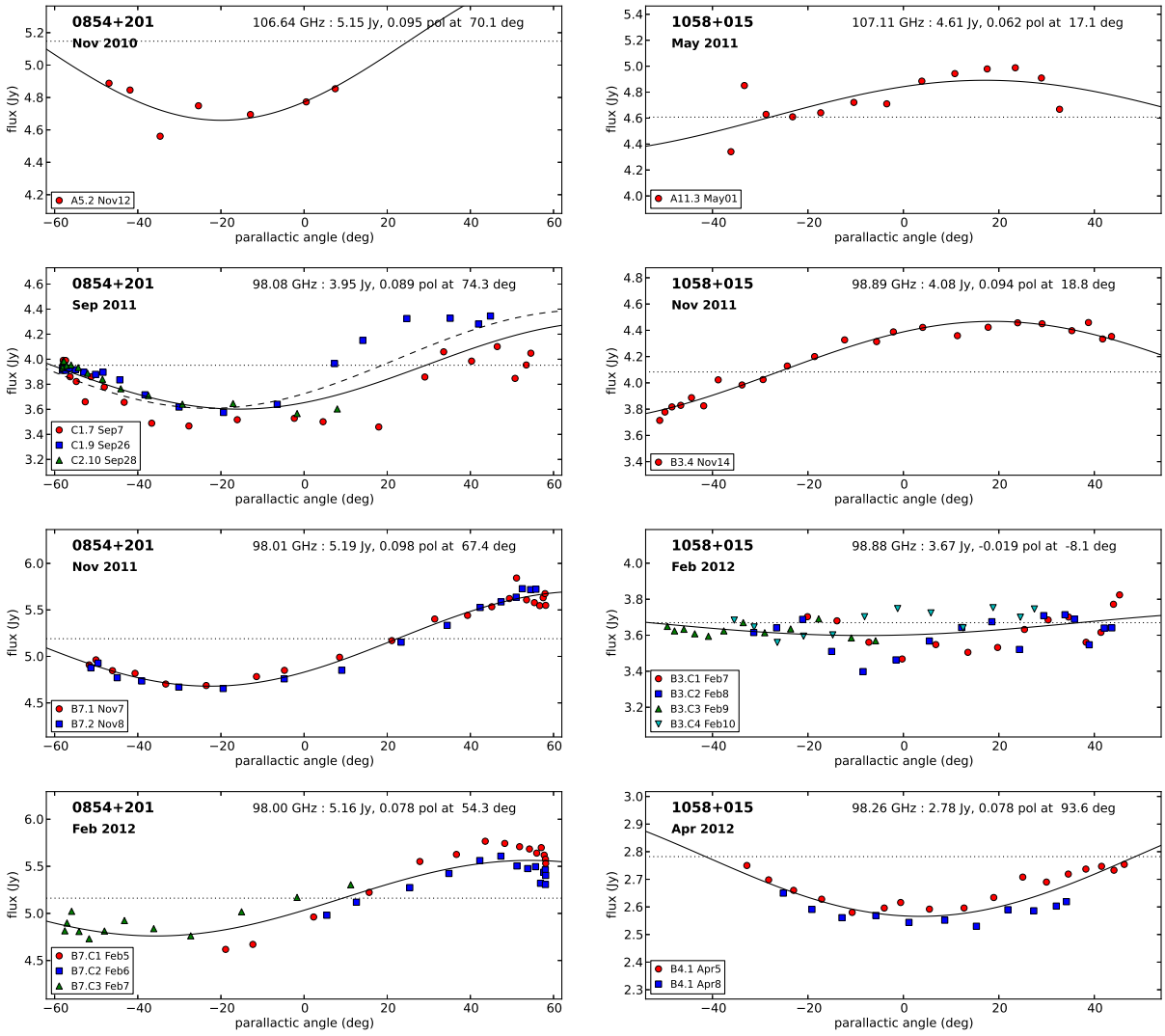

Figure A.2: Polarization of calibrators 0854+201 (left) and 1058+015 (right). In each panel, flux versus parallactic angle is plotted for the best datasets in the epoch (indicated in the upper left). The solid black line shows the fit, with the dotted black line indicating the fit Stokes I flux. Calibrator 0854+201 (left) is observed in four epochs, at 107 GHz in November 2010 and at 98 GHz in September 2011, November 2011 and February 2012. Calibrator 1058+015 (right) is observed in four epochs as well, at 107 Ghz in May 2011 and at 99 GHz November 2011, February 2012 and April 2012.

Appendix B

Monitoring of Secondary Calibrator Fluxes at CARMA

A record of historical secondary calibrator fluxes is maintained at CARMA through two types of monitoring: through dedicated flux calibration (fluxcal) tracks and by extracting calibrator fluxes from science tracks. In this chapter, fluxcal on science tracks is described, emphasizing the changes implemented in flux monitoring using science tracks in May 2012. (A description of dedicated fluxcal tracks may be found in CARMA Memo #59 , Bauermeister et al. 2012.) We briefly review the causes of variation in the measurements of secondary calibrator fluxes: both the intrinsic variability in the flux of calibration sources (the motivation for flux monitoring) as well as system-induced variations. We also present an overview of how the historical fluxes may be accessed by a CARMA user and how this record of fluxes should be used in the calibration of a science dataset.[1]

B.1 Introduction

B.1.1 Overview

Proper calibration of a dataset involves setting the flux scale using observations of a calibrator with a known flux. Typically, CARMA observations use three calibrators: a primary calibrator (ie., a planet), a bright bandpass calibrator and a less bright, but close-to-the-source, gain or phase calibrator to monitor the antenna gains over the course of the track. With perfect data, one can determine the flux of the bandpass and phase calibrators using the primary calibrator observation (using a program like **`bootflux`**). However, data are not always perfect and it is therefore always advised to check the derived calibrator fluxes against historical values. If the primary calibrator observation is of poor quality or even missing, it may be necessary to use a calibrator flux taken from historical values.

[1]This chapter is part of CARMA Memorandum Series #59, Bauermeister, Cook, Hull, Kwon & Plagge, and is reproduced with the permission of all coauthors.

There is an ongoing effort at CARMA to monitor the fluxes of secondary calibrators over time in order to maintain this historical record of fluxes. This record is used for the calibration of datasets as described above as well as in planning observations, allowing CARMA users to make informed decisions on which calibrators to observe. Calibrator fluxes are tracked in the three bands available (1cm, 3mm and 1mm) through two separate avenues: dedicated observations (see CARMA Memo #59, Bauermeister et al. 2012) and extraction of fluxes from science tracks (Fluxcal on Science Tracks, Section B.3). In both cases, the fluxes of the secondary calibrators are calibrated using a primary calibrator: typically Mars, Neptune, or Uranus. It is important to note that the planet models used are only known to $\sim 20\%$ and therefore the fluxes we derive are similarly uncertain at this level. Prior to May 2012, secondary calibrator fluxes from science tracks were assigned an error of 15% to reflect this model uncertainty. From May 2012 forward however, fluxes from science tracks are reported with measured uncertainties when possible (see Section B.3.2, step 11), which reflect the data quality but do not account for planet model uncertainties. The planet models and associated errors are discussed in detail in a separate memo on primary calibrators, Kwon et al., in preparation.

In this chapter, we clarify how the fluxes of these secondary calibrators are calculated from science tracks and describe various issues regarding flux variability that may be relevant to a user of CARMA data. A brief description of how one might use the flux monitoring data is given below.

B.1.2 How to Make Use of Flux Monitoring Data

All the secondary calibrator fluxes extracted from both the dedicated fluxcal tracks and science tracks are stored in the MIRIAD catalog file `FluxSource.cat`. This can be found in each installation of MIRIAD, but will only be as up-to-date as the MIRIAD install. The current version of FluxSource.cat for CARMA can be found on this internal site:
http://cedarflat.mmarray.org/information/carmaFluxSource.cat
The user may read the calibrator fluxes directly from the catalog file or use one of following interactive tools:

- the new website interface written by Ted Yu:
  http://carma.astro.umd.edu/cgi-bin/calfind.cgi
- the MIRIAD program **`calflux`**. Running `cvs update` in $MIRCAT will update to the latest version of the flux catalog.
- `xplore`, the CARMA calibrator locator tool by Ted Yu, which can be found at this url:
  http://cedarflat.mmarray.org/observing/tools/xplore.html
  Use File→Update to get the latest version of the flux catalog.

If you have a dataset with observations of a primary flux calibrator, a standard strategy for flux calibration is to first flag and bandpass calibrate the data as you would normally

then perform a phase-only **selfcal**. Running **bootflux** on the phase-only **selfcal**'d file will automatically calculate the true flux of the secondary calibrator over the course of the track (an averaging interval of 5 to 10 minutes is appropriate) using the planet brightness temperature written in the MIRIAD dataset by the CARMA system. If desired, the brightness temperature may be specified in the **bootflux** call by `primary=PlanetName,Tb`. It is wise at this point to compare the fluxes you derive to the historical fluxes recorded in `FluxSource.cat`, being sure to compare values taken at a similar date and frequency. Fluxes derived from science tracks from May 2012 onward also report the spectral index of the calibrator when it can be derived (see Section B.3.2). This can be used to extrapolate a flux to a different frequency in the band if desired, but should be used with caution. It is up to the discretion of the user to determine if the derived flux is appropriate or if some average from historical data should be used.

When using **bootflux**, it is important to keep the following points in mind. First, calibrator polarization, elevation-dependent gains and other issues can cause variation in the fluxes over the course of the track. See §B.2 for details. Second, the planet brightness temperature in the MIRIAD dataset is the planet model brightness temperature evaluated at the frequency of the LO. Therefore, if you are determining the flux in a window many GHz away from the LO, you may want to use a brightness temperature appropriate for the window via the `primary=PlanetName,Tb` keyword of **bootflux**.

The flux scale in your data can be set during the amplitude and phase gain calibration using the phase calibrator. For this discussion, we use an amplitude and phase **selfcal** for this step. If `options=apriori` is specified, the **selfcal** program will automatically read the `FluxSource.cat` file in your MIRIAD repository and select a flux appropriate for the date and frequency of your observation. This functionality should be used with caution: while some interpolation in time is performed, the frequency is mostly disregarded (the program only notes which of the three bands (1cm, 3mm, 1mm) the data is relevant for). Alternatively, the user can force a certain flux value in one of two ways: use the flux keyword of **selfcal** (this only works if `options=apriori` is NOT specified) or make a copy of `FluxSource.cat` in the working directory which contains the desired flux. The **selfcal** program will default to reading the local copy. A different flux catalog file can also be pointed to with the $MIRFLUXTAB variable.

Summary:

- Flag and bandpass calibrate (ie. **mfcal**) normally
- Phase-only **selfcal** with a short interval on the gain, passband and flux calibrators. Use `options=apriori` to treat the planet appropriately (as a disk).
- Run **bootflux**: ie. for the flux of 2232+117 from Uranus in the first wideband window
  ```
  bootflux vis=A1.phsc.uv select=source(2232+117,URANUS),-auto taver=10
  line=chan,1,1,39,39 primary=URANUS
  ```

- Compare the flux calculated by **bootflux** to historical fluxes from `FluxSource.cat` and decide on an appropriate flux for your calibrator. If desired, write the selected flux for your frequency and date into a local copy of `FluxSource.cat`.
- Perform an amplitude **selfcal**, setting the desired flux either in a local copy of `FluxSource.cat` or with the flux keyword of **selfcal** (and without `options=apriori`).

A full example script for the flux calibration of a typical dataset is provided in Appendix A of CARMA Memo #59.

B.2 Observed Flux Variation: Intrinsic and System-Induced

B.2.1 Intrinsic Variability

Monitoring the fluxes of secondary calibrators is important as these objects are in no way steady. For an extreme example of intrinsic variation, see Figure B.1, which shows the flux of 3C454.3 in each CARMA band as a function of time for the past four years (fluxes taken from `FluxSource.cat`).

B.2.2 Polarized Calibrators: 3 mm Perceived Variability

The 3mm feeds at CARMA are linearly polarized. The state of the system in 2011/2012 is such that the evector is defined at 90° so that the polarization of the data appears to be YY. Note that currently (Feb 2012), the data are incorrectly labelled as LL. For stokes I intensity I, linear polarization fraction p_{qu}, and polarization angle PA, the observed YY intensity as a function of parallactic angle χ is described by

$$YY = I\{1 - p_{qu}\cos[2(PA - \chi)]\}$$

This means that the 3mm flux of a polarized calibrator will appear to vary over the course of a track if the parallactic angle coverage is significant. This is illustrated in Figure B.2, which shows the flux versus parallactic angle of 0854+201 at 98 GHz from two datasets in November 2011.

B.2.3 Elevation Dependence

We have noticed in the past that some datasets show evidence for an elevation dependence in the derived flux, presumably arising from elevation-dependent gains. We merely note this here but do not investigate this effect.

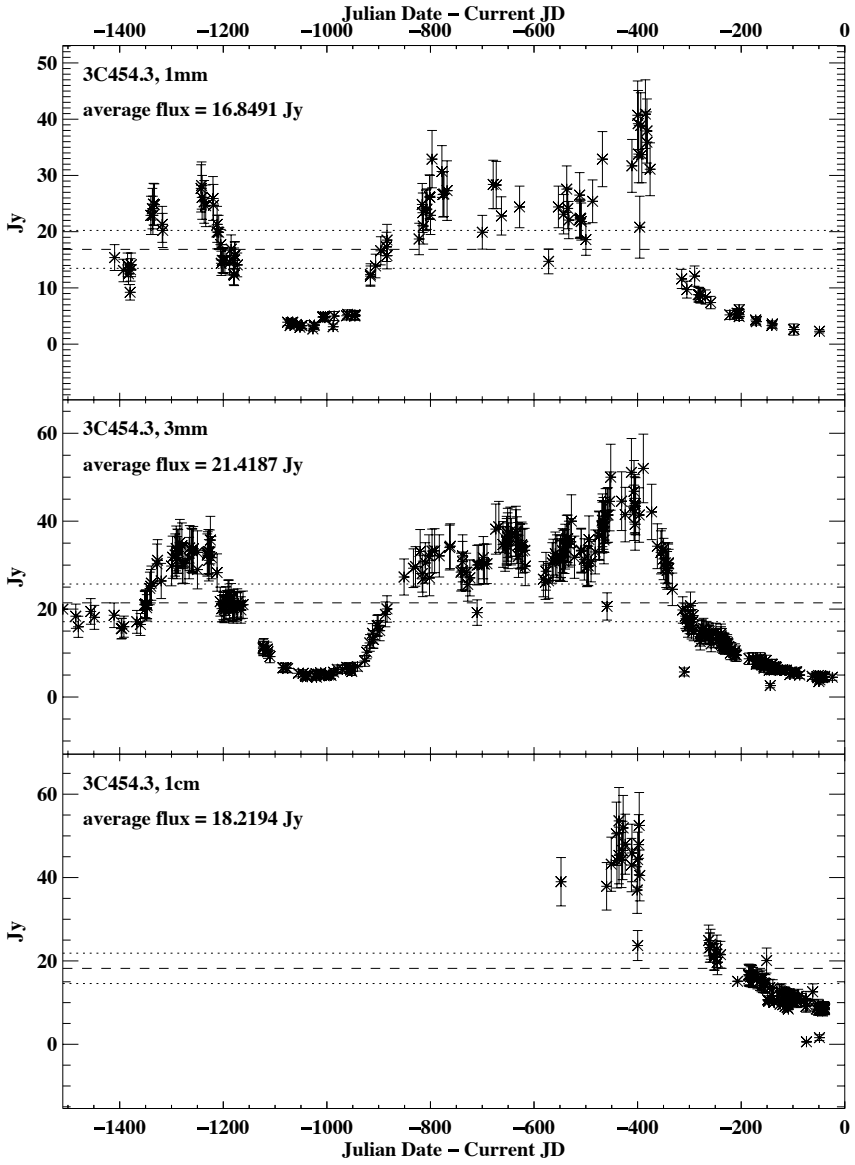

Figure B.1: Historical fluxes of the standard calibrator 3C454.3 (taken from `FluxSource.cat`) in each of the three CARMA bands. Time is plotted as 'Julian Date - Current JD' where the 'Current JD' is February 8, 2012. The dashed line indicates the average flux, with dotted lines showing plus and minus 20%.

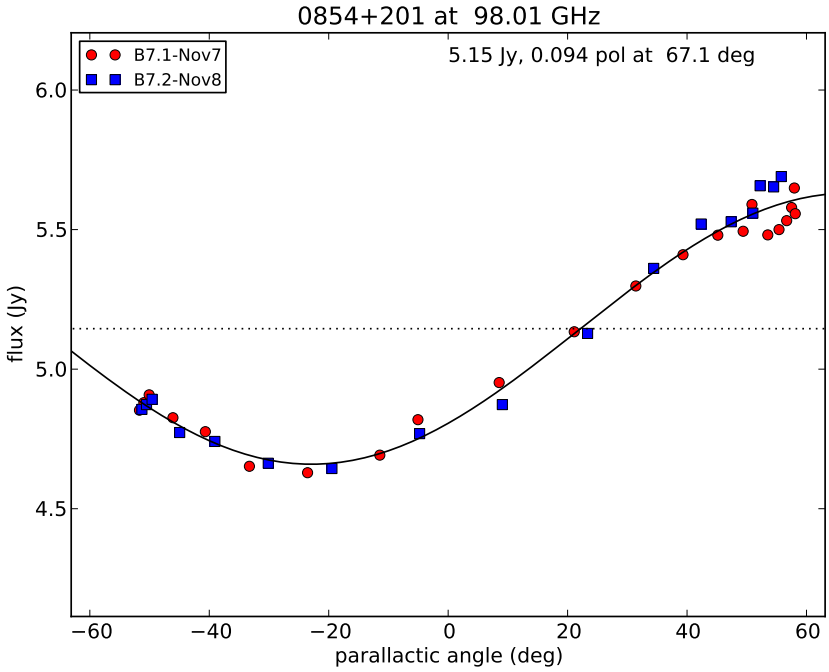

Figure B.2: Flux of 0854+201 versus parallactic angle at 98 GHz on November 7-8 2011 from datasets c0834.7D_98B7.1 and c0834.7D_98B7.2.

B.3 Fluxcal on Science Tracks

Prior to May 2012, the fluxes of secondary calibrators were extracted from science tracks with the interactive Python script `GetNewCalFlux.py`, written by Scott Schnee. Berkeley CARMA postdoc Frank Bigiel ran fluxcal on science tracks prior to February 2011, and Berkeley graduate students Amber Bauermeister, Statia Cook, Chat Hull and Katey Alatalo ran fluxcal on science tracks using this script until May 2012. This old script, `GetNewCalFlux.py`, was time-intensive to run and out-of-date, so the Berkeley graduate student team has developed a new fluxcal on science tracks reduction script, based on John Carpenter's flux extraction script, `fluxes.py`. The new script, `fluxcalOnScience.py`, has been running since May 2012, monitored by Amber Bauermeister. This task will be transferred to Manuel Fernández-López in the summer of 2012. The scripts and documentation for both the old and new fluxcal on science task can be found on the high site machines in ∼`obs/fluxcalOnScience/`.

We describe the new system for fluxcal on science tracks in detail in Section B.3.2. We also give a brief description of the old script in Section B.3.1 to inform the interpretation of secondary calibrator fluxes prior to May 2012.

calibrator name	3mm flux (Jy)	calibrator name	3mm flux (Jy)
0136+478	2.35	1911-201	2.00
0238+166	1.93	1924-292	10.18
0359+509	7.28	2148+069	2.99
0423-013	5.22	2229-085	2.72
0457-234	-	2232+117	2.67
0522-364	-	3C84	10.71
0530+135	2.26	3C111	3.12
0730-116	3.99	3C120	1.82
0854+201	4.60	3C273	14.34
0927+390	4.83	3C279	14.90
1058+015	3.81	3C345	4.43
1337-129	3.66	3C446	4.21
1517-243	1.81	3C454.3	22.18
1658+076	1.43	BLLAC	4.34
1733-130	3.93	MWC349	1.23
1751+096	4.51		

Table B.1: Secondary calibrators monitored by fluxcal on science tracks prior to May 2012, with average 3mm fluxes from `FluxSource.cat` (from March 2007 to February 2012). No historical fluxes were found for 0457-234 or 0522-364.

B.3.1 Flux Monitoring Prior to May 2012 (Manual)

The extraction of fluxes from science tracks prior to May 2012 was done using `GetNewCalFlux.py`. With this script, the secondary calibrators given in Table B.1 were monitored (this list is hard-coded into the script). Only science datasets which had one of these secondary calibrators as well as an acceptable primary calibrator (Mars, Uranus or Neptune) were processed.

The `GetNewCalFlux.py` script by Scott Schnee performs a simple calibration of each dataset, extracting the flux of the secondary calibrator in the first wide-band window in the dataset using **`bootflux`**, which uses the planet brightness temperature written in the dataset by the CARMA control system. The script displays plots of amplitude versus time and phase versus time on the calibrator, and amplitude versus uv distance on the planet so that the user can determine if any antennas or baselines are bad. The user must then flag bad data by hand and re-run the script. The error in the flux is set to either 15% of the flux value or the rms variation in the flux over the course of the track. The larger value is used, which is almost always 15% of the flux value.

Fluxes were extracted in this way for all data files on the high site which began with 'cx', 'c0' or 'c1' (science tracks) and which had acceptable primary and secondary calibrators (see above). We also made a cut based on the length of the track (typically must be longer than 1 to 2 hours) and the weather grade (B and above typically accepted). This flux

monitoring was kept up on a weekly basis: every Friday, one of the members of the fluxcal on science tracks team ran this analysis on the datasets from the past week on the high site computers. A rotation was kept so that each of the four team members did this task approximately monthly. More information on the week-to-week upkeep of fluxcal on science tracks can be found on the team's wiki site here:
http://badgrads.berkeley.edu/doku.php?id=carma_fluxcal

B.3.2 Flux Monitoring After May 2012 (Automated)

The automatic extraction of fluxes from science tracks is done on the archive computers at Illinois as tracks are copied to the archive. The script that handles the automated reduction is `fluxcalOnScience.py`, which is adapted from John Carpenter's automatic flux extraction script, `fluxes.py`. The reduction method in `fluxcalOnScience.py` is mostly the same as the original script, with added functionality for amplitude flagging, spectral index fitting and logging. In the following sections we describe the method in which fluxes are extracted by this script and then give an overview of how the script is used.

Method

The main steps of the reduction (with intermediate data files indicated in bold) are as follows

1. **Initial evaluation:** Determine the sources observed, the track length and weather grade. The weather grade is calculated from the average rmspath and tau230 values using the method in the quality script. Tracks must meet the following criteria in order to move forward:

   - Track is a science track: filename starts with 'cx', 'c0' or 'c1'.
   - Track must have a weather grade of B- or better.
   - Track must be at least 1 hour long.
   - Track must contain an acceptable primary calibrator: Mars, Uranus or Neptune.

2. **Remove bad windows** for sci2 and CARMA23 observations, writing **vis_sci2.mir**:

   - Sci2, 1cm: remove USB, windows 17-32
   - Sci2, 3mm: remove LSB, windows 1-16
   - CARMA23 (3mm): remove LSB, windows 1-8

   Note that as of this writing (May 2012), band 16 of the wide-band correlator is bad. Therefore, we remove windows 16 and 32 from sci2 tracks as well.

3. **Extract wide-band windows:** Read the correlator configuration and extract only the wide-band windows to **wb.mir**. At this point, we also extract only the LL polarization.

4. **Basic flagging:**

   - Flag shadowed antennas using **csflag**
   - Flag data at elevations above 85 degrees.
   - Flag 3 edge channels on each side of each window (controlled by EDGECHAN_FLAG)

5. **Flag spuriously large amplitudes:** This is done on each calibrator individually, with planets evaluated differently from other calibrators.

   - **Planets:** Use **uvmodel** with `options=divide` to divide the uv data by the planet model, writing **wb_planet.mir**. An average amplitude is calculated for each baseline using **uvaver** with `interval=10000`. The result is written to **wb_planet_avg.mir**. Note that the averaging method used for non-planet calibrators cannot be used here since **smauvplt** does not average planet data. The data divided by the model should have amplitude of 1 in the case of perfect data, so we consider any average data points outside (0.5,2.0) bad. Note that we only evaluate points within the first null since division by the model at the nulls results in large values which are not necessarily bad.
   - **All other calibrators:** The planet data are first removed from the dataset, writing **wb_noplanet.mir**, so that averaging can be done with **smauvplt**. The average amplitude of each baseline is extracted using **smauvplt**, `average=10000` and `options=scalar`. The minimum acceptable amplitude is set to 0.5 times the median of the average amplitudes (this is controlled by allowAmpFac_min). The maximum acceptable amplitude is set to the minimum of 1.5 times the median (controlled by allowAmpFac_max) and the absolute cut value. Historically (as recorded in `FluxSource.cat`) a flux over 55 Jy has not been observed. Therefore, we set the absolute cut value to 100 Jy for sources 3C273, 3C279, 3C454.3, 3C84 (historically the brightest) and 50 Jy otherwise. This absolute cut is in place in order to catch cases of extremely bad data which would drive the median amplitude so high that the bad data would not be caught by this method.

   Based on the criteria described above, in each window, each baseline in each calibrator observation (time slice) is evaluated as good or bad. The script then searches for trends in the bad points:

   - if $> 25\%$ of time slices are bad for a given baseline, the baseline is flagged
   - if $> 25\%$ of baselines in a time slice are bad, the time slice is flagged

- if $> 25\%$ of baselines with a particular antenna are bad in a particular time slice, flag the antenna in that time slice
- if an antenna is bad in $> 25\%$ of time slices, flag the antenna for all times

The parameter trendFraction controls the fraction (25%) of present data points above which a badness trend is established. For each window, if at least one time slice remains not flagged, with at least 50% of antennas not flagged, the window is considered good. Each calibrator is flagged for spurious amplitudes separately, but if a window is found to be bad for any calibrator, it is flagged for the entire dataset.

6. **Passband calibration:** An initial passband and phase-only gain calibration is performed using **mfcal** in order to calculate the signal to noise on each calibrator. The (non-planet) calibrator with the highest signal to noise is then used to calibrate the passband with **mfcal** using an interval of 0.5 minutes (controlled by parameter INTERVAL_PB). Antennas with average gain amplitudes within $\pm 30\%$ of the median gain amplitude are considered 'good'. If there are at least three 'good' antennas and the reference antenna is one of them, the passband calibration is considered successful. If successful, **pb.mir** is written, removing the 'bad' antennas. If not successful, see step 10.

7. **Phase-only self-calibrate** the planet and each calibrator separately using **selfcal** with an interval of 0.5 minutes (controlled by parameter INTERVAL_FLUXCAL), writing **primary.mir** and **source.mir** respectively.

8. **Derive the flux** of each calibrator in each window using **bootflux**. The planet brightness temperature is set for each window separately, using the following planet models:

   - Uranus: $(134.7\text{ K})(\nu/100\ GHz)^{-0.337}$ (CARMA control system power law)
   - Neptune: $(129.8\text{ K})(\nu/100\ GHz)^{-0.350}$ (CARMA control system power law)
   - Mars: For 3mm and 1mm data, the seasonal variation model returned by the MIRIAD program **marstb** is used (this model does not currently include diurnal variations). When running on the high site, the seasonal and diurnal variation model returned by `szaCalcMars` is used for the 1cm data. When running at Illinois, the 1cm flux is extrapolated using a straight line calculated from **marstb** values at 43 and 50 GHz, which fairly closely matches the `szaCalcMars` values.

9. **Fit the spectral index:** If there are enough wide-band windows, calculate the spectral index, α ($flux \propto \nu^{\alpha}$). If there are 2 wide-band windows, calculate α directly. If there are more than 2 wide-band windows, perform a least-squares fit on the fluxes in each window (using errors reported by **bootflux**). The fit gives the spectral index (and error) and the flux at the central frequency (and error). As an example, the

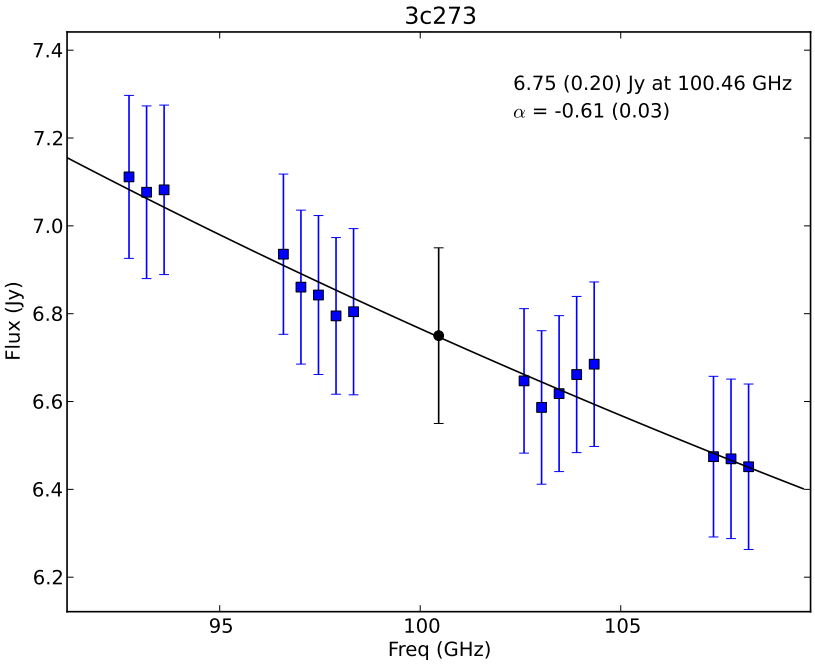

Figure B.3: Flux versus frequency for calibrator 3C273 in the dataset `c0834.5D_97B5.2.miriad`, from the `fluxcalOnScience.py` script. The blue points show the flux (with error bars showing the rms time variation) in each window. The black line shows the fit, with the derived flux (and error) at the central frequency indicated by the black point and error bar. The flux, flux error, spectral index (α) and spectral index error from the fit are listed in the top right corner of the plot.

resulting fit for calibrator 3C273 in dataset `c0834.5D_97B5.2.miriad` is shown in Figure B.3.

10. **Success?** If at least one calibrator flux was derived successfully, the script is finished. If not, the script will loop through steps 6 through 9 again using a different reference antenna. The antennas are ordered by median distance to other antennas, and used as the reference antenna starting with the smallest median distance. This is done in order to minimize atmospheric decoherence, which will have a larger effect on longer baselines.

11. **Report:** Table B.2 describes how the flux error, spectral index and the spectral index error are reported. In reporting the error in the flux, we find that the variation in the measured flux with time due to the weather and system is orders of magnitude larger than the error reported by **`bootflux`** based on the phase scatter of the data. Therefore, we only report an error when the calibrator is observed multiple times over

N_t	N_{wb}	flux	σ_{flux}	α	σ_α
1	1	**bootflux** value	-999.99	-	-
1	2	average value	-999.99	slope	-999.9
1	> 2	fit value	-999.99	fit value	fit error
> 1	1	median **bootflux** value	rms time variation	-	-
> 1	2	average value	rms time variation	slope	-999.99
> 1	> 2	fit value	time rms + fit error	fit value	fit error

Table B.2: Summary of what is reported (flux, flux error (σ_{flux}), spectral index (α), spectral index error (σ_α)) based on the number of wide-band windows (N_{wb}) and the number of times a calibrator is observed in a track (N_t). No spectral index is reported when only one wide-band window is present (indicated by -). When we are unable to accurately estimate the error in the flux or spectral index, the padding value of -999.99 is reported. For calibrators with > 1 time slice and > 2 wide-band windows, the flux error reported is the rms time variation and the fit error added in quadrature.

notScience	track does not start with 'c0', 'c1' or 'c2'
Len/Grade	track is shorter than 1 hour or has a weather grade worse than B-
NoPrimCal	track does not contain a primary calibrator (Mars, Uranus or Neptune)
noConfig	track does not contain a correlator configuration (**uvindex** output)
noWBwin	track does not contain any wide-band windows
allAmpFlag	all of the data were flagged in the amplitude flagging step
configProb0/1/2	more than one correlator configuration in the original file / after wide-band window extraction / after calibrator extraction
passband	unable to successfully passband calibrate with any refant
noGoodFluxes	unable to extract good fluxes with **bootflux**
planetRes	**bootflux** crashed with a fatal error, likely because the planet is resolved
bootfluxVar	the **bootflux** values varied by more than 25% for that calibrator (in this case, this error will be logged for each offending calibrator, with the number of offending observations in parenthesis next to the calibrator name)

Table B.3: Failure modes for automated fluxcal on science tracks script, `fluxcalOnScience.py`. If any of these are encountered (except bootfluxVar), fluxes are not derived for the calibrators in the dataset.

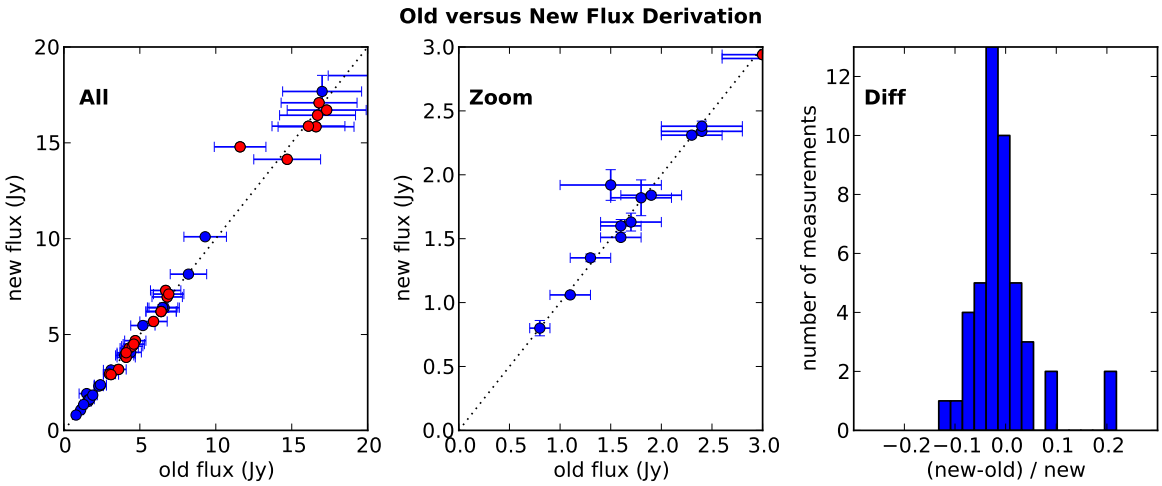

Figure B.4: Comparison of the fluxes derived by the old and new scripts. In the left and middle panels, the old flux is plotted against the new flux, with one-to-one correspondence indicated by the black dotted line. Errors are plotted in both dimensions when available. The old script flux errors are set to 15% for all calibrators. Points for which an error is not reported by the new script (see Table B.2) are plotted in red. The middle panel is the same as the left panel, showing only fluxes less than 3.0 Jy. The right panel shows a histogram of the fractional difference ((new-old)/new) in the derived flux, demonstrating that the old and new scripts almost always agree within 10%.

the course of the track. In this case, we calculate the standard deviation of the flux measurements in each window, and use the largest of these standard deviations as the error in the flux at the central frequency. When a fit is performed, we add the reported fit error in quadrature with the time variation error, but note that the effect of this is negligible since the fit error is always very small due to the nature of the fitting.

Logging and Failure Modes

The script outputs the derived fluxes (to be entered into `FluxSource_newadd.cat`) to the file `fluxcal.cat`. For each dataset, basic information and the nature of the rejection of the dataset (failure mode) is output to the file `fluxcal.log` so that those managing fluxcal on science tracks can monitor how well the script is extracting fluxes and be alerted to data issues. The possible failure modes are described in Table B.3.

Verification

Before transitioning to the new, automated script, the Berkeley team made several comparisons between the fluxes derived with the new script and the old script. We have

done a final comparison of one week's worth of datasets, with fluxes derived using the old and new scripts. The result is shown in Figure B.4. Most of the fluxes agree within 10%. It is worth noting that two of these outliers come from one dataset, which we carefully reduced by hand to find that the new script was finding the correct flux.

Management

The task of managing fluxcal on science tracks now consists of looking over the derived fluxes and associated logfile once a week to check that things are running smoothly and investigate any strange behavior that arises. Before final deployment, the vetted flux data in `fluxcal.cat` must be copied and added to the temporary holding catalog `FluxSource_newadd.cat` in MIRIAD CVS. The nightly script **`calbuild`** by Ted Yu merges `FluxSource_newadd.cat` into `FluxSource.cat`, the master flux table.

B.4 Summary

The fluxes of secondary calibrators are monitored in two ways at CARMA: through dedicated fluxcal tracks and by extracting calibrator fluxes from science tracks. In this memo we have described how each of these is carried out, emphasizing the changes recently implemented in flux monitoring using science tracks. We also describe how these fluxes may be used by a CARMA user and how the historical flux data can be accessed. We discuss both the intrinsic variability of calibration sources (the motivation for flux monitoring) as well as system-induced variations.

Bibliography

Abazajian, K. N., Adelman-McCarthy, J. K., Agüeros, M. A., et al. 2009, ApJS, 182, 543

Adelberger, K. L., Steidel, C. C., Pettini, M., et al. 2005, ApJ, 619, 697

Alves, J., Lombardi, M., & Lada, C. J. 2007, A&A, 462, L17

Aravena, M., Carilli, C., Daddi, E., et al. 2010, ApJ, 718, 177

Baldry, I. K., & Glazebrook, K. 2003, ApJ, 593, 258

Baldwin, J. A., Phillips, M. M., & Terlevich, R. 1981, PASP, 93, 5

Bauermeister, A., Blitz, L., & Ma, C.-P. 2010, ApJ, 717, 323

Bauermeister, A., Cook, S., Hull, C., Kwon, W., & Plagge, T. 2012, CARMA Memorandum Series, #59

Bayet, E., Gerin, M., Phillips, T. G., & Contursi, A. 2004, A&A, 427, 45

Bell, E. F. 2003, ApJ, 586, 794

Bell, E. F., & de Jong, R. S. 2001, ApJ, 550, 212

Bell, E. F., Papovich, C., Wolf, C., et al. 2005, ApJ, 625, 23

Blaauw, A. 1964, ARA&A, 2, 213

Blanton, M. R., Hogg, D. W., Bahcall, N. A., et al. 2003, ApJ, 592, 819

Blitz, L. 1997, in IAU Symposium, Vol. 170, IAU Symposium, ed. W. B. Latter, S. J. E. Radford, P. R. Jewell, J. G. Mangum, & J. Bally, 11

Bothwell, M. S., Kennicutt, R. C., & Lee, J. C. 2009, MNRAS, 400, 154

Bothwell, M. S., Smail, I., Chapman, S. C., et al. 2012, ArXiv e-prints, arXiv:1205.1511 [astro-ph.CO]

Bouché, N., Cresci, G., Davies, R., et al. 2007, ApJ, 671, 303

Bouché, N., Dekel, A., Genzel, R., et al. 2010, ApJ, 718, 1001

Boylan-Kolchin, M., Springel, V., White, S. D. M., Jenkins, A., & Lemson, G. 2009, MNRAS, 398, 1150

Briggs, D. S. 1995, in Bulletin of the American Astronomical Society, Vol. 27, American Astronomical Society Meeting Abstracts, #112.02

Brinchmann, J., Charlot, S., White, S. D. M., et al. 2004, MNRAS, 351, 1151

Bundy, K., Scarlata, C., Carollo, C. M., et al. 2010, ApJ, 719, 1969

Burton, W. B., Liszt, H. S., & Baker, P. L. 1978, ApJ, 219, L67

Cabanela, J. E., & Dickey, J. M. 2002, AJ, 124, 78

Carilli, C. L., Kohno, K., Kawabe, R., et al. 2002, AJ, 123, 1838

Carilli, C. L., Daddi, E., Riechers, D., et al. 2010, ApJ, 714, 1407

Cazaux, S., & Tielens, A. G. G. M. 2004, ApJ, 604, 222
Chabrier, G. 2003, PASP, 115, 763
Chiappini, C., Matteucci, F., & Gratton, R. 1997, ApJ, 477, 765
Chynoweth, K. M., Holley-Bockelmann, K., Polisensky, E., & Langston, G. I. 2011, AJ, 142, 137
Chynoweth, K. M., Langston, G. I., Holley-Bockelmann, K., & Lockman, F. J. 2009, AJ, 138, 287
Cole, S., Norberg, P., Baugh, C. M., et al. 2001, MNRAS, 326, 255
Condon, J. J., Cotton, W. D., & Broderick, J. J. 2002, AJ, 124, 675
Condon, J. J., Cotton, W. D., Greisen, E. W., et al. 1998, AJ, 115, 1693
Corbelli, E., Schneider, S. E., & Salpeter, E. E. 1989, AJ, 97, 390
Cullen, H., Alexander, P., Green, D. A., & Sheth, K. 2007, MNRAS, 376, 98
da Cunha, E., Charmandaris, V., Díaz-Santos, T., et al. 2010, A&A, 523, A78
Daddi, E., Dickinson, M., Morrison, G., et al. 2007, ApJ, 670, 156
Daddi, E., Dannerbauer, H., Stern, D., et al. 2009, ApJ, 694, 1517
Daddi, E., Bournaud, F., Walter, F., et al. 2010, ApJ, 713, 686
Dame, T. M. 1993, in American Institute of Physics Conference Series, Vol. 278, Back to the Galaxy, ed. S. S. Holt & F. Verter, 267
Dame, T. M. 2011, ArXiv e-prints, arXiv:1101.1499 [astro-ph.IM]
Dame, T. M., Hartmann, D., & Thaddeus, P. 2001, ApJ, 547, 792
Dannerbauer, H., Daddi, E., Riechers, D. A., et al. 2009, ApJ, 698, L178
Dekel, A., & Birnboim, Y. 2006, MNRAS, 368, 2
Dekel, A., Birnboim, Y., Engel, G., et al. 2009, Nature, 457, 451
Diehl, R., Halloin, H., Kretschmer, K., et al. 2006a, Nature, 439, 45
—. 2006b, Nature, 439, 45
Downes, D., & Solomon, P. M. 1998, ApJ, 507, 615
Dumke, M., Nieten, C., Thuma, G., Wielebinski, R., & Walsh, W. 2001, A&A, 373, 853
Dutton, A. A., van den Bosch, F. C., & Dekel, A. 2010, MNRAS, 405, 1690
Elbaz, D., Daddi, E., Le Borgne, D., et al. 2007, A&A, 468, 33
Elbaz, D., Dickinson, M., Hwang, H. S., et al. 2011, A&A, 533, A119
Engel, H., Tacconi, L. J., Davies, R. I., et al. 2010, ApJ, 724, 233
Fakhouri, O., & Ma, C.-P. 2009, MNRAS, 394, 1825
—. 2010, MNRAS, 401, 2245
Fakhouri, O., Ma, C.-P., & Boylan-Kolchin, M. 2010, MNRAS, 406, 2267
Fixsen, D. J., Bennett, C. L., & Mather, J. C. 1999, ApJ, 526, 207
Förster Schreiber, N. M., Genzel, R., Bouché, N., et al. 2009, ApJ, 706, 1364
Fraternali, F., & Binney, J. J. 2008, MNRAS, 386, 935
Gao, Y., & Solomon, P. M. 2004, ApJ, 606, 271
Garcia, A. M. 1993, A&AS, 100, 47
Geach, J. E., Smail, I., Moran, S. M., et al. 2011, ApJ, 730, L19
Geach, J. E., Smail, I., Moran, S. M., Treu, T., & Ellis, R. S. 2009, ApJ, 691, 783

Genzel, R., Tacconi, L. J., Gracia-Carpio, J., et al. 2010, MNRAS, 407, 2091
Ghez, A. M., Salim, S., Weinberg, N. N., et al. 2008, ApJ, 689, 1044
Gil de Paz, A., Boissier, S., Madore, B. F., et al. 2007, ApJS, 173, 185
Giovanelli, R., Haynes, M. P., Kent, B. R., et al. 2005, AJ, 130, 2598
González, V., Labbé, I., Bouwens, R. J., et al. 2010, ApJ, 713, 115
Graciá-Carpio, J., García-Burillo, S., Planesas, P., Fuente, A., & Usero, A. 2008, A&A, 479, 703
Greve, T. R., Papadopoulos, P. P., Gao, Y., & Radford, S. J. E. 2009, ApJ, 692, 1432
Hainline, L. J., Blain, A. W., Smail, I., et al. 2011, ApJ, 740, 96
Hanish, D. J., Meurer, G. R., Ferguson, H. C., et al. 2006, ApJ, 649, 150
Helfer, T. T., Thornley, M. D., Regan, M. W., et al. 2003, ApJS, 145, 259
Herbig, G. H., & Kameswara Rao, N. 1972, ApJ, 174, 401
Hernquist, L., & Springel, V. 2003, MNRAS, 341, 1253
Hibbard, J. E., & Mihos, J. C. 1995, AJ, 110, 140
Hibbard, J. E., Rupen, M., & van Gorkom, J. H., eds. 2001, Astronomical Society of the Pacific Conference Series, Vol. 240, Gas and Galaxy Evolution
Hippelein, H., Maier, C., Meisenheimer, K., et al. 2003, A&A, 402, 65
Hollenbach, D., & Salpeter, E. E. 1971, ApJ, 163, 155
Hopkins, A. M., & Beacom, J. F. 2006, ApJ, 651, 142
Hou, L. G., Han, J. L., Kong, M. Z., & Wu, X.-B. 2011, ApJ, 732, 72
Houck, J. R., Weedman, D. W., Le Floc'h, E., & Hao, L. 2007, ApJ, 671, 323
Howell, J. H., Armus, L., Mazzarella, J. M., et al. 2010, ApJ, 715, 572
Hubble, E. P. 1926, ApJ, 64, 321
Hunter, D. A., Zahedy, F., Bowsher, E. C., et al. 2011, AJ, 142, 173
Hurt, R. L., Turner, J. L., Ho, P. T. P., & Martin, R. N. 1993, ApJ, 404, 602
Ilbert, O., Salvato, M., Le Floc'h, E., et al. 2010, ApJ, 709, 644
Iono, D., Yun, M. S., & Ho, P. T. P. 2005, ApJS, 158, 1
Karachentsev, I. D., Karachentseva, V. E., Huchtmeier, W. K., & Makarov, D. I. 2004, AJ, 127, 2031
Karim, A., Schinnerer, E., Martínez-Sansigre, A., et al. 2011, ApJ, 730, 61
Kauffmann, G., Heckman, T. M., Tremonti, C., et al. 2003, MNRAS, 346, 1055
Keating, G. K., Barott, W. C., & Wright, M. 2010, in Society of Photo-Optical Instrumentation Engineers (SPIE) Conference Series, Vol. 7740, Society of Photo-Optical Instrumentation Engineers (SPIE) Conference Series
Kennicutt, Jr., R. C. 1998a, ARA&A, 36, 189
—. 1998b, ApJ, 498, 541
Kennicutt, Jr., R. C., Lee, J. C., Funes, José G., S. J., Sakai, S., & Akiyama, S. 2008, ApJS, 178, 247
Kennicutt, Jr., R. C., Tamblyn, P., & Congdon, C. E. 1994, ApJ, 435, 22
Kennicutt, Jr., R. C., Armus, L., Bendo, G., et al. 2003, PASP, 115, 928
Kereš, D., & Hernquist, L. 2009, ApJ, 700, L1

Kereš, D., Katz, N., Fardal, M., Davé, R., & Weinberg, D. H. 2009, MNRAS, 395, 160
Kereš, D., Katz, N., Weinberg, D. H., & Davé, R. 2005, MNRAS, 363, 2
Kewley, L. J., Rupke, D., Zahid, H. J., Geller, M. J., & Barton, E. J. 2010, ApJ, 721, L48
Kim, E., Kim, M., Hwang, N., et al. 2011, MNRAS, 412, 1881
Kovač, K., Oosterloo, T. A., & van der Hulst, J. M. 2009, MNRAS, 400, 743
Lacey, C. G., & Fall, S. M. 1985, ApJ, 290, 154
Lah, P., Chengalur, J. N., Briggs, F. H., et al. 2007, MNRAS, 376, 1357
Lanzetta, K. M., Wolfe, A. M., & Turnshek, D. A. 1995, ApJ, 440, 435
Larson, R. B., Tinsley, B. M., & Caldwell, C. N. 1980, ApJ, 237, 692
Lee, J. C., Kennicutt, Jr., R. C., Funes, S. J. J. G., Sakai, S., & Akiyama, S. 2009, ApJ, 692, 1305
Leroy, A. K., Walter, F., Brinks, E., et al. 2008, AJ, 136, 2782
Leroy, A. K., Walter, F., Bigiel, F., et al. 2009, AJ, 137, 4670
Leroy, A. K., Bolatto, A., Gordon, K., et al. 2011, ApJ, 737, 12
Liang, Y. C., Hu, J. Y., Liu, F. S., & Liu, Z. T. 2007, AJ, 134, 759
Lilly, S. J., Le Fevre, O., Hammer, F., & Crampton, D. 1996, ApJ, 460, L1
Lilly, S. J., Le Brun, V., Maier, C., et al. 2009, ApJS, 184, 218
Madau, P., Ferguson, H. C., Dickinson, M. E., et al. 1996, MNRAS, 283, 1388
Magdis, G. E., Rigopoulou, D., Huang, J.-S., & Fazio, G. G. 2010, MNRAS, 401, 1521
Magnelli, B., Saintonge, A., Lutz, D., et al. 2012, ArXiv e-prints, arXiv:1210.2760 [astro-ph.CO]
Maller, A. H., & Bullock, J. S. 2004, MNRAS, 355, 694
Maloney, P. 1993, ApJ, 414, 41
Mao, R.-Q., Schulz, A., Henkel, C., et al. 2010, ApJ, 724, 1336
Marengo, M. 2009, PASA, 26, 365
Mauersberger, R., Henkel, C., Walsh, W., & Schulz, A. 1999, A&A, 341, 256
McBride, J., Fakhouri, O., & Ma, C.-P. 2009, MNRAS, 398, 1858
Meier, D. S., Turner, J. L., Crosthwaite, L. P., & Beck, S. C. 2001, AJ, 121, 740
Miller, G. E., & Scalo, J. M. 1979, ApJS, 41, 513
Montero-Dorta, A. D., & Prada, F. 2009, MNRAS, 399, 1106
Motte, F., Andre, P., & Neri, R. 1998, A&A, 336, 150
Murray, N., & Rahman, M. 2010, ApJ, 709, 424
Myers, P. C. 2008, ApJ, 687, 340
Narayanan, D., Krumholz, M. R., Ostriker, E. C., & Hernquist, L. 2012, MNRAS, 421, 3127
Noeske, K. G., Faber, S. M., Weiner, B. J., et al. 2007, ApJ, 660, L47
Noordermeer, E., van der Hulst, J. M., Sancisi, R., Swaters, R. A., & van Albada, T. S. 2005, A&A, 442, 137
Noterdaeme, P., Petitjean, P., Ledoux, C., & Srianand, R. 2009, A&A, 505, 1087
Obreschkow, D., & Rawlings, S. 2009, MNRAS, 394, 1857
O'Meara, J. M., Prochaska, J. X., Burles, S., et al. 2007, ApJ, 656, 666

Omont, A., Petitjean, P., Guilloteau, S., et al. 1996, Nature, 382, 428
Pannella, M., Carilli, C. L., Daddi, E., et al. 2009, ApJ, 698, L116
Papadopoulos, P. P., Isaak, K. G., & van der Werf, P. P. 2007, ApJ, 668, 815
Papadopoulos, P. P., van der Werf, P., Xilouris, E. M., et al. 2011, ArXiv e-prints, arXiv:1109.4176 [astro-ph.CO]
Peek, J. E. G. 2009, ApJ, 698, 1429
Peek, J. E. G., Putman, M. E., & Sommer-Larsen, J. 2008, ApJ, 674, 227
Pei, Y. C., & Fall, S. M. 1995, ApJ, 454, 69
Pisano, D. J., Barnes, D. G., Gibson, B. K., et al. 2007, ApJ, 662, 959
Polychroni, D., Moore, T. J. T., & Allsopp, J. 2012, MNRAS, 422, 2992
Pound, M. W., & Teuben, P. 2012, in Astronomical Society of the Pacific Conference Series, Vol. 461, Astronomical Data Analysis Software and Systems XXI, ed. P. Ballester, D. Egret, & N. P. F. Lorente, 565
Prochaska, J. X., & Wolfe, A. M. 2009, ApJ, 696, 1543
Putman, M. E., Peek, J. E. G., & Joung, M. R. 2012, ARA&A, 50, 491
Rampazzo, R., Plana, H., Amram, P., et al. 2005, MNRAS, 356, 1177
Rao, S. M., Turnshek, D. A., & Nestor, D. B. 2006, ApJ, 636, 610
Reddy, N. A., Erb, D. K., Steidel, C. C., et al. 2005, ApJ, 633, 748
Reddy, N. A., Pettini, M., Steidel, C. C., et al. 2012, ApJ, 754, 25
Reddy, N. A., Steidel, C. C., Pettini, M., et al. 2008, ApJS, 175, 48
Regan, M. W., Thornley, M. D., Helfer, T. T., et al. 2001, ApJ, 561, 218
Rickard, L. J., & Blitz, L. 1985, ApJ, 292, L57
Riechers, D. A. 2011, ApJ, 730, 108
Riechers, D. A., Hodge, J., Walter, F., Carilli, C. L., & Bertoldi, F. 2011, ApJ, 739, L31
Riechers, D. A., Walter, F., Carilli, C. L., et al. 2006, ApJ, 650, 604
Robitaille, T. P., & Whitney, B. A. 2010, ApJ, 710, L11
Rodighiero, G., Daddi, E., Baronchelli, I., et al. 2011, ApJ, 739, L40
Rots, A. H. 1980, A&AS, 41, 189
Saintonge, A., Kauffmann, G., Kramer, C., et al. 2011, MNRAS, 415, 32
Salim, S., Rich, R. M., Charlot, S., et al. 2007, ApJS, 173, 267
Sancisi, R., Fraternali, F., Oosterloo, T., & van der Hulst, T. 2008, A&A Rev., 15, 189
Sanders, D. B., & Mirabel, I. F. 1996, ARA&A, 34, 749
Sanders, D. B., Scoville, N. Z., & Soifer, B. T. 1991, ApJ, 370, 158
Sanders, D. B., Scoville, N. Z., Young, J. S., et al. 1986, ApJ, 305, L45
Sault, R. J., Teuben, P. J., & Wright, M. C. H. 2011, in Astrophysics Source Code Library, record ascl:1106.007, 6007
Schaye, J., Dalla Vecchia, C., Booth, C. M., et al. 2010, MNRAS, 402, 1536
Schneider, S. E., Thuan, T. X., Mangum, J. G., & Miller, J. 1992, ApJS, 81, 5
Schwartz, P. R., Wilson, W. J., & Epstein, E. E. 1973, ApJ, 186, 529
Scoville, N., Aussel, H., Brusa, M., et al. 2007, ApJS, 172, 1
Scoville, N. Z., Yun, M. S., & Bryant, P. M. 1997, ApJ, 484, 702

Shetty, R., Glover, S. C., Dullemond, C. P., et al. 2011, MNRAS, 415, 3253
Shu, F. H., Adams, F. C., & Lizano, S. 1987, ARA&A, 25, 23
Simkin, S. M., van Gorkom, J., Hibbard, J., & Su, H.-J. 1987, Science, 235, 1367
Solomon, P. M., Downes, D., Radford, S. J. E., & Barrett, J. W. 1997, ApJ, 478, 144
Solomon, P. M., & Vanden Bout, P. A. 2005, ARA&A, 43, 677
Springel, V., White, S. D. M., Jenkins, A., et al. 2005, Nature, 435, 629
Springob, C. M., Haynes, M. P., Giovanelli, R., & Kent, B. R. 2005, ApJS, 160, 149
Stark, D. P., Ellis, R. S., Bunker, A., et al. 2009, ApJ, 697, 1493
Steidel, C. C., Adelberger, K. L., Giavalisco, M., Dickinson, M., & Pettini, M. 1999, ApJ, 519, 1
Strauss, M. A., Weinberg, D. H., Lupton, R. H., et al. 2002, AJ, 124, 1810
Tacconi, L. J., Genzel, R., Smail, I., et al. 2008, ApJ, 680, 246
Tacconi, L. J., Genzel, R., Neri, R., et al. 2010, Nature, 463, 781
Thilker, D. A., Braun, R., Walterbos, R. A. M., et al. 2004, ApJ, 601, L39
Tremonti, C. A., Heckman, T. M., Kauffmann, G., et al. 2004, ApJ, 613, 898
van Gorkum, J. 1993, in Astrophysics and Space Science Library, Vol. 188, The Environment and Evolution of Galaxies, ed. J. M. Shull & H. A. Thronson, 345
Wakker, B. P., & van Woerden, H. 1997, ARA&A, 35, 217
Wakker, B. P., York, D. G., Howk, J. C., et al. 2007, ApJ, 670, L113
Walter, F., Brinks, E., de Blok, W. J. G., et al. 2008, AJ, 136, 2563
Wang, J. L., Xia, X. Y., Mao, S., et al. 2006, ApJ, 649, 722
Weiß, A., Downes, D., Neri, R., et al. 2007, A&A, 467, 955
Weiß, A., Downes, D., Walter, F., & Henkel, C. 2005a, A&A, 440, L45
Weiß, A., Walter, F., & Scoville, N. Z. 2005b, A&A, 438, 533
Welch, J., Backer, D., Blitz, L., et al. 2009, IEEE Proceedings, 97, 1438
Westmeier, T., Braun, R., & Thilker, D. 2005, A&A, 436, 101
Williams, P. K. G., Law, C. J., & Bower, G. C. 2012, PASP, 124, 624
Wolfe, A. M., Gawiser, E., & Prochaska, J. X. 2005, ARA&A, 43, 861
Wong, T., & Blitz, L. 2002, ApJ, 569, 157
Wright, M., & Corder, S. 2008, SKA Memorandum Series, #103
Yao, L., Seaquist, E. R., Kuno, N., & Dunne, L. 2003, ApJ, 588, 771
York, D. G., Adelman, J., Anderson, Jr., J. E., et al. 2000, AJ, 120, 1579
Yun, M. S., Ho, P. T. P., & Lo, K. Y. 1994, Nature, 372, 530
Zwaan, M. A., Meyer, M. J., Staveley-Smith, L., & Webster, R. L. 2005, MNRAS, 359, L30
Zwaan, M. A., & Prochaska, J. X. 2006, ApJ, 643, 675